Univerisità degli Studi di Padova

CISAS "G.Colombo " Centro Interdipartimentale di Studi e Attività Spaziali

Scuola di Dottorato di Ricerca in Scienze Tecnologie e Misure Spaziali
Indirizzo di Misure Meccaniche per l'Ingegneria e lo Spazio

Ciclo XXIII

ANALYSIS, SIMULATION AND TESTING OF ADVANCED ELECTRODYNAMIC SYSTEMS FOR SPACE PROPULSION

*

Analisi, simulazione e testing di sistemi elettrodinamici avanzati per la propulsione spaziale

Direttore della Scuola: Ch. mo Prof. Giampiero Naletto

Supervisori: Ch. mo Prof. Enrico C. Lorenzini and Prof. Daniele Pavarin

Supervisore esterno: Prof. Em. Francis F. Chen

Dottorando: Davide Curreli
<davide.curreli@unipd.it>
<davide.curreli@gmail.com>

Padova, January 2011

Dedicato a mia madre e mio padre,
per il loro sostegno continuo,
e dedicato a mia moglie Chiara
per ogni nostro giorno insieme

Contents

Introduction **1**

1 Equilibrium theory of helicon discharges **3**
1.1 Plasma-Wave coupling . . . 3
1.1.1 Helicon and Trivelpiece-Gould mode-coupling . . . 3
1.1.2 Coupling with non-uniform densities . . . 9
1.1.3 Antenna Excitation . . . 10
1.1.4 Power deposition . . . 10
1.1.5 Generalizations of the plasma-wave coupling . . . 13
1.2 Macroscopic transport . . . 13
1.2.1 Remarks on the transport problem . . . 13
1.2.2 Transport models in non-magnetized discharges . . . 14
1.2.3 Analysis of collisional processes in Argon . . . 17
1.3 Discharge equilibrium . . . 23
1.3.1 Radial equilibrium model . . . 23
1.3.2 Analytical treatment of the singularity . . . 26
1.3.3 Case of constant neutral density and temperature . . . 29
1.3.4 Ionization balance . . . 31
1.3.5 Neutral depletion . . . 32
1.3.6 Energy balance . . . 35

2 Numerical modeling **39**
2.1 The HELIC-EQM code . . . 39
2.1.1 HELIC code . . . 39
2.1.2 EQM code . . . 40
2.1.3 The iterative process . . . 41
2.2 Physical results using HELIC-EQM . . . 45
2.2.1 Edge-peaked energy deposition . . . 45
2.2.2 Discharge profiles . . . 46
2.2.3 A reference case for experiments . . . 47

2.2.4 Low Pressure Effects and B-peak . . . 52
2.3 Modeling particle kinetics . . . 55
2.3.1 Single particle collider . . . 55
2.3.2 A numerical method for the free-fall regime . . . 55
2.3.3 Radial 1D PiC . . . 59
2.3.4 F3MPIC . . . 67

3 Experimental validation using Langmuir probes 69
3.1 UCLA experimental setup . . . 69
3.1.1 Vacuum plant . . . 69
3.1.2 Pressure probes . . . 69
3.1.3 Plasma source . . . 71
3.1.4 Magnetostatic field . . . 72
3.1.5 RF power supply . . . 72
3.1.6 Antenna . . . 73
3.1.7 Matching network . . . 73
3.2 RF compensated Langmuir probes . . . 73
3.2.1 Probes construction . . . 73
3.2.2 RF compensation . . . 74
3.2.3 Probe positioning . . . 75
3.2.4 Acquisition system . . . 76
3.2.5 Test types . . . 76
3.3 Langmuir probe data . . . 77
3.3.1 Analysis of the experimental I-V traces . . . 77
3.3.2 Experimental results . . . 84
3.4 Comparison of experimental data with theory and discussion . . . 117
3.5 An experimental note about the influence of stray elements on the impedance matching . . . 121
3.5.1 High-L loads . . . 123
3.5.2 Low-L loads . . . 126

4 Applications 129
4.1 Plasma propulsion using helicon sources . . . 129
4.1.1 Propulsive parameters . . . 129
4.1.2 Identification of thruster configurations . . . 135
4.2 Propellantless propulsion using tethers . . . 143
4.2.1 Exploitation of environmental plasma for propulsion . . . 143
4.2.2 Electrodynamic force and power . . . 143
4.2.3 New insights on the orbital dynamics of an EDT . . . 146
4.2.4 Equilibrium positions . . . 151
4.2.5 Self-powering at equilibrium positions . . . 153

4.2.6 Applications in the Jupiter Plasma Torus 156

Conclusion **163**

Bibliography **167**

A Plasma waves **173**
A.1 Dielectric tensor of a cold plasma ($T = 0$) 173
A.2 Dielectric tensor with fluid collisions 177
A.3 Generalization to non-Maxwellian plasmas 177
A.4 Finite temperature ($T \neq 0$) Maxwellian plasma 181
A.5 Plasma with two Maxwellian populations 183
A.6 Finite Larmor radius effects 183

List of Figures

1.1 Values of the Stix components S, D, P in the cold approximation for (a) a typical Deuterium fusion plasma, and (b) a typical helicon Argon plasma . 4

1.2 (a) Dispersion relation of Helicons and Trivelpiece-Gould waves; (b) range of k_{min} and k_{max} of the helicon branch vs. the frequency 6

1.3 RF fields inside a plasma cylinder for two radial profiles of plasma density, a uniform profile (results are in blue) and a parabolic profile (results are in black). On the first row of plots there are: the two profiles of $n(r)$ uniform and parabolic, both starting at $n = 5 \times 10^{17}$ m^{-3}, the radial profile of power deposition $P(r)$, and the axial profile of power deposition in unbounded conditions. The 2^{nd}, 3^{rd} and 4^{th} rows show the real components of magnetic field, electric field and plasma currents respectively. Imaginary components are not reported; fields and currents are evaluated at the following conditions: plasma radius=10 cm, antenna located on the plasma surface $r_a = 10$ cm, external conducting boundary at $r_c = 20$ cm, wave numbers $m = 0$, $k = 10$ rad/m, magnetostatic field $B_0 = 250$ Gauss, plasma of Argon, homogeneous neutral gas at $p_0 = 3.0$ mTorr, $T_e = 5$eV, antenna current $I_0 = 1.0$ A, frequency $f = 13.56$ MHz; calculated fields pertains to the axial coordinate $z = 0$, i.e. they are evaluated on the antenna plane. . . 11

1.4 Antenna spectra for the $m = +1$ component of several antenna geometries, for a current $I_0 = 1.0$ A 12

1.5 (a) Interaction potential versus internuclear separation for Ar atoms; atomic units are 27.2 eV and 0.529×10^{-10} m; (b) Total σ_t, viscosity σ_v and inelastic σ_{vuv}, σ_i cross sections for symmetric Ar atom - Ar atom collisions. Both figures are adopted from [13]. 18

1.6 Frequencies of electron-ion and electron-electron Coulomb collisions versus the plasma density for three values of electron temperature 19

1.7 Argon cross-sections (a) ion-neutral; (b) electron-neutral. 21

1.8 (a) electron-Argon collision probabilities mediated over a Maxwellian [figure adopted from [21]], (b) source rate vs. neutral pressure 21

1.9 Illustration of the short-circuit effect 24

1.10 (a) Analytical subsonic solution (for q=k=1.0); (b) comparison of the subsonic solution with the numerical integration of the full equation. 28
1.11 (a) Solutions of Eq.1.74 for three different values of k; in each case the sheath edge ρ_a occurs at a different value of ρ, (b) Solutions of Eq.1.74 for 15 mTorr of Argon and $K_B T_e = 3$ eV, yielding v/C_s (black), n/n_0 (blue) (red, right scale); the latter two are related by the Boltzmann relation. The abscissa is normalized so that the sheath edge occurs at $r = a$. The curves retain the same shape for any value of a. 29
1.12 Comparison of the solutions for constant n_n and KT_e at different pressures regimes; at high pressures (black curve at 100 mTorr, or 13.3 Pa) the plasma solution, showed in the $n/n(0)$ graph, gets closer to Bessel diffusive solution (Eq. 1.43); at lower pressures (red curve at 20 mTorr = 2.67 Pa, and blue curve at 5 mTorr = 0.67 Pa) the solution shifts continuously toward the free-fall (Eq. 1.45); the calculation has done for Argon in a discharge of 2.5 cm of radius. 30
1.13 Relation between T_e and pressure in Argon discharges of various radii. . . 33
1.14 Neutral depletion effect for an Argon discharge at initial pressure of $p_0 =$ 1 mTorr = 0.13 Pa and 400K (a) the different plasma profiles, (b) plasma potentials, (c) neutral pressure, (d) electron temperature. Neutrals are depleted at the center from the center of the discharge; the electron temperature is affected by a fast rise when neutrals are depleted. 36
1.15 Energy required to make one ionization vs. electron temperature. 37

2.1 Geometry of the HELIC code (Figure credit: [23]) 39
2.2 EQM inner cycle 42
2.3 HELIC-EQM cycle 43
2.4 Radial energy deposition profiles for three selected cases, with different magnitudes of the TG mode (densities of 12.6, 5.0 and 1.6 $\times 10^{17}$ m^{-3}, B = 65 Gauss and tube radius is 2.5 cm), and the resulting profiles from the EQM solution 46
2.5 Radial profiles obtained by iteration of HELIC-EQM, for a 15 mTorr = 2 Pa helicon discharge at 65 Gauss with 400 W of RF at 13.56 MHz and an $m = 0$ antenna, (a) deposited power per unit current and unit length, (b) drift velocity normalized to the Bohm velocity, (c) potential, (d) plasma density, (e) neutral pressure, (f) electron temperature. 48
2.6 Radial profiles obtained by iteration of HELIC-EQM, for a 15 mTorr = 2 Pa helicon discharge at 65 Gauss with 400 W of RF at 27.12 MHz and an $m = 0$ antenna, (a) deposited power per unit current and unit length, (b) drift velocity normalized to the Bohm velocity, (c) potential, (d) plasma density, (e) neutral pressure, (f) electron temperature. 49

2.7 Radial profiles obtained by iteration of HELIC-EQM, for a 15 mTorr = 2 Pa helicon discharge at 120G with 1000W of RF at 27.12 MHz and an $m = 0$ antenna, (a) deposited power per unit current and unit length, (b) drift velocity normalized to the Bohm velocity, (c) potential, (d) plasma density, (e) neutral pressure, (f) electron temperature. 50

2.8 Radial profiles obtained by iteration of HELIC-EQM, for a larger tube at lower pressure of 5 mTorr = 0.67 Pa, helicon discharge at 250 Gauss with 400 Watt of RF at 13.56 MHz and an $m = 0$ antenna, (a) deposited power per unit current and unit length, (b) drift velocity normalized to the Bohm velocity, (c) potential, (d) plasma density, (e) neutral pressure, (f) electron temperature. 51

2.9 B_0=500 Gauss 53

2.10 B_0=300 Gauss 53

2.11 B_0=100 Gauss 54

2.12 Low pressure behavior for decreasing magnetic field for the cases B_0=80, 40, 20, 10 Gauss 54

2.13 Ion losses toward the wall in a magnetized cylinder 55

2.14 Scheme of the discretization 57

2.15 Long-mean-free path solution in planar geometry, with constant ionization [6] 60

2.16 (a) Cylindrical random function inside the interval $[0, ..., 1]$, and (b) its behavior for random numbers. Particles fall more likely on the external region of the interval, due to deformation in cylindrical topology. 62

2.17 Tests of loading 5000 particles in cylindrical geometry: (a) Uniform distribution; (b) Gaussian in the middle; (c) a double *erf* function in the middle and in the edge. 64

2.18 Sheath formation at the wall of an Argon plasma cylinder, as calculated with the radial 1D PiC (GRIDPIC), and comparison with the analytical curve. . 66

2.19 Schematics of the F3MPIC code. 68

3.1 UCLA experimental apparatus 70

3.2 The two tested plasma sources (a) stubby tube (b) elongated source 71

3.3 (a) Magnetic field lines of the Neodimium toroid; (b) magnetic field intensity along the symmetry axis of the Neodimium toroid (here the z axis starts from the center of the toroid) 72

3.4 Electric scheme of the RF circuit, with the L-type matching box in the standard configuration 73

3.5 (a) Apparatus for testing the RF choke of the Langmuir probes; (b) internal impedances in the RF choke 74

3.6 Testing with the oscilloscope of the RF choke, by using a synthetic RF signal of $V_{in}^{p-p} = 10$ Volt: (a) without the choke impedance (ordinate 1 division = 5 Volts), (b) with two chokes at 13.56 and 27.12 MHz (ordinate 1 division = 0.2 Volt) . . . 75
3.7 View of the Langmuir probe inside the cylinder of the plasma source 75
3.8 Test of the HIDEN acquisition system with a Zener diode ECG5121A, nominal Zener voltage of -7.5 Volts . . . 76
3.9 (a) Example of Langmuir probe potential ramp between -100/+30 Volts, with error bars on the applied input voltage; (b) collected current over 5 different ramps, with the averaged IV line, and error bars over the values of measured currents; (c) standard deviation of the collected current: data are more scattered in the electronic current region than the ionic region; (d) averaged spline of the IV trace (black), and first derivative of the splined curve (blue). . . . 79
3.10 (a) First derivative of the splined current; (b) ion current fit with the OML model; (c) electron current fit with a Maxwellian; . . . 81
3.11 Power scan at 13.56MHz and for a fixed pressure of 15.0mTorr, inside the helicon source, (a) experimental setup, with the Langmuir probe position marked with a red dot; (b) experimental IV traces for increasing power levels; (c) plasma density vs. power; (d) electron temperature vs. power; (e) plasma potential vs. power; (f) estimate of the ioniation fraction. [res1a] 86
3.12 Ion and electron current fit for a 15.0 mTorr Argon plasma, inside the helicon source, with RF power of (a), (b) 50 Watt; (c), (d) 80 Watt; (e), (f) 100 Watt. [res1a] . . . 87
3.13 Ion and electron current fit for a 15.0 mTorr Argon plasma, inside the helicon source, with RF power of (a), (b) 200 Watt; (c), (d) 300 Watt; (e), (f) 350 Watt. [res1a] . . . 88
3.14 Power scan at 13.56MHz and for a fixed pressure of 15.0mTorr, downstream, (a) experimental setup, with the Langmuir probe position marked with a red dot; (b) experimental IV traces for increasing power levels; (c) plasma density vs. power; (d) electron temperature vs. power; (e) plasma potential vs. power; (f) estimate of the ioniation fraction. [res1b] . . . 90
3.15 Ion and electron current fit for a 15.0 mTorr Argon plasma, downstream, with RF power of (a), (b) 100 Watt; (c), (d) 200 Watt; (e), (f) 300 Watt. [res1b] . . . 91
3.16 Ion and electron current fit for a 15.0 mTorr Argon plasma, downstream, with RF power of (a), (b) 400 Watt; (c), (d) 800 Watt; (e), (f) 1000 Watt. [res1b] . . . 92
3.17 Axial scan at 13.56MHz along the cylinder. [res03] . . . 94
3.18 Axial scan, ion and electron current fit, at locations $z = 3, 8, 9$ cm respectively [res03] . . . 95

3.19 Axial scan, ion and electron current fit, at locations $z = 10, 11, 14$ cm respectively [res03] 96
3.20 Radial scan at 13.56MHz and 400 Watt along the radius of the chamber. [2a] 97
3.21 Radial scan at 13.56MHz and 400 Watt along the radius of the chamber. [2b] 98
3.22 Radial scan at 13.56MHz and 400 Watt and several B fields, along the radius of the chamber. [res06] 99
3.23 Power scan at several pressures (a) experimental setup, with the Langmuir probe position marked with a red dot; (b) experimental IV traces at 3.0mTorr; (c) plasma density vs. power; (d) electron temperature vs. power; (e) plasma potential vs. power; (f) estimate of the ioniation fraction. [4a] 102
3.24 Ion and electron fit at 10.0 mTorr for powers of (a) (b) 50 Watt, (c) (d) 100 Watt, (e) (f) 300 Watt [res4a] 103
3.25 Ion and electron fit at 7.5 mTorr for powers of (a) (b) 50 Watt, (c) (d) 100 Watt, (e) (f) 300 Watt [res4a] 104
3.26 Ion and electron fit at 5.0 mTorr for powers of (a) (b) 50 Watt, (c) (d) 100 Watt, (e) (f) 250 Watt [res4a] 105
3.27 Ion and electron fit at 3.0 mTorr for powers of (a) (b) 50 Watt, (c) (d) 100 Watt, (e) (f) 250 Watt [res4a] 106
3.28 Pressure scan at low-power, inside the helicon source, (a) experimental setup, with the Langmuir probe position marked with a red dot; (b) experimental IV traces at 150 Watt; (c) plasma density vs. power; (d) electron temperature vs. power; (e) plasma potential vs. power; (f) estimate of the ioniation fraction. [4b] 107
3.29 Ion and electron current fit (100 Watt RF power) of (a) 10 mTorr; (b) 3.0 mTorr; (c) 2.0 mTorr [res4b] 108
3.30 Ion and electron current fit (100 Watt RF power) of (a) 1.8 mTorr; (b) 1.7 mTorr; (c) 1.6 mTorr [res4b] 109
3.31 Power scan at 27.12MHz and for a fixed pressure of 15.0mTorr, inside the helicon source, (a) experimental setup, with the Langmuir probe position marked with a red dot; (b) experimental IV traces for increasing power levels; (c) plasma density vs. power; (d) electron temperature vs. power; (e) plasma potential vs. power; (f) estimate of the ioniation fraction. [res07] 111
3.32 Axial scan at 27.12MHz and 400 Watt along the cylinder. [res09] 112
3.33 Radial scan at 27.12MHz and 400 Watt along the radius of the chamber. [res08] 113
3.34 Tests on the 2-cm inner diameter source, 27.12MHz, $B = (1000 \pm 100)$ Gauss, $p_0 = (10 \pm 5)$ mTorr (a) design of the tube, with the Langmuir probe entrance on its side; (b) photo of the experimental apparaturs; (c) plasma density vs. power; (d) electron temperature vs. power; (e) plasma potential vs. power; (f) experimental IV traces for increasing power levels. [res12] . . 115

3.35 Ion and electron current fit (a) 100Watt; (b) 200Watt; (c) 250Watt [res12] . 116
3.36 Comparison of measured plasma density with the values calculated by the HELIC-EQM code, as a function of RF input power. 118
3.37 Axial power deposition along the axis of the cylinder, obtained from HELIC-EQM. 119
3.38 Comparison of measured electron temperature with the values calculated by the HELIC-EQM code, as a function of RF input power. 119
3.39 Example of radial profiles obtained at convergence after HELIC-EQM iterations, $P_{RF} = 200$ Watt. Starting from the left corner on top: $P(r)$ [Ohm/m] power deposition, v_r/C_s ratio between the radial drift velocity and the local Bohm acustic velocity, ϕ [Volt] plasma potential, n [m^{-3}] plasma density, p [mTorr] neutral pressure, T_e [eV] electron temperature; the three Real components of the RF magnetic field B_r, B_ϕ, B_z [μT], of the RF electric field E_r, E_ϕ, E_z [V/m], and of RF plasma currents J_r, J_ϕ, J_z [A/m^2] (fields are normalized for an antenna current of $I_0 = 1.0A$). 120
3.40 Standard matching network configuration 121
3.41 (a) HP (Hewlett Packard) 4195A network analyzer, (b) Rohde & Schwart LRT BN6100 inductance meter 122
3.42 (a) Experimental test board; nodes are equally spaced, for an easier evaluation of stray inductances (b) stray inductance of two portions of the test board 123
3.43 Experimental tests on high-inductance load: (a),(c) circuits, (b),(d) comparison of measured and calculated impedances 124
3.44 Experimental tests on high-inductance antenna and with the matching box: (a),(c) circuits, (b),(d) comparison of measured and calculated impedances . 125
3.45 Experimental tests on low-inductance antenna: (a),(c) circuits, (b),(d) comparison of measured and calculated impedances 127
3.46 Experimental tests on low-inductance antenna: (a),(c) circuits, (b),(d) comparison of measured and calculated impedances 128

4.1 (a) Ideal specific impulse vs. atomic mass number A (number of nucleons), for three values of the electron temperature; (b) ideal specific impulse vs. electron temperature, for three values of atomic mass number. A Bohm factor $\alpha = 2.0$ has been assumed, i.e. ions are supposed to be accelerated twice the Bohm velocity, as expected from double layers experiments. . . . 131
4.2 Ideal thrust and specific impulse vs. Bohm parameter ($\alpha = v_i/C_s$) for a helicon thruster of $r = 1.0$ cm-radius using (a) hydrogen, (b) neon, (c) argon. 132
4.3 Ideal thrust and specific impulse vs. Bohm parameter ($\alpha = v_i/C_s$) for a helicon thruster of $r = 2.5$ cm-radius using (a) hydrogen, (b) neon, (c) argon. 133
4.4 Non-ideal thrust [mN] and specific impulse [s] vs. ionization fraction [%] . . 134

4.5 Different value of plasma resistance for different diameter of the plasma source versus plasma density at a fixed value of the magnetic field 136
4.6 Different value of plasma resistance for different source length for a fixed antenna type feeding frequency magnetic field and plasma radius as function of plasma density 136
4.7 Different value of plasma resistance for different background pressure at fixed plasma density and otehr operative conditions 137
4.8 Plasma source evolution within an helicon thruster 138
4.9 Different value of plasma resistance for different value of the magnetic field for different plasma densities (on a discharge of 10cm of diameter) 139
4.10 Low-B field peak in a small plasma cavity of 2 cm diameter and 6 cm long. 140
4.11 (a) radial power deposition profile for different antennas; (b) axial power deposition profile for different antennas 141
4.12 Design scheme adopted for the thruster design 142
4.13 Bare tether schematic (generator mode). The two graphs shows the profiles of the current I, of the tether potential ϕ_t and of the plasma potential ϕ_p as a function of tether abscissa z. 144
4.14 Gravitational actions on the tether. 147
4.15 Geometry of synodic plane with non-dimensional quantities. 149
4.16 (a) Non-dimensional force component f_ξ and (b) f_η required to maintain an equilibrium position with respect to the synodic frame as a funciton of the angle α. 154
4.17 Non-dimensional force components (f_ξ, f_η) required to stay in equilibrium in the synodic frame at locations (marked by dots) different than classical Lagrangian points. 155
4.18 Electron density at Jupiter according to Divine and Garrett model (adapted from [51]). 158
4.19 Equilibrium locations of an EDT as a function of the angle α in the Jupiter-Io system, on the orbital path of the second primary (Io). 159
4.20 Useful power at equilibrium for a librating tether vs. spacecraft mass. . . . 160
4.21 (a) EDT at equilibrium in the Jupiter-Io system, and (b) small oscillations around the equilibrium position. 161
4.22 (a) Electrodynamic force and (b) generated power vs orbital revolutions (Io's $T_{rev} = 1.77$ days) by a 20-km EDT at equilibrium at Jupiter obtained with the higher fidelity model EDT3BODY. These results are in accordance with the simplified model, which gives $F_{el} = 0.064\ N$ and $P_u = 1082\ W$. 162

A.1 Values of the Stix components S, D, P for a single-species electrons plasma 175

List of Tables

3.1 Tungsten tip of the Langmuir probes 74
3.2 List of electronic components used during tests 122

4.1 Helicon thruster, identified configurations 142

Acknowledgements

My words of gratitude are to all the people who helped to make this thesis possible.

At first, I would like to express my deep gratitude to my supervisors at the University of Padova, Prof. Enrico Lorenzini and Prof. Daniele Pavarin. They gave a continue encouragement and invaluable suggestions during this work. I would like to express sincere gratitude to Enrico, for his detailed and constructive comments, for his patience and honesty, for the work we did together, and for his expertise on tethers. A sincere and very special thanks to Daniele, for his enthusiasm, for the strong motivation he inspired me, for the sleepless nights, and most of all for his continuous and strong support all the time.

Furthermore I want to express my deepest gratitude to Prof. Francis F. Chen, my advisor at UCLA, it has been an honor to work with him. The theoretical discussions, his leading role in Laboratory during the experiments, and his endless expertise on Plasma Physics, have given an essential and inestimable contribution. He gave me the possibility to work in the most proficent way, and this research would have not been the same without him. A special thanks goes also to Ande, his wife, they both helped me a lot during my life in Los Angeles.

I want to thank also the PhD School of CISAS "G. Colombo" Università di Padova, and its fellowship, that made my permanence at UCLA possible.

I would like to give a warm thank to colleagues and friends, and in particular to Federico Moretto, Marco Manente, Davide Rondini, all the guys "al lab del cannone", and also to Umberto, Fabio, and all the guys in Treviso. My thanks also goes to all the people who have helped along the way, and influenced my formation.

Last but not the least, I want to thank my family. My parents, my sister Beatrice and all other members of my family, for their lovely and never-ending spiritual and material support throughout my life. And most of all, thanks to my wife Chiara, my fixed star, for waiting for me so many times, and for making every day something new and special.

Vita

1982 Born in Treviso, Italy.

2001–2004 B.S. in Aerospace Engineering, University of Padova

2004–2007 M.S. in Aerospace Engineering, University of Padova

Summer 2008 Max-Planck-Institut fur Plasmaphysik, IPP Summer University on Plasma Physics and Fusion Research

2009–2010 Research scholar at UCLA, University of California - Los Angeles, Low Temperature Plasma Technology Laboratory

2011 PhD in Sciences Technologies and Measures for Space

Scientific publications

- D. Curreli and F. F. Chen, Equilibrium theory of cylindrical discharges with special application to helicons, (in press) Plasma Sources Sci. Tech.
- Curreli D. and F. F. Chen, A Novel Equilibrium theory of Helicon Discharges, 63rd Gaseous Electronics Conference and 7th International Conference on Reactive Plasmas, 4-8 October, Mason de la Chimie, Paris
- D. Curreli, E. C. Lorenzini, C. Bombardelli, M. Sanjurjo-Rivo, F. R. Lucas, J. Pelaez, D. J. Scheeres and M. Lara, Three-body dynamics and self-powering of an electrodynamic tether in a plasmasphere, Journal of Propulsion and Power, Vol. 26, N. 3, May-June 2010
- D. Zanutto, D. Curreli, E. C. Lorenzini, Dynamics of an electrodynamic tether around perturbed equilateral positions of the three-body problem, (in press) Journal of Guidance, Control and Dynamics
- J. Pelaez, M. Lara, C. Bombardelli, F. R. Lucas, M. Sanjurjo-Rivo, D. Curreli, E. C. Lorenzini and D. J. Scheeres, Periodic orbits of the Hill-tether satellite problem originated from the L2 collinear point, (in press) Journal of Guidance, Control and Dynamics
- Curreli D., Lorenzini, E. C., Bombardelli, C., Sanjurjo-Rivo, M., Lucas F. R., Peláez, J., Scheeres, D. J., Lara, M., Exploration of the Jupiter Plasma Torus with a self-powered electrodynamic tether, AAS 09-240, presented at 19th AAS/AIAA Space Flight Mechanics Meeting, 8-12 February 2009, Savannah, Georgia (GA)

- D. Pavarin, F. Ferri, M. Manente, D. Rondini, D. Curreli, Y. Guclu, D. Melazzi, S. Suman, G. Bianchini, D. Packan, P. Elias, J. Bonnet, A. Cardinali, R. Deangelis, F. Mirizzi, A. Tuccillo, O. Tudisco, E. Ahedo, Y. Protsan, A. Loyan, F. Piergentili, K. Grue, P. Van Put, A. Selmo, K. Katsonis, M. Pessana, J. Carlsson, V. Lancellotti (2010). Helicon Plasma Hydrazine.Combined Micro Project Overview and Development Status. In: Space Propulsion Conference. San Sebastian, Spain, 3-6 May 2010

- D. Pavarin, F. Ferri, M. Manente, Curreli D., Y. Guclu, D. Rondini, M. Mariutto, L. Tasinato, J. Carlsson, R. De Angelis, D. Pakan, K. Grue, P. Van Put, R. Tijsterman, A. Selmo, A. Loyan, K. Katsonis (2009). Experimental Set-up to test a 50 W Helicon plasma thruster. In: 31st International Electric Propulsion Conference

- D. Pavarin, F.Ferri, M. Manente, J.Carlsson, E. Ahedo, C.Bramanti, D. Curreli , Y. Güçlü , G. Markelov, D. Melazzi, D.Rondini, S .Suman, Design of 50 W helicon plasma thruster, 31st International Electric Propulsion Conference IEPC 2009, Ann Arbor, Michigan, USA, 20-24 September 2009

- Lorenzini E. C., Curreli D. and Zanutto D., Exploration of the Galilean Moons using electrodynamic tethers for propellantless maneuvers and self-powering, Proceedings IAU Symposium No. 269, 2010, International Astronomical Union, Galileo's Medicean Moons: Their Impact on 400 Years of Discovery

- Curreli, D., Lorenzini E. C., Bombardelli C., Sanjurjo-Rivo M., Lucas F. R., Pelaez J., Scheeres D. and Lara M., (2009) Exploration of the Jupiter Plasma Torus with a self-powered electrodynamic tether. In: Advances in the Astronautical Sciences (AAS) vol. 09-240, ISBN/ISSN: 0065-3438 13) Pavarin D., Manente M., Guclu Y., Curreli D., Bettanini C., Zaccariotto M., Walker M., Palmer D., Carlsson J., Bramanti C., and Lorenzini E., Feasibility study of medium power helicon thruster, Joint Propulsion Conference, July 2008

- Bombardelli, C., Lorenzini E., Curreli D., Sanjurjo-Rivo M., Lucas F. R., Pelaez J., Sheeres D. J., and Lara M., Io exploration with electrodynamic tethers, 2008 AIAA/AAS Astrodynamics Specialist Conference, 18-21 August 2008, Honolulu, Hawaii, USA

- Sanjurjo-Rivo M., Lucas F. R., Pelaez J., Bombardelli C., Lorenzini E. C., Curreli D., Scheeres D. J., and Lara M., On the dynamics of a tethered system near the collinear libration points, 2008 AIAA/AAS Astrodynamics Specialist Conference, 18-21 August 2008, Honolulu, Hawaii, USA

- Curreli D., Guclu Y. Francesconi A., Pavarin D., Angrilli F., Numerical formulation of the jet damping torque for space vehicles with thrust vector control, presented at XIX AIDAA congress, Aerotecnica Missili e Spazio, 17-21 Sept 07, Forlì, Italy

- Bettella A., Manente M., Benini E., Guclu Y., Curreli D., Moretto F., Martini S., Pessana M., Walloschek T., De Rosa M., Kachler T. and Pavarin D., Turbo-pump pressurization concept for hybrid propulsion thrusters application to launch vehicles, AIAA 2008-4934, 44th Joint Propulsion Conference & Exhibit, 21-23 July 2008, Hartford, CT

- Guclu Y., Curreli D., Francesconi A., Pavarin D., Angrilli F., Numerical implementation of the equations describing the rigid-body dynamics of a variable mass rocket with internal flow, Aerotecnica Missili e Spazio, 17-21 Sept 07, Forlì, Italy

- D. Curreli, D. Rondini, M. Manente, D. Pavarin, 3D PiC code validation report, EU FP7 HPH.com, D2.5.2_HPHcom-UPD-RP-010

- D. Curreli, D. Rondini, M. Manente, D. Pavarin, 3D PiC code user manual, EU FP7 HPH.com, D2.4.3_HPHcom-UPD-MA-004

- D. Curreli, D. Rondini, M. Manente, D. Pavarin, 3D wave code validation result, EU FP7 HPH.com, D2.1.7_HPHcom-UPD-RP-008

- D. Curreli, D. Rondini, M. Manente, D. Pavarin, 3D wave code user manual, EU FP7 HPH.com, D2.1.8_HPHcom-UPD-MA-002

- Pelaez, J., Sanjurjo-Rivo, M., Lara, M., Lorenzini, E. C., Curreli, D., Sheeres, D. J., Bombardelli, C., and Izzo, D., Dynamics and Stability of Tethered Satellites at Lagrangian Points, Tech. Rep. Final Report Ariadna Study 07-4201, Advanced Concept Team ESA, November 2008, available online: http://www.esa.int/gsp/ACT/ariadna/studies.htm

- Rondini D., Guclu Y., Curreli D. and Pavarin D., HyRoCode User's Manual - Hybrid Propulsion Study Engine Performance Model, ENG 304, Thales Alenia Space and European Space Agency

- Curreli D., Guclu Y., Francesconi A. and Pavarin D., VEGASEP Manual code, ELV Fiat-Avio Group and ASI Agenzia Spaziale Italiana

Abstract

Helicon plasma sources are an attractive means of plasma production in advanced applications of space propulsion thanks to their high ionization efficiency. By means of a compact helicon source, it is possible to enhance the performances of a small propulsive apparatus from a range of almost negligible values (few micro-Newton of thrust and few tens of seconds of specific impulse) to a range useful for many applications (thrust of milli-Newton and 1000s seconds of specific impulse). However, the design of such a system is complicated by the great inter-correlations between the involved parameters, and by the complex physical mechanisms involved. Moreover, thruster operation involve physical regimes which are not common in industrial plasma sources. In this research program, helicon physics has been deeply analyzed in a innovative way, not limiting the study to helicon wave analysis with dielctric tensors, but recognizing that the electromagnetic wave propagation must be closely related to macroscopic transport. An equilibrium theory of an helicon discharge has been derived, where both the plasma-wave local coupling of the RF antenna field with the plasma, and the transport of plasma species at the macroscopic level, are considered. The theory has been practically implemented on a code and validated with experiments in Laboratory. The theory has allowed to close the correlations between the design parameters and to identify preliminary design configurations of helicon thrusters.

Grazie alla loro elevata efficienza, le sorgenti al plasma di tipo helicon sono un attraente mezzo di produzione di plasma per applicazioni avanzate di propulsione spaziale. Per mezzo di una compatta sorgente helicon, è possibile incrementare le prestazioni di un piccolo apparato propulsivo, da un range di valori pressoché trascurabili (pochi micro-Newton di spinta e qualche decina di secondi di impulso specifico) ad un range utile per molte applicazioni (spinta del milli-Newton e migliaia di secondi di impulso specifico). Tuttavia il design di un tale sistema è complicato dalla grande inter-correlazione tra i parametri coinvolti, e dai complessi meccanismi fisici coinvolti. Inoltre il regime operativo del thruster avviene in regimi fisici non comuni per plasmi di sorgenti industriali. In questo programma di ricerca la fisica fondamentale degli helicon è stata attentamente studiata, non limitando le analisi al problema di accoppiamento d'onda con tensore dielettrico, ma riconoscendo che il problema elettromagnetico è strettamente connesso al traporto macroscopico. E' stata sviluppata una teoria dell'equilibrio di una scarica helicon, dove sono tenuti in considerazione sia l'accoppiamento locale plasma-onda del campo RF (radiofrequenza) dell'antenna

con il plasma, che il trasporto delle specie di plasma a livello macroscopico. La teoria è stata implementata in un codice e validata con esperimenti in Laboratorio. La teoria ha permesso di chiudere le correlazioni fra i parametri di design e di identificare delle configurazioni preliminari di propulsori helicon.

Introduction

The next generation of plasma propulsors for space applications relies on the development of high efficiency plasma sources. Presently the most efficient cold plasma source is the helicon source, which is based on radio frequency excitation of whistler waves confined inside a cylindrical tube. For a given amount of input power, a helicon source obtains more plasma with consequent larger thrust than all other plasma source alternatives. Helicon waves are in principle compatible with any kind of propellant, which allows maximization of system specific impulse. The helicon source is therefore a good choice for plasma spacecraft that must optimize on-board resources.

A basic version of the helicon thruster comprises only two elements: helicon source and magnetic nozzle. Plasma is created and sustained via helicon wave power deposition and subsequently accelerated in the magnetic nozzle. The magnetic nozzle requires an expanding magnetic field of opportune geometry. Thrust from plasma fluid acceleration through the nozzle is similar to conventional rockets, but with plasma propellant instead of gas dynamic flow and with magnetic field in concert with exit nozzle shape. The design of helicon thrusters therefore requires a good comprehension of the helicon physics.

In the present work, a great emphasis has been dedicated to helicon sources and to their fundamental physics. The underlying physics of helicons is here deeply investigated, including both the plasma-wave coupling problem and the macroscopic transport problem, and their relationship with an equilibrium model. The highly non-uniform power deposition of the plasma wave in the plasma cylinder has been taken into account in the model. A numerical code able to solve the equilibrium problem has been derived, and used to predict the absolute values of plasma density and the other relevant parameters of the plasma discharge. The theoretical results have then been compared with measurements, with a dedicated experimental campaign. Experiments were done at the Low Temperature Plasma Technology Laboratory of University of California Los Angeles (UCLA), hosted by Prof. Francis F. Chen. The measurements were done by means of radio-frequency compensated Langmuir probes. A comparison of measurements with code predictions has revealed the absolute agreement of numerical and measured data, within their uncertainties.

The equilibrium theory of helicon discharges has then been applied for the preliminary design of an helicon thruster. The expected performances have been estimated with the theory. Finally, a comparison of the helicon thruster with a propellantless system is pre-

sented. Electrodynamic tethers have been considered as a propellanteless system. Tethers use plasma from environment to get a thrust, instead of creating plasma inside the system. Innovative applications of electrodynamic tethers are discussed.

Chapter 1

Equilibrium theory of helicon discharges

1.1 Plasma-Wave coupling

1.1.1 Helicon and Trivelpiece-Gould mode-coupling

Helicons are circularly polarized plasma waves propagating in a bounded plasma. They occur in a range of frequencies much lower than the electron cyclotron frequency and the plasma frequency, but higher than the lower hybrid resonance, $\omega_{LH} < \omega << \omega_{ce} << \omega_p$. This range of frequencies is far from all the characteristic resonances of the plasma, as shown in the example of Figure 1.1. The figure shows the frequency response[1] of two different plasmas: a typical Deuterium plasma used in magnetic fusion, and a typical helicon Argon plasma. The principal resonances can be easily recognized in the two cases. In the second case, helicon waves occur in a range between 10 and 100 MHz, inside an interval of frequencies far from resonances. Despite the absence of resonances within this range, the plasma-wave coupling is well known for its high efficiency, such that high plasma densities can be obtained in practical devices.

The analytical solution for a uniform plasma in cylindrical domains was obtained for the first time by Klozenberg in 1965 [1], and then generalized to the case of non-uniform plasmas by Chen and Arnush in 1997 [2], [3], [4]. Accordingly to these models, the relevant behavior of helicons can be seen using a fluid model for electrons, satisfying the following set of equations:

$$m_e \frac{\partial \vec{v}}{\partial t} + m_e(\vec{v} \cdot \nabla)\vec{v} = -e(\vec{E} + \vec{v} \times \vec{B}_0) + \frac{1}{n_0}\nabla \cdot \pi + \frac{1}{n_0}\nabla p - m_e \nu \vec{v} \tag{1.1}$$

[1] The figures show the trend of the three independent components of the Stix tensor versus the frequency; equations are recalled in Appendix A.1.

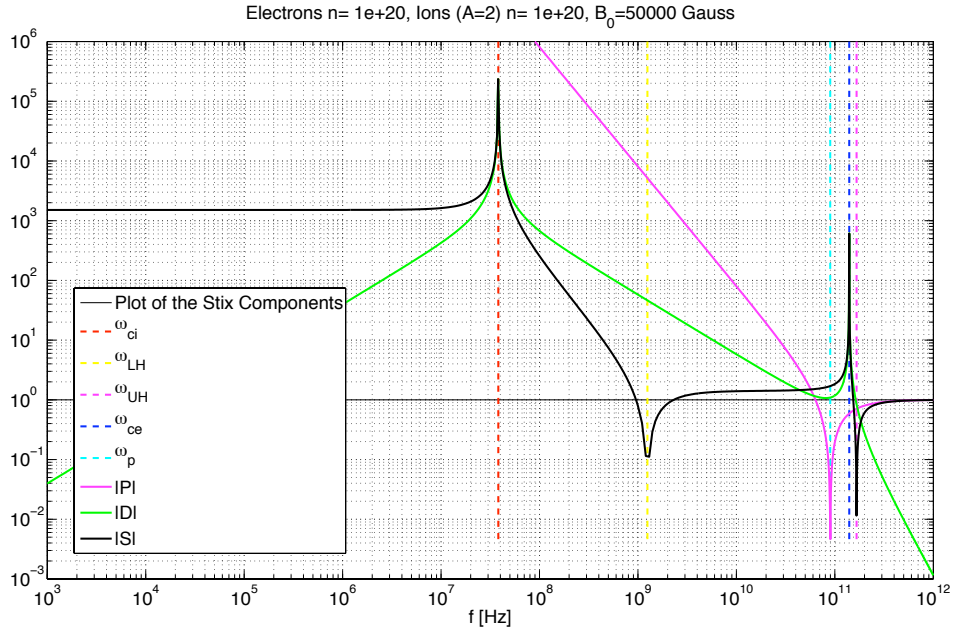

(a)

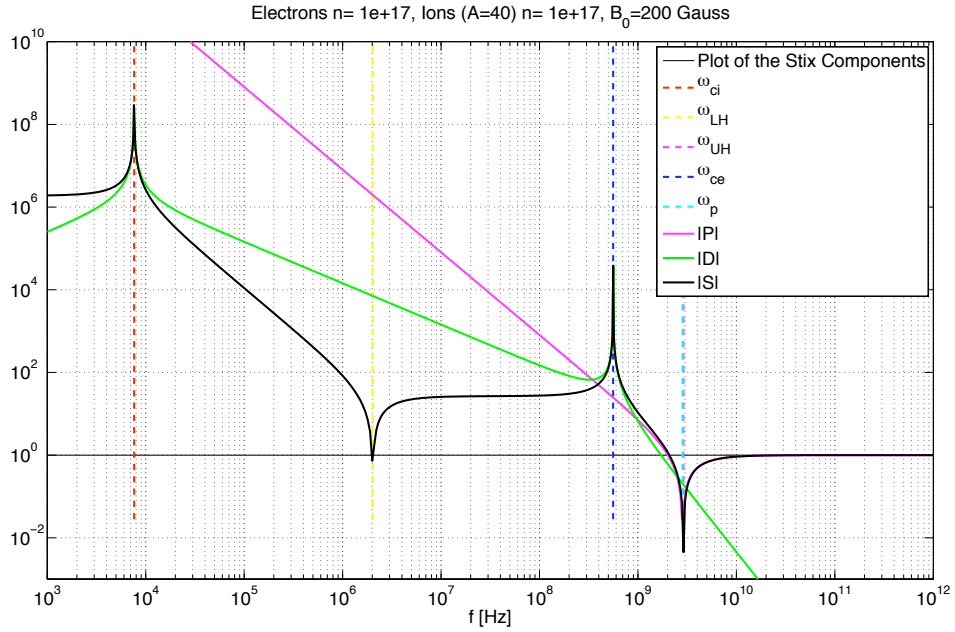

(b)

Figure 1.1: Values of the Stix components S, D, P in the cold approximation for (a) a typical Deuterium fusion plasma, and (b) a typical helicon Argon plasma

together with the Maxwell equations:

$$\nabla \cdot \vec{B} = 0 \tag{1.2}$$

$$\nabla \times \vec{E} = i\omega\vec{B} \tag{1.3}$$

$$\nabla \times \vec{B} = \mu_0\vec{j} - i\omega\epsilon_0\vec{E} \tag{1.4}$$

This system of equation can be simplified to a handling form after simple considerations on the more relevant terms. The magnetic viscosity term $(\nabla \cdot \pi)/n_0$ can be neglected because it is important only when the electron Larmor radius $r_{L,e}$ is comparable with the radial wavelength of the waves in the plasma. It turns out that this is an important effect only in the regime of very-low magnetic fields, below $B_0 \sim 10$ Gauss, for high energy electrons $kT_e > 15$ eV, that is when $r_{L,e}$ is comparable with the short-wavelength TG modes at about 1 mm. For the ordinary electrons encountered in the helicon sources at $kT_e \approx 3$ eV, the magnetic viscosity is relevant only below ≈ 6 Gauss, a regime of transition where the helicon wave is becoming evanescent. The pressure term $(\nabla p)/n_0$ is the sum of kinetic temperature and density gradient effects. When finite-Larmor-radius effects are neglectable, the term $(\nabla p)/n_0$ is neglectable too, because it is always smaller than the $e\vec{E}$ term. To include ∇p effects, the warm-plasma theory should be used [5]. This will be addressed in Appendix A.3. In non-uniform plasmas, a finite electron temperature T_e cause drift-waves, but the frequency of this waves is much lower than that of helicons, and the two effects can be distinctly treated.

After these simplifications, and assuming first-order perturbations with harmonic dependence $\exp[i(m\theta + kz - \omega t)]$, the motion of fluid electrons is governed by:

$$-i\omega m_e\vec{v} = -e(\vec{E} + \vec{v} \times \vec{B}_0) - m_e\nu\vec{v} \tag{1.5}$$

Assuming a uniform magnetic field along the z axis, $\vec{B}_0 = B_0\hat{z}$, neglecting ion motion in the plasma current, $\vec{j} = -en_0\vec{v}$, and assuming a uniform density profile $n(r) = n_0$, Eq. 1.5 gives:

$$\vec{E} = -\frac{B_0}{en_0}(i\delta\vec{j} + \hat{z} \times \vec{j}) \tag{1.6}$$

where $\delta = \omega/\omega_c + i\nu/\omega_c$ is the ratio between the frequency and the cyclotron frequency, corrected with the collisional term. Substituting the Maxwell equations in Eq. 1.6 and neglecting the displacement current, the helicons governing equation can finally be obtained:

$$\delta\nabla \times \nabla \times \vec{B} - k\nabla \times \vec{B} + k_w^2\vec{B} = 0 \tag{1.7}$$

where $k_w^2 = \delta k_s^2$ is the wave number of a whistler wave propagating in the free space, and $k_s = \omega_p/c$ is the skin number, which is the ratio between the plasma frequency ω_p and the speed of light.

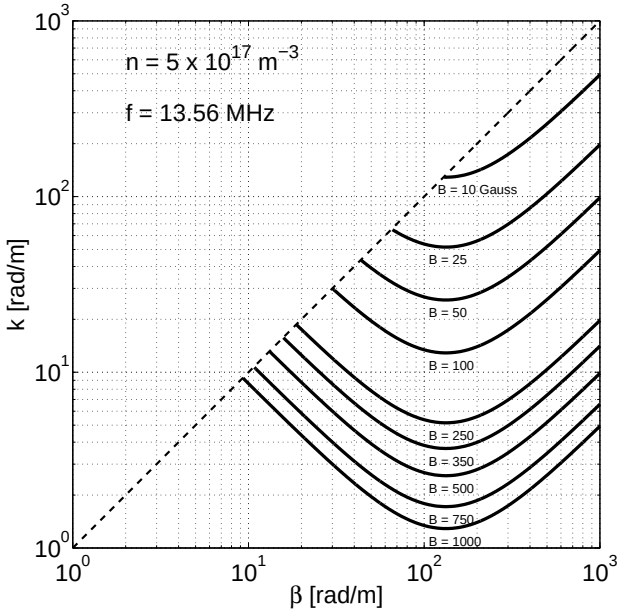

(a)

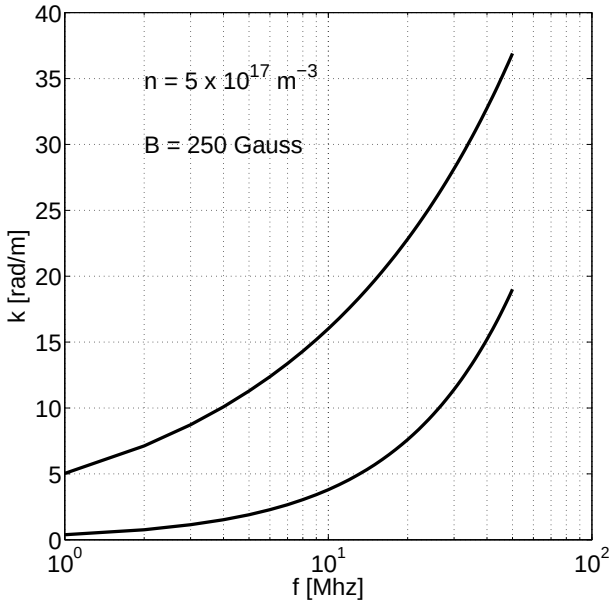

(b)

Figure 1.2: (a) Dispersion relation of Helicons and Trivelpiece-Gould waves; (b) range of k_{min} and k_{max} of the helicon branch vs. the frequency

The characteristic equation associated to Eq. 1.7 gives the dispersion relation:

$$\delta\beta^2 - k\beta + k_w^2 = 0 \tag{1.8}$$

The second-order term $\delta\beta^2$ compares in virtue of the finite electron mass. When the electron mass goes to zero, $m_e \to 0$, then also delta goes to zero $\delta \to 0$, and the classical dispersion relation of helicons is recovered:

$$m_e \to 0 \quad : \quad \beta = k_w^2/k \tag{1.9}$$

For each axial mode k, the Eq. 1.8 states that two radial wave modes are allowed for the propagation of the plasma wave:

$$\beta_{1,2} = \frac{1}{2}\left(\frac{q_e}{m_e}\right) B_0 \left[\frac{k}{\omega} \mp \sqrt{\left(\frac{k}{\omega}\right)^2 - \frac{4\mu_0 m_e n_0}{B_0}}\right] \tag{1.10}$$

where the lower scripts refer to:

$$1: \quad \text{Helicon mode} \tag{1.11}$$

$$2: \quad \text{Trivelpiece-Gould mode} \tag{1.12}$$

The first mode β_1 is the Helicon mode: it is a low radial mode with high radial wavelength, which can propagate from the radial boundary until the axis. When the electron mass vanishes $m_e \to 0$ the H mode is a pure TE mode, with $E_z = 0$. The second mode β_2 is the Trivielpiece-Gould mode [53], which is an electron cyclotron wave; it has an electrostatic character plus an electromagnetic part which is clearly manifest only at low magnetic fields. The TG mode has short radial wavelengths and thus it is rapidly absorbed in the external shells of the plasma cylinder. Figure1.2.a shows an example of the Helicon and TG dispersion relation in the kappa-beta plane. For the conditions considered, the helicon branch becomes evanescent under magnetostatic fields of about 10 Gauss. In Fig. 1.2.b the range $k_{min} < k < k_{max}$ of the helicon branch is reported as a function of the frequency, where $k_{min} = 2\delta k_s$ and $k_{max} = k_s\sqrt{\delta/(1-\delta)}$.

The governing wave equation Eq.1.7 is solved by factorization [1]:

$$(\beta_1 - \nabla\times)(\beta_2 - \nabla\times)\vec{B} = 0 \tag{1.13}$$

meaning that the solution is the superimposition of two normal modes:

$$\vec{B} = \vec{B}_1 + \vec{B}_2 \tag{1.14}$$

Each one of the two modes $\vec{B}_j$ $(j = 1, 2)$ is obtained from the solution of an Helmholtz equation:

$$\nabla^2 \vec{B}_1 + \beta_1^2 \vec{B}_1 = 0 \tag{1.15}$$

$$\nabla^2 \vec{B}_2 + \beta_2^2 \vec{B}_2 = 0 \tag{1.16}$$

The general solution in cylindrical coordinate is given by:

$$B_{r,j} = A_j \left[(\beta_j + k) J_{m-1}(T_j r) + (\beta_j - k) J_{m+1}(T_j r) \right] \tag{1.17}$$

$$B_{\theta,j} = i A_j \left[(\beta_j + k) J_{m-1}(T_j r) - (\beta_j - k) J_{m+1}(T_j r) \right] \tag{1.18}$$

$$B_{z,j} = -2 i A_j T_j J_m(T_j r) \tag{1.19}$$

where

$$T_j^2 = \beta_j^2 - k^2 \tag{1.20}$$

is the transverse wave number, m is the azimuthal wave number, and J_m are the usual Bessel functions of the first kind. The coefficients A_j depend on the boundary conditions, and a detailed treatment on how to obtain them can be found in [2], for both the conducting and the dielectric boundary cases.

When the boundary is conductive ($E_\theta = E_z = 0$ and $j_z = 0$ at $r = a$, with a radius of the plasma cylinder), the k modes are quantized inside the cylinder, meaning that only certain modes of propagation are allowed. Experimentally only the first one or two of these modes can be observed, because of damping of higher modes.

When the boundary is insulating (B_r, E_z continuos at $r = a$), the k modes are still quantized, but they densely sample the region $k_{min} < k < k_{max}$; when dumping is also considered, the quantization disappears and the region is filled with continuity. The range $k_{min} < k < k_{max}$ constrains the admissible plasma densities n_0 to the following values:

$$\frac{k^2}{4\mu_0 m_e} \left(\frac{B_0}{\omega} \right)^2 < n_0 < k^2 \frac{m_e}{\mu_0 e^2} \left(\frac{\omega_c - \omega}{\omega} \right) \tag{1.21}$$

After the magnetic field $\vec{B}$ is solved, all the other fields are easily derived. The plasma current is (β_j/μ_0) times the magnetic field:

$$\vec{j}_j = \frac{\beta_j}{\mu_0} \vec{B}_j \tag{1.22}$$

Eq. 1.22 states that the plasma current is always aligned with the magnetic field, and since $\vec{j}$ is also parallel to the electrons fluid velocity $\vec{v}$, this means that electrons oscillate parallel to the RF magnetic field. The only disalignment between $\vec{j}$ and $\vec{B}$ is given by the displacement current, here neglected for simplicity, but this contribute is always small compared to the fields inside the plasma.

The electric field is then obtained from Eq. 1.6:

$$E_{z,j} = \left(-\frac{i\omega m_e}{e^2 n_0} + \nu\frac{m_e}{e^2 n_0}\right)\left(\frac{\beta_j}{\mu_0}\right) B_{z,j} \tag{1.23}$$

$$E_r = \frac{\omega}{k}B_\theta - \frac{i}{k}\frac{\partial E_z}{\partial z} \tag{1.24}$$

$$E_\theta = \frac{m}{kr}E_z - \frac{\omega}{k}B_r \tag{1.25}$$

1.1.2 Coupling with non-uniform densities

When the density is not uniform along the cylinder radius, the fundamental equation Eq.1.7 is modified by the addition of a source term:

$$\delta\nabla\times\nabla\times\vec{B} - k\nabla\times\vec{B} + k_w^2\vec{B} = -\frac{n_0'(r)}{n_0(r)}[-\delta_0\hat{r}\times(\nabla\times\vec{B}) + i(\nabla\times\vec{B})_r\hat{z}] \tag{1.26}$$

The source term on the right-hand side of Eq.1.26 vanishes when the density profile is uniform. In the general case of non-uniform density, the magnetic field $\vec{B}$ inside the plasma results to be a combination of two normal functions $\vec{b}_{1,2}(r)$, which reduce to the Helicon and Trivelpiece-Gould modes when the density profile is uniform. The oscillating magnetic field along the radius is now given by:

$$\vec{B}(r) = \frac{H_2\vec{b}_1(r) - H_1\vec{b}_2(r)}{D}K_\phi \tag{1.27}$$

where K_ϕ is the Fourier transform of the antenna current (sec. 1.1.3), and H, D are the following combination of modified Bessel functions:

$$H_{1,2} = \frac{kb}{Ta}p_m(b)\mu_0 G_{1,2} - i\frac{m}{a}\frac{k_0^2}{T^2}\rho_m F_{1,2} \tag{1.28}$$

$$G_{1,2} = j_{r1,2}(a) + i\frac{m}{a}\frac{k_0^2}{T^2}\frac{1}{\mu_0}b_{z1,2}(a) + \frac{k}{T}q_m[\omega\epsilon_0 e_{n1,2}(a)] \tag{1.29}$$

$$F_{1,2} = -ib_{r1,2}(a) + \frac{k}{T}p_m(a)b_{z1,2}(a) - i\frac{m}{aT^2}\mu_0[\omega\epsilon_0 e_{z1,2}(a)] \tag{1.30}$$

$$D = F_1G_2 - F_2G_1 \tag{1.31}$$

where

$$p_m(r) = \frac{K_m'(Tr)I_m'(Tc) - K_m'(Tc)I_m'(Tr)}{K_m(Ta)I_m'(Tc) - K_m'(Tc)I_m'(Ta)} \tag{1.32}$$

$$q_m = \frac{K_m'(Ta)I_m(Tc) - K_m(Tc)I_m'(Ta)}{K_m(Ta)I_m(Tc) - K_m(Tc)I_m(Ta)} \tag{1.33}$$

$$\rho_m = \frac{K_m(Tb)I_m(Tc) - K_m(Tc)I_m(Tb)}{K_m(Ta)I_m(Tc) - K_m(Tc)I_m(Ta)} \tag{1.34}$$

Figure 1.3 shows a comparison of the RF fields occurring inside an homogeneous plasma with the fields of an analogous case non-homogeneous.

1.1.3 Antenna Excitation

In the physical space the antenna current $\vec{j}_A$ lies on a cylindrical surface of radius b:

$$\vec{j}_A(r,\phi,z) = \delta(r-b)\vec{K}(\phi,z) \tag{1.35}$$

Fourier tranforming $\vec{K}(\phi,z)$ gives $\vec{K}(m,k)$. The two components of $\vec{K}(m,k)$ will be denoted as (K_ϕ, K_z); for some standard antenna geometries they are:

$$K_\phi = I_0 \qquad \text{Loop antenna (m=0)} \tag{1.36}$$

$$K_\phi = -\frac{2I_0}{\pi}\frac{kL}{2m}\frac{\sin(kL/2-m\theta)}{kL/2-m\theta} \qquad \text{Fractional helix of twist angle } 2\theta \text{ (m odd)} \tag{1.37}$$

and (for solenoidality of the current):

$$K_z(m,k) = -\frac{m}{bk}K_\phi(m,k) \tag{1.38}$$

Figure 1.4 shows the values of K_ϕ, K_z and $|K_\phi|^2$, evaluated with Eq. 1.37, for several antenna geometries. The plots of the power spectra $|K_\phi|^2$ show that increasing the twist angle θ of a fractional helix antenna allows to direct the antenna power in one axial direction, i.e. parallel to the magnetostatic field.

1.1.4 Power deposition

The specific power deposited into the plasma at each point is given by the projection of the electric field on the plasma currents[2]. Then the total power deposited is obtained by integrating over the desired volume:

$$P = \frac{1}{2}\int_V \vec{E}^* \cdot \vec{J}_{pl} dV = \frac{|I_0|^2}{2}(R+iX) \tag{1.39}$$

where R is the plasma resistance, X the plasma reactance, I_0 the antenna current, and the upper script * denotes the conjugate of the vector. The power is transferred by means of both collisional resistive heating and non-collisional heating (Landau damping). In usual conditions, most of the power is transferred by collisional phenomena thanks to the TG wave, absorbed in a thin layer at the edge of the plasma cylinder.

[2]Being a square complex matrix, the dielectric tensor ϵ_{ij} can be uniquely written as the sum of an Hermitian component plus a skew-Hermitian component, $\epsilon_{ij} = \epsilon^H_{ij} + \epsilon^S_{ij}$ where $\epsilon^H_{ij} = 1/2(\epsilon_{ij} + \epsilon^{(*)}_{ij})$ and $\epsilon^S_{ij} = 1/2(\epsilon_{ij} - \epsilon^{(*)}_{ij})$. The upper script $^{(*)}$ here denotes the conjugate transpose of the matrix. The skew-Hermitian part of the dielectric tensor is associated to the irreversible dissipation of power per unit volume, $P_{abs} = \omega/(8\pi)\vec{E}_0^*[\epsilon^S]\vec{E}_0$. The total absorbed power is thus given by the integral of P_{abs} on the plasma volume.

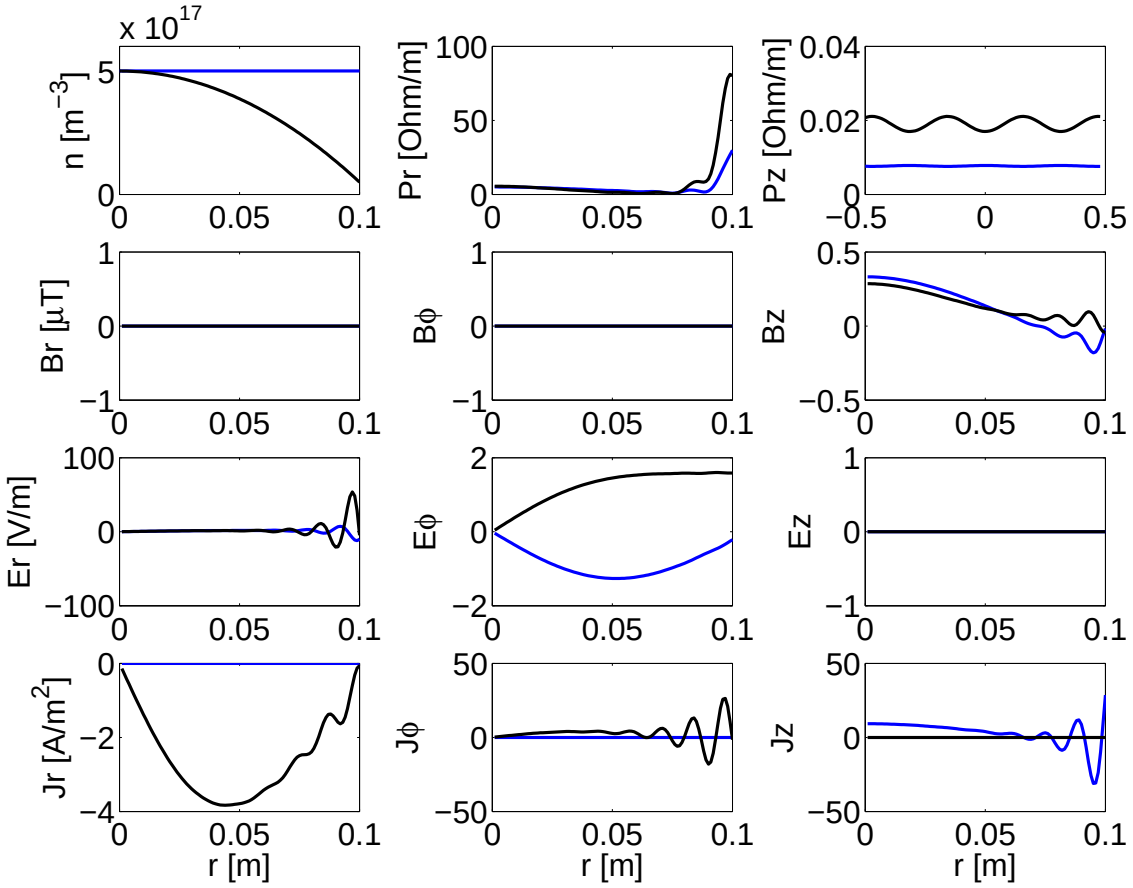

Figure 1.3: RF fields inside a plasma cylinder for two radial profiles of plasma density, a uniform profile (results are in blue) and a parabolic profile (results are in black). On the first row of plots there are: the two profiles of $n(r)$ uniform and parabolic, both starting at $n = 5 \times 10^{17}$ m^{-3}, the radial profile of power deposition $P(r)$, and the axial profile of power deposition in unbounded conditions. The 2^{nd}, 3^{rd} and 4^{th} rows show the real components of magnetic field, electric field and plasma currents respectively. Imaginary components are not reported; fields and currents are evaluated at the following conditions: plasma radius=10 cm, antenna located on the plasma surface $r_a = 10$ cm, external conducting boundary at $r_c = 20$ cm, wave numbers $m = 0$, $k = 10$ rad/m, magnetostatic field $B_0 = 250$ Gauss, plasma of Argon, homogeneous neutral gas at $p_0 = 3.0$ mTorr, $T_e = 5$eV, antenna current $I_0 = 1.0$ A, frequency $f = 13.56$ MHz; calculated fields pertains to the axial coordinate $z = 0$, i.e. they are evaluated on the antenna plane.

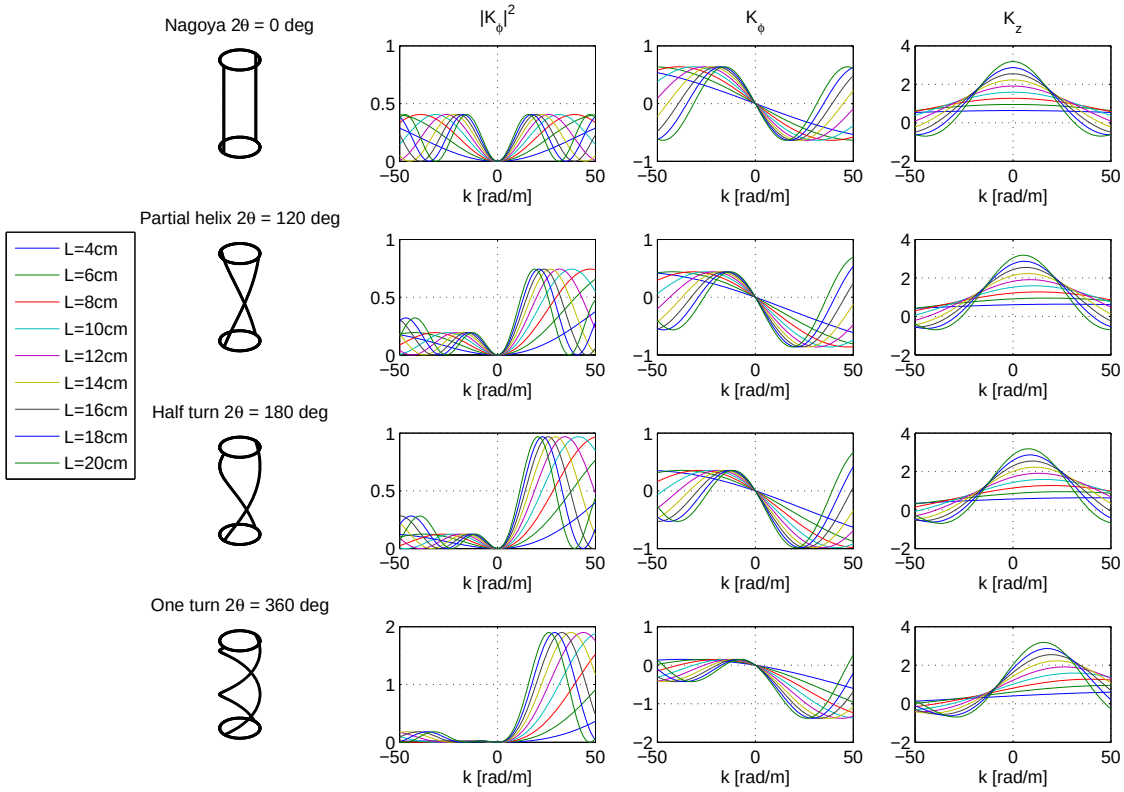

Figure 1.4: Antenna spectra for the $m = +1$ component of several antenna geometries, for a current $I_0 = 1.0$ A

1.1.5 Generalizations of the plasma-wave coupling

The theory presented up to here can be generalized in order to include plasma effects that departs from cold-wave theory, as for example thermal effects, i.e. effects related to a finite temperature of each plasma species. Other effects are the finite number of plasma species, the kinetic effects of a non-Maxwellian distribution function, and finite Larmor radius effects. This can be accomplished semi-analytically by including inside the dielectric tensor more complex formulations. The most important generalizations are reported in the Appendix A.3.

1.2 Macroscopic transport

The theory of plasma-wave coupling presented up to here describes how the fields excited by the antenna can deposit power into the plasma for given arbitrary profiles of n, n_n and T_e (plasma density, neutral density and electron temperature). The theory prescribes a deposition governed by two families of plasma waves, occurring as a consequence of the finite-geometry of the plasma cylinder. When the plasma density is non-uniform along the radius, the absorption is greatly altered with respect to the case of uniform density. However, the plasma-wave coupling theory is not consistent by itself, since it only states how much power goes into the plasma for given profiles. The actual radial profiles have to be obtained by solving another set of equations, that account for the macroscopic transport of ions, electrons and neutrals inside the plasma cylinder. At equilibrium the species will be in a configuration depending on how the plasma is forced by the wave, and how the ions/electrons/neutrlas interact together.

In the present section we will address this problem, that will be addressed as the macroscopic transport problem. All the quantities, comprising the power deposition, will be taken into account locally, with energy deposition described by the theory of plasma-wave coupling. In this way, a general model of equilibrium valid for cylindrical plasma sources excited by RF fields (ICP and helicon sources) will be derived.

1.2.1 Remarks on the transport problem

The equilibrium of the discharge depends on the macroscopic balances of electrons, ions and neutral species. In stationary conditions, the discharge is sustained by means of electron impact ionization on neutral atoms. At frequencies in the helicon range, the ions are not affected by the RF wave, due to their inertia. All the power is transferred to the electrons. Power is expended to sustain the plasma, and to overcome losses. Electrons are heated locally by the electromagnetic fields, and power is transferred from electrons to the neutral gas by collisions. Only the fraction of electrons with energies higher than the ionization threshold is useful for obtaining new ions and new electrons from neutral atoms. As will be seen later in more detail, the power deposition process inside an helicon discharge is

strongly non-uniform. This locally affects the electron heating, and as a consequence the global equilibrium of the plasma cylinder.

1.2.2 Transport models in non-magnetized discharges

Here the classical transport models studied for discharges are briefly recalled. Classically, the transport quantities at equilibrium in a cylindrical discharge at pressure p_0 and of characteristic size L^* are described by different models in different regimes. The discriminant between the regimes is quantified by a non-dimensional number like the ratio between the mean-free-path and a characteristic size, $Kn = \lambda/L^*$ (Knudsen number), or the product between the pressure and the characteristic size, $Pa = p_0 L^*$ (Paschen number). The characteristic size of the discharge is usually the diameter of the cylinder, or its length, depending on the problem. The mean free path hasn't a unique definition. More than one mean free path can thus be defined, depending on the nature of the collisions. When the discharge is non-magnetized, three regimes of transport can be recognized, the diffusive regime, the free-fall regime and the intermediate regime.

Diffusion limit

At high pressures, the mean free path is much smaller than L^*, and a fluid model is appropriate. In this diffusion mode, the radial transport is dominated by ambipolar fluxes. When the discharge is sustained by volume ionization, the balance of the system is determined by the equilibrium between diffusion and ionization:

$$D_a \nabla^2 n + < \sigma v >_{ion} n_n n = 0 \tag{1.40}$$

where D_a is the macroscopic ambipolar diffusion coefficient:

$$D_a = \frac{\mu_i D_e + \mu_e D_e}{\mu_i + \mu_e} = [\mu_e >> \mu_i] \approx D_i + \frac{\mu_i}{\mu_e} D_e = [\mu = eD/KT] \approx D_i \left(1 + \frac{T_e}{T_i}\right) \tag{1.41}$$

where n is the plasma density, n_n is the neutral gas density and $< \sigma v >_{ion}$ is the rate constant of ionization. In a cylindrical geometry the density in radial direction is thus governed by the following Bessel equation:

$$D_a \frac{1}{r} \frac{d}{dr} \left(r \frac{dn}{dr} \right) + < \sigma v >_{ion} n_n n = 0 \tag{1.42}$$

which has the classical solution in term of Bessel functions. In the limiting case of null boundary condition $n(r = R) = 0$ the solution is[3]:

$$n(r) = n_0 J_0 \left(2.405 \frac{r}{R} \right) \tag{1.43}$$

[3] In practical cases, the density at the edge of the cylinder is never zero, so the case is just a theoretical limit.

where J_0 is the Bessel function of the first kind and n0 is the plasma density on the axis. Substituting the solution inside the original Bessel differential equation, the relation at steady state between the ionization rate and the system dimension is obtained, $n_0 < \sigma v >_{ion} R^2 = 5.78 D_a$. This condition states that the ionization frequency is equal to the wall loss frequency. When a cylinder of finite length is considered, the plasma density results to be equal to the Schottky profile, evaluated for null boundary conditions $n(r = R) = n(z = \pm l) = 0$:

$$n(r, z) = n_0 \cos\left(\frac{\pi}{2l} z\right) J_0\left(2.405 \frac{r}{R}\right) \tag{1.44}$$

where l is the plasma half-length, which is equal to half the length of the discharge minus the width of the sheath at the endwall.

Free-fall solution

At very low pressure the mean free path is much greater than L^*, and the kinetic free-fall approach due to Tonks and Langmuir [6] offers the solution to the problem. In this regime, ions can be considered collisionless. In presence of an electric field they are subject to a free-fall acceleration, and the ion velocity can be obtained from energy conservation, $v_i^2 = -2e\phi/M_i$, where e is the elementary charge, ϕ the potential, and M_i the ion mass. Assuming Maxwellian electrons the ion velocity results $v_i^2 = 2C_s^2 \log(n/n_0)$, where C_s is the ion Bohm velocity. This expression of the ion velocity can be substituted in the continuity equation to solve for the plasma density. In a monodimensional slab, the resulting non-linear differential equation is the following:

$$\frac{d(nv_i)}{dx} = \frac{d}{dx}\left[n\left(2C_s^2 \log\frac{n}{n_0}\right)^{1/2}\right] = n_n < \sigma v >_{ion} \tag{1.45}$$

This equation has an analytical solution, solved for the first time by Tonks and Langmuir by means of a power series [6]. A closed form has been obtained later, by means of Dawson functions:

$$\exp\left(\frac{\Phi(\zeta)}{T_e}\right) = \sqrt{\frac{T_e}{2}} \int_0^{\zeta} \frac{\exp\left(\frac{\Phi(\zeta)}{T_e}\right)}{\sqrt{\Phi(\zeta) - \Phi(z)}} dz \tag{1.46}$$

where $\zeta = x n_n < \sigma v >_{ion}$. The solution shows a plasma density on the radial boundary of one half to one third that along the discharge.

Intermediate regime

The regime of intermediate pressures is the more difficult to treat, because in principle the discharge medium does not exhibits neither fluid nor single-particle behavior. When the ambipolar drift velocity at the wall is taken equal to the Bohm velocity, $v(r = R) = C_s$, a

finite value of plasma density is obtained at the boundary. This kind of analysis has been pursued in 1962 by Person [7].

Kino and Shaw [8] first tried to treat the intermediate pressure regime with a fluid approach, and they found that fluid theory is applicable also to collisionless discharges.

The transition between the diffusion mode at high pressure and the Langmuir mode at very low pressures, was then analyzed by Self and Ewald [9] in 1966; they found 1D-distributions of plasma density coinciding with the Schottky profile at high pressures and with Langmuir profile at very low pressures. They made the simplifying assumption to have an ion-neutral collision frequency ν_{in} independent on drift velocity.

Later Godyak [10] found analytical solutions for the constant mobility case, assuming to have a Bohm velocity at the plasma boundary. The solution has been found with a diffusion approximation, assuming that the ambipolar drift velocity is proportional to the ambipolar field, $v = (e/m\nu_{in})E_{amb}$. In this case the solution for a rectilinear slab and for cylindrical geometry are, respectively:

$$n(x) = n_0 \cos\left[\frac{\pi}{2}(1-\delta_x)\frac{x}{d}\right] \tag{1.47}$$

$$n(r) = n_0 J_0 \cos\left[2.4(1-\delta_r)\frac{r}{R}\right] \tag{1.48}$$

where $\delta_x = D/(v_s l) << 1$, with l the plasma half-length, and $\delta_r = D/(v_s R) << 1$. The corresponding ratios between the plasma density in the center of the discharge and at the plasma boundary are:

$$\frac{n(x=L)}{n_0} = \frac{\pi}{2}\frac{D}{v_s l} = 1.57\frac{\lambda_i}{l}\left(\frac{T_e}{T_g}\right)^{1/2} \tag{1.49}$$

$$\frac{n(r=R)}{n_0} = 1.25\frac{D}{v_s l} = 1.25\frac{\lambda_i}{R}\left(\frac{T_e}{T_g}\right)^{1/2} \tag{1.50}$$

These profiles are in accord with the previous analysis of Self and Evald.

The solutions for the low pressure case showed up to now all assume a constant mobility, and they are consequently applicable only at relatively high values of the Paschen parameter $Pa = p_0 L^*$, corresponding to the case when the ionization frequency has still a local meaning. At lower values of the Paschen parameter (corresponding to lower pressures or smaller discharges, or both), the constant mobility approximation is no more satisfied. In this oligo-collisional regime the ion-neutral collisions are dominated by charge exchange, and diffusion becomes non-linear. The mobility is no more constant, the ambipolar diffusion equation is no more valid, and the solutions obtained for constant mobility must be corrected.

A first study where the mobility is considered variable with the drift velocity has been done by Cervenan and Matisovitz [11], where the following relation is obtained for the ratio of densities:

$$\frac{n(r=R)}{n_0} \approx 0.6\left(\frac{\nu_{ioniz}}{\nu_{ioniz}+\nu_{in}}\right)^{1/2} \tag{1.51}$$

where $\nu_{ioniz} = n_n < \sigma v >_{ion}$ is the ionization frequency.

Godyak [10] identified as the main parameter the ratio between the electron energy relaxation length and the plasma dimension, $\lambda_{eT}/L^* << 1$, and obtained solutions confirmed by experimental evidence for the two following cases:

1. $\lambda_{eT} > L^*$ in the low pressure regime,
2. $\lambda_{eT} < L^*$ in the high pressure regime.

The main results of such analysis can be found in the Godyak monography [10].

1.2.3 Analysis of collisional processes in Argon

The species composing the plasma (ions, electrons, neutrals, etc.) interact together by means of collisional processes. Depending on the substances, the involved collisional features can span over a considerable parameter space. Here we will take into account Argon gas. In fact, Argon has been chosen for the experimental validations, for practical reasons like easiness of its availability, safety during Laboratory operations, electropositivity of its plasma, and large spread of use in the Laboratories, and thus portability of the results.

Neutral-neutral collisions

In the hard shell limit, Argon atoms have an atomic radius of 71 pm (calculated covalent atomic radius, [12]), and a geometrical spherical cross section of $\sigma_n = \pi(r_{Ar} + r_{Ar})^2 = 6.33 \times 10^{-20}$ m^{-2}. For discharge pressures within the range from 1 to 20 mTorr, this would lead to a neutral-neutral mean free path in the range $\lambda_{nn} \approx 50 - 2.4$ cm respectively. This range overlaps the usual diameter of discharges, going from 1 cm for very small discharges, to 40-50 cm, or more, for larger chambers. According to these values, the neutrals would result only slightly collisional, and in some case they should be not collisional at all. For Argon at room temperature and at pressure of 10 mTorrs, the number density is $n_n = p_0/(K_B T_n) = 3.2 \times 10^{20}$ m^{-3}, and thus the neutral-neutral mean free path is $\lambda_{nn} = 1/n_n\sigma_n \approx 5$ cm. When flowed in a small cylindrical discharge of 2 cm in diameter and 15 cm in length, they could have few chances to collide among each other, and they should be treated as free particles. However, considering only the geometrical cross section leads to a wrong evaluation of the cross section.

A more refined evaluation of Argon atom-atom scattering cross sections is done in greater detail by Phelps et al. [13] over a wide range of energies (10^{-2} - 10^4 eV) and using a quantum mechanical model. A comparison with several experiments and with the results of other authors is also done. Figures 1.5.a shows the interaction potential of two Argon atoms versus their internuclear separation[4], and 1.5.b shows the total σ_t, viscosity σ_v and

[4]We note that when a new neutral atom enters into the plasma, its ionization potential decreases in the order of $O(e^2 n_e^{1/3}(me^4/h^2T)^{1/2})$. The decrease is due to presence of other ions, and to electrons collisions. This decrease in ionization potential is almost always neglected in the calculations.

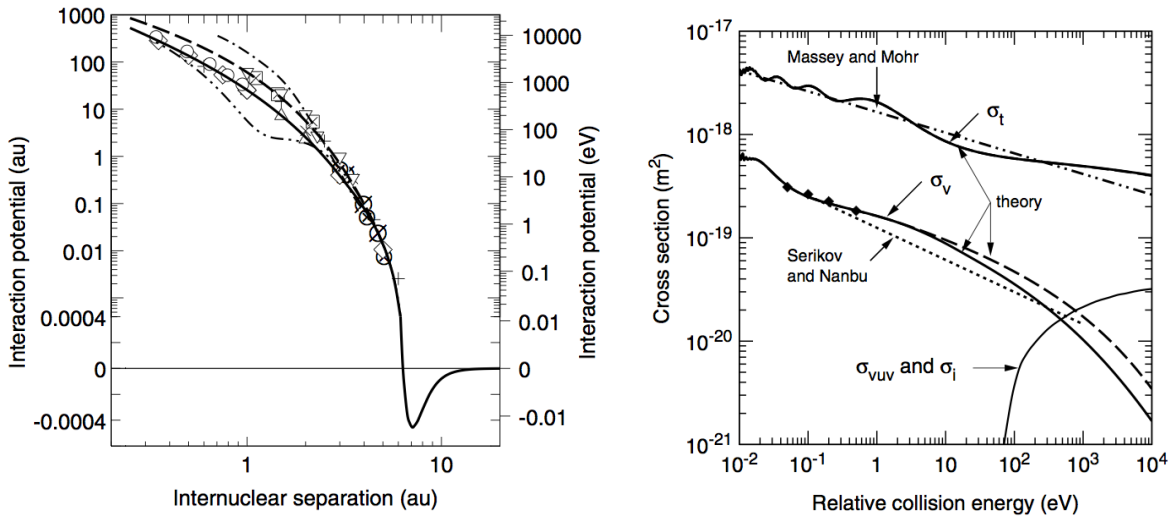

(a) (b)

Figure 1.5: (a) Interaction potential versus internuclear separation for Ar atoms; atomic units are 27.2 eV and 0.529×10^{-10} m; (b) Total σ_t, viscosity σ_v and inelastic σ_{vuv}, σ_i cross sections for symmetric Ar atom - Ar atom collisions. Both figures are adopted from [13].

inelastic σ_{vuv}, σ_i cross sections for symmetric Ar atom - Ar atom collisions. The Phelps neutral-neutral cross sections will be used in our models of neutrals.

Coulomb collisions

Before treating Coulomb collisions, we have to consider quasineutrality of the plasma inside the discharge. The electron density inside the discharges can cover a large range, going from 10^8 cm^{-3} for low-power and low-efficiency discharges, to 10^{14} cm^{-3} for high-power and high-efficiency discharges. Laboratory plasma obtained with helicon sources are usually in the range 10^{10} cm^{-3} - 10^{13} cm^{-3}. Electron temperatures span a range of few electronvolts, usually around 3 eV. The Debye radius is thus $\lambda_D = \sqrt{K_B T_e \epsilon_0 / ne^2} \approx 0.13$ mm - 1.3×10^{-3} mm. For helicons it is $\lambda_D = 0.13$ mm - 4.1×10^{-3} mm. Even in the case of very low-density discharges, the Debye radius is much smaller than the characteristic size of the discharge, and the plasma can thus be considered quasi-neutral. Furthermore, a single charge could not live in the plasma even when the plasma density is low and the gas pressure is high. In fact, the relaxation time is proportional to ϵ_0/σ, where ϵ_0 is the vacuum permittivity and σ is the conductibility of the plasma. The worst case in this case is for ions, which have the lowest mobility. In the low density case of 10^{16} m^{-3} at pressures around 20 mTorr, the Argon charge-exchange is around 200 kHz, and the conductibility

results $\sigma = ne^2/M_i\nu_{ch.ex} = 10^{16}(1.6\times10^{-19})^2/6.7\times10^{-26}2\times10^5 \approx 10^{-2}\ \Omega^{-1}m^{-1}$, with a relaxation time of the order of 0.1 nanoseconds. Thus an isolated charge can't live inside the plasma much more than this time, and it is rapidly expelled out.

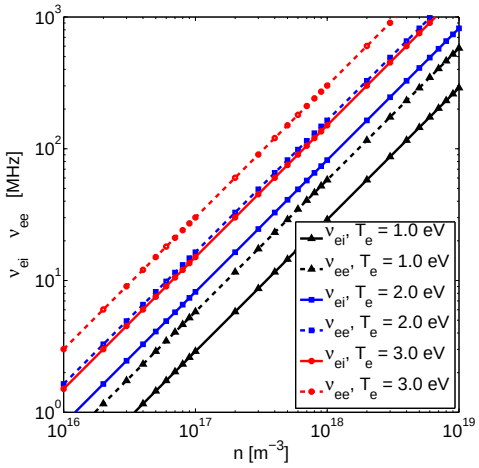

Figure 1.6: Frequencies of electron-ion and electron-electron Coulomb collisions versus the plasma density for three values of electron temperature

Electron-ion Coulomb collisions are characterized by many small-angle deflections. When the electron and the ion are considered as isolated charges, their relative motion is purely orbital. In this case a 90-dregrees deflection happens when the electron swing by the ion coming from a distance h, called the impact parameter. In a quasineutral plasma, the effect of small-angle deflections is to amplify the parameter h of a factor $\log\Lambda$, the Coulomb parameter, resulting in even greater cross sections. In cold plasmas the Coulomb parameter is $\log\Lambda \approx 10$. An approximate formula of the ion-electron collision frequency is:

$$\nu_{ei} \approx 2.9\times10^{-6} n[\mathrm{cm}^{-3}]\log\Lambda/T_e[\mathrm{eV}]^{3/2} \tag{1.52}$$

For the usual electron temperatures of 3 eV, the collision frequency is $\nu_{ei} \approx 5.58\times10^{-6}n[\mathrm{cm}^{-3}]$, and in the range of helicon plasma densities $10^{10}-10^{13}$ [cm^{-3}] it is comprised between 56 kHz and 56 MHz. With an electron thermal velocity of $v_e = \sqrt{2K_BT_e/m_e} \approx 1.03\times10^6$ m/s, the resulting mean free path is in the range $\lambda_{ei} = v_e/\nu_{ei} \approx 18$ m - 1.8 cm respectively. Common RF helicon discharges work at 13.56 MHz or 27.12 MHz, corresponding to a mean free path $\lambda_{ei,13.56} \approx 7.6$ cm and $\lambda_{ei,27.12} \approx 3.4$ cm respectively.

Electron-electron Coulomb collisions can be treated similarly to electron-ion collisions, and the resulting approximated collision frequency is:

$$\nu_{ee} \approx 5.8\times10^{-6} n[\mathrm{cm}^{-3}]\log\Lambda/T_e[\mathrm{eV}]^{3/2} \tag{1.53}$$

In this case the two particles involved have the same mass, and the orbits are both affected considerably by the collisional process. Electron-electron collisions have thus the main effect to redistribute their energy, so that in stationary conditions they thermalize to a Maxwellian distribution for velocities, and to a Boltzmann distribution for their number density. For the same example as before, with electrons at 3 eV, the resulting collision frequency is $\nu_{ee} \approx 11.16 \times 10^{-6} n[\mathrm{cm}^{-3}]$, and in the usual range of helicon plasma densities $10^{10} - 10^{13}$ [cm^{-3}] it is comprised between 112 kHz and 112 MHz. The resulting mean free path is in the range $\lambda_{ee} = v_e/\nu_{ee} \approx 9$ m - 9 mm respectively. Here we see that for low density helicon discharges in the 10^{10} cm^{-3} range, the electron-electron mean free path can be greater than the discharge size. Electrons have the time to thermalize only if they stay inside the discharge for a time high enough to collide many times among each other, in order to maximize their entropy. In other words, electrons thermalize only if their collision frequency is much higher than their loss frequency at the walls. Only when this condition is satisfied, electrons can be treated as a thermalized medium. The flux of electrons to the wall can hardly be predicted, because it is strictly dependent on the whole transport balance of the particular discharge considered, and it can vary among regimes and configurations of the discharges. Roughly speaking, the ion Bohm flux at the walls is one-half the density in the bulk, and assuming a local quasineutrality, the electron flux is $\Gamma_e = nC_s/2$, with C_s the ion Bohm velocity. The loss frequency of electrons is thus $\nu_{e,wall} = \Gamma_e A$, with A the plasma contacting surface of the discharge. Helicon Argon plasma ($10^{10} - 10^{13}$ [cm^{-3}]) with 3 eV electrons has a Bohm velocity of $C_s = 2680$ m/s. Their flux of electrons at the wall is $\Gamma_e \approx 1.3 \times 10^{19} - 1.3 \times 10^{22}$ electrons/m^2/s. A small cylindrical helicon source of 2 cm in diameter and 15 cm long has thus an electron loss frequency of $\nu_{e,wall} \approx 1.3 \times 10^{17}$ - 1.3×10^{17} electrons/s.

Ion-neutral collisions

Ion-neutral collisions in Argon, showed in Figure 1.7.a, are always dominated by charge-exchange collision phenomena for all the interesting ion energies. This collisional process is much greater than the electron-neutral processes, exceeding them of two orders of magnitude. The charge-exchange cross section is higher than the neutral-neutral cross section because the two particles do not have to geometrically collide in order to exchange one electron. Charge-exchange collisions are responsible of ion scattering even though the trajectories of the particles are not modified. One of the most comprehensive studies of of the charge exchange between gaseous ions and atom was done in 1962 by Ralph and Francis [14]. Their charge exchange cross section for ions immersed in their parent neutral atoms are reported in Fig. 1.7.a. A brief history of studies regarding the resonant charge-echange has been briefly recalled in [15], recalled as the “Sena effect”.

When the resonant charge-exchange collision happens, the neutral and plasma particles exchange their velocity. The neutral ”gains” energy and ion loose energy. After the collision event, the neutrals are faster and they easily reach the wall of the discharge, but they cannot

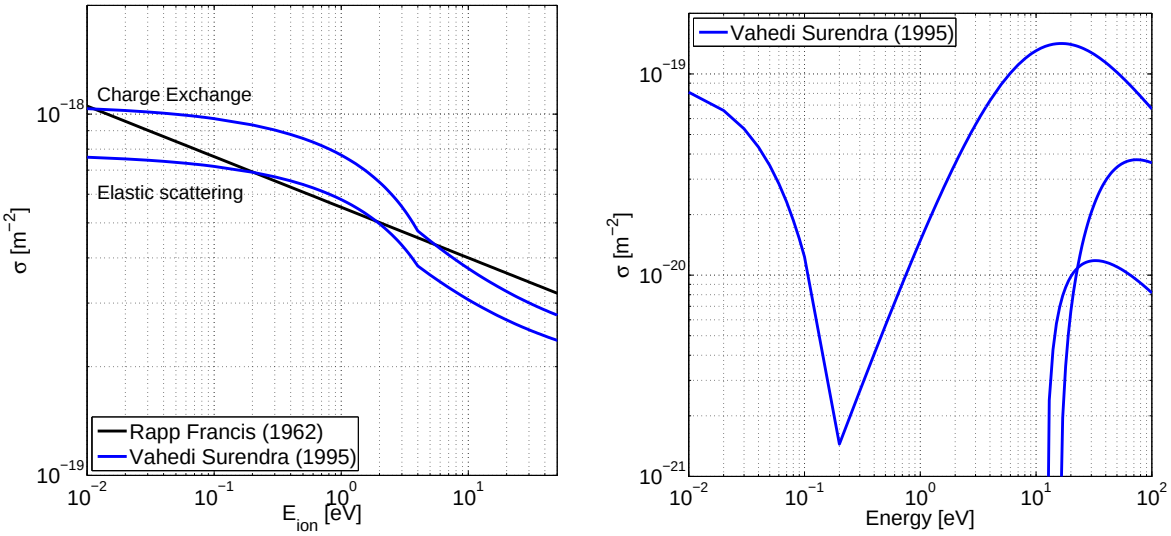

(a) (b)

Figure 1.7: Argon cross-sections (a) ion-neutral; (b) electron-neutral.

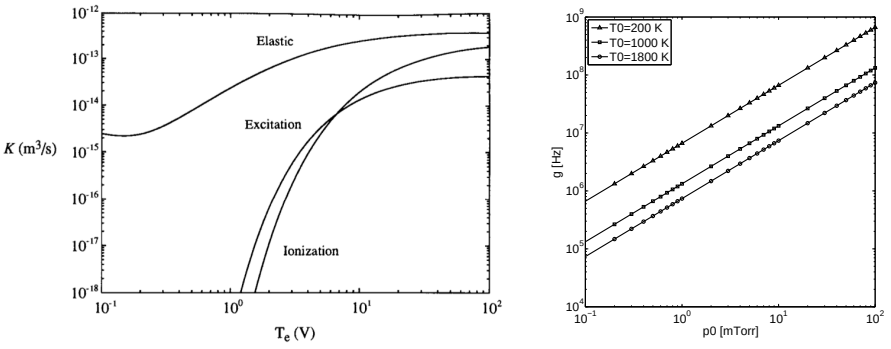

(a) (b)

Figure 1.8: (a) electron-Argon collision probabilities mediated over a Maxwellian [figure adopted from [21]], (b) source rate vs. neutral pressure

leave the plasma. They will elastically collide with the wall. In the very low collisional regime, the radial movement of the neutral will be something like a ping-pong between the walls. Since we are considering no azimuthal and no axial variations, what is important for neutrals is their ratio between their mean free path and the source diameter (the Knudsen number). In the range we are interested, at p0 = 3 mTorr, the mean free path goes from 20 to 100 cm (approx), and with the source of 10 cm in diameter this means they are reflected 2-10 times by the walls during the time between two collisions. At the next collision event, the fast neutral could collide either with another neutral or with another ion. The first event is more likely, and the effect is to redistribute its higher energy to other colder neutrals. The process continue until neutral thermalize to an higher temperature. This temperature is given by the equilibrium with resonant charge exchange collisions. After that neutrals are thermalized, since it's equally likely that they can gain energy from resonant charge-exchange collisions, or that they can loose energy among them for elastic collisions.

Referring to the same example as before, the Argon gas at room temperature and $p_0 = 10$ mTorr, with ions at $T_i = 0.01$ eV, has a charge-exchange cross section equal to $\sigma_{ch.ex} \approx 10^{-18}$ m^{-2}, and an associated mean free path equal to $\lambda_{ch.ex} = 1/(n_n \sigma_{ch.ex}) \approx 3$ mm. Charge-exchange processes is thus a relevant process also in very small discharges, and can affect greatly the transport phenomena of the discharge. Figure **??** shows charge-exchange frequency in Argon as a function of gas pressure (charge-exchange data at low T_i has been analyzed by Sheldon).

Electron-neutral collisions

Electron-neutral collisions are distinguished into three kinds: elastic, excitation and ionization. Figure 1.7.b [Vahedi 1993] shows the three electron-neutral cross sections as a function of the energy of the impacting electron for Argon. The highest cross section is due to elastic scattering. As can be seen from the curve of elastic scattering, Argon atoms has a large Ramsaurer effect with a low peak around 0.2-0.4 eV. In the usual range of electron energies of 3-10 eV, the elastic scattering cross section is in the range $\sigma_{el} = 6$ - 10×10^{-20} m^{-2}. For example, the same gas as before at room temperature and $p_0 = 10$ mTorr, with electrons at 3 eV, has an electron-neutral mean free path equal to $\lambda_{en,el} = 1/n_n \sigma_{el} \approx 5$ cm. This means that electrons elastically collide with neutrals as often as neutrals collide among themselves. The other two kinds of electron-neutral interactions are inelastic and have a smaller cross section. The electron-neutral ionization event is fundamental for the discharge ignition and sustainment. Figure 1.8.a shows the electron-Argon collision probabilities mediated over a Maxwellian, and Figure 1.8.b shows the source rate $g = n_n < \sigma v >_{ion}$ as a function of neutral pressure p_0 for three different values of neutral temperature. The electron-neutral excitation collision is the lowest, but plays a fundamental role in the evaluation of losses for line radiation. Excitation phenomena play also an important role for the spectral characterization of the discharge.

1.3 Discharge equilibrium

1.3.1 Radial equilibrium model

We consider a plasma in an infinite circular cylinder of radius a in which all quantities depend only on the coordinate r. There is a uniform, coaxial magnetic field $B\hat{z}$. Ions are accelerated by electric fields, which are scaled to an electron temperature of around 3 eV. At 100 Gauss, the ion Larmor radius r_{Li} at $KT_i = 3$ eV is equal to 18 cm, which is usually larger than a. Hence, the ions can be considered unmagnetized. At 1000 Gauss, r_{Li} is of order 1.8 cm, which may be smaller than a but radial electric fields $\vec{E}$ can only cause the ions to drift in the ignorable direction θ. There are no azimuthal E-fields in steady state, there being no dc current in the z direction. Hence, we can ignore the effect of B on ion motions even at 1000 Gauss. Radial ion motion is controlled by E_r and charge-exchange collisions with neutrals. At 3 eV, argon ions have a mean free path of order 14 cm at 1 mTorr and 0.7 cm at 20 mTorr, and therefore neither the collisionless nor the highly collisional limit is applicable. The ion equation of motion in equilibrium is

$$Mn\vec{v}\cdot\nabla\vec{v} = en\vec{E} - K_BT_i\nabla n - Mn\vec{v}\nu_{io} \tag{1.54}$$

Here M is the ion mass, n the quasineutral plasma density, $\vec{v}$ the ion fluid velocity, and ν_{io} the charge-exchange collision frequency, whose evaluation is analyzed in Sec.1.2.3. Since $\vec{E}$ is scaled to $T_e >> T_i$, we can simplify by neglecting the KT_i term. Defining

$$\vec{E} = -\nabla\phi, \quad \eta \equiv -e\phi/K_BT_e, \quad \text{and} \quad c_s \equiv (K_BT_e/M)^{1/2} \tag{1.55}$$

we can write the radial component of Eq. 1.54 as

$$v\frac{dv}{dr} = -\frac{e}{M}\frac{d\phi}{dr} - \nu_{io}v = \frac{K_BT_e}{M}\frac{d\eta}{dr} - \nu_{io}v = c_s^2\frac{d\eta}{dr} - \nu_{io}v \tag{1.56}$$

where $v = v_r$.

The ion equation of continuity is

$$\nabla\cdot(n\vec{v}) = Q(r) = nn_nP_i(r), \tag{1.57}$$

where $P_i(r)$ is an ionization probability given by

$$P_i(r) \equiv < \sigma v >_{ion} (r) \tag{1.58}$$

Here n_n is the density of neutral argon and $< \sigma v >_{ion}$ is a radially dependent ionization probability varying sensitively with $T_e(r)$. With quantities varying only with radius, Eq. 1.57 can be written

$$\frac{dv}{dr} + v\frac{\ln n}{dr} + \frac{v}{r} = n_nP_i(r) \tag{1.59}$$

We next consider electrons. Their equation of motion is

$$mn\vec{v}\cdot\nabla\vec{v} = -en(\vec{E}+\vec{v}\times\vec{B}) - K_BT_e\nabla n - mn\vec{v}(\nu_{eo}+\nu_{ei}) \tag{1.60}$$

where the collision frequencies are with neutrals and ions. Since the electrons are magnetized, classical diffusion theory [17] would predict that their rate of diffusion across $\vec{B}$ would be slower than that of the unmagnetized ions. This would give rise to a plasma potential that is more negative at the center than at the edge. In experiment, the opposite is observed: the potential peaks at the center just as does the density, in agreement with Boltzmann's relation Eq. 1.61.

$$n = n_0\exp(e\phi/K_BT_e) = n_0\exp(-\eta) \tag{1.61}$$

The reason for this is that plasmas are not infinitely long, and electrons can reach the ends of the chmaber well before they can reach the periphery. In this case the Simon short-circuit effect [18] must be taken into account. We therefore give a pictorial explanation of it.

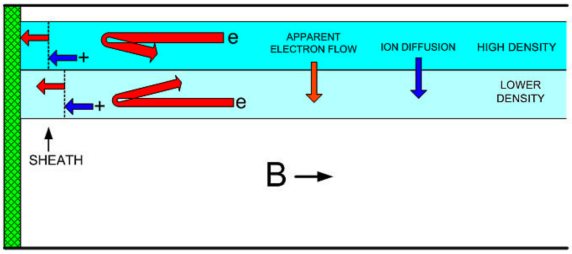

Figure 1.9: Illustration of the short-circuit effect

One end of a finite-length discharge in a magnetized field is shown in Fig. 1.9. Electrons are strongly magnetized so that they are lost mainly at the endplates. The ions enter the end sheaths with the Bohm velocity C_s defined in Eq.1.55. Electrons are much faster but must leave at the same rate to keep the plasma neutral along each field line [5], and therefore a sheath sets up to form a Coulomb barrier for the electrons. Let the endplates be at ground, $\phi = 0$. The plasma potential ϕ_p is positive to retain the electrons. Consider the two tubes of plasma shown, with the tube nearer the wall containing more plasma because the ionization is higher there. The unmagnetized ions will then diffuse toward the lower-density region. The magnetized electrons cannot follow, but the sheaths at the end can re-adjust. The sheath in the high-density region becomes thinner, allowing more electrons to reach the endplate. The sheath in the low-density region becomes thicker,

[5] This is obviously true if the endplates are insulating, but it is also true if the endplates are conducting. In that case, electrons can move across B inside the endplate. However, they cannot be injected into a low-density region unless the endplate is emitting, and we assume that the endplates are not thermionic.

so fewer electrons reach the endplate. The result is that the sheaths adjust so that more electrons are taken out of the tubes where there are to many electrons as the ions leave, and fewer electrons are lost where there are too few electrons as the ions enter. It appears that electrons have moved across the B-field from high to low density to follow the ions, but in actuality the electrons never crossed the B-field. There was only a slight adjustment of the flow of electrons through the sheaths. Thus, $\phi_p(r)$ adjusts so that ions and electrons leave each tube at the same rate. This mechanism allows electrons to arrive at their most probable distribution, the Maxwellian one. This results in a $\phi(r)$ which obeys the Boltzmann equation Eq.1.61 even across field lines.

More specifically, the ion flux at the sheath edge is nC_s, and the electron flux is nv_{the}, where the electron thermal velocity in one direction is the $v_{the} = (KT_e/2\pi m)^{1/2}$. Thus, equal fluxes requires

$$\frac{e\phi_p}{K_B T_e} = \ln\left(\frac{M}{2\pi m}\right)^{1/2} \tag{1.62}$$

This is the condition for the floating potential of a probe and does not involve the density at all. Each tube can have an arbitrary density and potential, independent of its neighbors. This is, of course unreal, since tubes can communicate with one another through ion motions. As the ions move radially, the electrons can follow via the short-circuit effect. Hence, the electrons are not restrained by the magnetic field, and Eq. 1.61 is valid over the whole plasma.

We can now combine equations into a single equation for the ion fluid velocity v in the radial direction. From Eq. 1.61 we have

$$\frac{d\ln n}{dr} = -\frac{d\eta}{dr} \tag{1.63}$$

Inserting this into Eq. 1.59 gives

$$\frac{dv}{dr} - v\frac{d\eta}{dr} + \frac{v}{r} = n_n P_i(r) \tag{1.64}$$

Eq. 1.56 can be written as

$$\frac{d\eta}{dr} = \left(v\frac{dv}{dr} + \nu_{io} v\right) C_s^{-2} \tag{1.65}$$

Finally, substituting this into Eq. 1.64 yields an ordinary differential equation for v:

$$\frac{dv}{dr} + \frac{v}{r} - \frac{v^2}{C_s^2}\left(\frac{dv}{dr} + \nu_{io}\right) = n_n P_i(r) \tag{1.66}$$

Defining

$$\nu_{io} = n_n < \sigma v >_{cx} \equiv n_n P_c(r) \tag{1.67}$$

where $< \sigma v >_{cx}$ is the Ar^+-Ar charge-exchange probability, we now have

$$\frac{dv}{dr} + \frac{C_s^2}{C_s^2 - v^2}\left(\frac{v}{r} - \frac{v^2}{C_s^2} n_n P_c(r) - n_n P_i(r)\right) = 0 \tag{1.68}$$

The "plasma solution" given by this ordinary differential equation clearly diverges at a radius $r = r_a$, where $v = C_s$. The Bohm criterion for sheath formation is satisfied at r_a, and that radius can be identified as the discharge tube radius a if the sheath thickness is negligible. The value of r_a apparently depends on the physical quantities n_n, C_s, P_c and P_i, but it will turn out that the dependence is very weak. Normalizing v to C_s by

$$u \equiv v/C_s \tag{1.69}$$

we can write Eq. 1.68 as

$$\frac{du}{dr} + \frac{1}{1-u^2}\left[\frac{u}{r} - \frac{n_n}{C_s}(u^2 P_c + P_i)\right] = 0 \tag{1.70}$$

Here r is still dimensional, and this equation will be solved later. It will be convenient to rewrite this equation as

$$\frac{du}{dr} - \frac{1}{1-u^2}\left[\frac{n_{nP_i}}{C_s}(1 + ku^2) - \frac{u}{r}\right] = 0 \tag{1.71}$$

where

$$k \equiv P_c/P_i = < \sigma v >_{cx} / < \sigma v >_{ion} \tag{1.72}$$

Since $n_n P_i/C_s$ has dimensions of $(\text{length})^{-1}$, we now introduce a dimensionless independent variable ρ defined by

$$\rho \equiv (n_n P_i/C_s) r \tag{1.73}$$

obtaining

$$\frac{du}{d\rho} = \frac{1}{1-u^2}\left[1 + ku^2 - \frac{u}{\rho}\right] \tag{1.74}$$

1.3.2 Analytical treatment of the singularity

The radial diffusion equation Eq.1.74 is of the form:

$$\frac{du}{d\rho} = \frac{1}{1-u^2}\left[q + ku^2 - \frac{u}{\rho}\right] \tag{1.75}$$

where:

$$\rho = r/a \qquad \text{non-dimensional radius} \tag{1.76}$$

$$u = v_r/C_s \qquad \text{radial Mach} \tag{1.77}$$

$$q = aQ/C_s \qquad \text{ionization term} \tag{1.78}$$

$$k = a\nu_{io}/C_s \qquad \text{charge exchange term} \tag{1.79}$$

The equation is solved together with the two conditions at the boundaries:

$$u(0) = 0 \qquad \text{Axial-symmetry} \tag{1.80}$$

$$u(1) = 1 \qquad \text{Bohm sonic condition} \tag{1.81}$$

The ordinary differential equation Eq.1.75 together with the two conditions at the two points $\rho = 0$ (Eq. 1.80) and $\rho = 1$ (Eq. 1.81) constitute a boundary value problem.

Near the axis the drift motion of the plasma is subsonic,

$$u << 1, \tag{1.82}$$

and there the transport equation becomes

$$\frac{du}{d\rho} \approx q + (k+q)u^2 - u/\rho \tag{1.83}$$

In this case, and when the parameters q, k are constant, the following analytical solution is found:

$$u(\rho) = \left(\frac{p}{k+q}\right) \frac{C_1 K_1(-p\rho) - I_1(p\rho)}{-C_1 K_0(-p\rho) + I_0(p\rho)} \tag{1.84}$$

where $p = \sqrt{-q(k+q)}$, the constant C_1 depends on the boundary condition, and $I_{0,1}$ $K_{0,1}$ are the modified Bessel functions of 1^{st} and 2^{nd} kind respectively. Substituting the axis-symmetry condition of radial Mach equal zero at the axis,

$$u(0) = 0 \tag{1.85}$$

the value of C_1 is calculated. The l'Hopital rule has to be used to solve the indeterminate form of the limit,

$$C_1 = \lim_{\rho \to 0} \frac{\left(\frac{p}{k+q}\right)(C_1 K_1(-p\rho) - I_1(p\rho))}{-C_1 K_0(-p\rho) + I_0(p\rho)} = 0^{\pm} \tag{1.86}$$

The subsonic solution is thus given by:

$$u_{subsonic}(\rho) = -\left(\frac{p}{k+q}\right) \frac{I_1(p\rho)}{I_0(p\rho)} \qquad \text{subsonic solution } (u < 0.3), p = \sqrt{-q(k+q)} \tag{1.87}$$

This analytical solution is of great practical utility to treat the equation near the axis, where the differential equation is singular and the plasma is still subsonic. Figure 1.10.a shows the real component of the subsonic solution versus ρ, with $q = k = 1.0$; Figure 1.10.b shows the comparison of the subsonic solution with the numerical integration of the full equation done with an adaptive Runge-Kutta of 4^{th}-5^{th} order. The error of the analytical approximation is small up to $u < 0.3$, as expected from the subsonic approximation.

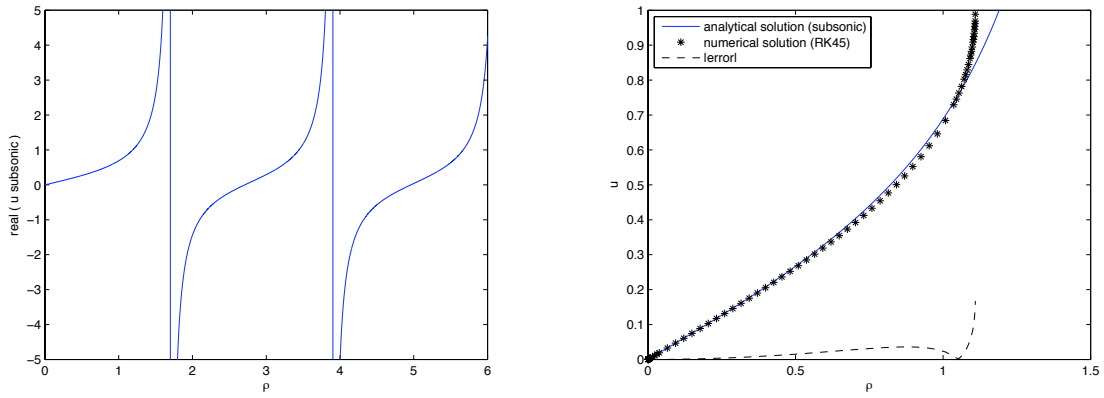

(a) (b)

Figure 1.10: (a) Analytical subsonic solution (for q=k=1.0); (b) comparison of the subsonic solution with the numerical integration of the full equation.

The subsonic solution can also be used to obtain a rough estimate of that particular ρ where the solution becomes singular, $u(1) = 1$, by finding the first positive zero near the origin of the following equation:

$$I_0(p\rho) + \left(\frac{p}{q+k}\right) I_1(p\rho) = 0 \tag{1.88}$$

The full radial drift equation, Eq. 1.75, exhibits interesting properties of "self-similarity", i.e. their solutions are always the same when an opportune renormalization is done. From the solution $u(\rho)$ of the associated Cauchy problem,

$$\frac{du}{d\rho} = \frac{1}{1-u^2}\left(q + ku^2 - \frac{u}{\rho}\right) \tag{1.89}$$

$$u(0) = 0 \tag{1.90}$$

the radial location of the Bohm singularity can be determined:

$$\rho_{Bohm} = \left\{\rho : \lim_{\rho \to \rho_{Bohm}} u(\rho) = 1\right\} \tag{1.91}$$

Then the renormalization is done by means of the formal substitution:

$$\rho \to \frac{\rho}{\rho_{Bohm}} \tag{1.92}$$

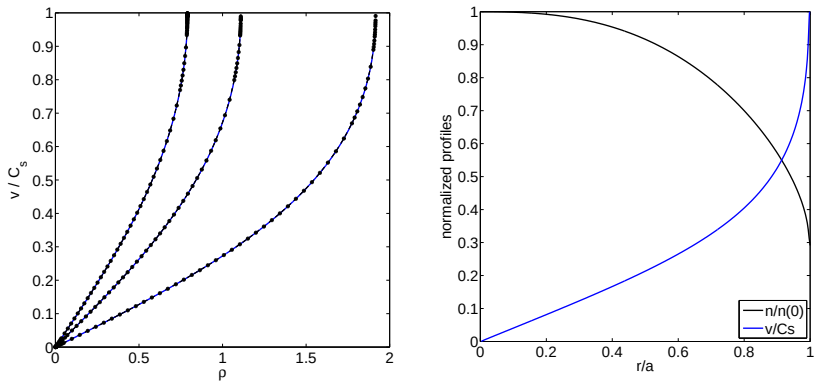

(a) (b)

Figure 1.11: (a) Solutions of Eq.1.74 for three different values of k; in each case the sheath edge ρ_a occurs at a different value of ρ, (b) Solutions of Eq.1.74 for 15 mTorr of Argon and $K_BT_e = 3$ eV, yielding v/C_s (black), n/n_0 (blue) (red, right scale); the latter two are related by the Boltzmann relation. The abscissa is normalized so that the sheath edge occurs at $r = a$. The curves retain the same shape for any value of a.

1.3.3 Case of constant neutral density and temperature

In this case k is a constant. Eq. 1.74 is a nonlinear ordinary differential equation which can be solved numerically. Using a variable step Runge-Kutta method, we obtain a unique solution for each k, starting with $u = 0$ at $\rho = 0$. Three such solutions are shown in Fig. 1.11.a, each with a radius ρ_a where $v = C_s$. Since the sheath edge must be located at this point, the curves can be renormalized to fit a dishcarge tube of radius a by setting r/a equal to ρ/ρ_a. From the solutions for $v(r)$, Eqs. 1.65 and 1.63 can be used to find $\eta(r)$ and $n(r)/n_0$. Figure 1.11.b shows the radial profiles of v/C_s, n/n_0 and $-\eta(r)$ for one case of fixed K_BT_e and neutral pressure p_0.

The nature of Eq. 1.74 is revealed when the parameters n_n, C_s or P_i in Eq. 1.71 are varied. The values of ρ_a change, but the renormalized curves of Fig. 1.11.b remain the same regardless of magnitudes of these parameters. The profiles are identical when plotted against r/a. The solutions of Eq. 1.74 are self-similar. The curves of Fig. 1.11.b are independent of the numerical value of a. These renormalized curves change only when the nonlinear term ku^2 changes.

The ratio P_i/P_c cannot actually be varied since the ions are accelerated to a velocity v/C_s, given by the universal curve of Fig. 1.11.b, where v is a function of r/a. Hence, the collision frequency ν_{io} is *not* $n_n < \sigma v >_{cx}$ averaged over a Maxwellian ion distribution at

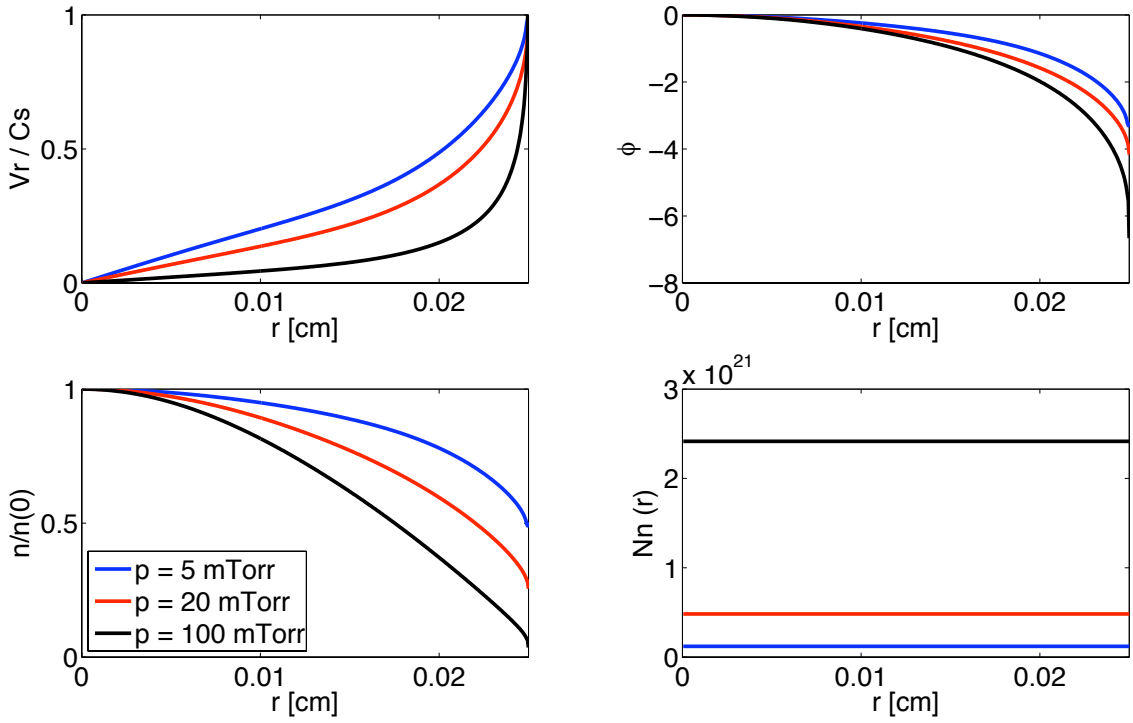

Figure 1.12: Comparison of the solutions for constant n_n and KT_e at different pressures regimes; at high pressures (black curve at 100 mTorr, or 13.3 Pa) the plasma solution, showed in the $n/n(0)$ graph, gets closer to Bessel diffusive solution (Eq. 1.43); at lower pressures (red curve at 20 mTorr = 2.67 Pa, and blue curve at 5 mTorr = 0.67 Pa) the solution shifts continuously toward the free-fall (Eq. 1.45); the calculation has done for Argon in a discharge of 2.5 cm of radius.

a temperature T_i as given by Eq.1.67, but is fixed by the known velocity at each radius:

$$\nu_{io} = n_n \sigma_{cx}(E_i) v(r) \tag{1.93}$$

where v is the fraction of C_s given by the universal curve in Fig. 1.11.b, and the ion energy is $E_i = 1/2 M v^2$. The charge-exchange cross section as a function of E_i is given in Sec. 1.2.3. We can neglect T_i relative to T_e, so ν_{io} is a function of T_e and not T_i. It is a much weaker function of T_e than ν_{ion}. With use of Eq. 1.93 for $n_n P_c(r)$, the ratio $P_c(r)/P_i(r)$ depends only on T_e, and the function $k(r) = P_c(r)/P_i(r)$ will vary in a predictable way as $v(r)$ changes, taking into account the variation of ν_{io} as the ions are accelerated radially. This feature will be included in future graphs, including those in which n_n and T_e are not constant. The normal procedure of calculating a pre-sheath and matching it to the Debye sheath is no longer necessary. Our simple equation takes collisions and ionization into account exactly throughout the plasma and pre-sheath.

That such universal radial profiles, valid for any discharge diameter, can be obtained is a direct consequence of the use of the short-circuit effect to make the electron Boltzmann relation valid across the magnetic field. Since the magnetic field dod not enter into the calculations so far, these results are valid for any cylindrical discharge when end losses can be neglected. Furthermore, Eq. 1.74 naturally defines the sheath edge since $du/d\rho \to \infty$ when $u = 1$, $v = C_s$. There is no need to calculate a pre-sheath and to match it to the Debye sheath since all collisions and ionizations have been taken into account at every radius up to the sheath edge.

1.3.4 Ionization balance

Equation 1.70 for the radial profiles allows for n_n and T_e to vary with radius. We shall first consider how T_e varies when n_n is uniform. It is well known [19] that ionization balance requires T_e to vary with neutral pressure p_0. This can be seen easily in a rough calculation. Let the plasma have a volume V and a surface area A. In steady state, the rate of ion production is $dN/dt = V \bar{n}_e n_n < \sigma v >_{ion}$, where $\bar{n}_e$ is averaged over the plasma. Ions are lost to the walls at the rate $-dN/dt = A n_i(a) C_s = A n_e(a) C_s$. Equating these two gives

$$\frac{2}{a} \frac{n_e(a)}{\bar{n}_e} = n_n \frac{< \sigma v >_{ion}}{C_s} \equiv n_n f(T_e) \tag{1.94}$$

The ratio between n_e at the sheath edge and the average n_e is about 1/2, depending on the collision mechanism, so for a given discharge geometry n_n is inversely related to the function $f(T_e)$ as defined above. The absolute value of n_e has canceled out. Evaluation of $< \sigma v >_{ion}$ is given in Sec. 1.2.3.

Equation 1.94 is an appropriate ionization balance averaged over the whole discharge. *Local* ionization balance at each radius r can be evaluated as follows. Let $n_T(r)$ be the total number of ions in a shell of width dr at r. The input of ions into the shell per unit

length (with $n_e = n_i = n$) is

$$\frac{dn_T(r)}{dt} = 2\pi r dr \cdot n(r) n_n(r) < \sigma v >_{ion} (T_e) \tag{1.95}$$

The loss of ions from the shell is

$$-\frac{dn_T(r)}{dt} = 2\pi r dr \nabla \cdot [n(r)v(r)] = 2\pi r dr \frac{1}{r}\frac{d}{dr}[rn(r)v(r)\ ] \tag{1.96}$$

Equating these gives

$$\frac{1}{nr}\frac{d}{dr}(rnv) = n_n P_i(T_e) \tag{1.97}$$

where n, n_n and v are functions of r found from the solution of Eq. 1.70. This is the local equivalent of Eq. 1.94.

We can now calculate the $T_e - p_0$ relation when n_n is uniform, with neutral depletion neglected. This is found by simultaneously solving Eqs. 1.70 and 1.97 requiring that the Bohm sheath condition $v = C_s$ be met at $r = a$. For a given pressure, and a given discharge radius, there is only one T_e satisfying both Eqs. 1.70 and 1.97. Solving the system of equations, and repeating this for various pressures gives the $T_e - p_0$ relationship for a given gas, as shown in Fig. 1.13 for Argon. Each radius a will have a different curve, since the surface-to-volume ratio varies as $1/a$. These are for uniform pressure, and end losses are neglected. The variation of T_e with r is negligibly small because of the sensitivity of P_i to T_e.

1.3.5 Neutral depletion

To treat neutral depletion, we need to develop an equation for $n_n(r)$. Motion of the neutral gas can be treated with the diffusion equation if their mean free paths are short enough. The total collision cross section ν_{nn} between neutral argon atoms is given by Phelps et al. [13] and varies only between 2 and 3 $\times 10^{-14}$ cm^2 for $K_B T_n$ between 0.05 and 1.0 eV. This is the likely range of neutral energies before and after a charge-exchange collision. The corresponding mean free path varies from 0.1 cm at 20 mTorr to 1.5 cm at 1 mTorr. The use of the diffusion equation is therefore justified unless the discharge tube is very small.

Except for very narrow tubes, the neutral flux Γ is given by

$$\Gamma = n_n \nu_n = -D \nabla n_n \tag{1.98}$$

where the diffusion coefficient D is defined by

$$D = K_B T_n / M \nu_{nn} \tag{1.99}$$

Nuetrals are lost by ionization and are replenished by injection of gas from outside the plasma. With Eq. 1.98, the equation of continuity for neutrals can be written

$$\nabla \cdot \Gamma = -D \nabla^2 n_n - \nabla D \cdot \nabla n_n = -n_n n P_i \tag{1.100}$$

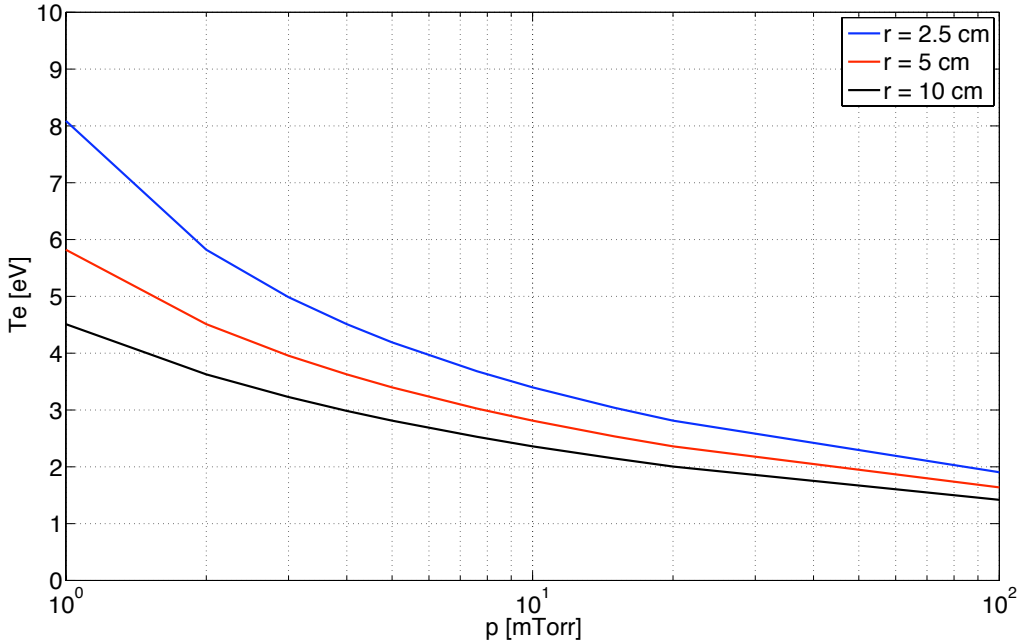

Figure 1.13: Relation between T_e and pressure in Argon discharges of various radii.

where P_i is the ionization probability defined by Eq. 1.58. This equation is to be solved subject to a boundary condition which is the source term for the neutrals.

Since the neutrals are injected at locations that differ from machine to machine, we have to make a reasonable model that will apply to all machines. The positions of the inlet and outlet are arbitrary. A baffle in the pump line is often used to limit the pumping speed at high pressures. We make the basic approximation that the input flux $\Gamma(a)$ is uniform uniform in the azimuthal and axial directions regardless of the positions of the input tube and the pump line. This preserves the one-dimensional nature of the problem. Let p_0 be the pressure in mTorr at the inlet. This is related to the neutral density by $n_n = N_0 p_0$, with $N_0 = 3.3 \times 10^{13}$ cm^{-3}. This follows from the ideal gas law for monoatomic gases at 20 C (293 K or 0.025 eV). The boundary condition is then

$$\Gamma(a) = n_n \nu_{th0} = N_0 p_0 (K_B T_n / 2\pi M)^{1/2} \tag{1.101}$$

Before the discharge is struck, there is a balance between the input and output of gas. The input is usually given in SCCM (standard cubic centimeters per minute), where 1 SCCM $= 4.17 \times 10^{17}$ sec^{-1}. The pumping speed S is given in liters/sec, usually limited by the conductance of a baffle. One l/sec at a pressure p_0 is $10^3 N_0 p_0 = 3.3 \times 10^{16}$ atoms/sec. The neutral pressure is therefore 12.7 SCCM/S mTorr. In the presence of plasma, however, the neutrals are heated and T_n may be different at the input and output. After a charge exchange collision, the neutral acquires an ion energy or order of 1 eV. After an ionization, the new ion has an energy above 0.025 eV and travels to the wall, where it is neutralized and reenters the plasma as a neutral. The mean free paths are short, so the neutrals are thermalized at a higher temperature. Since the degree of ionization is usually less than 1%, we shall neglect the difference in T_n between the input and output. The working hypothesis is that the fast neutrals and ions strike the wall and come back into the discharge as cool neutrals. These neutrals are distributed uniformly by collisions. The same flux leaves the boundary and enters the pump. Therefore, these processes do not change the overall input and output rates, so the boundary condition of Eq. 1.101 is still valid. With neglect of variations in T_n, D is constant; and Eq. 1.100 becomes

$$D \nabla^2 n_n = n_n n P_i \tag{1.102}$$

which is to be solved with the boundary conditions 1.101 and $n d_n/dr = 0$ at $r = 0$.

The program EQM (described in detail in Section 2.1) solves the three Eqs. 1.70, 1.97 and 1.102 simultaneously using a Boundary Value solver, with a 4th order Runge-Kutta to perform the integrations. An examples where neutral depletion is significant is shown in Fig. 1.14. The Figure shows the dramatic effect of higher electron density at low pressure. With higher ionization fraction, less than half the neutrals reach the axis. The corresponding $K_B T_e$ profiles show the inverse relation between T_e and n_n predicted by Eqs. 1.94 and 1.97. When n_n falls to the order of the electron density, as in the $n_0 = 5 \times 10^{18}$ m^{-3} case, $K_B T_e$ has to rise to extraordinary values (in theory) to provide the requisite

ionization at such low pressures. These temperatures are, of course, unrealistic. Argon's inelastic threshold is around 12 eV, so that radiation losses limit KTe to approximatively 4 eV. An increase of the tube diameter to 10 cm would lead to little additional effects on the relative profiles.

The problem is that we have not yet considered energy balance. To do so requires more detail about the ionization and energy loss processes. In the following section, the problem of the local energy balance between input power and losses is discussed. We will address the discussion to RF-heated plasma discharges.

1.3.6 Energy balance

The total rf power P_{in} absorbed by the plasma is, by definition,

$$P_{in} = \int_0^a P(r) r dr \tag{1.103}$$

where $P(r)rdr$ is the power deposited into each cylindrical shell. $P(r)$ is calculated by integration over the local power deposition $\vec{E}^* \cdot \vec{J}$, where $\vec{E}$ and $\vec{J}$ are the rf electric field and current of the helicon wave. P_{in} can also be calculated from the antenna loading. If I_0 if the peak antenna current and R is the load resistance seen by the antenna, P_{in} is also given by

$$P_{in} = 1/2 R I_0^2 \tag{1.104}$$

R is the same as the plasma resistance R_p arising from electron collisions with ions and neutrals, and including Landau damping. Note, however, that P_{in} differs from the power P_{rf} from the power supply because of losses R_c in the circuitry. At low densities an R_c of 0.5Ω can be comparable to R_p. The relation is [20]

$$P_{in} = P_{rf} \frac{R_p}{R_p + R_c} \tag{1.105}$$

First let us calculate *overall* energy balance. The power lost from the plasma, P_{out}, consists of three terms: W_i, W_e and W_r, where W_i and W_e are the kinetic energies carried out by ions and electrons leaving the plasma, and W_r is the (mostly radiative) loss by electrons making inelastic collisions. Each ion leaving the plasma carries out an energy consisting of $1/2 K_B T_e$ of Bohm energy entering the sheath plus a sheath drop of about $5.4 K_B T_e$ in argon [19], so it carries out about $6 K_B T_e$. W_i has two terms, the first due to flow to the sidewall and the second due to flow to the endplates:

$$W_i = \left[n(a) C_s(a) 2\pi a L + 2 \int_0^a n(r) C_s(r) 2\pi r dr \right] 6 K_B T_e \tag{1.106}$$

Here we had to choose a length L of the plasma. If the plasma is nonuniform axially, L can be estimated from the power deposition profile $P(z)$ given by the integration of the

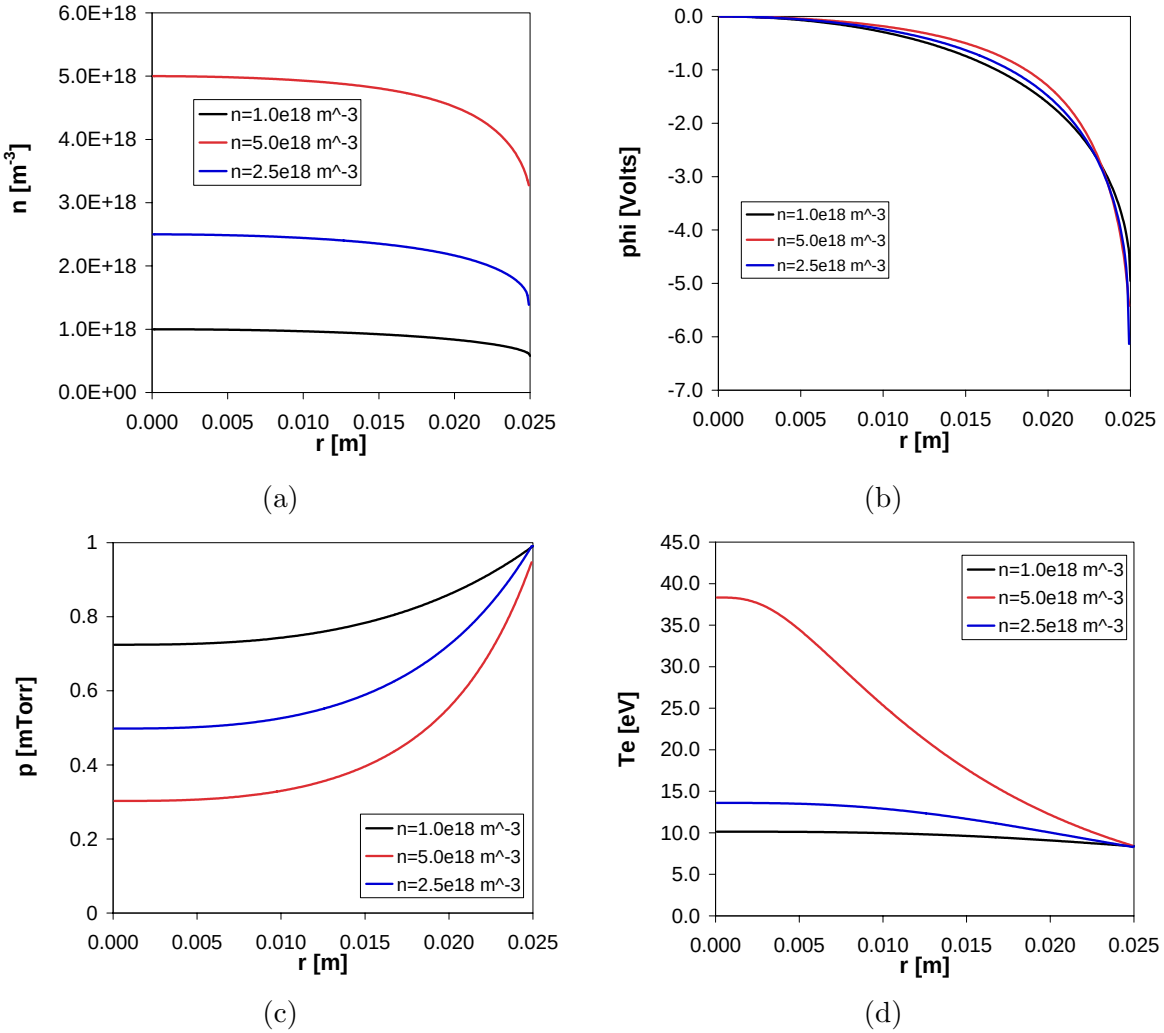

Figure 1.14: Neutral depletion effect for an Argon discharge at initial pressure of $p_0 = 1$ mTorr $= 0.13$ Pa and 400K (a) the different plasma profiles, (b) plasma potentials, (c) neutral pressure, (d) electron temperature. Neutrals are depleted at the center from the center of the discharge; the electron temperature is affected by a fast rise when neutrals are depleted.

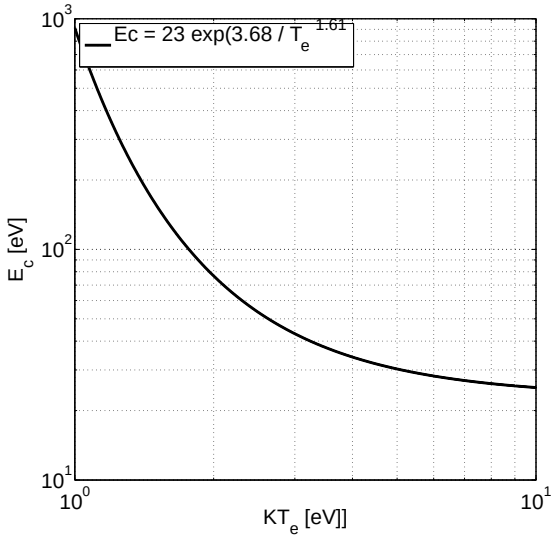

Figure 1.15: Energy required to make one ionization vs. electron temperature.

$\vec{E}^* \cdot \vec{J}$ contributions at each z. This can give an equivalent length if the plasma density varies axially. Electrons leave mostly via the endplates, but the total flux has to equal the ion flux. Each electron carries out an energy [19] of about $2K_BT_e \approx W_i/3$. Thus the conductive losses in watts are

$$W_i + W_e \approx (4/3)eW_i \quad \text{Watts} \tag{1.107}$$

where Roman "e" is the electron charge in coulombs.

The inelastic loss W_r can be found from the E_c curve calculated by Vahedi [21]. E_c is the amount of energy expended by an average electron in making an ionization, taking into account the radiative losses in all the inelastic collisions made before the ionization. This depends on the temperature. The Vahedi curve of Argon (Fig. 1.15) can be fitted by the function

$$E_c(eV) = 23\exp(3.68/T_{eV}^{1.61}) \tag{1.108}$$

where T_{eV} is T_e in eV. The loss dW_r from each shell of unit length at radius r is then E_c times the local ionization rate:

$$dW_r = 2\pi r dr n_n(r) n(r) < \sigma v >_{ion} E_c \tag{1.109}$$

Defining

$$F(T_e) \equiv E_c(T_e) < \sigma v >_{ion} (T_e) \tag{1.110}$$

We write this as

$$dW_r = 2\pi r dr n_n(r) n(r) F[T_e(r)] \tag{1.111}$$

Once $n(r)$, $n_n(r)$, and $T_e(r)$ have been determined by the EQM program, the total W_r in watts can be calculated by integration:

$$W_r = \mathrm{e}L \int_0^a n_n(r) n(r) F[T_e(r)] 2\pi r dr \quad \text{Watts} \tag{1.112}$$

where Roman "e" is again the electron charge in coulombs. The total P_{out} is then

$$P_{out} = W_i + W_e + W_r \tag{1.113}$$

which can be equated to P_{in} from Eq. 1.104 to yield the absolute value of plasma density $n(r)$ for any given value of antenna current I_0.

To evaluate local energy balance, we simplify the problem by neglecting the conductive losses, which are small compared with W_r. The input of energy to each cylindrical shell is given by the integrand of Eq. 1.103. The loss of energy to each shell is given by the integrand of Eq. 1.112 (including eL). Equating local P_{in} to local P_{out} determines the temperature profile $T_e(r)$. That is, when the input $P(r)$ is high, there will be more ionization there. This requires a high loss rate, which is accomplished by an increased T_e and, hence, a larger $F(T_e)$ in Eq. 1.112. A nonuniform deposition of rf energy giving a nonuniform ionization profile is expressed via the electron temperature profile.

Chapter 2

Numerical modeling

2.1 The HELIC-EQM code

2.1.1 HELIC code

The calculation of the equilibrium of an helicon discharge is done using an iterative process between two codes, HELIC and EQM, the former solving the plasma-wave coupling, the latter solving the macroscopic equilibrium. From the iteration of the two codes together, the absolute values of the discharge are obtained.

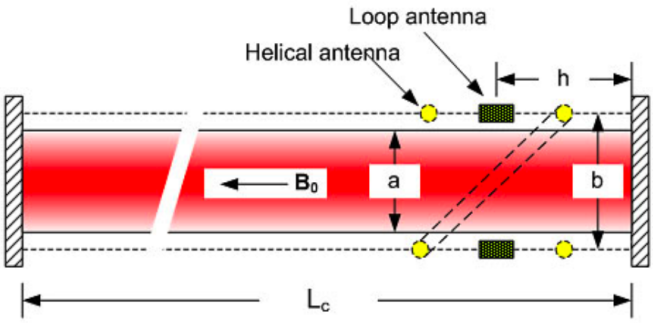

Figure 2.1: Geometry of the HELIC code (Figure credit: [23])

The HELIC code solves the problem of plasma-wave coupling (Sec. 1.1) with a cold plasma tensor on a plasma cylinder of geometry like in Fig.2.1. Its basic physics relies on a fluid electrons model together with the Maxwell equations and full displacement current. HELIC allows to calculate the electromagnetic fields occurring inside the plasma, the plasma currents, and the derived quantities. HELIC accepts as an input the radial profiles of plasma density, neutral pressure and electron temperature. Profiles are accepted

in the form of parametric functions of the radius. HELIC was developed at UCLA, details can be found in [2], [3], and [4].

2.1.2 EQM code

EQM solves the macroscopic transport along radial direction of plasma and neutrals, using the physical model described in Sec.1.3. EQM accepts the following inputs: the gas type, the radius of the cylindrical discharge, the temperature of neutrals, the total amount of RF power used, the radial profile of power absorption (an input coming from HELIC), and the effective axial extension of power deposition (estimated from the P(z) of HELIC). EQM gives in output all the quantities of plasma, neutrals and electrons along the radius. More specifically, it calculates the profiles of plasma drift velocity, plasma potential, plasma density, neutral pressure and electron temperature. From the iteration of the two codes together, the radial equilibrium of the helicon discharge is obtained.

The three basic equations solved by EQM are the plasma drift equation, the diffusion equation of neutrals, and the energy equation of electrons. They are solved with the four conditions at the boundaries. When only the conditions at the axis are assigned, the problem is simply a Cauchy-type initial value problem, which can be solved analytically or by means of standard numerical methods. However, in our case the boundary conditions are assigned in more than one location, and the problem turns from being an initial value problem to a boundary value problem (BVP). Due to its importance for the radial equilibrium of the helicon discharge, we will address it as the "helicon equilibrium BVP". Standard solution methods are the shooting and relaxation methods. When the domain of integration is not specified, a simple way to solve the problem is to consider it as a free-boundary problem. In this case the calculation is done by means of a re-parametrization of the independent variable within the interval [0,1]. In this way it is the size of the domain to be calculated as an output. This corresponds to evaluate which is the radial size of the discharge when all the other parameters are known. In EQM it is the radial size of the cylinder to be known $r = a$, and the mathematical problem is different than a free-boundary. The helicon equilibrium BVP solved by EQM can be stated as following. For a cylindrical discharge of given radius a, and a given profile of power absorption, find the profiles of plasma and neutrals satisfying the four boundary conditions.

EQM solves the helicon equilibrium BVP by means of a dedicated shooting method. The inner cycle of EQM is showed in Figure 2.2. The shoot is done on the two quantities at the axis $n(0)$ and $p(0)$, that are the plasma density and the neutral pressure respectively. Then the integration of the ODE system is done with a standard 4th order Runge-Kutta routine. Numerical tests with a more refined integrator, a quality-controlled adaptive step Adam-Bashforth-Moulton 11th-order PECE (Predictor Evaluation Correction Evaluation), didn't revealed a greater accuracy such to justify the bigger computational effort. The numerical integration starts near the axis of the cylinder, displaced of a small quantity dr from the axis. The calculation of the initial condition at $r = dr$ was done using an analytic

subsonic solution. The integration then continues up to the other boundary at $r = a$, where a check of the quantities at the other boundary is done. Initial quantities at the axis are then corrected as a function of the difference between the calculated and the desired boundary conditions in $r = a$. The process is iterated until the boundary conditions are correctly obtained within an admissible tolerance (usually to the third significant digit).

Since EQM treats quantities in real physical units, it allows to evaluate the amount of plasma density and of neutral pressure inside the discharge for a given RF power. It is from the iterative process with the HELIC code that the actual value of radial profiles is then obtained. Among many other information, the two codes together allow to predict which is the plasma density that can be obtained for a given helicon discharge and a given amount of RF power. The physical meaning of the helicon equilibrium BVP is even greater. For a tube of a given size a, the plasma is forced to satisfy the axis-symmetry of the discharge and the sonic velocity at its edge. Its profile along the radius and the amount of density will depend on how electrons absorb the power from the helicon wave. As a consequence, the plasma can configure itself along the radius only according to the profiles that are solution of the helicon equilibrium BVP. Different pressure regimes and different powers can force the plasma to jump into different radial configurations, as observed for example in the Big Blue Mode case [55].

2.1.3 The iterative process

The iterative process between HELIC and EQM is showed in Figure 2.3. The helicon discharge is described by a set of parameters, comprising its size, the neutral gas, the antenna, the RF power used and the magnetic field. An initial profile of power absorption is chosen as a first guess (ex. constant along the radius, or coming from a previous simulation). The first run is done by EQM, which calculates the profiles of $n(r)$, $n_n(r)$ and $T_e(r)$. In order to use these profiles with HELIC, they must be fitted with parametric functions. The fitting of the plasma profile is done with all the curves allowed by HELIC for $n(r)$, and then the fit with the minimum sum of squares due to error is chosen. HELIC can treat with a 3-parameters (s, t, fa) curve,

$$\frac{n}{n_0} = \left[1 - \left(\frac{r}{a}\right)^s (1 - f_a^{1/t})\right]^t \tag{2.1}$$

or with a 6^{th} degree polynomial,

$$\frac{n}{n_0} = 1 + a_1 \frac{r}{a} + a_2 \left(\frac{r}{a}\right)^2 + ... + a_6 \left(\frac{r}{a}\right)^6 \tag{2.2}$$

In almost all cases the 6^{th} degree polynomial fits better the plasma profile. The fitting of the neutral density and of the electron temperature is done similarly, with the 3-parameters curve (only for p showed):

$$\frac{p}{p_0} = f_a + (1 - f_a)\left[1 - \left(\frac{r}{a}\right)^s\right]^t, \quad f_a = \frac{p_a}{p_0} \tag{2.3}$$

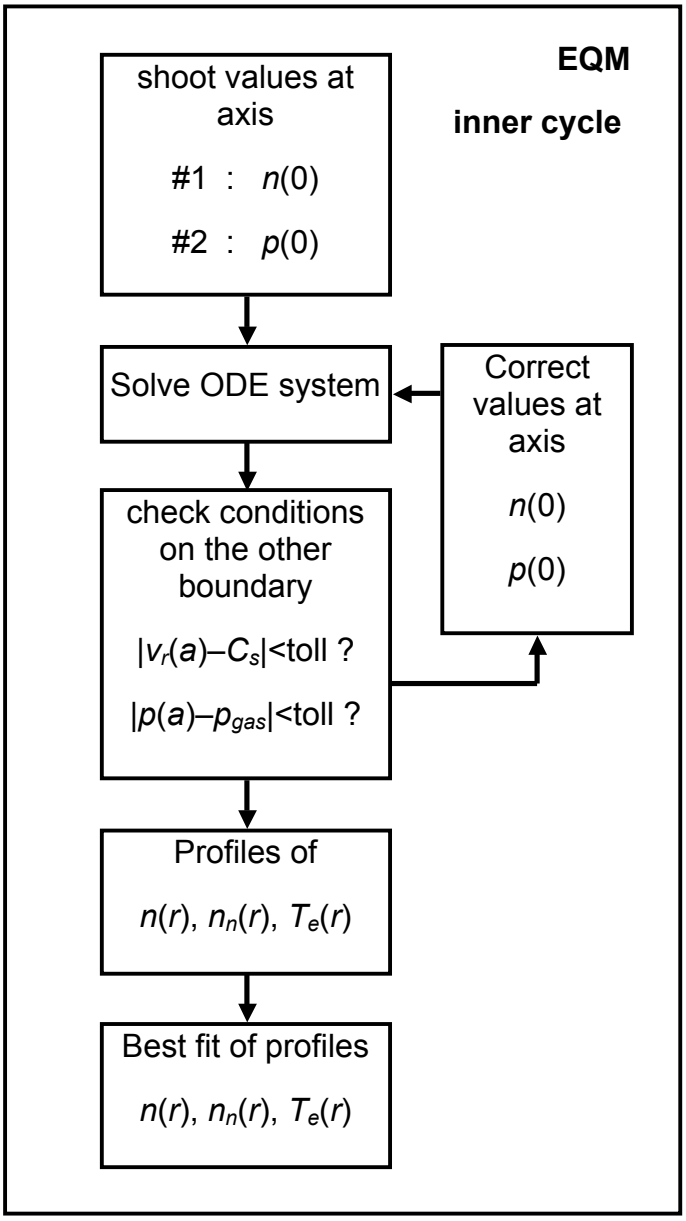

Figure 2.2: EQM inner cycle

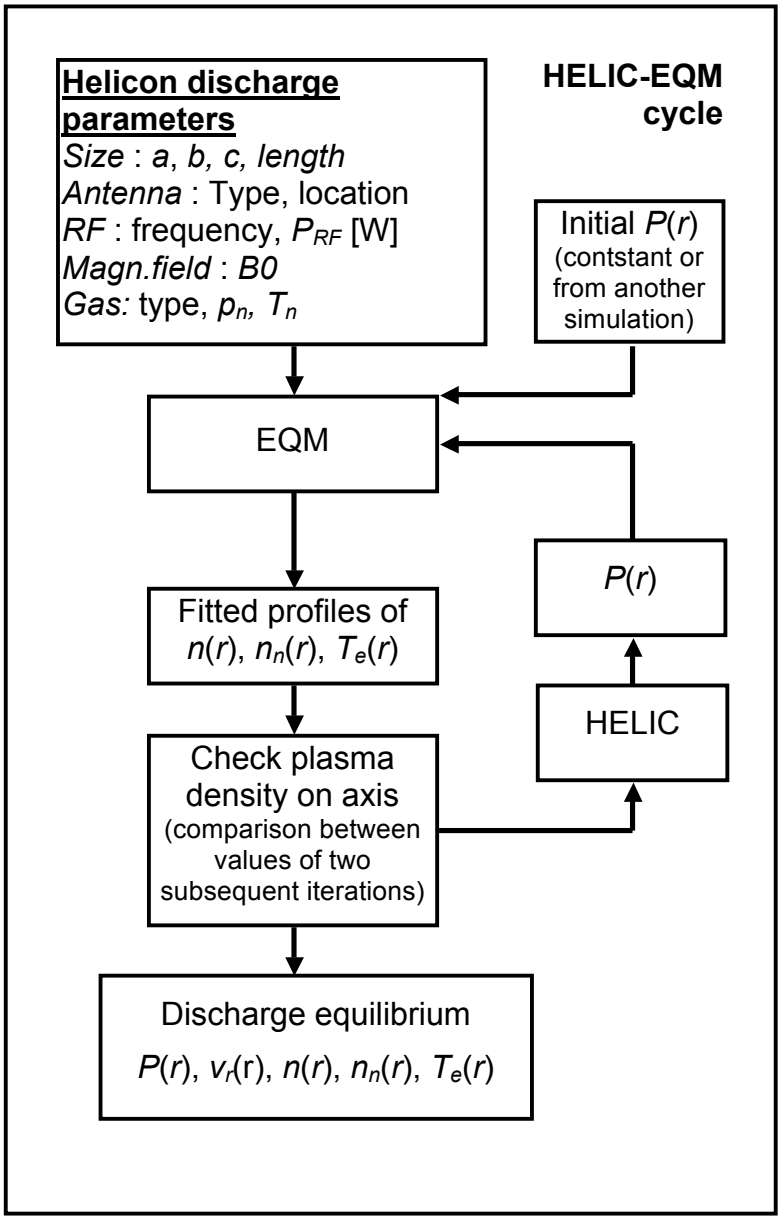

Figure 2.3: HELIC-EQM cycle

here the subscript 0 indicates quantities at the axis, and the subscript a quantities at the plasma edge. After the fitting procedure, an input file for HELIC is written, containing all the parameters of the curves. HELIC then solves the electromagnetic fields propagating inside the plasma for those assigned profiles, it calculates the plasma current, and evaluates the power absorption in radial and axial direction of the discharge. HELIC can provide the plasma resistive load R for an antenna current of 1 Ampere, and also the profiles of $P(r)$ and $P(z)$, that are respectively the radial profile of power deposition integrated over the axis, and the axial profile of power deposition integrated over (r, θ) planes. Since the antenna current is supposed to be equal to $I_0 = 1$ Ampere, the power in Watts is

$$P'_{RF,HELIC} = R/2 \tag{2.4}$$

This can be verified also integrating $P(r)$ along the radius,

$$P'_{RF,HELIC} = \int_0^a P(r) r dr \tag{2.5}$$

and seeing that it is equal to half the resistance R provided by HELIC. The factor 2π is already taken into account by HELIC during the evaluation of $P(r)$. Supposing axial uniformity, the input RF power P'_{RF} [Watt] is distributed into each radius as:

$$P'_{RF}(r) = P'_{RF} \frac{P(r) r dr}{\int_0^a P(r) r dr} \tag{2.6}$$

The quantity $P'_{RF}(r)$ [Watt] given by this equation is the fraction of the input power P'_{RF} [Watt] going into each cylindrical shell of the discharge. To obtain the power density [W/m^3] a last step is needed. The quantity $P'_{RF}(r)$ [Watt] has to be divided by the volume of the cylindrical shell,

$$P_{in}(r) = \frac{P'_{RF}(r)}{2\pi r dr \cdot L_z} \tag{2.7}$$

and so finally the power density along radius is obtained. Here L_z is the effective axial extension of power deposition. It quantifies how long the helicon power absorption is along the axial direction. It can be estimated from the $P(z)$ graph given in output by HELIC.

The new profile of power absorption is then used back as an input in EQM, and the process is iterated until convergence. The check on convergence is done on the $n(r)$ and $P(r)$ profiles, and the process ends when the difference between two subsequent iterations is smaller than a fixed tolerance. The number of iterations depend on the initial $P(r)$ chosen, and for reasonable profiles the procedure converges in less than a dozen of iterations. From the iterations of HELIC-EQM the absolute (physical units) values of the helicon discharge can be calculated. In this paragraph we show the obtained radial profiles of $n(r)$, $P_{RF}(r)$, $\phi(r)$, $n_n(r)$, $v_r(r)$, $T_e(r)$ occurring inside an helicon discharge for the cases of interest.

The sensitivity of the results of HELIC-EQM is mainly influenced by the two free parameters of the code. The first one is the effective axial extension of power deposition L_z,

and the second one is the temperature of neutrals T_n. The former is the greatest source of uncertainty. It is introduced to quantify how long is the axial region of the discharge interested in the RF power absorption. It serves to overcome the intrinsic limitation of EQM stemming from the assumption to have no variations in axial direction. The parameter L_z is estimated from the axial absorption of power $P(z)$ calculated by HELIC. Due to the uncertainties in the estimation of L_z, all the results are here presented for the expected range of L_z. The dependence of plasma density on neutral temperature is high at low T_n, but it decreases when neutrals become hotter. Uncertainty on temperature of neutrals is neglectable with respect to uncertainty on L_z.

2.2 Physical results using HELIC-EQM

The density, temperature, and neutral density profiles resulting from the highly nonuniform rf energy deposition of the combined helicon and TG waves have been computed by iterating between the EQM and HELIC codes together. Initially, EQM is solved with uniform ionization, giving $n(r)$, $Te(r)$, and $n_n(r)$. These profiles are fitted with a 6-degree polynomial to be entered into HELIC to obtain $P(r)$. Energy balance yields $Te(r)$. This profile, representing nonuniform ionization, is then entered into EQM to obtain new profiles of n, T_e, and n_n. The process is repeated until it converges. It normally takes only five or six iterations for convergence. In the following paragraphs few results of physical interest obtained with the HELIC-EQM program will be shown.

2.2.1 Edge-peaked energy deposition

In helicon discharges, the TG mode causes highly non-uniform ionization such that the source $Q(r)$ in Eq.1.57 has a large peak near the edge of the plasma. This occurs because the TG mode deposits rf energy near the edge, raising T_e there, thus exponentially increasing the ionization rate at the edge. Nonetheless, measured density profiles are always peaked on axis. How this happens can be seen from Eq.1.61, the Boltzmann relation. Initially, ionization produces a peak in density near $r = a$. With Boltzmann electrons, the potential ϕ has to follow the density, so it also peaks near $r = a$, resulting in an inward electric field. The ions are driven inward by $E(r)$, and the electrons follow them via the short-circuit effect. The density created near the boundary is pushed inwards by the electric field. This process can be followed in time-dependent calculations. In steady state, the only possible density profile is peaked at the center; a time-independent profile peaked at the edge is not possible. Figure 2.4.a shows three $P(r)$ curves produced by HELIC under different conditions [22]. One is highly peaked at the edge; the second is less peaked; and the third has almost equal contributions from the TG and H modes. The density profiles produced by EQM for these three cases are shown in Fig.2.4.b. Case 1 has more density at large radii, but in all cases the density is peaked on axis. The $P(r)$ profiles here are not consistent with the $n(r)$ profiles, but this shows that hollow profiles are never produced. "Hollow"

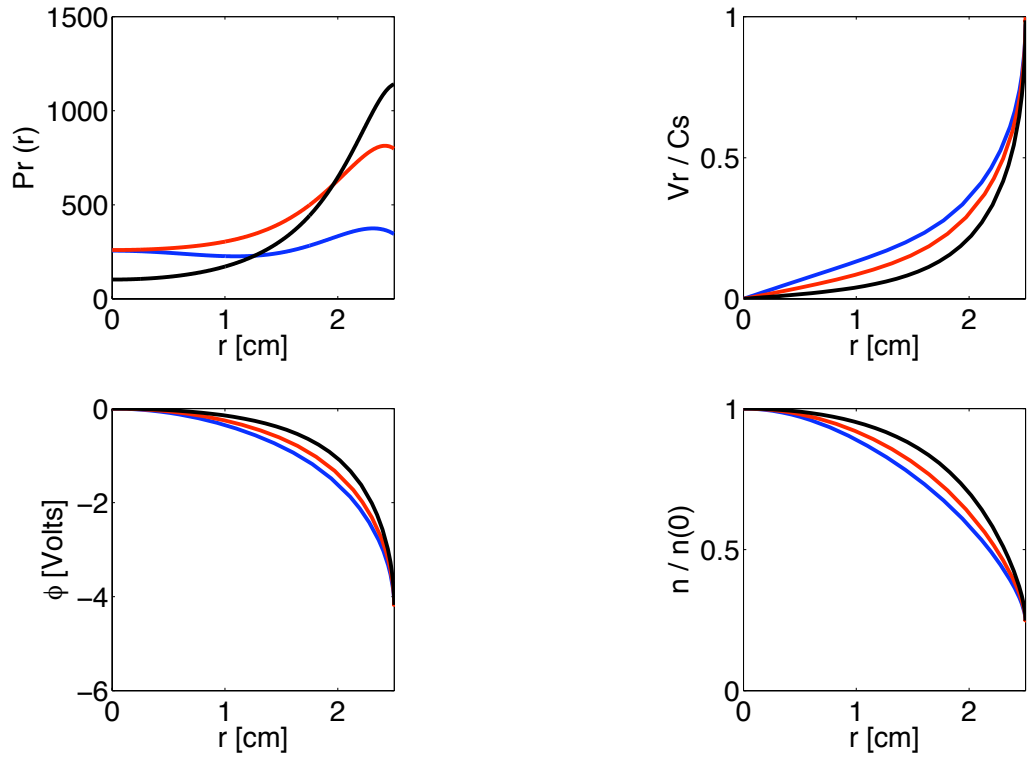

Figure 2.4: Radial energy deposition profiles for three selected cases, with different magnitudes of the TG mode (densities of 12.6, 5.0 and 1.6 $\times 10^{17}$ m^{-3}, B = 65 Gauss and tube radius is 2.5 cm), and the resulting profiles from the EQM solution

density profiles do not occur in this steady-state theory, and we have never observed them. However, they have been seen in experiments by others. In those cases either the discharge was pulsed or other conditions prevented the short-circuit effect from being operative.

2.2.2 Discharge profiles

We next show results in which the $P(r)$ profiles from HELIC are completely consistent with the $n(r)$ profiles from EQM, as obtained by iteration between the two programs. Several cases are reported in Figs. 2.5, 2.6,2.7 and 2.8. With large TG-mode deposition at the edge, electron temperature T_e is high there and, hence, high ionization at the edge, giving rise to the flat density profiles at the center. The 120-G, 1kW, 27.12 MHz case has larger TG deposition at the edge, giving a flatter density profile. The higher density in that case also leads to higher neutral depletion: 0.8 mTorr compared with 0.4 mTorr in the analogous

lower power case. Note that the dip of $P(r)$ in Fig. 2.7 is reflected in the $T_e(r)$ profile.

In Fig 2.8, we show a larger plasma 10 cm rather than 5 cm in diam, the pressure is lower at 5 mTorr, and the B-field is higher. Neutral depletion is higher because of the lower pressure. At the center of Fig 2.8, Te varies inversely with the pressure according to ionization balance, but near the edge Te rises from the Trivelpiece-Gould heating there. These two regions are better separated with the larger diameter. Note that the short-circuit effect cannot transport electron temperature across B; the heat conductivity is still reduced by the magnetic field. The absorption is high on axis, with a resulting "triangular" density profile of plasma.

2.2.3 A reference case for experiments

As a reference case for the experiments, we will consider the case in Fig. 2.5. Here we will give details about how this simulation has been performed. A 15 mTorr (2 Pa) Argon helicon discharge of radius $a = 2.5$ cm, with a single loop $m = 0$ antenna at 13.56 MHz is considered. The magnetic field at the antenna is 65 Gauss. The two codes HELIC-EQM have been iterated together with an input RF power of 200 Watts. The simulation is done considering neutrals at Tn=400 K and an axial extension of power deposition L_z=30 cm. The parameter L_z has been estimated from the $P(z)$ graph given by HELIC. The plot of the plasma drift velocity has been normalized with respect to the local Bohm velocity. The plot shows that the Bohm velocity is reached at the edge of the plasma, where the quasineutrality is violated and the sheath solution begins. The plasma density at the edge n(a) is 0.45 times the density in the axis, proving that the Bohm sheath edge hypothesis n(a)=n(0)/2 is valid in first approximation. Neutral pressure exhibits a small neutral depletion, higher powers would have involved more depletion of neutrals. The electron temperature is almost flat, and it increases near to the wall, as expected in a region of higher power density and with less plasma. As can be seen from the P(r) graph, the helicon discharge is ionized primarily at the edge by Trivelpiece-Gould (TG) waves, but the observed density profiles is peaked at the center. The calculated equilibrium condition gives the radial equilibrium conditions of the discharge, with the plasma-wave helicon coupling taken into account.

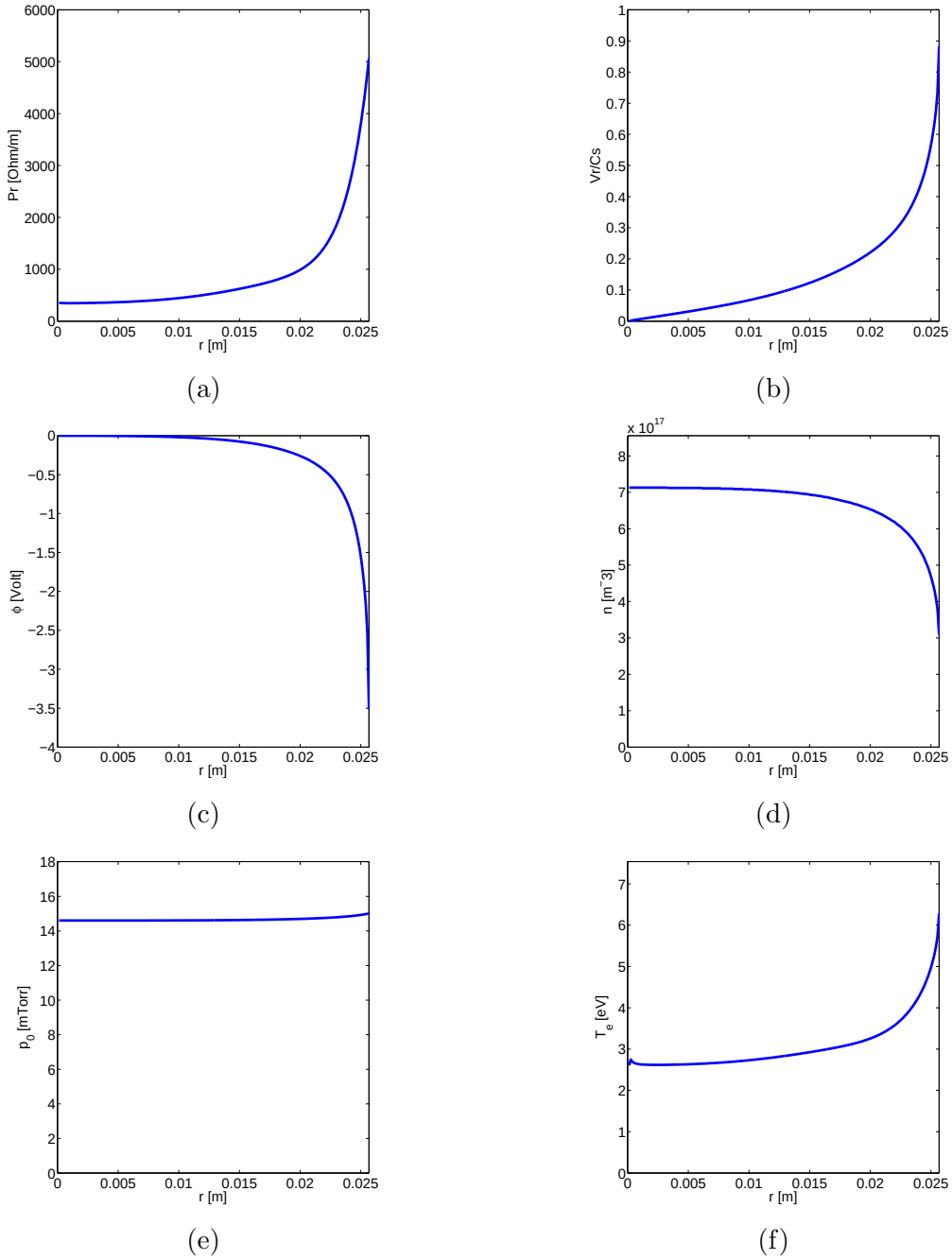

Figure 2.5: Radial profiles obtained by iteration of HELIC-EQM, for a 15 mTorr = 2 Pa helicon discharge at 65 Gauss with 400 W of RF at 13.56 MHz and an $m = 0$ antenna, (a) deposited power per unit current and unit length, (b) drift velocity normalized to the Bohm velocity, (c) potential, (d) plasma density, (e) neutral pressure, (f) electron temperature.

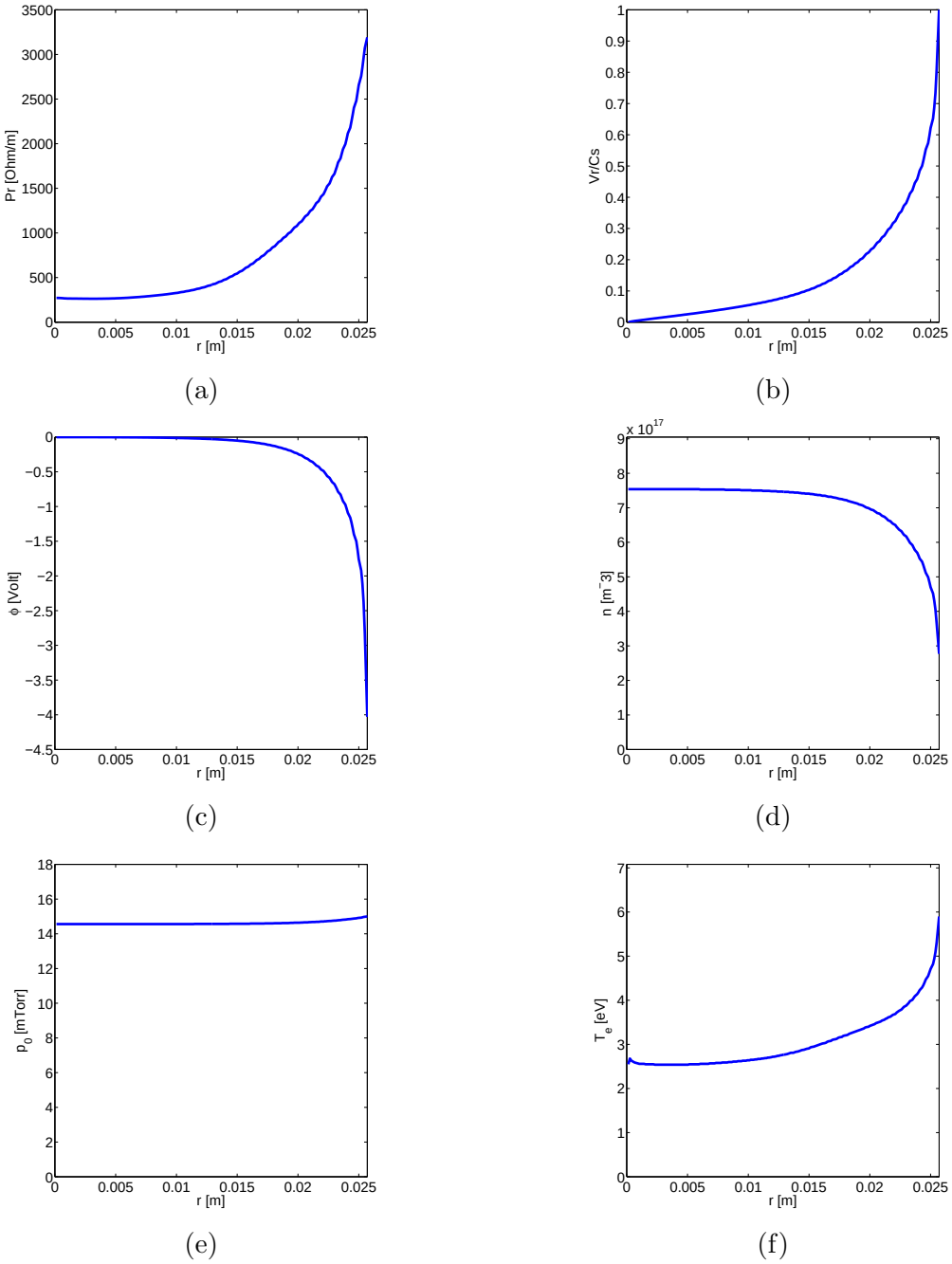

Figure 2.6: Radial profiles obtained by iteration of HELIC-EQM, for a 15 mTorr = 2 Pa helicon discharge at 65 Gauss with 400 W of RF at 27.12 MHz and an $m = 0$ antenna, (a) deposited power per unit current and unit length, (b) drift velocity normalized to the Bohm velocity, (c) potential, (d) plasma density, (e) neutral pressure, (f) electron temperature.

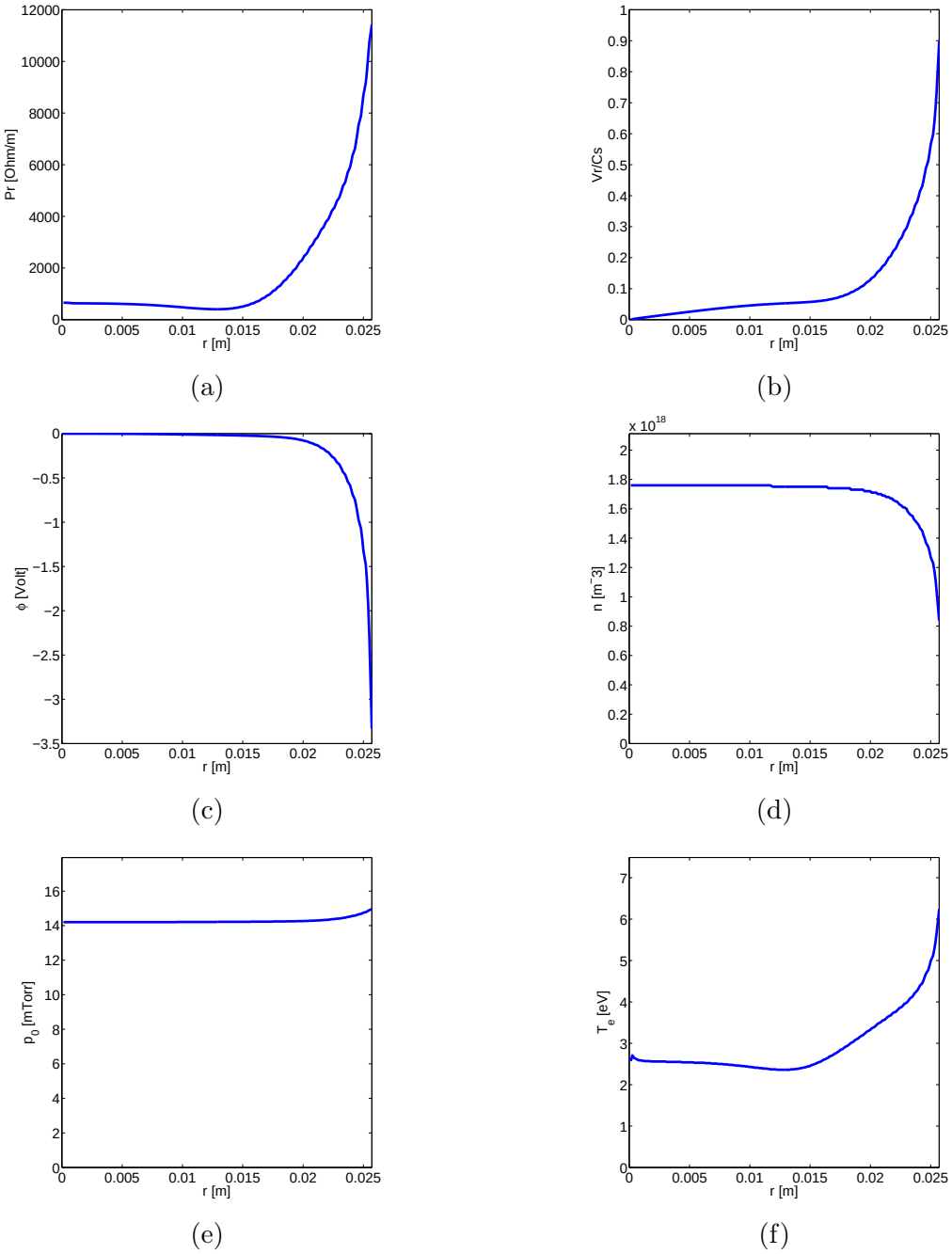

Figure 2.7: Radial profiles obtained by iteration of HELIC-EQM, for a 15 mTorr = 2 Pa helicon discharge at 120G with 1000W of RF at 27.12 MHz and an $m = 0$ antenna, (a) deposited power per unit current and unit length, (b) drift velocity normalized to the Bohm velocity, (c) potential, (d) plasma density, (e) neutral pressure, (f) electron temperature.

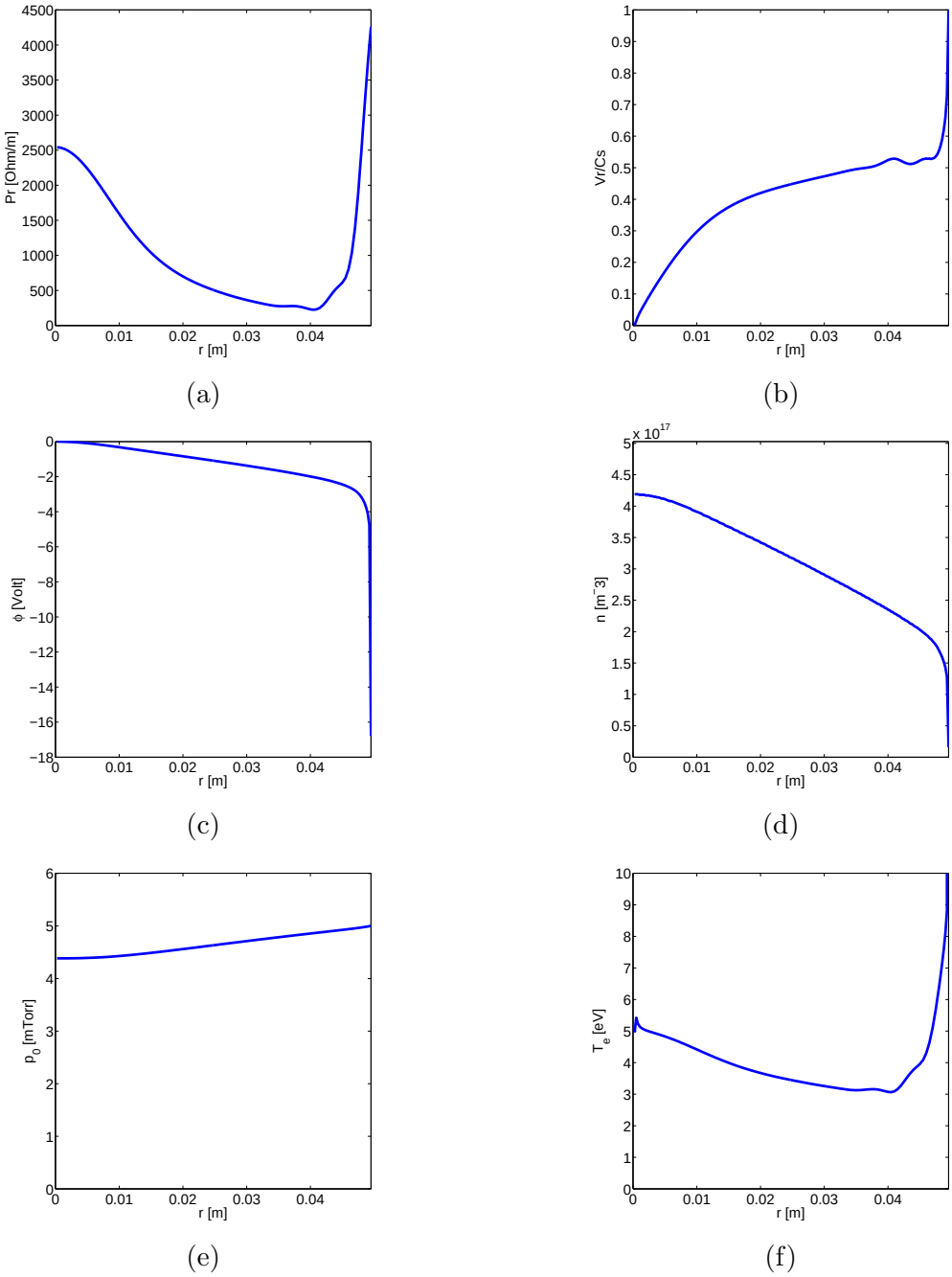

Figure 2.8: Radial profiles obtained by iteration of HELIC-EQM, for a larger tube at lower pressure of 5 mTorr = 0.67 Pa, helicon discharge at 250 Gauss with 400 Watt of RF at 13.56 MHz and an $m = 0$ antenna, (a) deposited power per unit current and unit length, (b) drift velocity normalized to the Bohm velocity, (c) potential, (d) plasma density, (e) neutral pressure, (f) electron temperature.

2.2.4 Low Pressure Effects and B-peak

In the low pressure range (approximatively below 0.4 Pa, i.e. below 3 mTorr) the collisional deposition of the Trivelpiece Gould mode gradually becomes less effective due to the decreasing collisionality[1]. In this regime the mode of deposition can shift from being edge-localized and collisional in its nature to –for sufficiently large discharges– centered-localized and wave-heated dominated. For a given pressure, this "mode-shifting" can be maximized in the range of low magnetic fields, where a peak in plasma resistance has been observed between $40 < B_0 < 80$ Gauss. Here we present the numerical simulations where this phenomenon was observed.

A helicon discharge with a tube radius of 5 cm and length 2 meters, with a 16-cm-long half-helic antenna of 11 cm diameter, emitting at f= 13.56 MHz has been considered. A first set of simulations was done to assess the effect of neutrals on power deposition at a fixed magnetic field $B_0 = 500$ Gauss. The results are shown in Figure 2.9. Each figure shows P_r versus the radius, with the cylinder axis placed at r=0. In each graph the P_r is parametrized on plasma density for six assumed values in the range $n = 10^{11} - 10^{12}$ cm^{-3}. When pressure is decreased, the absolute value of P_r decreases too, and the penetration depth of the TG wave increases. At the lowest pressure considered, a small increase of the coupling at the center is observed.

The magnetic field was thus decreased from 500 to 300 and 100 Gauss, Figs. 2.10, 2.11, where the deposition at the center is seen to be gradually increased. At 100 Gauss and low pressure, the deposition is markedly centered.

This effect can be maximized when the magnetic field is further decreased to the range:

$$40 < B_0 < 80 \quad \text{[Gauss]} \tag{2.8}$$

as reported also in Fig. 2.12. Within this interval the Helicon central-peaked deposition becomes dominant. The helicon nature of this deposition is revealed when B_0 is decreased below this range. In fact, below $B_0 < 20$ Gauss the Helicon wave becomes a superficial evanescent wave, and the centered-peaked deposition disappears (Fig. 2.12). This peculiarity of the H-TG waves interaction was not seen for discharges working in the ICP mode $B_0 = 0$. The low-B field peak was also studied and observed by Chen [23].

[1] This also has an electrical drawback on the efficiency of the power coupling, according to Eq.1.105, because at some point the plasma resistance becomes comparable with the stray resistance of the coupling circuit.

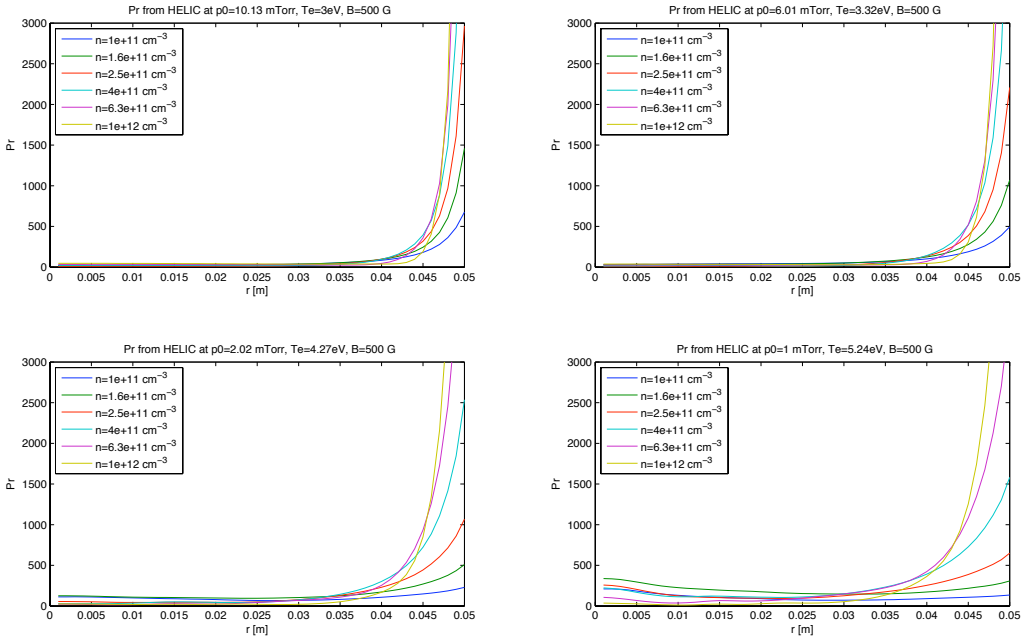

Figure 2.9: B_0=500 Gauss

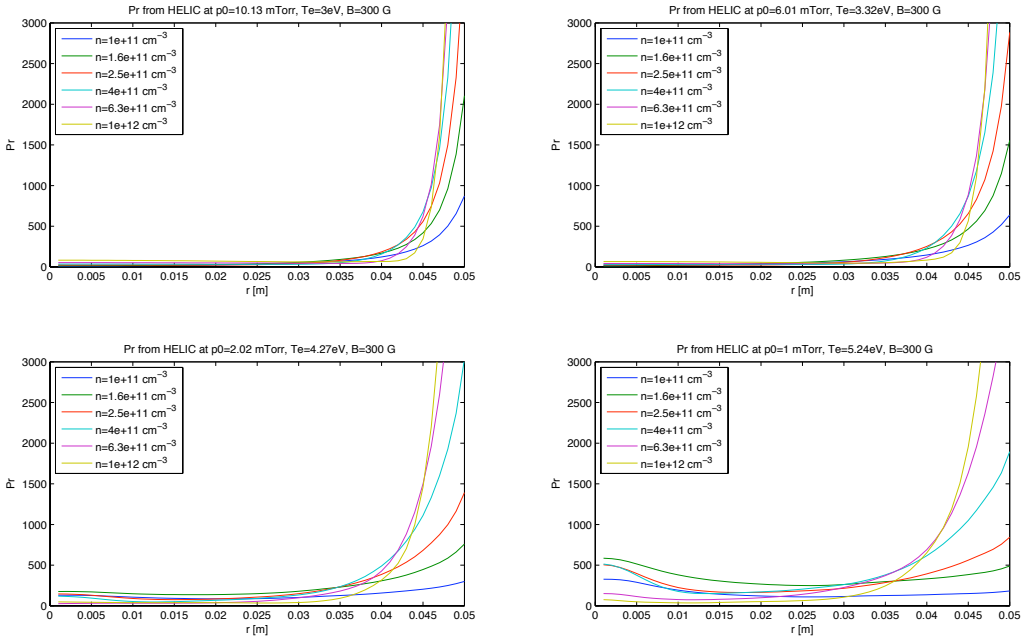

Figure 2.10: B_0=300 Gauss

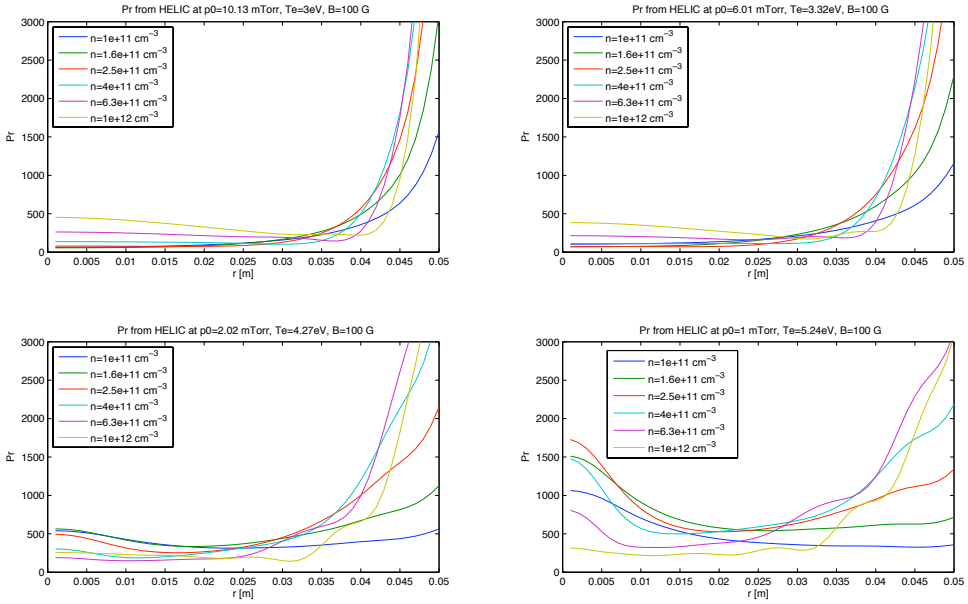

Figure 2.11: B_0=100 Gauss

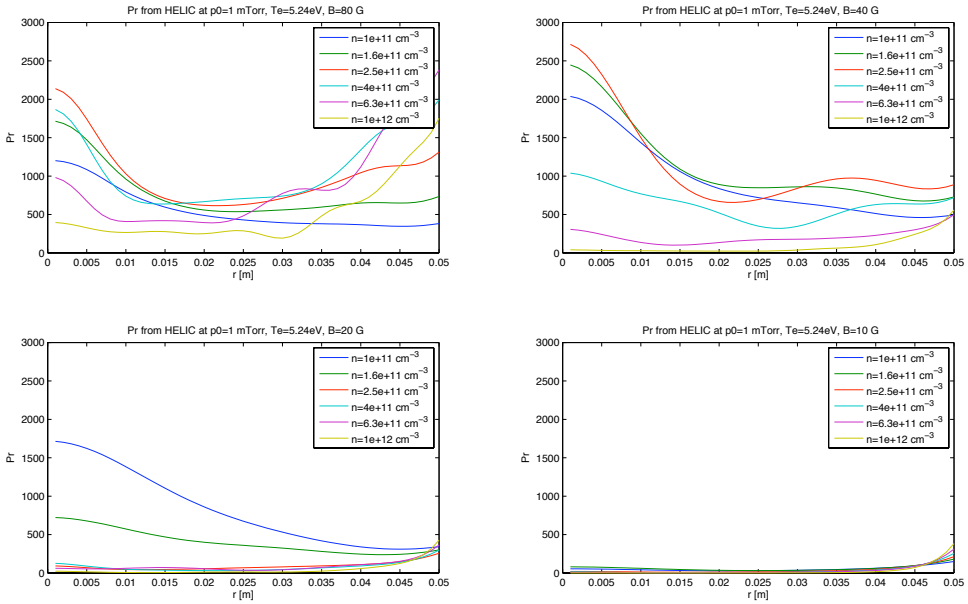

Figure 2.12: Low pressure behavior for decreasing magnetic field for the cases B_0=80, 40, 20, 10 Gauss

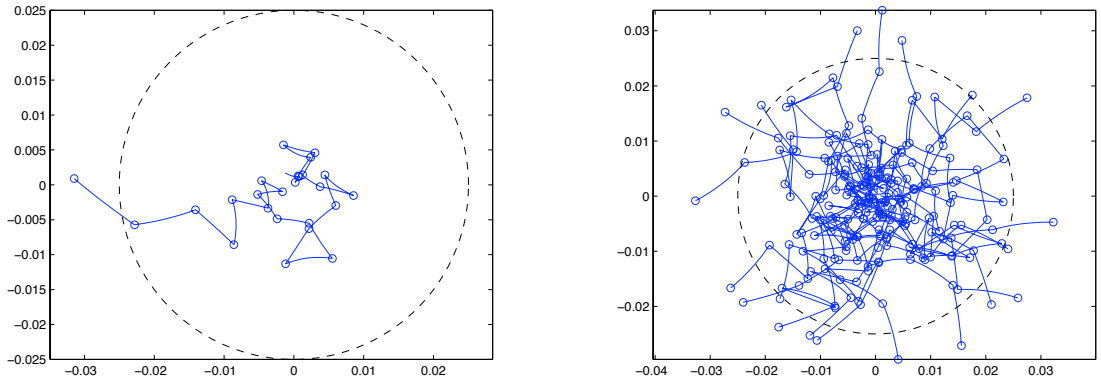

(a) (b)

Figure 2.13: Ion losses toward the wall in a magnetized cylinder

2.3 Modeling particle kinetics

2.3.1 Single particle collider

The confinement time of a charged particle inside the plasma cylinder has been estimated using a simple Monte Carlo single-particle collider. Figure 2.13.a shows an example. A single-ionized argon ion generated near the axis of the discharge, moving with its thermal velocity and colliding mostly by charge-exchange with neutral atoms. An axial magnetic field of 100G parallel to the axis of the discharge bends slightly the trajectories of ions among two subsequent collisions. The motion is integrated numerically with an Adam-Bashforth-Moulton routine. Ions are accelerated outward by the ambipolar electric field, due to the plasma density gradient.

2.3.2 A numerical method for the free-fall regime

At very low pressures the mean free path between two collisions is much greater than the size of the discharge. The fluid treatment of the transport ceases to be valid. Following an approach first proposed by Tonks and Langmuir[2] [6], we can consider the ion mean free path to be much greater than the characteristic size of the discharge; in this case, ions generated at a location x start at rest and move under the action of the ambipolar electric

[2]In their work [6] the two authors showed an analytical solution using power series, for few simple cases where the analytical treatment was possible; in the present paragraph we develop a method for treating with arbitrary $Q(x)$.

field out of the discharge. The density of ions at a given location x_j is given by:

$$n(x_j) = x_j^{-\beta} \int_0^{x_j} \frac{Q(x)x^\beta dx}{v_x} \tag{2.9}$$

with:

$$\beta = 0 \qquad \text{Plane geometry} \tag{2.10}$$
$$\beta = 1 \qquad \text{Cylindrical geometry} \tag{2.11}$$
$$\beta = 2 \qquad \text{Spherical geometry} \tag{2.12}$$

where $Q(x)$ is the number of new particles generated at a location x (different than x_j) per unit volume and unit time, v_x is the velocity of particles at the position dx. The Boltzmann equation gives the local electron density:

$$n_e = n_0 \exp\left(\frac{q_e\phi}{K_B T_e}\right) \tag{2.13}$$

In the free-fall model, the velocity v_x is obtained from energy balance between the point x and x_j:

$$v_x = \sqrt{\frac{2q_e}{M_i}\left(\phi(x) - \phi(x_j)\right)} \tag{2.14}$$

and substituing in Eq. 2.9 it results:

$$n(x_j) = x_j^{-\beta} \int_0^{x_j} \frac{Q(x)x^\beta dx}{\sqrt{\frac{2q_e}{M_i}\left(\phi(x) - \phi(x_j)\right)}} \tag{2.15}$$

Quasineutrality ensures that $n = n_e$ and thus:

$$n_0 \exp\left(\frac{q_e\phi}{K_B T_e}\right) = x_j^{-\beta} \int_0^{x_j} \frac{Q(x)x^\beta dx}{\sqrt{\frac{2q_e}{M_i}\left(\phi(x) - \phi(x_j)\right)}} \tag{2.16}$$

An analytic solution of Eq. 2.16 can be found for simple cases. Tonks and Langmuir [6] expressed the solution in a power series for the cases of $Q(x)$ generation proportional to the electron density and for a constant ionization along the domain. A solution in term of Dawson functions can also be obtained. However, we are interested in its solution for a completely generic Q, and thus a numerical scheme must be obtained.

We rewrite Eq. 2.14 of the velocity by substituting Boltzmann electrons, and it results:

$$v_x = C_s^* \left(\log \frac{n(x)}{n(x_j)}\right)^{1/2} \tag{2.17}$$

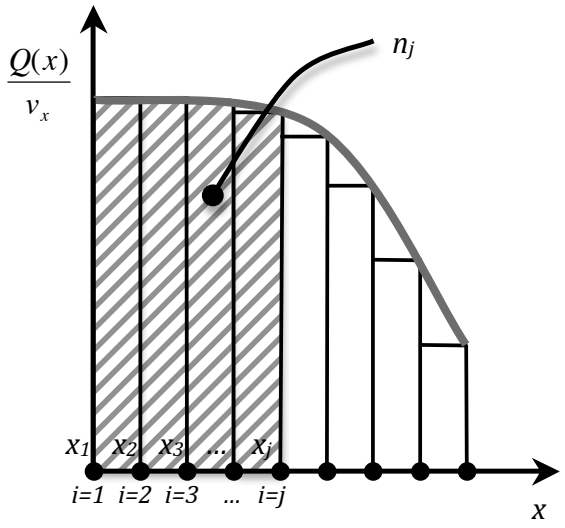

Figure 2.14: Scheme of the discretization

where $C_s^* = \sqrt{2K_BT_e/M_i}$ is an opportune Bohm velocity. Substituting Eq. 2.17 in Eq. 2.9, we get:

$$n(x_j) = \frac{x_j^{-\beta}}{C_s^*} \int_0^{x_j} Q(x) x^{\beta} [\log n(x)/n(x_j)]^{-1/2} dx \tag{2.18}$$

From Eq. 2.18 it can be seen that $\partial n/\partial x$ must be minor than zero in order to have a real solution. The density $n(x_j)$ at a given location depends on particles produced at all locations at higher-potential. The difficulty in the solution of Eq. 2.18 is that the unknown n_j compares on both sides of the equation, and inside the integral.

The discrete form of Eq. 2.18 is:

$$n_j = \frac{n_j^{-\beta}}{C_s^*} \sum_{i=1}^{j-1} Q_i x_{i+\frac{1}{2}}^{\beta} \left[\log \frac{n_i}{n_j}\right]^{-\frac{1}{2}} \Delta x_i \tag{2.19}$$

where the symbols Q_i, n_i, n_j means $Q(x_i), n(x_i), n(x_j)$, the radial step is $\Delta x_i = x_{i+1} - x_i$, and the coordinate is kept at the middle step $x_{i+\frac{1}{2}} = (x_i + x_{i+1})/2$. Figure 2.14 shows a scheme of the discretization, assumed of the first order type. To calculate the density at a given n_j we thus have to solve a non-liner set of equations where the unknown n_j is contained also inside the summation. When the value on axis is assigned n_0, this

corresponds to solve the following equations:

$$n_1 = n_0 \tag{2.20}$$

$$n_2 = \frac{n_2^{-\beta}}{C_s^*} \cdot \frac{Q_1 x^{\beta}_{1+\frac{1}{2}} \Delta x_1}{(\log n_1/n_2)^{1/2}} \tag{2.21}$$

$$n_3 = \frac{n_3^{-\beta}}{C_s^*} \cdot \left[\frac{Q_1 x^{\beta}_{1+\frac{1}{2}} \Delta x_1}{(\log n_1/n_3)^{1/2}} + \frac{Q_2 x^{\beta}_{2+\frac{1}{2}} \Delta x_2}{(\log n_2/n_3)^{1/2}} \right] \tag{2.22}$$

$$n_4 = \frac{n_4^{-\beta}}{C_s^*} \cdot \left[\frac{Q_1 x^{\beta}_{1+\frac{1}{2}} \Delta x_1}{(\log n_1/n_4)^{1/2}} + \frac{Q_2 x^{\beta}_{2+\frac{1}{2}} \Delta x_2}{(\log n_2/n_4)^{1/2}} + \frac{Q_3 x^{\beta}_{3+\frac{1}{2}} \Delta x_3}{(\log n_3/n_4)^{1/2}} \right] \tag{2.23}$$

$$... \tag{2.24}$$

$$n_j = \frac{n_j^{-\beta}}{C_s^*} \cdot \left[\frac{Q_1 x^{\beta}_{1+\frac{1}{2}} \Delta x_1}{(\log n_1/n_j)^{1/2}} + \frac{Q_2 x^{\beta}_{2+\frac{1}{2}} \Delta x_2}{(\log n_2/n_j)^{1/2}} + ... + \frac{Q_{j-1} x^{\beta}_{j-1+\frac{1}{2}} \Delta x_{j-1}}{(\log n_{j-1}/n_j)^{1/2}} \right] \tag{2.25}$$

where the unknowns are $n_1, n_2, ..., n_j$. When we try to numerically solve the equations, several inconveniences occur. A forward solution from top to bottom is not feasible, because the ratios n_{j-1}/n_j comparing inside the logarithms are different for each equation. Equations have to be solved one-by-one, and for each j-location the zero of a non-linear function in the unknown n_j must be found. A particular caveat must be taken due to the presence of the $(\log n_i/n_j)^{1/2}$ term, since the solution is near to the interval of complex solutions where $n_i/n_j \leq 1$. When using a non-linear zero search algorithm, the search interval $[a...b]$ must be decided a-priori in order to avoid the solutions become imaginary. From the choice of the two bounds of the search interval it depends the success of the numerical scheme. For the choice of the two bounds we note from Eq. 2.18 that the solution n_j at each radial step is a monotonic function, and it is thus comprised between $n_{j-1} < n_j < n_{j+1}$. The bound n_{j-1}, called b is simple to estimate because the solution already calculated at the previous radial step can be used, $b = n_{j-1} - \delta$, where δ is a small number $\delta \sim O(n_0/10^{12})$. The bound n_{j+1}, called a, is unknown, and at step j it can only be estimated. It turns out that a fast and practical choice is to put: $a = 9/10b$. This works good until the Bohm location is reached. In that region the coefficient $9/10$ of a must be increased toward unity as a function of $\partial n/\partial r$, which is going locally to infinity.

The implementation of the present numerical method has been done by using Maple as a symbolic manipulator for the automatic construction of the hundred-terms equations Eq. 2.21 - 2.25, which it should be unfeasible to treat by hand. The zeros-finding function is then a common bisection. The calculation needs some computer resources when over-hundred terms are required, due to the symbolic manipulation of high-j terms. For $j \sim 100$, usual computational time is of the order of some minute on a X-11 based Dual-Core machine, and of several tens of minutes on a Windows-based pc.

As a test of the algorithm, the long mean free path case in planar geometry ($\beta = 0$) with constant ionization has been obtained. Tonks and Langmuir obtained an analytical solution for the same problem [6]. Figure 2.15.b shows the potential profile along the coordinate, resulting the same reported in [6]. The first graph 2.15.a is more interesting from the computational point of view, because it shows the behavior of the numerical scheme. It shows the real value of $f_j = Q_j/v_{xj}$ as a function of n/n_0 and for all the iterations. The zeros of f_j are the values of the density n_j. In this graph computations begins from the point (1,0). In this point the density is equal to the value at the axis. The trend of $Re(f_j)$ is such that two zeros exist. The first one is the actual value of the density, in the location near $n/n_0 = 1$. This is the physical value of the density, and the one that must be obtained from the numerical scheme. All physical values obtained at each iteration have been marked with a star on the $Re(f_j) = 0$ axis. The second value is on the opposite side, near $n/n_0 = 0$, and it is unphysical. When iterations go on, the two values get closer, until they meet. The physical values decreases, as expected for plasma density, and the unphysical values increases. In this example, they meet near $n/n_0 = 0.5$. In that location the two solutions are very close one to the other, and they are very hard to be distinguished by the numerical scheme. In the limit they meet in a single point, where f_j becomes a negative function tangent to the axis $Re(f_j) = 0$ in one point. This is the location where the quasineutral behavior of the plasma is broken off, and the sheath solution begins.

2.3.3 Radial 1D PiC

A comprehensive calculation of all the plasma solution, i.e. comprising the quasi-neutral region, the pre-sheath and the space-charge region (sheath), would require a great analytical efforts. The transport equation Eq. 1.74 is able to treat naturally the sheath and the presheath until the plasma reaches the Bohm velocity, where the solution becomes singular. The sheath region is treated easily using a Particle-in-Cell method. Here we give a schematic description of a 1D electrostatic PiC code developed for the treatment of plasma near the boundaries of the cylinder. The PiC can work both with slabs and cylinders (Cartesian and Cylindrical geometry), and with Bolztmann electrons or kinetic electrons, depending on needs.

Radial grid For the analysis of the problem, a 1D domain along the axis r, with $0 < r < r_a$, has been considered. The 1D domain has been discretized in N_r cells of equal size $\Delta r = r_a/N_r$, each cell marked with index $k = 1, 2, \ldots, N_r$. Cells are separated by nodes, placed at coordinates $r_i = 0, \Delta r, 2\Delta r, 3\Delta r, ..., r_a$. Nodes are marked with index $i = 1, 2, ..., m$ where $m = N_r + 1$.

Initial plasma density profile The initial density profile $n(r)$ is assumed to be know, and it can be just an initial guess, or it could come from another simulation code evaluating power deposition (HELIC, etc.).

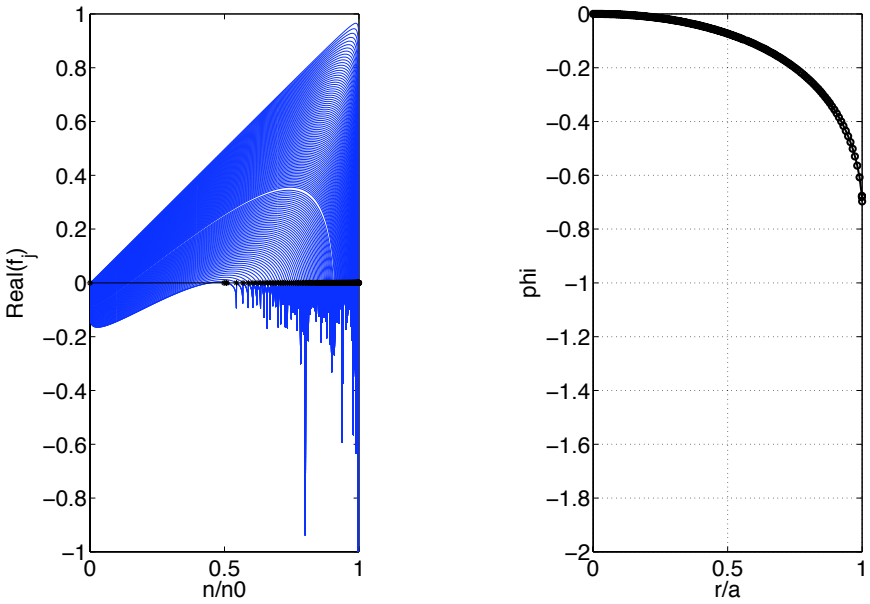

Figure 2.15: Long-mean-free path solution in planar geometry, with constant ionization [6]

Particles discretization The total number N_p of physical particles contained inside the domain,

$$N_p = \int_0^{r_a} n(r)dr \qquad \text{(Cartesian)} \tag{2.26}$$

$$N_p = \int_0^{r_a} n(r)rdr \qquad \text{(Cylindrical)} \tag{2.27}$$

has been discretized in a number N_c of computational particles, with $N_p/N_c >> 1$. A ratio N_p/N_c as small as possible is achievable; the ideal limit of $N_p/N_c = 1$ means that all physical particles contained inside the domain have their numerical counterpart. In practice, small simulation codes developed on laptops allows to treat easily with only 10^3–10^5 particles.

Initial state vector At the beginning of the simulation, positions and velocities has to be assigned to each computational particle (a procedure called "particle loading"). Particles are placed at random initial positions inside the domain, $0 < r < r_a$, and they are spatially distributed with a probability density following the plasma density profile $n(r)$. At each particle is then assigned a radial velocity v_r, in random direction (positive or negative along radius), and with a module depending on the

velocity distribution function. In the practical implementation, some difficulty arise because random number generators always provide random numbers comprised in the interval $[0, ..., 1]$. Thus, we must find a procedure that, given a random number in the interval $[0, ..., 1]$, gives a location R comprised between $0 < R < r_a$ following the arbitrary function $n(r)$. The cumulative distribution of the normalized profile allows to do this, here we resume the required passages. The density profile has to be normalized with respect to the total number of physical particles in the domain,

$$\tilde{n}(r) = n(r)/N_p \tag{2.28}$$

where

$$N_p = \int_0^{r_a} n(r)dr \approx \sum_{k=1}^{N_r} N_p^k = \frac{1}{2}(r_{i+1} - r_i)(n_{i+1} + n_i) \qquad \text{(Cartesian)} \tag{2.29}$$

$$N_p = \int_0^{r_a} n(r)rdr \approx \sum_{k=1}^{N_r} N_p^k = \frac{1}{2}(r_{i+1}^2 - r_i^2)(n_{i+1} + n_i) \qquad \text{(Cylindrical)} \tag{2.30}$$

The integration along the azimuthal direction would lead to an additional factor of 2π. Each cell of the grid thus contains the following number of physical particles:

$$N_p^{(k)} = \int_{\Delta r_k} \tilde{n}(r)dr \approx \frac{1}{2}\sum_{i=1}^{N_r}(r_{i+1} - r_i)(\tilde{n}_{i+1} + \tilde{n}_i) \qquad \text{(Cartesian)} \tag{2.31}$$

$$N_p^{(k)} = \int_{\Delta r_k} \tilde{n}(r)rdr \approx \frac{1}{2}\sum_{i=1}^{N_r}(r_{i+1}^2 - r_i^2)(\tilde{n}_{i+1} + \tilde{n}_i) \qquad \text{(Cylindrical)} \tag{2.32}$$

with $k = 1, ..., N_r$ and where $N_p^{(k)}$ is the cumulative distribution function of the normalized density profile, which is a normalized quantity $\sum_{k=1}^{N_r} N_p^{(k)} = 1$. The discrete cumulative distribution of $N_p^{(k)}$ is:

$$F_j = \sum_{k=1}^{j} N_p^{(k)} \qquad (j = 1, 2, ..., N_r) \tag{2.33}$$

The cumulative F_j is a number in the interval $[0, ..., 1]$, and its derivative keeps track of the original $n(r)$ density profile, but in the interval $[0, ..., 1]$. The pendency of F_j is higher where the original density is higher, and thus a random number $[0, ..., 1]$ will fall more likely in regions at higher density. The value of F_j can thus be used for particle loading with practical random number generators.

The particle is then placed inside the cell at a random position depending on the topology of the reference frame:

$$R = r_{indx} + dr \cdot \text{rand}[0, ..., 1] \qquad \text{(Cartesian)} \tag{2.34}$$

$$R = r_{indx} + dr(1 - A_{rnd}/A_k) \qquad \text{(Cylindrical)} \tag{2.35}$$

where

$$A_k = \int_{r_i}^{r_{i+1}} r dr = \frac{r_{i+1}^2 - r_i^2}{2} \tag{2.36}$$

$$A_{rnd} = \int_{r_i}^{r_i + dr \cdot \text{rand}[0,...,1]} r dr = \frac{(r_i + dr \cdot \text{rand}[0,...,1])^2 - (r_i)^2}{2} \tag{2.37}$$

In Cartesian coordinates the position is equiprobable between the two nodes, and in Cylindrical coordinates it is a more complicated function of radius (deriving from the cylindrical topology) shown in Fig. 2.16.

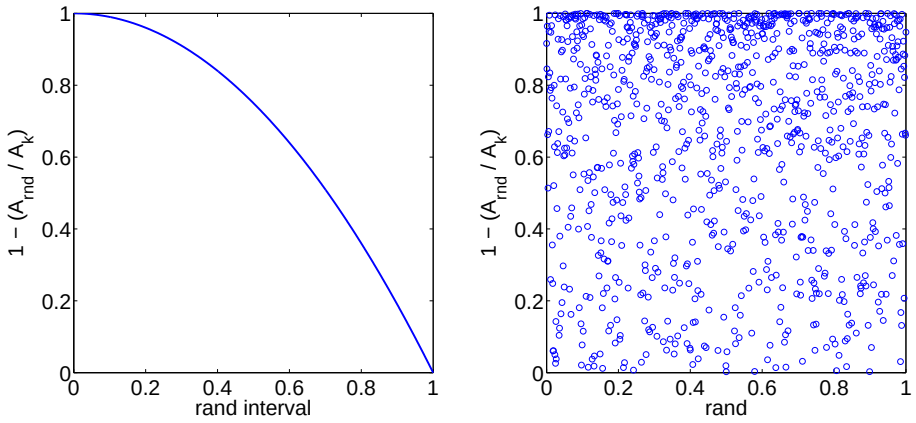

Figure 2.16: (a) Cylindrical random function inside the interval $[0, ..., 1]$, and (b) its behavior for random numbers. Particles fall more likely on the external region of the interval, due to deformation in cylindrical topology.

As an example, in cylindrical coordinates: a 5 cells radial grid in a cylindrical domain of radius 0.1 with a constant density profile along the radius has an adimensional number of physical particles $N_p^{(k)} = [0.04, 0.12, 0.20, 0.28, 0.36]$. Its discrete cumulative distribution will thus be $F_j = [0.04, 0.16, 0.36, 0.64, 1.0]$. The random number $r = 0.53928$ will state that the particle is fallen in the cell $k = 3$, and thus it's comprised between the nodes $i = 3$ and $i = 4$.

Figure 2.17 shows three examples of 5000 particles in cylindrical coordinates with different density distributions $n(r)$ along the radius: (a) a uniform distribution; (b) Gaussian in the middle; (c) a double *erf* function higher in the middle and in the edge.

Plasma Source A source volumetric rate $Q(r)$ has been assumed to generate new plasma particles inside the domain,

$$Q(r) = n_0(r)n(r) < \sigma v >_{ion} \tag{2.38}$$

where $n_0(r)$ is the number density of neutral atoms, and $< \sigma v >_{ion}$ is the ionization volumetric rate electron-neutrals, which is a function of electron temperature T_e. The new particles coming from the source are generated at random locations inside the domain, and with a probability density proportional to the distribution $Q(r)$.

Electrostatic potential The electric potential ϕ is calculated from the numerical solution of the Poisson equation:

$$\nabla^2\phi = -q_e(n_i - n_e)/\epsilon_0 \tag{2.39}$$

This requires to invert an opportune elliptic matrix which discretizes the Laplacian operator. When the Boltzman electrons are used, the density n_e is evaluated with the Boltzman relation; when, instead, the PiC is used in its kinetic-kinetic version, both n_i and n_e are discretized particles.

Electrostatic Field Once the potential ϕ is known, the electrostatic field $E = -\nabla\phi$ on nodes can be evaluated with a central space 2nd-order discretization:

$$E_i = -\frac{\phi_{i+1} - \phi_{i-1}}{r_{i+1} - r_{i-1}} \tag{2.40}$$

and at boundaries the derivative can be estimated with a 1st-order forward space scheme:

$$E_1 = -\frac{\phi_2 - \phi_1}{r_2 - r_1} \qquad E_m = -\frac{\phi_m - \phi_{m-1}}{r_m - r_{m-1}} \tag{2.41}$$

Interpolation of fields The electrostatic field is then interpolated at particles location, to have the actual electric field acting on each particle at its specific location. The two procedures of particle interpolation and weighting must be one the opposite of the other, and they must follow a the same dual scheme. Particle shape has been assumed to be linear (first order). Particle localization inside the cells is made easier thanks to the equally-spaced grid. The index k of the cell is given by:

$$k = 1 + |\text{floor}(R/dr)| \tag{2.42}$$

where the function floor rounds the real number to the first integer toward minus infinity. The nodes confining with the k cell are placed between indexes k and $k+1$.

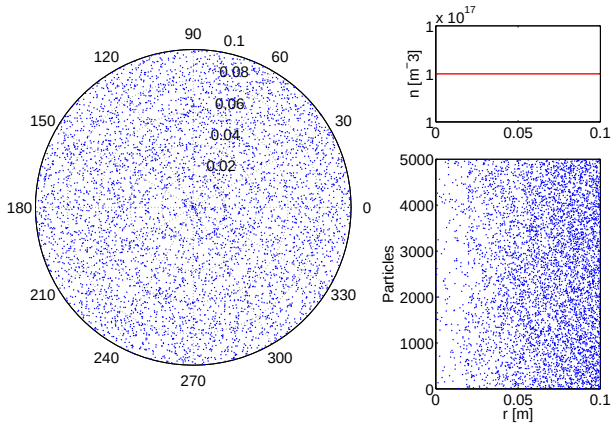

(a)

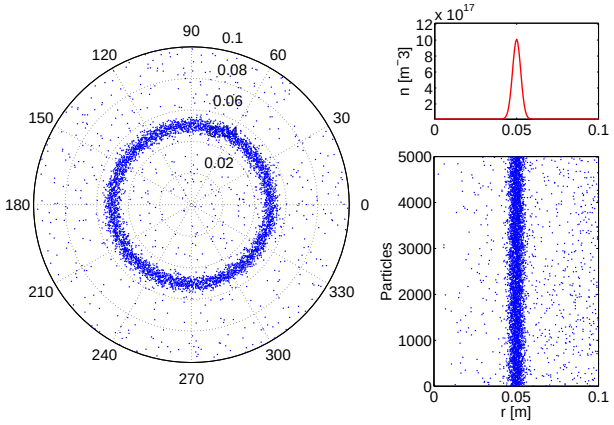

(b)

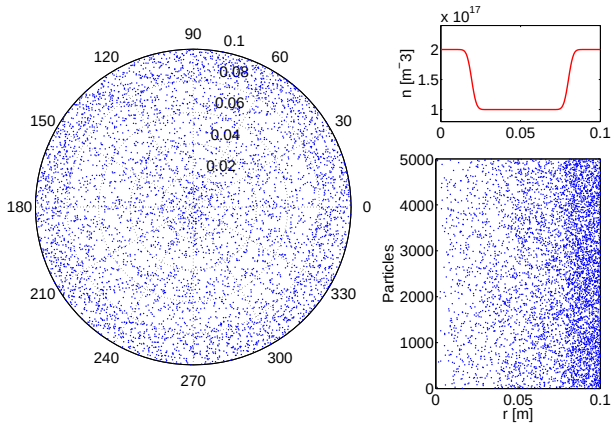

(c)

Figure 2.17: Tests of loading 5000 particles in cylindrical geometry: (a) Uniform distribution; (b) Gaussian in the middle; (c) a double *erf* function in the middle and in the edge.

The linear interpolation of E at each particle location R_j, with $j = 1, ..., N_c$, is given by:

$$E_j = E_k \left(1 - \frac{R_j - r_k}{r_{k+1} - r_k}\right) + E_{k+1} \left(\frac{R_j - r_k}{r_{k+1} - r_k}\right) \qquad \text{(Cartesian)} \tag{2.43}$$

$$E_j = E_k \left(1 - \frac{R_j^2 - r_k^2}{r_{k+1}^2 - r_k^2}\right) + E_{k+1} \left(\frac{R_j^2 - r_k^2}{r_{k+1}^2 - r_k^2}\right) \qquad \text{(Cylindrical)} \tag{2.44}$$

In Cartesian coordinates the weights of the two values at the nodes are the same, and the interpolation is simply a linear weight depending of the distance between the two nodes. In cylindrical coordinates the electric field E_{i+1} placed at a greater radial station will weight more on the particle than the electric field at a smaller radial station E_i due to deformation in cylindrical coordinates.

Moving particle The motion of each particle is advanced in time by numerical integration of the Newton-Lorentz equation. The algorithm implemented is a Boris-Bunemann leapfrog algorithm, which guarantees 2nd-order accuracy.

Flag particles went outside Particles that have gone outside the region $0 < r < r_a$ are flagged as "unused", and their trajectory is no more taken into account. The memory locations of this particles will be filled at the following step with data of new particles coming from source, for optimization of computational resources.

New particles from source New particles are added inside the domain.

Weighting All the particles are then weighted back on the grid, by calculating the weights W_i $(i = 1, 2, ...m)$. Particle shape has been assumed to be linear. Weighting of particles must be done using the same identical procedure used for the interpolation, and thus:

$$W_k = \frac{R_j - r_k}{r_{k+1} - r_k} \qquad \text{(Cartesian)} \tag{2.45}$$

$$W_k = \frac{R_j^2 - r_k^2}{r_{k+1}^2 - r_k^2} \qquad \text{(Cylindrical)} \tag{2.46}$$

and

$$W_{k+1} = 1 - W_k \tag{2.47}$$

Assuming particles of finite shape can help to overcome many numerical approximations, intrinsic to the discretization process (it also serves to avoid divergences in point-like particles used in classical kinetic theory and electromagnetism). The charge density at a point $\vec{r}'$ of a point particle placed at $\vec{r}$ is changed from $q\delta(\vec{r}' - \vec{r})$ to $qS(\vec{r}' - \vec{r})$.

New density profile A new density profile is then evaluated at nodes location,

$$n_i = (W_i/\Delta r)(N_p/N_c) \qquad \text{(Cartesian)} \tag{2.48}$$

Time cycle The new density is used as input for the subsequent time step, and the evolution is iterated for all the time steps desired.

Validation Despite the great simplicity of a 1D PiC code, a validation procedure was required, since the code was written from scratch. As an example, Fig. 2.18 shows the comparison of the calculated and the theoretical sheath profile at the wall of an Argon plasma.

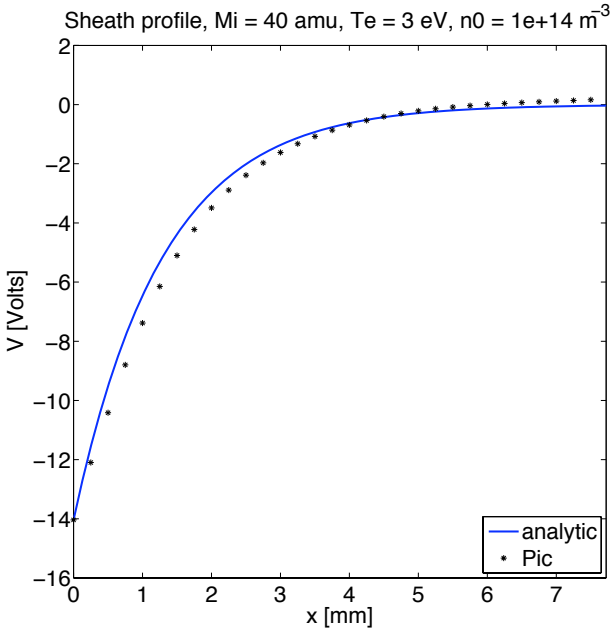

Figure 2.18: Sheath formation at the wall of an Argon plasma cylinder, as calculated with the radial 1D PiC (GRIDPIC), and comparison with the analytical curve.

2.3.4 F3MPIC

F3MPIC is a 3D PIC code developed in the framework of HPHcom[3]. F3MPIC can handle a generic plasma of n-species evolving inside an arbitrary 3D geometry discretized with an unstructured mesh of tetrahedra. F3MPIC uses and integrates several open source codes [4] for management of subtasks. The volume is discretized in a 3D tetrahedral mesh generated using Gmsh, and the mesh quality is optimized using the 3D Delaunay-Voronoi algorithm of NETGEN. Each species of the plasmas is represented by N charged macroparticles. The trajectories of the macroparticles are evaluated by integration of the Newton-Lorentz equation using a Boris–Leapfrog scheme. The positions and velocities allow to obtain the charge and current densities at each time step, necessary for the resolution of the electromagnetic fields. The values of the densities and currents sources on mesh nodes are obtained using a linear weighting. The electromagnetic fields generated by the interacting particles are obtained using a Finite Element approach, by means of a modified version of GetDP. The sparse matrix resulting from the discretization is solved using Sparskit, or more optimized and parallelizable solvers from the PETSc library. Figure 2.19 is a scheme of the structure of F3MPiC.

[3]Helicon Plasma Hydrazine.combined micro, www.hphcom.eu

[4]F3MPIC uses the following open source codes:

1. **Gmsh** (http://geuz.org/gmsh/): a three-dimensional finite element mesh generator with built-in pre- and post-processing facilities, developed by Christophe Geuzaine and Jean-François Remacle;
2. **GetDP** (http://geuz.org/getdp/): a General Environment for the Treatment of Discrete Problems, developed by Patrick Dular and Christophe Geuzaine;
3. **NETGEN** (http://www.hpfem.jku.at/netgen/): an automatic 3D tetrahedral mesh generator; developed mainly by Joachim Schöberl, significant contributions made by Johannes Gerstmayr (STL geometry) Robert Gaisbauer (OpenCascade interface).
4. **MuPPar** : a text file parser developed to easily parse input informations into a generic software, developed by Davide Rondini;
5. **CMake** (http://www.cmake.org/): a cross-platform, open-source build system;
6. **Sparskit** (http://wwwusers.cs.umn.edu/ saad/software/SPARSKIT/ sparskit.html): a basic toolkit for sparse matrix computations, developed by Yousef Saad;
7. **PETSc** (http://www.mcs.anl.gov/petsc/petsc-2/index.html): a suite of data structures and routines for the scalable (parallel) solution of scientific applications modeled by partial differential equations. It employs the MPI standard for parallelism. Developed by Argonne National Laboratory (U.S. Department of Energy laboratory).

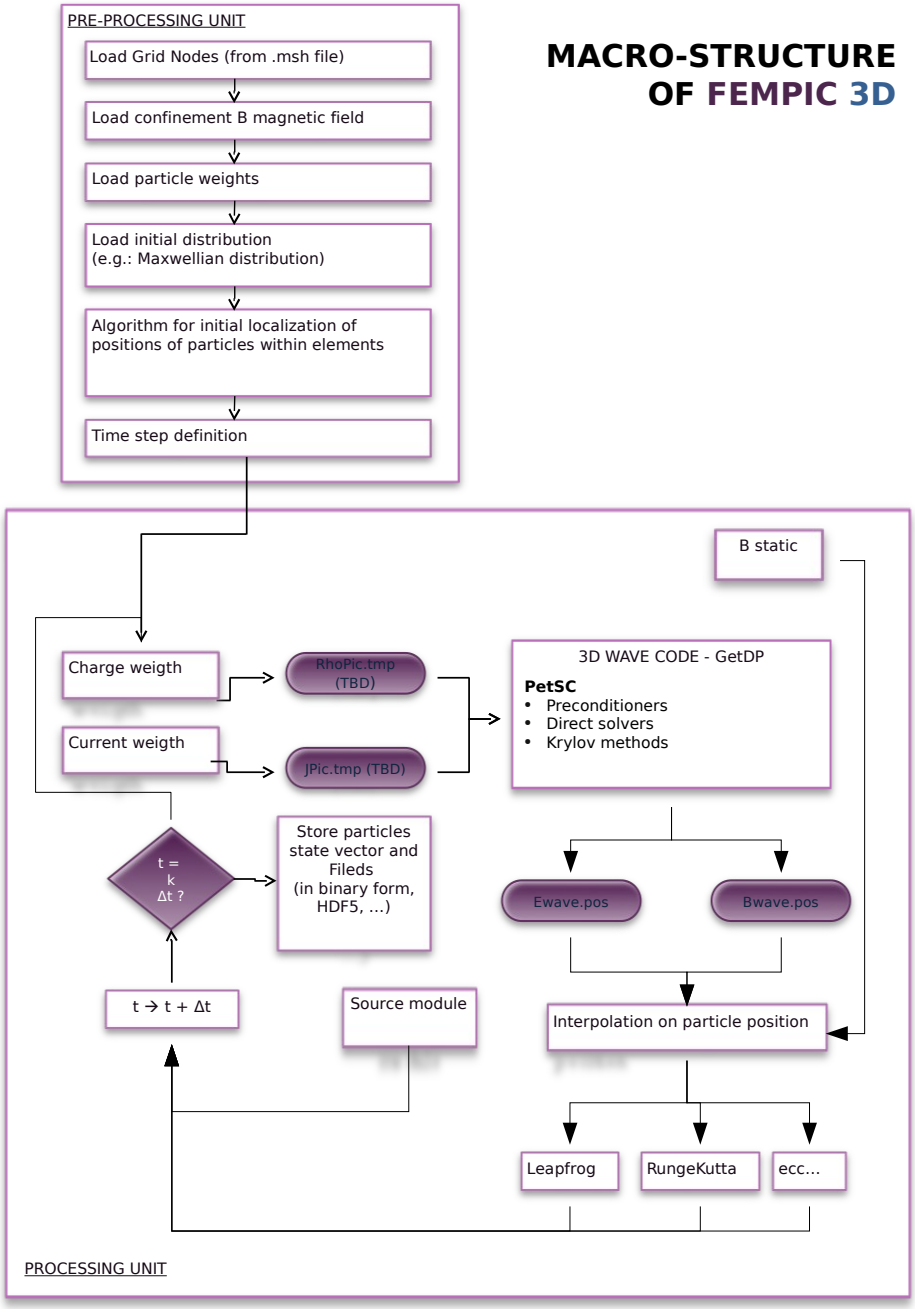

Figure 2.19: Schematics of the F3MPIC code.

Chapter 3

Experimental validation using Langmuir probes

3.1 UCLA experimental setup

3.1.1 Vacuum plant

The UCLA[1] experimental apparatus used for the characterization of the thruster is shown schematically in Figure 3.1. It was composed by two vacuum chambers (14) and (7), each chamber with an independent vacuum plant. The first chamber (14) was 30.5 cm, 12 inches, of diameter, the second chamber (7) was of 36 cm, 14.34 inches, of diameter. The two chambers shared the same Argon tank (1). The plant was configured in order to be able to run experiments independently in the two chambers.

Each of the two vacuum plants had two-stages of vacuum. A first roughing pump (9), (16) was used to reach pressures of the order of few Pascal. Then a turbomolecular pump (8), (15) allowed to reach the high vacuum in the range 6×10^{-4}-10^{-5} Pascal (5.0-10.0$\times10^{-6}$ Torr). All the surfaces exposed to vacuum were treated and cleaned with acetone (the low vapor tension of acetone enhances a rapid evaporation of residuals attached to the surfaces like water drops or vapor, human breath, sweat residuals from handling, etc.).

3.1.2 Pressure probes

The pressure of neutral gas was monitored using Convectron gauges (19), (23), Baratron gauges (17), and ion gauges (21), (25):

1. **Convectron** convection-enhanced Pirani thermal conductivity gauge. The gauge determines the pressure indirectly from the thermal conductivity property of the gas

[1]F. F. Chen's laboratory LTPTL, Low Temperature Plasma Technology Laboratory, University of California Los Angeles

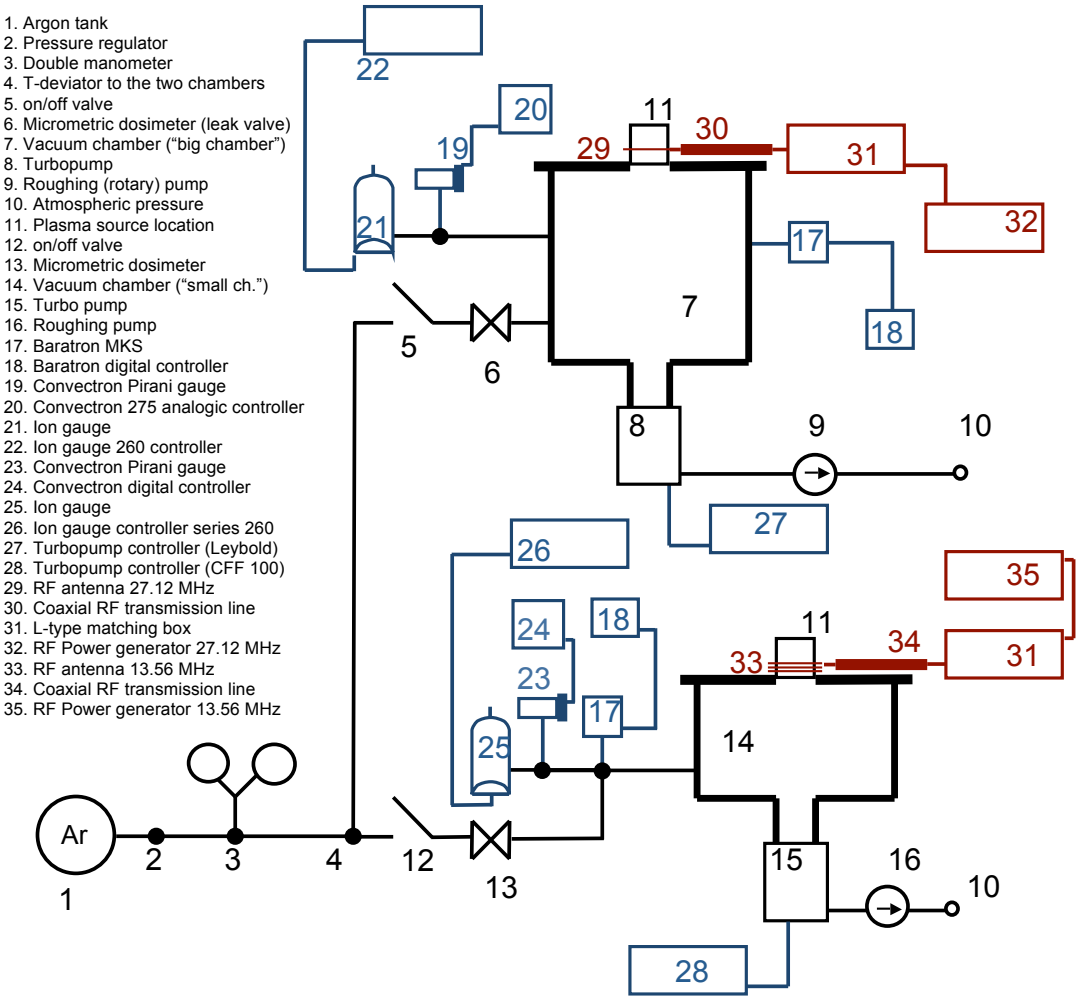

Figure 3.1: UCLA experimental apparatus

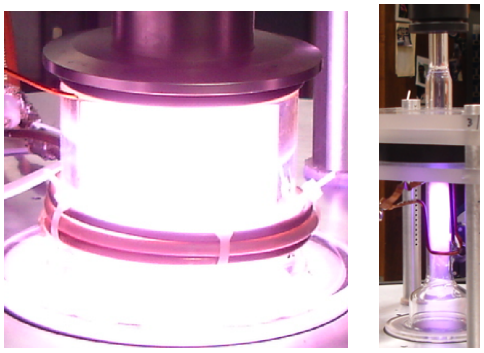

(a) (b)

Figure 3.2: The two tested plasma sources (a) stubby tube (b) elongated source

medium. This kind of gauge (ex. Granville-Phillips 275) is an industry standard in the measurements of rough vacuum.

2. **Baratron** is a direct (gas independent) pressure/vacuum capacitance manometer. It measures the true pressure (force/unit area). The measurement is insensitive to the type of gas being measured, other gauges, such as Pirani, thermocouple and ion gauges, do not measure true pressure and therefore their readings will be gas-type sensitive. The high sensitivity of the baratron was preserved by not taking the sensible surface in direct contact with the plasma, to avoid etching on one of the arms of its capacitive transducer.

3. **Ionization gauge** For high-vacuum measurements (below 0.133 Pascal, 1 mTorr), a hot cathode Penning ionization gauge was used. This kind of gauge measures electrical ions produced when the gas is bombarded with electrons

The three probes were mounted on the chambers as depicted in Fig.3.1. The interesting range for experiments was below 1-2 Pascals (7.5-15 mTorrs). The convectron and the Ion Gauge were calibrated for Nitrogen; the corresponding values of Argon were obtained by means of a conversion chart.

3.1.3 Plasma source

The plasma source (11) was mounted on the top of the chamber. Plasma was injected downward. The source was a cylindrical tube made of quartz or Pyrex (both materials are dielectric), with inner diameter of 5.4 cm (2.1 inches) and length 5.6 cm (2.2 inches).

3.1.4 Magnetostatic field

A Neodimium toroid was used for providing the necessary magnetostatic field. The toroid had an internal diameter of 7.6 cm, external diameter of 12.7 cm and height 2.54 cm, 3x5x1 inches magnets.

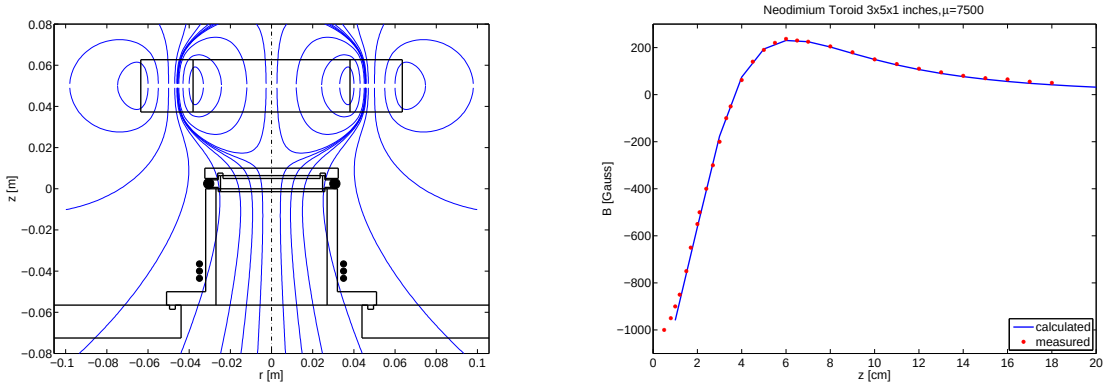

(a) (b)

Figure 3.3: (a) Magnetic field lines of the Neodimium toroid; (b) magnetic field intensity along the symmetry axis of the Neodimium toroid (here the z axis starts from the center of the toroid)

Neodymium allows one of the highest magnetizations, and is thus interesting for aerospace applications thanks to its low B-over-mass ratio. Even lower B-over-mass ratios could in principle be obtained using superconducting materials.

The magnetization vector was directed parallel to the symmetry axis of the magnet. Figure 3.3.a shows the magnetic lines of the toroid, together with stubby tube, dimensions are to to scale. Figure 3.3.b shows the intensity of the magnetic field along the axis of the toroid. The continuous line is the numerically calculated value of the field. Points are measures taken with a gaussmeter.

3.1.5 RF power supply

Two radio frequency power supplies were used:

1. RFPP (RF30R model) at 13.56 MHz, 50 Ω, with a range between 0 and 3000 W, water-cooled

2. RF-20-XXVII at 27.12 MHz, 50 Ω, with a range 0-2000 Watt, air cooled.

Regulation of input power was possible through the digital controller of the generator, with a one-Watt step precision, as provided by the manufacturer. The forward and reflected

power was monitored on the display of the generator. The small chamber (14) was usually dedicated to 13.56 MHz experiments, and the larger chamber (7) to 27.12 MHz experiments.

3.1.6 Antenna

Several kind of antennas was tested. Figure 3.7 shows a single loop antenna ($m = 0$) that has been used. Its impedance was adjusted choosing among 1,2,3 turns around the source tube. A water-cooling circuit was shared by the generator and the antenna. The cooling system was made with a chiller and by using a copper pipe for the antenna.

3.1.7 Matching network

A L-type matching circuit was used between the 50Ω RF power supply and the antenna, for impedance matching. The circuit was composed by two variable capacitors C_1 and C_2, placed in "standard" or "alternate" configuration, plus a transmission line of opportune length. The values of the capacitors and the length of the transmission line were calculated in order to guarantee the plasma coupling at 50Ω with the RF generator.

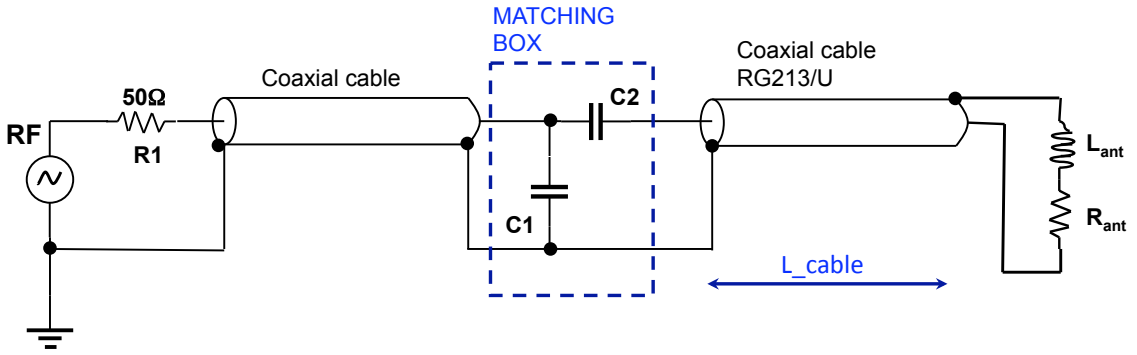

Figure 3.4: Electric scheme of the RF circuit, with the L-type matching box in the standard configuration

3.2 RF compensated Langmuir probes

3.2.1 Probes construction

Plasma parameters were measured with RF-compensated Langmuir probes, expressly fabricated for the experiments. Probes consisted mainly of two elements, the tungsten tip and the radio-frequency compensation system.

The plasma-contacting tip of the probe was a tungsten cylinder of 3-10 mils in diameter. The size of the plasma-contacting tip is reported in Table 3.1.

Probe	L±1 [mm]	diam±0.025 [mm]
ChenB 80903	10	0.254
ChenB 100317	6	0.254

Table 3.1: Tungsten tip of the Langmuir probes

3.2.2 RF compensation

The RF compensation system used for the experimental tests was composed by a notch LC passive filter located in the proximity of the probe tip. The plasma-contacting electrode was made of nickel or tungsten, depending on expected plasma densities. The electrode had a surface able to satisfy the condition on impedances [63]:

$$\frac{e\tilde{V}_{rf}}{K_B T_e}\left|\frac{Z_x}{Z_{ck}}\right| << 1 \tag{3.1}$$

Values of the LC components were chosen to have a RF signal choked at the desired frequency. Each RF choke was tested with an apparatus showed in Fig.3.5.a, where Z_{SFG} is the impedance of the synthesized function generator Z_{choke} is the impedance of the choke system, R_{load} is a known load resistance (ex. 1000 Ohm), and Z_{OSC} is the impedance of the digital storage oscilloscope Since the impedances Z_{SFG} and Z_{OSC} were unknown, a preliminary test was always done without the choke, to calibrate the response of the oscillator.

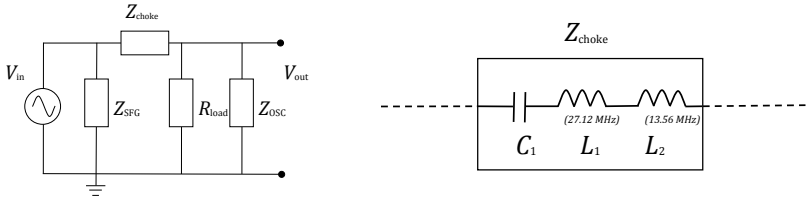

(a) (b)

Figure 3.5: (a) Apparatus for testing the RF choke of the Langmuir probes; (b) internal impedances in the RF choke

Figure 3.6 shows an example. Figure 3.6.a shows the RF synthetic signal produced by the SFG and measured with the oscilloscope, without the choke chain. The test was done in an interval of frequencies from 10 MHz to 30 MHz, by generating a frequency ramp with the SFG. A marker signal was put at 27.12 MHZ, corresponding to the small luminous spot in the figure. The input peak-to-peak RF voltage was $V_{in}^{p-p} = 10$ Volt for all the frequencies, and thus a flat reading would have expected. The reading on the vertical axis is of 5 Volts per division, so the right voltage is read only on the lower range of the frequencies around

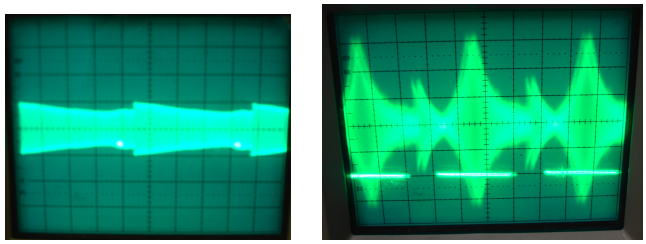

(a) (b)

Figure 3.6: Testing with the oscilloscope of the RF choke, by using a synthetic RF signal of $V_{in}^{p-p} = 10$ Volt: (a) without the choke impedance (ordinate 1 division = 5 Volts), (b) with two chokes at 13.56 and 27.12 MHz (ordinate 1 division = 0.2 Volt)

10-12 MHz. At higher frequencies the measured voltage V_{out} was decreasing, a behavior attributed to the impedance Z_{OSC} of the Tektronix oscilloscope. After the addition of the choke to the circuit, the output changed to the one in Fig. 3.6.b. Now the scale of the vertical axis is 0.2 Volt per division. The horizontal line is a marker signal starting at 13.56 MHz and ending at 27.12 MHz, to put in evidence the two frequencies of interest. The RF signal is choked at the two frequencies of interest, 13.56 MHz and 27.12 MHz. The electric scheme of the choke is showed in Fig. 3.5.b. The values of the components (as measured with a BK precision 875A) were: $C_1 = 114 \pm 10$ pF (100 pF nominal, 200 Volt), $L_1 = 58 \pm 10\mu$H (56 μH nominal) and $L_2 = 115 \pm 10\mu$H (180 μH nominal).

3.2.3 Probe positioning

The probes were mounted on special interfaces allowing one-dimensional movements of the probe inside the chamber. One allowed radial scans in the plasma plume of the thruster, the other for axial scans inside the source cylinder.

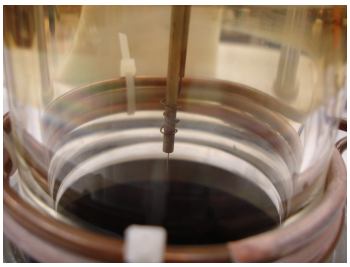

Figure 3.7: View of the Langmuir probe inside the cylinder of the plasma source

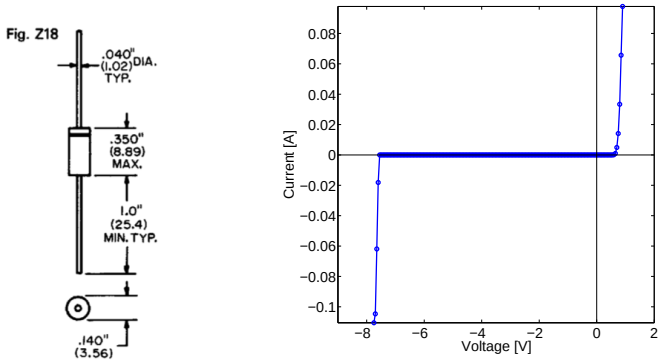

Figure 3.8: Test of the HIDEN acquisition system with a Zener diode ECG5121A, nominal Zener voltage of -7.5 Volts

3.2.4 Acquisition system

The Langmuir probe was connected to an HIDEN controller , feeding the input potential V to the probe. Figure 3.8 shows a test with the I-V characteristic of a Zener diode ECG5121A, with a nominal Zener voltage of -7.5 Volts. The cable from the probe to the HIDEN was filtered by wrapping it around a small ferromagnetic toroid. The HIDEN was then connected to a normal Windows-PC with the original HIDEN ESP software dedicated for acquisitions. The software allows to export .csv files containing the sampled I-V values for each probe scan. From the HIDEN software the following parameters was setted: the range of the scan (usually -100/+20 Volts), the samples per scan, the gain range, the sample dwell time, the start dwell, the minimum cycle period and the number of scans.

3.2.5 Test types

1. **Power scan** Langmuir probe acquisitions at increasing power has been taken for several magnetic configurations. This campaign of tests has been done in order to study the influence of RF power and magnetic field topology on plasma density n and electron temperature T_e. The low-power range between 50 and 400 Watts has been characterized.

2. **Spatial scan** Radial and axial scans have been done by moving the Langmuir probe inside the chamber and taking data at each station. The movement of the probe was made possible by means of a dedicated chamber access. The plasma density along radius of the diffusion chamber exhibits a density peak in the center of the chamber.

3.3 Langmuir probe data

3.3.1 Analysis of the experimental I-V traces

Choice of the method of analysis. Despite the constructive simplicity of a Langmuir probe, the analysis of its measured I-V characteristic is not straightforward. Classical methods of analysis are the ABR, BRL and OML methods. The method based on the Orbital Motion Limited (OML) theory was proposed by Langmuir [59], and developed by Chen [60], [48], [64]. The model describes the collection of a plasma on a solid conductive body placed at potential V_p (probe potential) by using orbital theory of plasma particles. The exact solution for a cylinder is [59]:

$$I_{OML} = q_e A_{probe} j_r F \qquad j_r = \frac{1}{2} n \left(\frac{2K_B T}{\pi m} \right)^{1/2} \tag{3.2}$$

$$F = \frac{s}{a} \mathrm{erf}(\Phi^{1/2}) + e^{\eta} \mathrm{erfc}(\eta + \Phi)^{1/2} \tag{3.3}$$

$$\eta = -\frac{q_e(V_p - V_s)}{K_B T}, \qquad \Phi = \frac{s^2}{s^2 - a^2} \eta \tag{3.4}$$

where A_{probe} is the probe area, j_r is the random flux of either species, a is the probe radius, s an assumed sheath radius, q_e the particle charge, V_p the probe potential, and V_s the space (plasma) potential. When $T_i << T_e$ the model is very accurate for ions, and it predicts a collection current proportional to the square root of the applied potential:

$$I_{i,OML} \approx \frac{n q_e S}{\pi} \left(\frac{2q_e(V_s - V_p)}{M_i} \right)^{1/2} \tag{3.5}$$

where M_i is the ion mass. The range of validity of the OML theory should be limited to low–density and low-collisionality plasmas, where particles trajectories could in principle be treated as single charges orbiting inside the potential of the probe. However, Chen showed that the OML model can be successfully applied to high density plasmas [48] and even to high-density RF plasmas [64]. The validity of the OML model in regimes such different is still an open and unresolved question. The OML method has been adopted for the treatment of the Langmuir probe data during activities at UCLA. The procedure used for data analysis can be summarized with the following points.

1. Acquisition of experimental data and averaging. Rough experimental data from the acquisition system, digitally sampled by the HIDEN A/D converter, are stored in a file in the form of a measured current (Amperes) with respect to the input applied potential (Volts)

$$(V_p, I_p)_j \qquad j = 1, ..., N_{samples} \tag{3.6}$$

Convention for positive current $I > 0$ is when the *electron current* is positive. Collected data are averaged over several acquisitions. The value of the imposed potential V_p is

recorded in digital form with 5 significant digits. The accuracy of the acquisition system on the imposed potential is smaller than < 0.1 mV, that is below the last significant recorded digit. As a consequence, the numerical value of the imposed potential doesn't change between two subsequent acquisitions when all other settings remains the same. Figure 3.9.a shows an example of potential ramp, between -100.00 and +30 Volt. The value of the current is stored with 5 significant digit by the acquisition system, and the quantization error depends on the range set during the acquisition (0.1, 1.0, 10.0, 100.0 mA). Fig. 3.9.b shows an example of current I_p collected from the plasma over 5 subsequent potential ramps, with the plasma remaining stationary. The small variability of the results can qualitatively be appreciated from the figure. Figure 3.9.c shows the standard deviation of the measured current, averaged over the scan number

$$\sigma_{I_p} = [1/(N_{scans} - 1) \sum_{j=1}^{N_{scans}} (I_p^{(j)} - \bar{I}_p)^2]^{1/2} \tag{3.7}$$

$$\bar{I}_p = (1/N_{scans}) \sum_{j=1}^{N_{scans}} I_p^{(j)} \tag{3.8}$$

The figure highlights that experimental data are more scattered in the electronic-current region than in the ionic region, as expected. The maximum standard deviation reaches the range of 1.0 mA for the particular case reported in the figure.

2. Averaged spline of measured current. A spline of the measured current averaged over the aspect ratio of the probe tip is done using a moving average filter of $\pm N_b$ samples before and after the i-esim sample,

$$I_i^+[mA] = -1000 \sum_{k=i-N_b}^{i+N_b} \frac{I_{p,k}}{AR(2N_b+1)} \qquad i = 1 + N_b, ..., N_{samples} - N_b \tag{3.9}$$

where

$$AR = 1 + \frac{R_{probe}}{2L_{probe}} \tag{3.10}$$

is the aspect ratio of the plasma-exposed cylindrical conducting tip of the probe, of radius R_{probe} and lenght L_{probe}. The error on the size of the tip geometry has revealed to be also the most important source of error on the interpretation of the IV curves within the procedure of the OML analysis. After the splining procedure, the array of measured data is reduced in size from $N_{samples}$ to $N_{samples} - 2N_b$. Usually $N_b = 5$ has been used, that means a span of 11 samples is considered for the splining. Figure 3.9.d shows an example of splined current I_i^+ (black curve), together with absolute error bars obtained with propagation of error from formula Eq.3.9

$$\Delta I_i^+ = \left| \frac{\partial I_i^+}{\partial(AR)} \Delta(AR) \right| + \left| \frac{\partial I_i^+}{\partial(I_{p,k})} \Delta(I_{p,k}) \right| = \left| \frac{I_{p,k}}{AR^2} \Delta AR \right| + \left| \frac{\Delta I_m}{AR} \right| \tag{3.11}$$

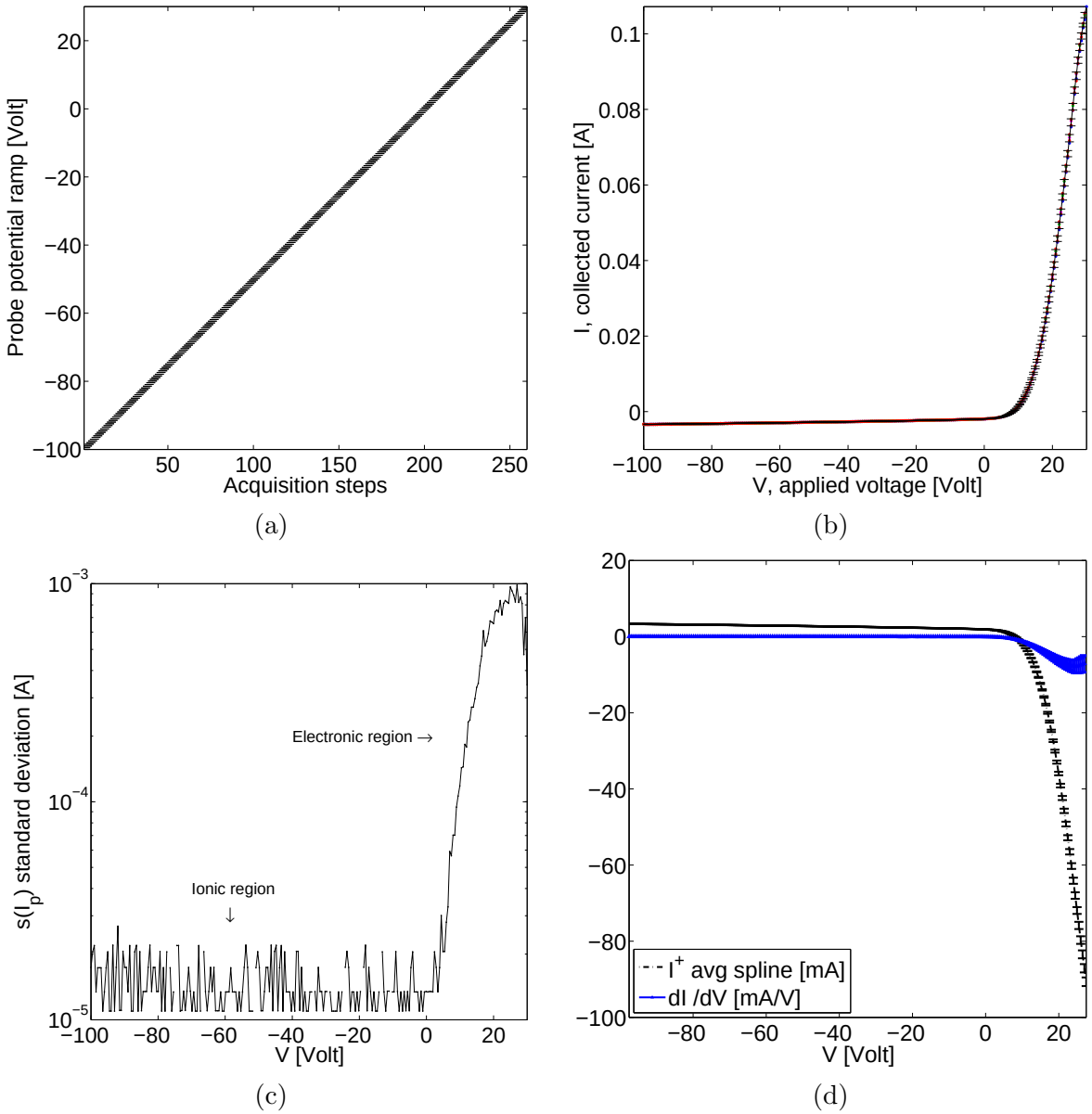

Figure 3.9: (a) Example of Langmuir probe potential ramp between -100/+30 Volts, with error bars on the applied input voltage; (b) collected current over 5 different ramps, with the averaged IV line, and error bars over the values of measured currents; (c) standard deviation of the collected current: data are more scattered in the electronic current region than the ionic region; (d) averaged spline of the IV trace (black), and first derivative of the splined curve (blue).

where the index k is intended summed over the filter span $N_{samples} < k < N_{samples} - 2N_b$. The error on the aspect ratio AR is purely geometry-dependent:

$$\Delta(AR) = \left|\frac{\Delta R_{probe}}{L_{probe}}\right| + \left|\frac{R_{probe}}{L^2_{probe}}\Delta L_{probe}\right| \approx O(10^{-2}) \tag{3.12}$$

as results for typical R and L of $R = (5.0 \pm 0.5)$ mils $= (0.127 \pm 0.013)$ mm, and $L = (6 \pm 1)$ mm.

3. First guess of plasma parameters (n, T_e, V_s)**.** The space potential V_s is the voltage at which the minimum of the first derivative of the I-V characteristics occurs:

$$V_s = \min\left\{V, \frac{dI}{dV}\right\} \tag{3.13}$$

The first derivative is obtained from the measures I^+ using a first or second order finite difference scheme:

$$\frac{dI}{dV} = \frac{I_{i+1} - I_i}{2(V_{i+1} - V_i)} + O(\Delta V) \tag{3.14}$$

$$\frac{dI}{dV} = \frac{I_{i+1} - I_{i-1}}{2(V_{i+1} - V_{i-1})} + O(\Delta V^3) \tag{3.15}$$

Propagation of errors on derivatives Eq.3.14 and 3.15 is of immediate evaluation. One example is reported in Fig.3.10. At first, the electron temperature is estimated by noting that T_e is approximated by:

$$T_e \approx \frac{I^+}{dI/dV} \tag{3.16}$$

From the space potential and the electron temperature, the plasma potential curve can be obtained:

$$\eta = \frac{V_s - V_p}{T_e} \tag{3.17}$$

The first guess of plasma density can be estimated using formulas for ion saturation current[2],

$$n(I_{sat}) = \frac{1}{2}\frac{|I_i^{sat}|}{A_{probe}C_s} \tag{3.18}$$

or the electron saturation current,

$$n(E_{sat}) = \frac{3.7|I_e^{sat}|}{A_{probe}\sqrt{T_e}} \tag{3.19}$$

[2]Generally speaking, the approximated value that can be obtained from the ion saturation current is 1.5-2.0 times higher than the value obtained from the OML fitting, even if this assertion is empirical and not always true.

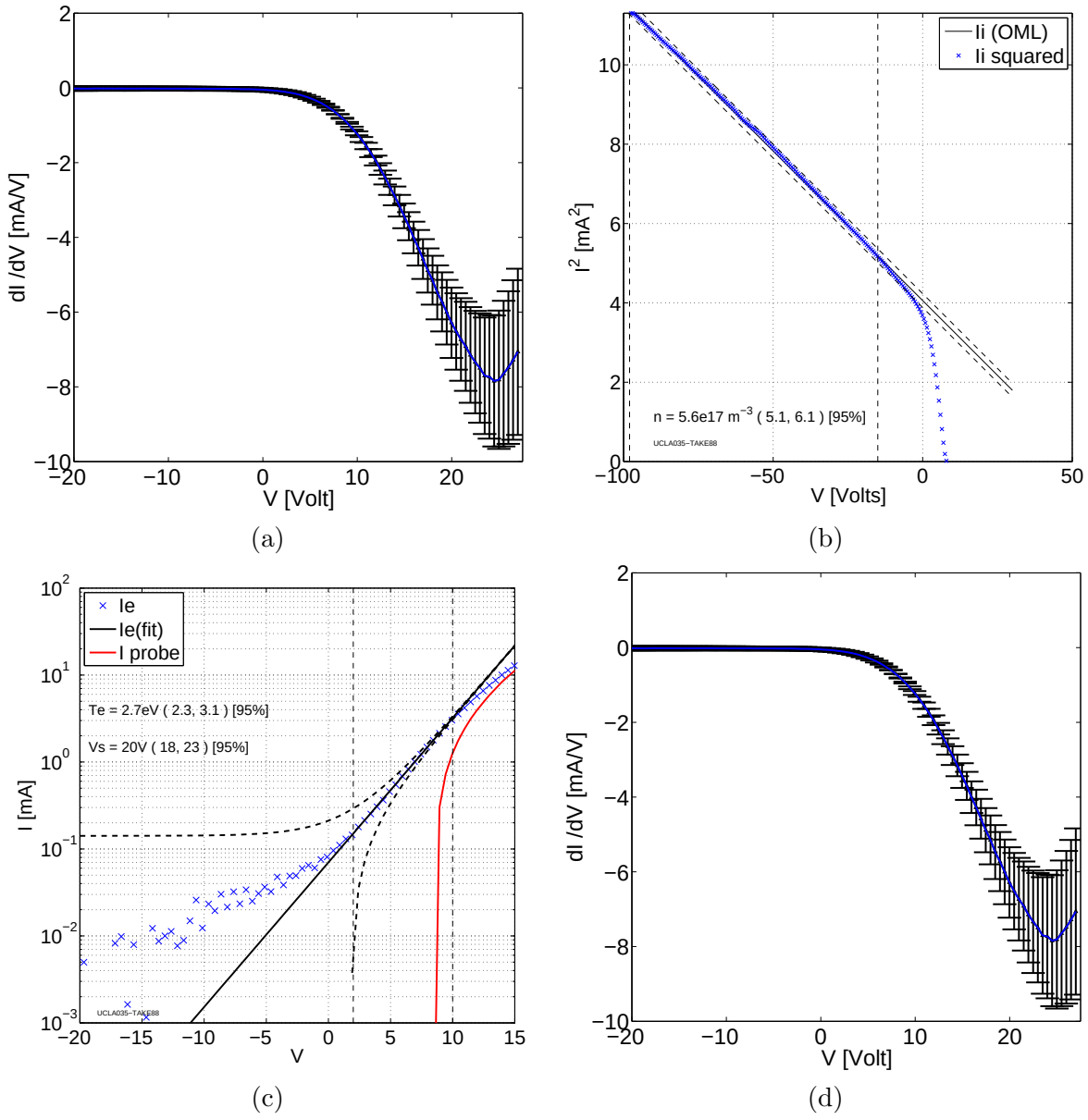

Figure 3.10: (a) First derivative of the splined current; (b) ion current fit with the OML model; (c) electron current fit with a Maxwellian;

With the values found from the initial guess, it is possible to make a first graphical check of the difference between theory and experiment.

4. Ion current fit. From the OML theory, the ion current is:

$$I_{i,OML} = 7.05 A_{probe} n \sqrt{\frac{\eta T_e}{M_i}} \tag{3.20}$$

The unknown parameters (V_s, T_e, n) are calculated from the experimental data from the minimization of the quadratic errors between the experimental data and the OML theoretical model in the ion region of the characteristic,

$$\min \left\{ (n, V_s), \epsilon_{I_i^2} \right\} \tag{3.21}$$

where

$$\epsilon_{I_i^2} = \sum_{k=1}^{N_{samples}} (\Delta I_i^2)_k \tag{3.22}$$

$$\Delta I_i^2 = \left| (I_i^+)^2 - (I_{i,OML})^2 \right| \tag{3.23}$$

The Nelder-Mead simplex direct search minimization method has been used as a numerical tool for the minimization of the least squares, with typical iteration numbers of 50-70 and a total function evaluations around 100. The method has the great advantage to be derivative-free [61]. The deviation on the density is finally given by:

$$\sigma_{n^2}^2 = \left(\frac{\partial f}{\partial V_p} \right)^2 \sigma_{V_p}^2 + \left(\frac{\partial f}{\partial (I_i^2)} \right)^2 \sigma_{I_i^2}^2 + \left(\frac{\partial f}{\partial A_{probe}} \right)^2 \sigma_{A_{probe}}^2 \tag{3.24}$$

where

$$f = f(V_p, I^2, A_{probe}) \equiv n^2 = \frac{M_i I_i^2}{7.05^2 A_{probe}^2 (V_s - V_p)} \tag{3.25}$$

Because of its parabolic trend, the ion current is conveniently plotted in an (V, I_i^2) graph (Fig. 3.10.b), where the experimental ion current $(I^+)^2$ can easily be compared with the theoretical current $I_{i,OML}^2$ along a line. The two vertical dashed lines in Fig. 3.10.b enclose the interval within the fitting has been done.

5. Electron current fit. The electron temperature T_e is inferred from the electronic current I_e in a region of probe potentials after the transition of the IV characteristic and before the electron saturation. Electron current is corrected from the ion current using the following rule:

$$I_e = \begin{cases} \eta > 0 & \begin{cases} I_e^* > 0 & I_e[mA] = I_e^* + I_{i,OML} \\ I_e^* \leq 0 & I_e = \epsilon_{min} \end{cases} \\ \eta \leq 0 & \begin{cases} I_p > 0 & I_e[mA] = I_e^* \\ I_p \leq 0 & I_e = \epsilon_{min} \end{cases} \end{cases} \tag{3.26}$$

where

$$I_e^*[mA] = 1000 I_p / AR \tag{3.27}$$

and ϵ_{min} is a minimum error level, equal to the error of digital quantization on the amplitude of the current output signal, equal to $\epsilon_{min} = 10^{-5}$ mA in the HIDEN acquisition system. For potentials V_p close to the plasma potential, electrons remain Maxwellian, and the following theoretical model of collection of Maxwellian electrons on a probe has been used:

$$I_e^{FIT} = (268 n A_{probe} \sqrt{T_e}) \exp\left(\frac{V_p - V_{s1}}{T_e}\right) \tag{3.28}$$

Again, a best fit of experimental data with the theoretical collection model has been done; the same Nelder-Mead simplex direct search method has been used for the minimization problem:

$$\min\{(T_e, V_{s1}), \epsilon_{I_e}\} \tag{3.29}$$

where

$$\epsilon_{I_e} = \sum_{k=1}^{N_{samples}} (\Delta I_e)_k \tag{3.30}$$

$$\Delta I_e = \left|\log I_e - \log I_e^{FIT}\right| \tag{3.31}$$

The deviations of electron temperature and plasma potential is finally given by:

$$\sigma_{T_e}^2 = \left(\frac{\partial g}{\partial V_p}\right)^2 \sigma_{V_p}^2 + \left(\frac{\partial g}{\partial I_e}\right)^2 \sigma_{I_e}^2 + \left(\frac{\partial g}{\partial A_{probe}}\right)^2 \sigma_{A_{probe}}^2 + \left(\frac{\partial g}{\partial n}\right)^2 \sigma_n^2 \tag{3.32}$$

$$\sigma_{V_{s1}}^2 = \left(\frac{\partial h}{\partial V_p}\right)^2 \sigma_{V_p}^2 + \left(\frac{\partial h}{\partial I_e}\right)^2 \sigma_{I_e}^2 + \left(\frac{\partial h}{\partial A_{probe}}\right)^2 \sigma_{A_{probe}}^2 + \left(\frac{\partial h}{\partial T_e}\right)^2 \sigma_{T_e}^2 \tag{3.33}$$

where[3]

$$g = g(V_p, I_e, A_{probe}, n) = T_e : \frac{T_e}{2} \log T_e - T_e \log\left[\frac{I_e}{268 n A_{probe}}\right] - V_{s1} + V_p = 0 \tag{3.34}$$

$$h = h(V_p, I_e, A_{probe}, T_e) \equiv V_{s1} = V_p - T_e \left[\log\left(\frac{I_e}{268 n A_{probe}}\right) - \log T_e^{1/2}\right] \tag{3.35}$$

The convenient graph for a plot of the electron current is the semi-log $(V, \log I_e)$, where the exponential electron current appears to be as a line. Figure 3.10.c shows an example. The two bounds of the interval selected for the fitting are also evidenced with two vertical lines; the plasma remains Maxwellian within the interval. At higher potentials, the electron current saturates. At lower potentials, the plasma is usually still Maxwellian within the range of uncertainty. However, the uncertainty of experimental data is here higher because of subtraction of the ion current. Deviations from the Maxwellian (like ion/electron beams, hot electron populations, etc.) cannot usually be appreciated with confidence due to the higher uncertainty in the transition region.

[3]Derivatives of the implicit function g were solved numerically

3.3.2 Experimental results

An example of the experimental apparatus used for the validations is shown in Figure 3.11.a. The cylindrical Pyrex source of 5 cm of inner diameter was mounted on top of the cylindrical vacuum chamber, with their axis aligned. The top end of the source was covered with a metallic backplate, necessary for a constructive reflection of the helicon wave and for short circuiting the plasma. The radio frequency antenna ($m = 0$) was wrapped around the Pyrex source, and fed with radio-frequency power through the power generator. The matching between the generator and the load was obtained with an L-type matching network with two adjustable vacuum capacitors. The magnetic field along the axis of the source cylinder was obtained with a Neodimium magnet with the magnetization vector parallel to the symmetry axis of the source cylinder, placed above the chamber at an adjustable distance, in order to have the desired value of the magnetic field at the antenna location. The plasma is created inside the source tube, and then expands down inside the chamber. All the test were made using Argon. Before each test the air pressure inside the chamber was floored down to the 10^{-6} Torr range, in order to have less than 0.001% of residual air during the acquisitions. The Argon was injected into the chamber from the top plate or from the sides of the chamber, depending on the needs.

Power scan at 13.56MHz, inside the helicon source, Figs. 3.11, 3.12 and 3.13.

This experimental campaign was oriented to measure the plasma parameters vs. the input RF power for a fixed gas pressure[4]. The interesting range occurs between 1.0 and 20 mTorr (0.013-2.67 Pascal). The pressure inside the system was thus set at the value of (15.0 ± 0.1) mTorr, measured with the baratron before the ignition of the plasma. Before the ignition of the RF power and of the plasma, the chamber was uniformly filled by the gas. After the ignition of the RF power, the values of the capacitors in the matching box were adjusted until the condition of zero reflected power was obtained. The monitoring of the reflected power was possible thanks to a digital forward/backward meter included in the RF generator, with a precision of ± 1 Watt on the reading, as provided by the manufacturer. A Langmuir probe was fit inside the Pyrex cylinder through an aperture of 5mm on the metallic plate at the top. The tip of the probe was placed as indicated by the red dot in Fig.3.11.a, inside the Pyrex source and at the center of the antenna. Tests were done in the range from 1 to 400 Watt of input power. The experimental IV curves obtained with the HIDEN acquisition system are shown in Fig.3.11.b. From the analysis of the curves (with the procedure described in Sec. 3.3.1), the values of plasma density (Fig.3.11.c), electron temperature (Fig.3.11.d) and plasma potential (Fig.3.11.e) have been

[4]In plasma thrusters experiments the usual regulation is done on the mass-flow, and not on chamber pressure. However, the behavior of plasma at low powers has been found to be much more influenced by the local gas pressure than by its mass flow; a pressure-dependent characterization has been considered more important for the basic understanding of the plasma behavior and for the validation of the theoretical model.

obtained. Furthermore an estimate of the ionization fraction has been possible, as the ratio n/N_n of the plasma density over the neutral-gas density (Fig.3.11.f). Figure 3.11.c shows that at low powers of 1-100 Watt, the plasma density is in the range 10^{16}-10^{17} m^{-3}. The fit of the ion current from the I-V characteristics are reported in Fig. 3.12.a, 3.12.c and 3.12.e, for the three cases of 50,80 and 100 Watt respectively. Ion currents follows the OML I-square line in a wide range of probe potentials, from -100 up to -20 Volts[5]. At higher power levels, of 100-400 Watts, the plasma density increases within the range 10^{17}-10^{18} m^{-3}. Three curves of the ion current for powers of 200, 300 and 400 Watt are shown in Fig. 3.13.a, 3.13.c and 3.13.e respectively. Experimental data correctly follows the OML I-square line within a $< 5\%$. The greater uncertainty of the measure descends from the uncertainty of the geometrical size of the probe tip. Again, the plasma density estimated from values of ionic current at saturation are higher than the value descending from the OML fitting.

The electron current $\log I_e$ exhibit a linear Maxwellian trend versus the applied potential. The values of the resulting temperature of electrons is reported in Fig. 3.11.d, together with the value of the plasma potential obtained from the non-linear LS fit. The temperature increases from 1eV to 4eV in the low-power range 1-100W, and then stabilizes to a value around 3eV in the range 100-400W. There is no evidence of increasing electron temperature for increasing RF powers. Furthermore, the electron current can be approximated by a Maxwellian within a 10% of approximation. The increase of RF power appears to affect the range of more energetic electrons; however, the uncertainty in this range is too affected by ion subtraction, and useful consideration on high-energy electrons cannot be inferred. The power is expended to sustain a plasma of increasing density, the power being dissipated in inelastic collisions and losses at the boundaries. How the amplitude of the RF power affects the electron energy distribution function remains an open question for an helicon plasma. Some clues can be inferred by looking carefully at the I_e traces, reported in Figs. 3.11.b, 3.11.d, 3.11.f, 3.12.b, 3.12.d and 3.12.f for powers of 50, 80, 100, 200, 300 and 350 Watt respectively. At low powers the electron behavior is well approximated by the Maxwellian fit. For increasing powers, the behavior near saturation changes. The Maxwellian fit is bended downward and the I_e line becomes a I_e curve: the absolute value of the curvature of I_e increases. According to Druyvesteyn [62], the distribution of electrons can be inferred from the second derivative of probe data. Numerical trials have revealed that the noise due to error propagation on the second derivative becomes too high to infer unambiguous conclusions about the results. However, a detailed study on the kinetic effects of the RF field on the electron energy distribution appears to be the proper path of future investigations.

[5]It's worthwhile to note that the ion saturation current of, say for example at 100 Watt, $I_{ion}^{sat} \approx 0.96$ mA would lead to a plasma density of $n_{ion}^{sat} \approx I_{ion}^{sat}/(q_e A_{pr} C_s) \approx 2.5 \times 10^{17}$ m^{-3} ($T_e = 3$ eV), which would have been higher than the value obtained from the fitting of the whole OML ion region, $n_{ion}^{OML} = (1.60 \pm 0.05) \times 10^{17}$ m^{-3}. At 300 Watt $I_{ion}^{sat} \approx 3.32$ mA, $n_{ion}^{sat} \approx I_{ion}^{sat}/(q_e A_{pr} C_s) \approx 8.8 \times 10^{17}$ m^{-3} ($T_e = 3$ eV) instead of $n_{ion}^{OML} = (5.5 \pm 0.2) \times 10^{17}$ m^{-3}, which is 1.6 times higher.

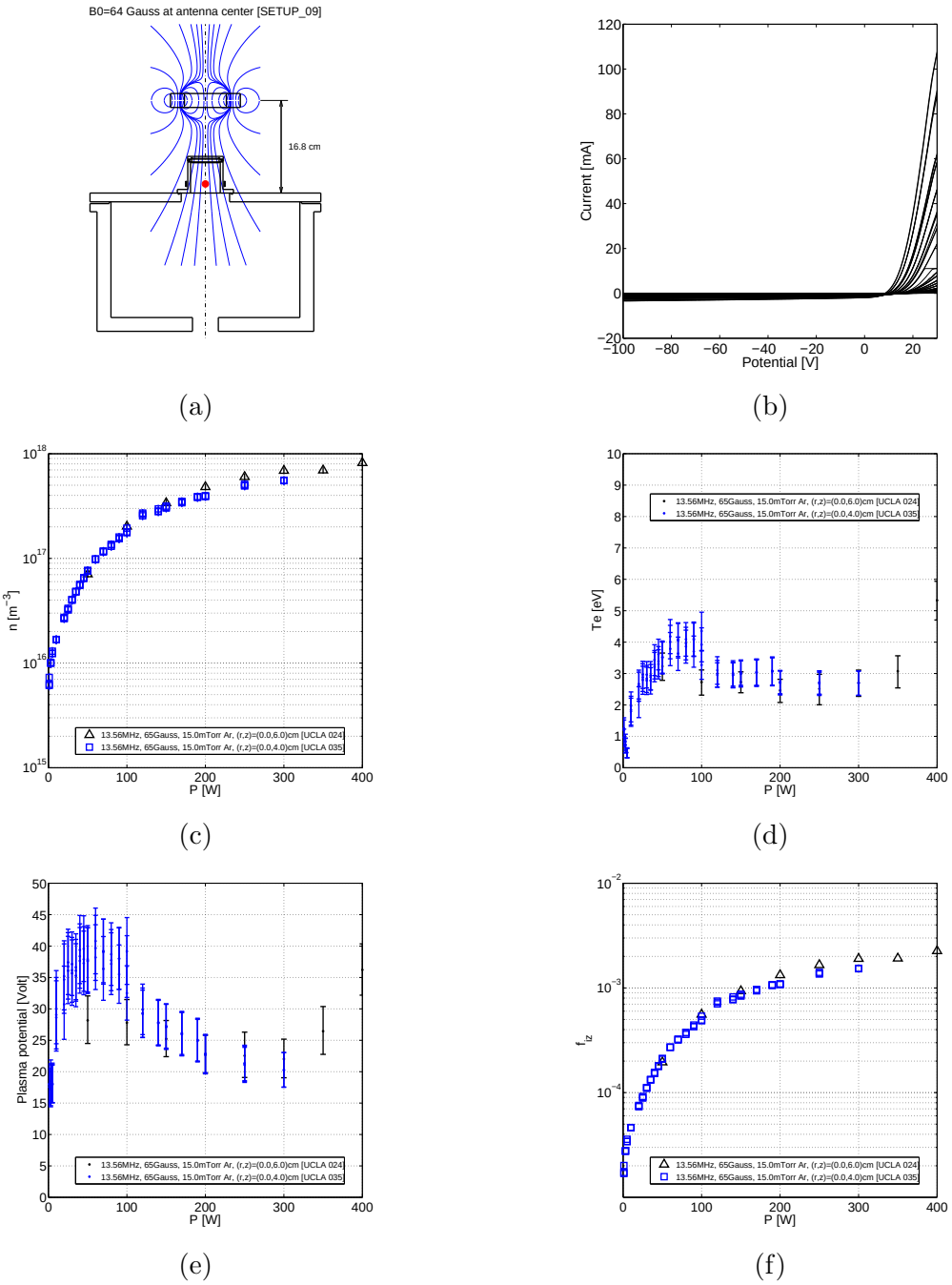

Figure 3.11: Power scan at 13.56MHz and for a fixed pressure of 15.0mTorr, inside the helicon source, (a) experimental setup, with the Langmuir probe position marked with a red dot; (b) experimental IV traces for increasing power levels; (c) plasma density vs. power; (d) electron temperature vs. power; (e) plasma potential vs. power; (f) estimate of the ioniation fraction. [res1a]

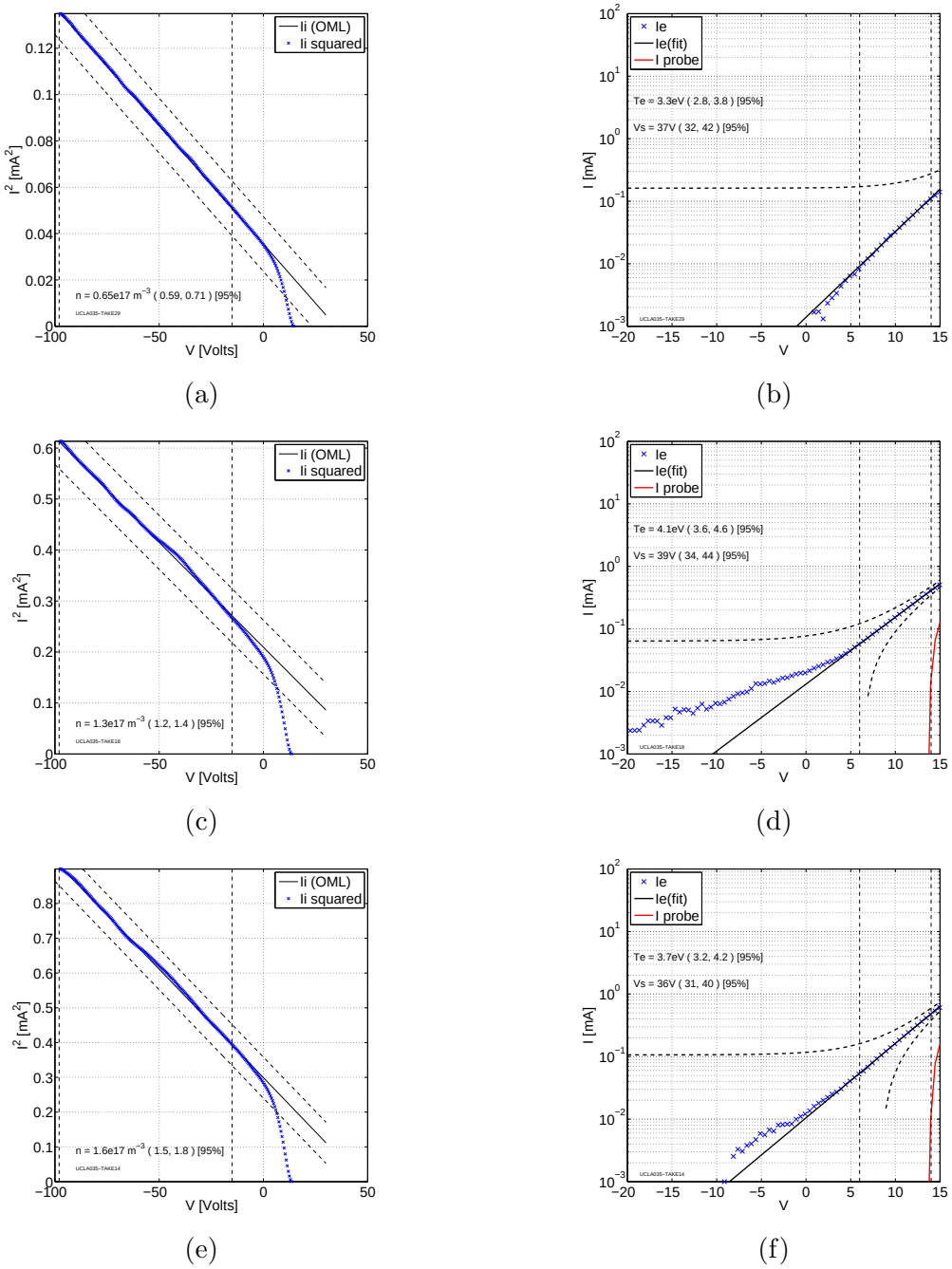

Figure 3.12: Ion and electron current fit for a 15.0 mTorr Argon plasma, inside the helicon source, with RF power of (a), (b) 50 Watt; (c), (d) 80 Watt; (e), (f) 100 Watt. [res1a]

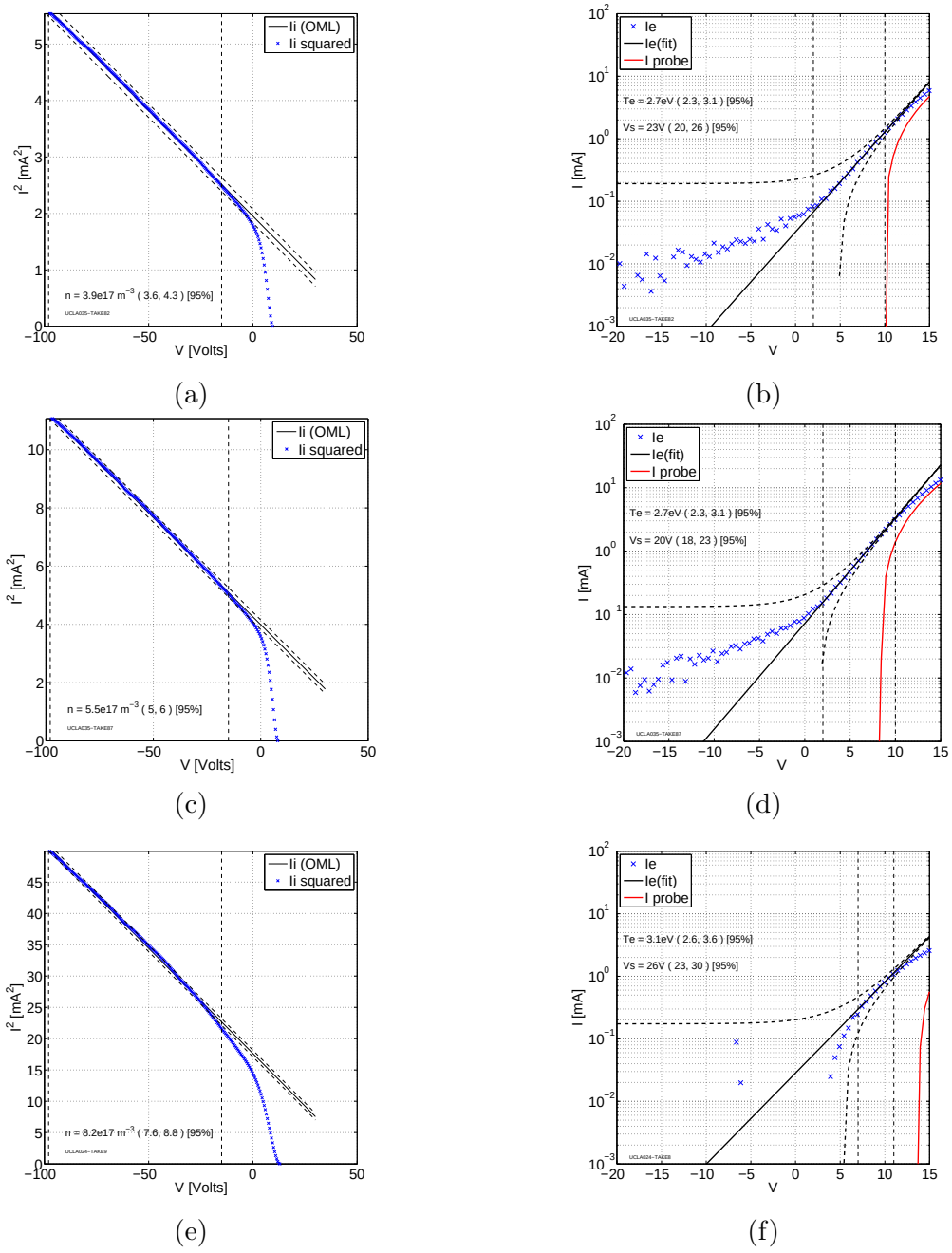

Figure 3.13: Ion and electron current fit for a 15.0 mTorr Argon plasma, inside the helicon source, with RF power of (a), (b) 200 Watt; (c), (d) 300 Watt; (e), (f) 350 Watt. [res1a]

Power scan at 13.56MHz, downstream conditions, Figs. 3.14, 3.15 and 3.16.

Tests with Langmuir probes placed downstream inside the chamber (probe position marked with a red dot in Fig. 3.14.a) revealed the behavior of the plasma far from the helicon source. A power scan in the range 50-1000 Watt at constant neutral gas pressure was made. The experimental IV traces are reported in Fig. 3.14.b. The resulting plasma density is approximatively 4-5 times less than inside the source. The 10^{18} m^{-3} range of plasma density is hardly reached even at very high power $\approx$1 kWatt. The resulting electron temperature is reported in Fig. 3.14.d. It begins is in a range of 1eV - 2eV at very low power (50-100 Watt), and then increases to a stationary value around 2.5eV for higher power levels. The electron temperature remains constant with respect to RF power. The plasma potential at that location occurs in the usual range of 10-20Volt. Figures 3.15 and 3.16 show the fits of ion and electron currents. The Maxwellian character of electrons is easily understood when inelastic collisions of electrons with neutral gas is taken into account. In fact, the ionization fraction downstream is approximatively in the 0.1% range, as reported in Fig. 3.14.f.

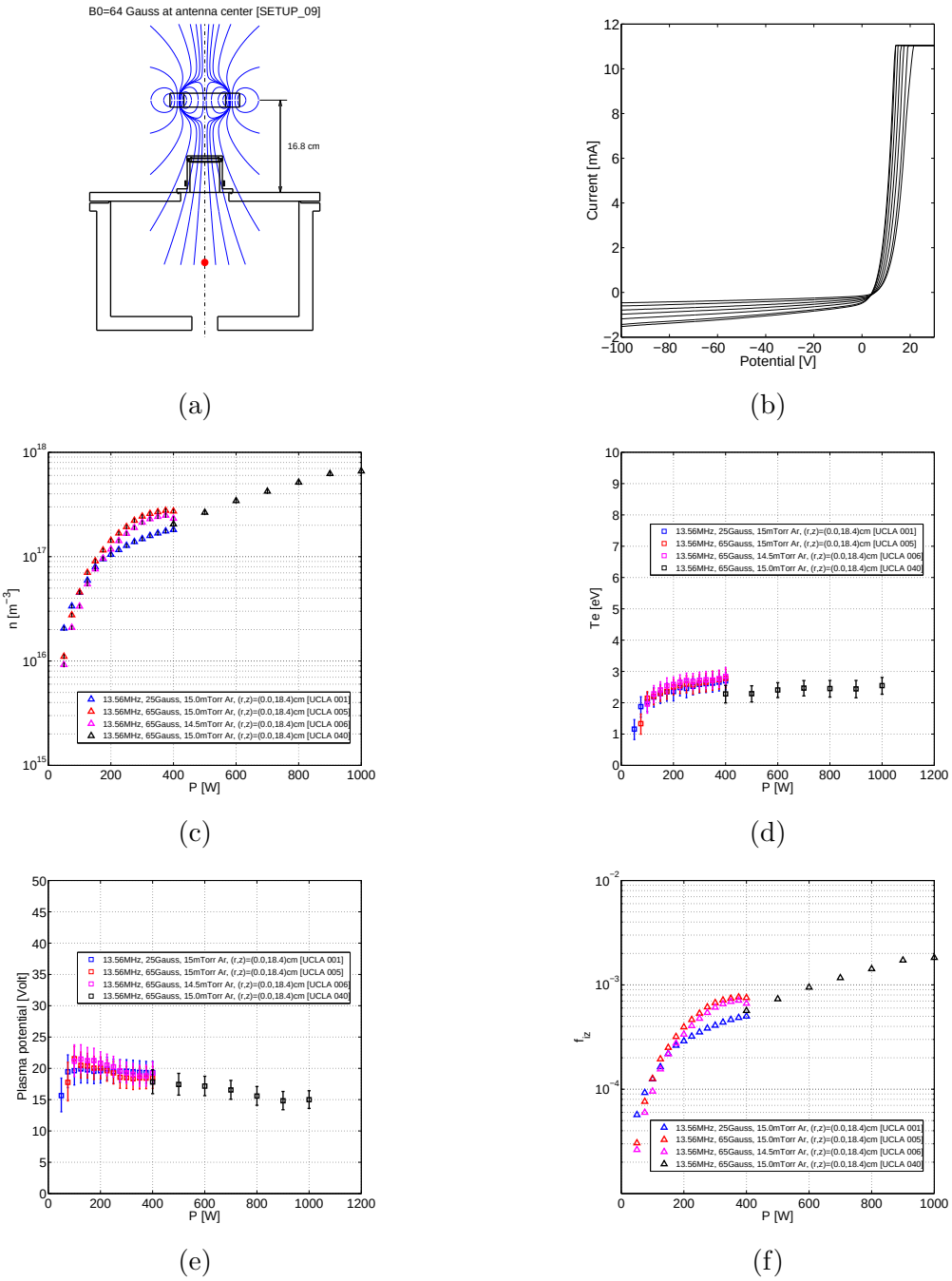

Figure 3.14: Power scan at 13.56MHz and for a fixed pressure of 15.0mTorr, downstream, (a) experimental setup, with the Langmuir probe position marked with a red dot; (b) experimental IV traces for increasing power levels; (c) plasma density vs. power; (d) electron temperature vs. power; (e) plasma potential vs. power; (f) estimate of the ioniation fraction. [res1b]

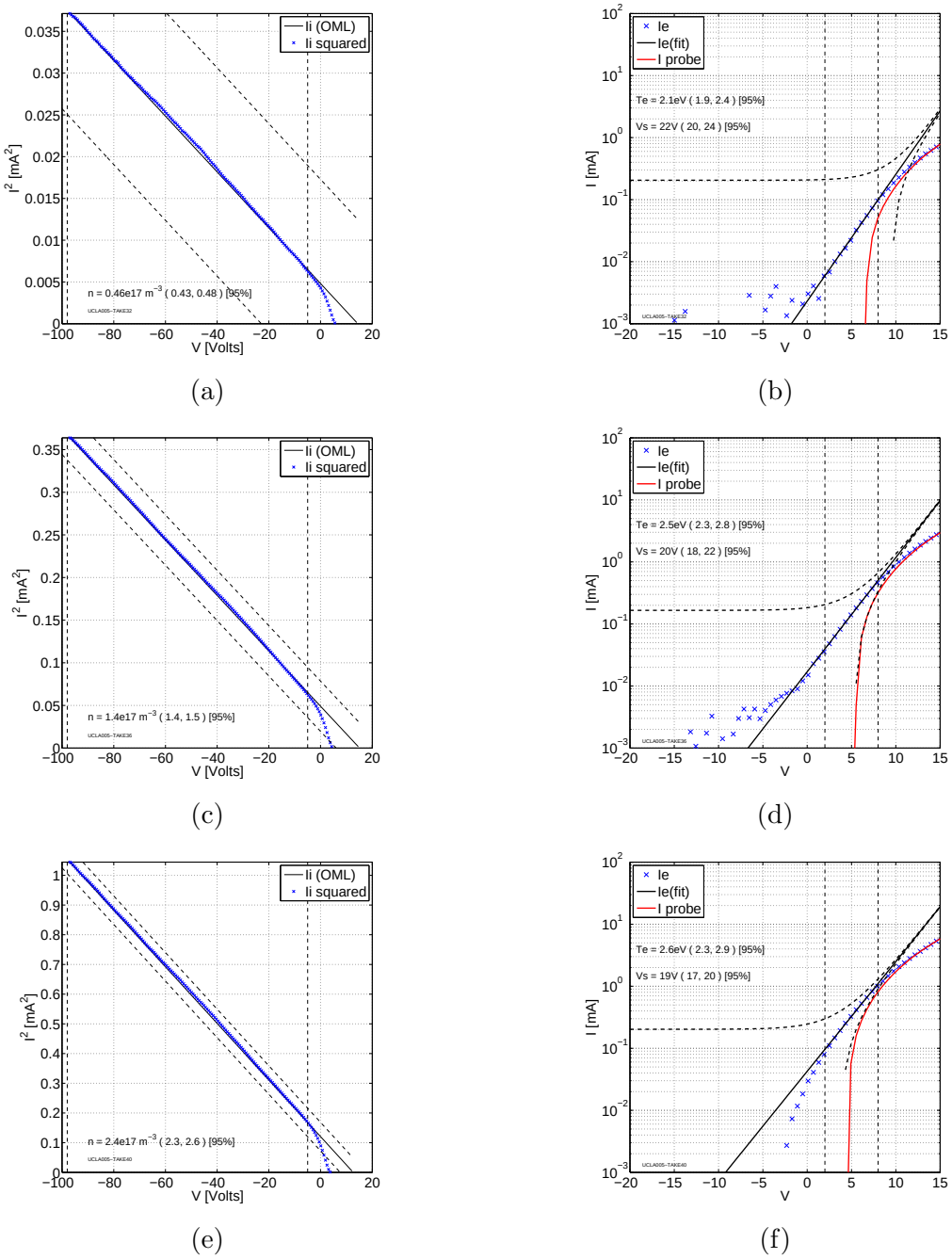

Figure 3.15: Ion and electron current fit for a 15.0 mTorr Argon plasma, downstream, with RF power of (a), (b) 100 Watt; (c), (d) 200 Watt; (e), (f) 300 Watt. [res1b]

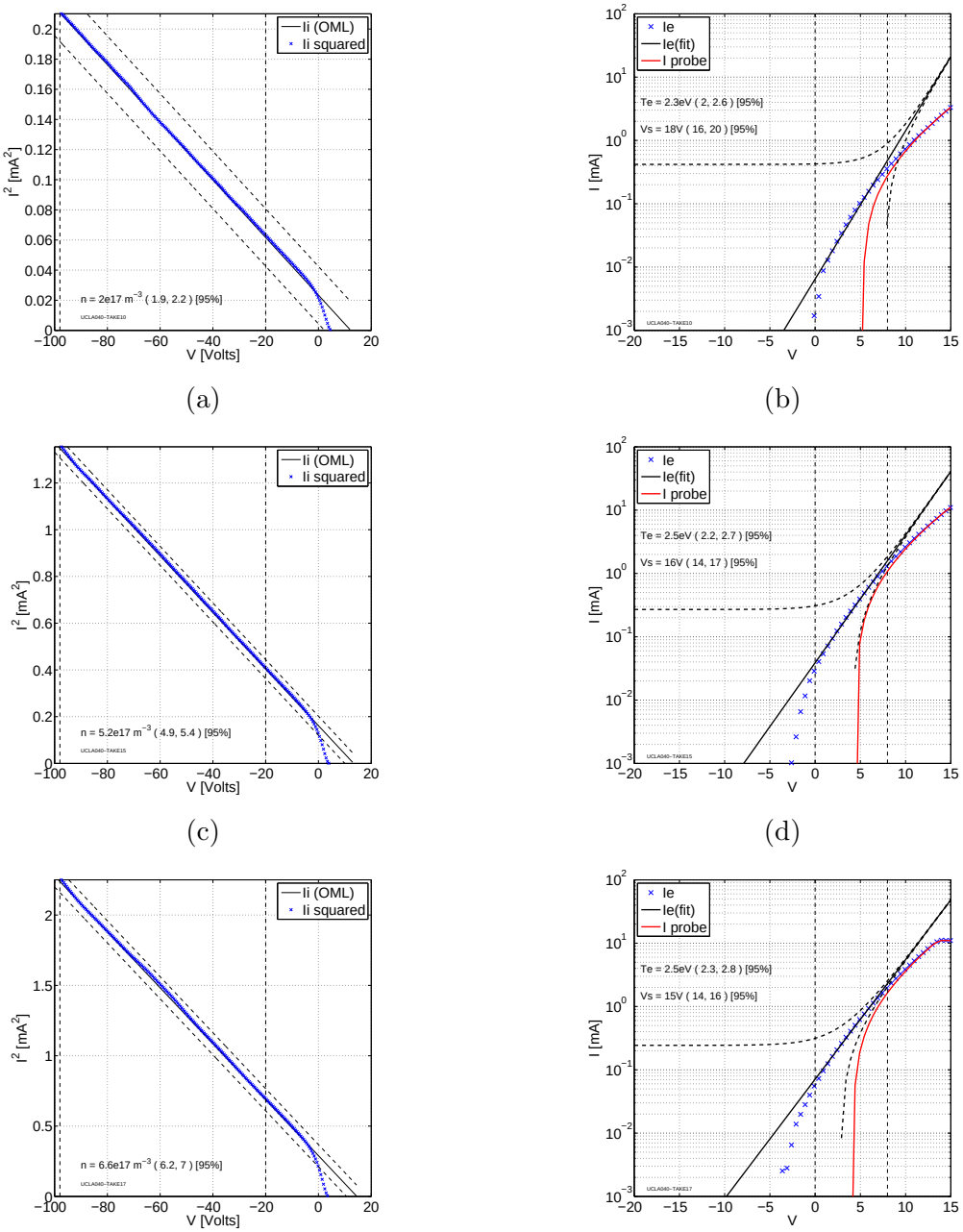

Figure 3.16: Ion and electron current fit for a 15.0 mTorr Argon plasma, downstream, with RF power of (a), (b) 400 Watt; (c), (d) 800 Watt; (e), (f) 1000 Watt. [res1b]

Axial scan at 13.56MHz, inside the source, Figs. 3.17, 3.18 and 3.19.

The spatial structure of the plasma was measured by means of moveable Langmuir probes. Figure 3.17 shows a scan along the axis of the source cylinder, and down inside the expansion chamber. The path of the scan has been marked with a red line in Fig. 3.17.a, and the measured IV traces are reported in Fig. 3.17.b. Figure 3.17.c shows the resulting plasma density versus the axis z, measured starting from the backplate of the Pyrex cylinder. The antenna location occurs at $z = 5$ cm. The highest plasma density occurs near the backplate, and then decreases gradually downstream inside the chamber. The electron temperature (Fig. 3.17.d) is high in the 2.8eV - 3.2eV range inside the source, and decreases to 2.5eV downstream. One of the most interesting spatial feature is seen from the trend of the plasma potential (Fig. 3.17.e), where a potential drop has been found. The electron fit curves exhibit a big change at that location, as showed in Figs. 3.18.b, 3.18.d, 3.18.f, 3.19.b, 3.19.b, 3.19.d and 3.19.f, corresponding to acquisitions at locations $z = 3, 8, 9, 10, 11, 14$ cm respectively (before, across and after the potential drop). Before the potential drop and immediately before, Fig. 3.18.b and 3.18.d, the electron temperature is in the range of 2.5eV-3.0eV, with plasma potentials in the range of 20V. When the drop is encountered, the electron curve exhibits a considerable shift downward to $\approx$ 13V, Fig. 3.18.f 3.19.b the temperature, remaining at the same value of $\approx$ 2.5eV. Downstream the potential drop raises to values around 15-20 Volts. Ion density is not affected by the drop (3.17.c), the phenomenon is electronic in nature.

Radial scan at 13.56MHz, downstream, Figs. 3.20, 3.21 and 3.22.

The radial plasma structure inside the chamber has been probed with moveable Langmuir probes under many conditions. Figs. 3.20, 3.21 and 3.22 are a summary of few interesting cases. The radial profile of plasma density is reported in Fig. 3.20.c, for a case at 15mTorr and 400 Watt of RF power. The profile is peaked at the center of the cylinder. Electron temperature (3.20.d) is lower than inside the source cylinder, being in the 2.5eV - 3.0eV range at the center. The profile of temperature than decreases toward the walls, from 3.0eV down to the 1.0eV range. Plasma potentials are in the range 15-20 Volts. Figure 3.21 shows radial scans at 100W and 15mTorr, for two different magnetic fields at the antenna of 65 and 25 Gauss. The magnetic field was adjusted by moving the permanent magnet along the axis (Fig. 3.21.a and 3.21.b). The plasma density is peaked at the center, where it is in the range 4-5$\times 10^{16}$ m^{-3}, and decreases toward the walls. The electron temperature is always below 2.5eV, with plasma potentials of 15-20V or lower. The magnetic field does not affect neither the absolute value of the plasma density, nor the radial shape of the plasma. Tests reported in Fig. 3.22 show a comparison of downstream profiles for three different magnetic fields of 65, 90 and 140 Gauss. The profiles are always peaked at the center of the discharge. The plasma density is not considerably affected by the value of B. The value of electron temperature and plasma potential are all comparable, within the uncertainties of the measurements.

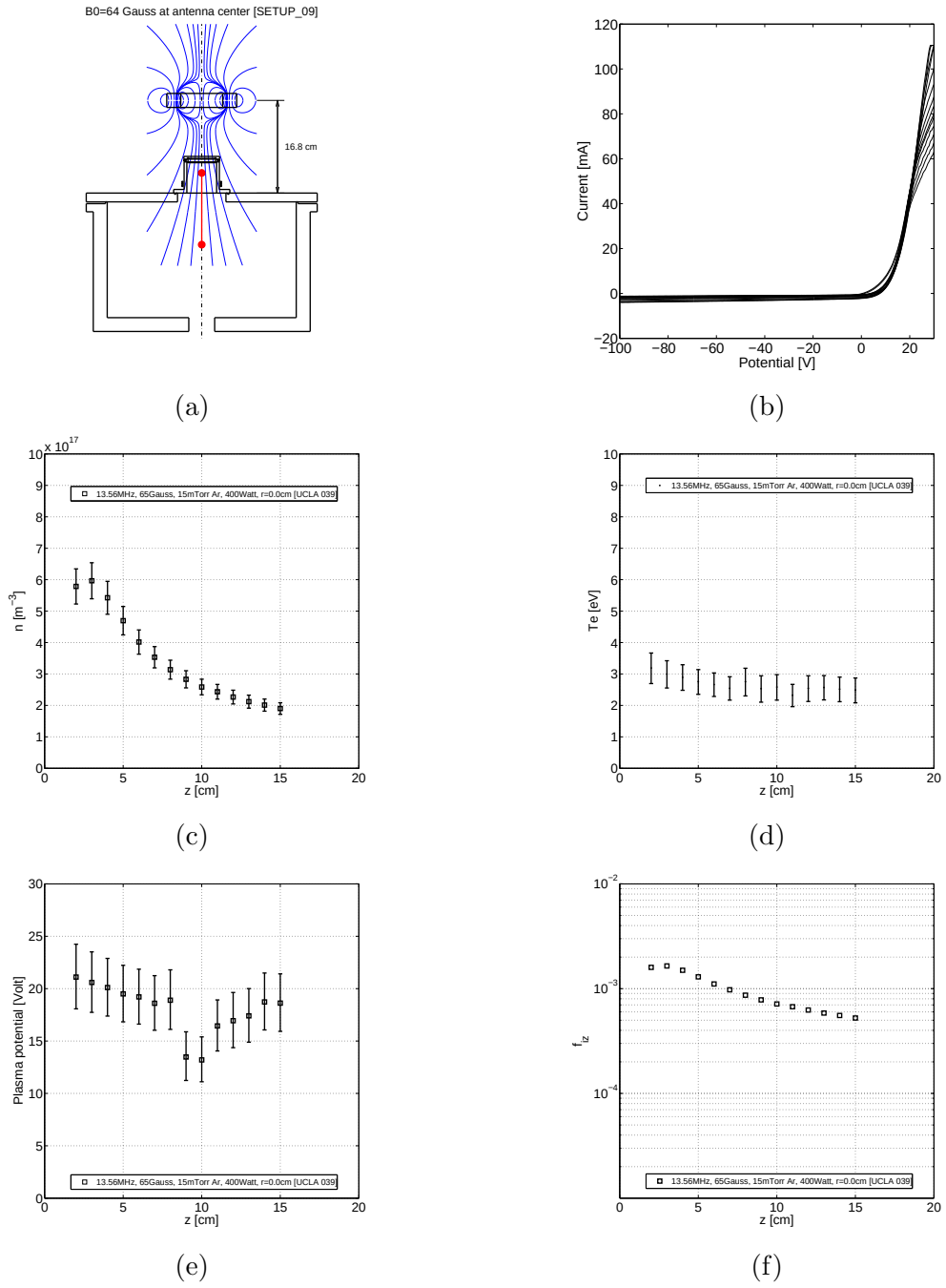

Figure 3.17: Axial scan at 13.56MHz along the cylinder. [res03]

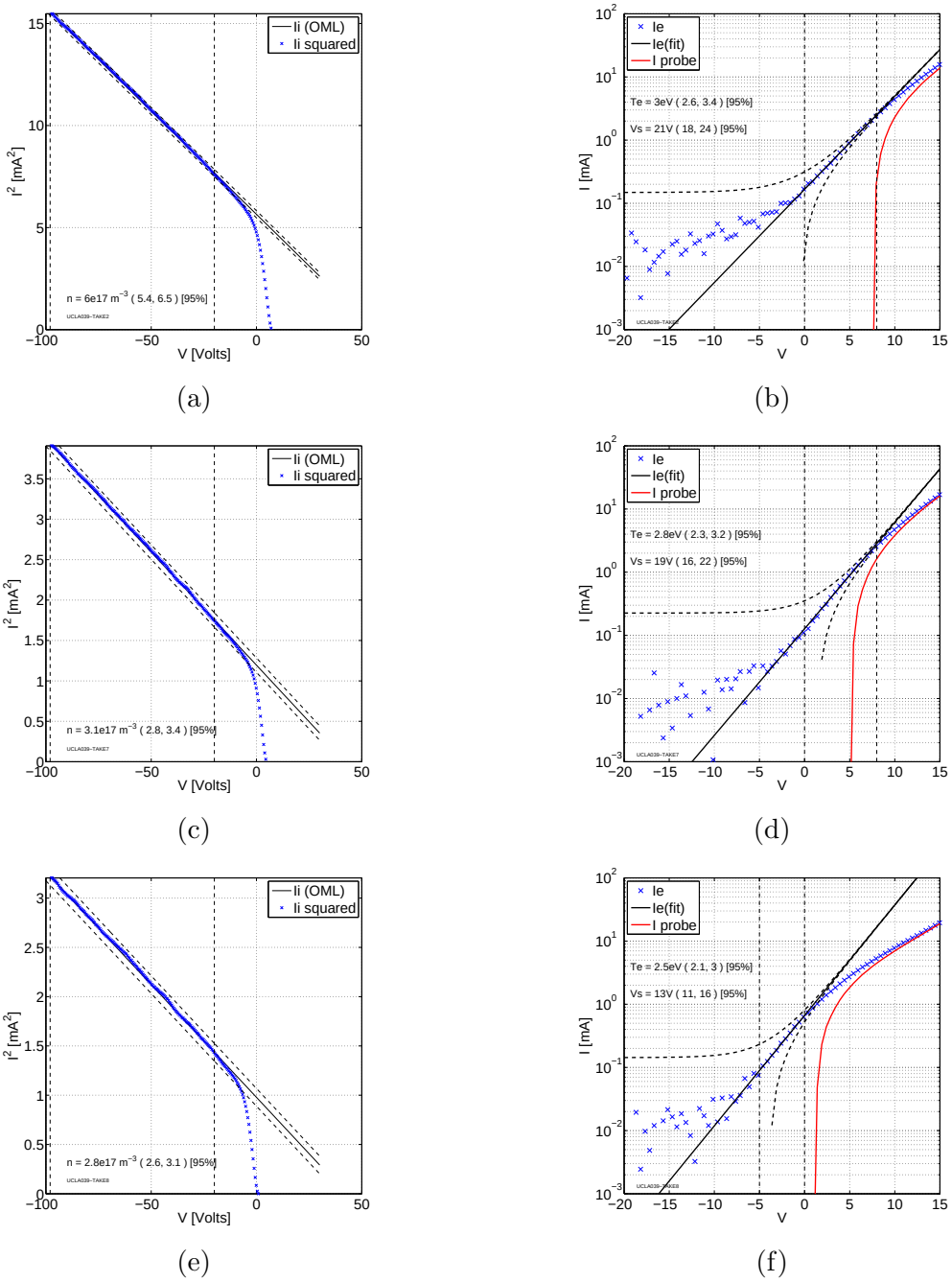

Figure 3.18: Axial scan, ion and electron current fit, at locations $z = 3, 8, 9$ cm respectively [res03]

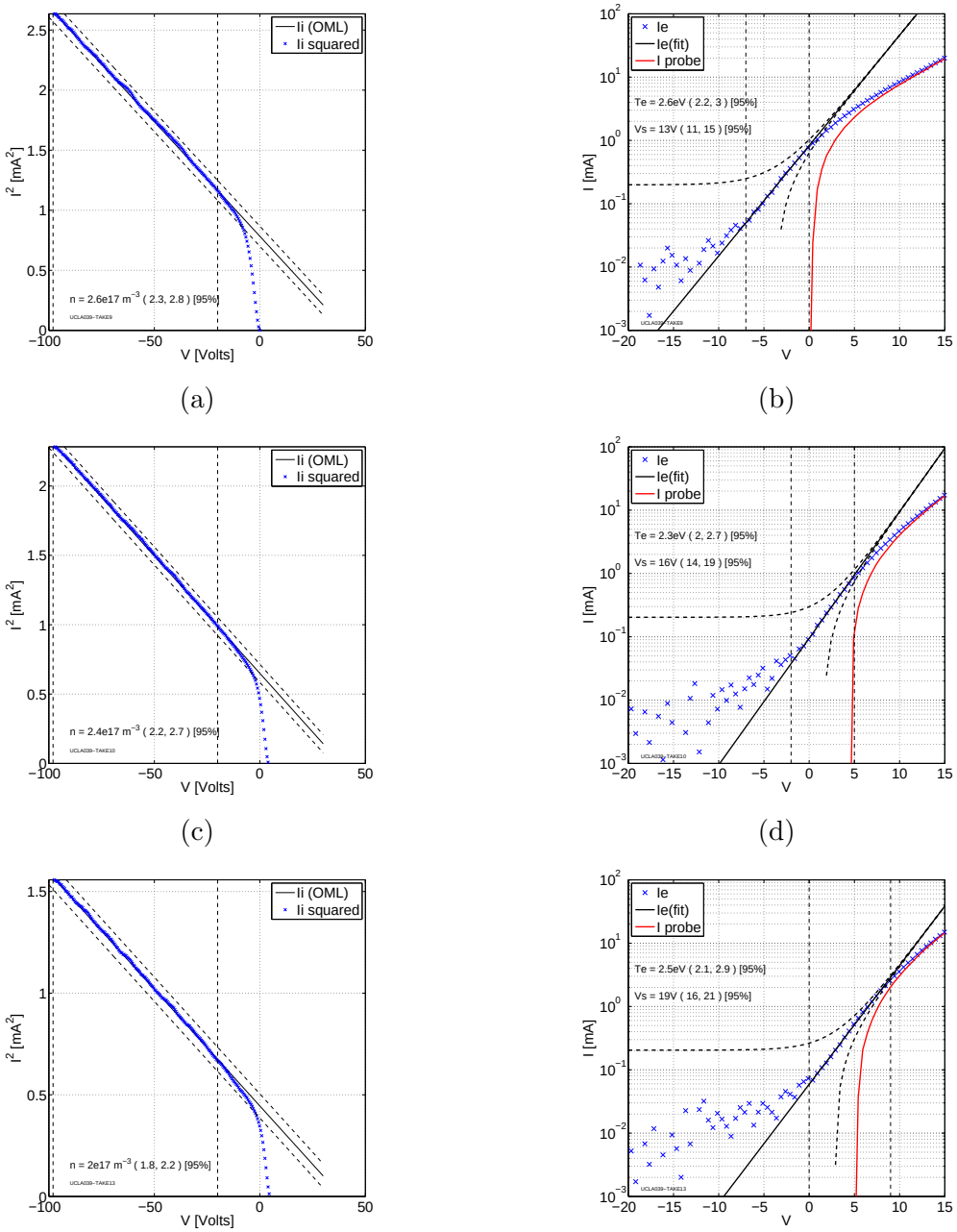

Figure 3.19: Axial scan, ion and electron current fit, at locations $z = 10, 11, 14$ cm respectively [res03]

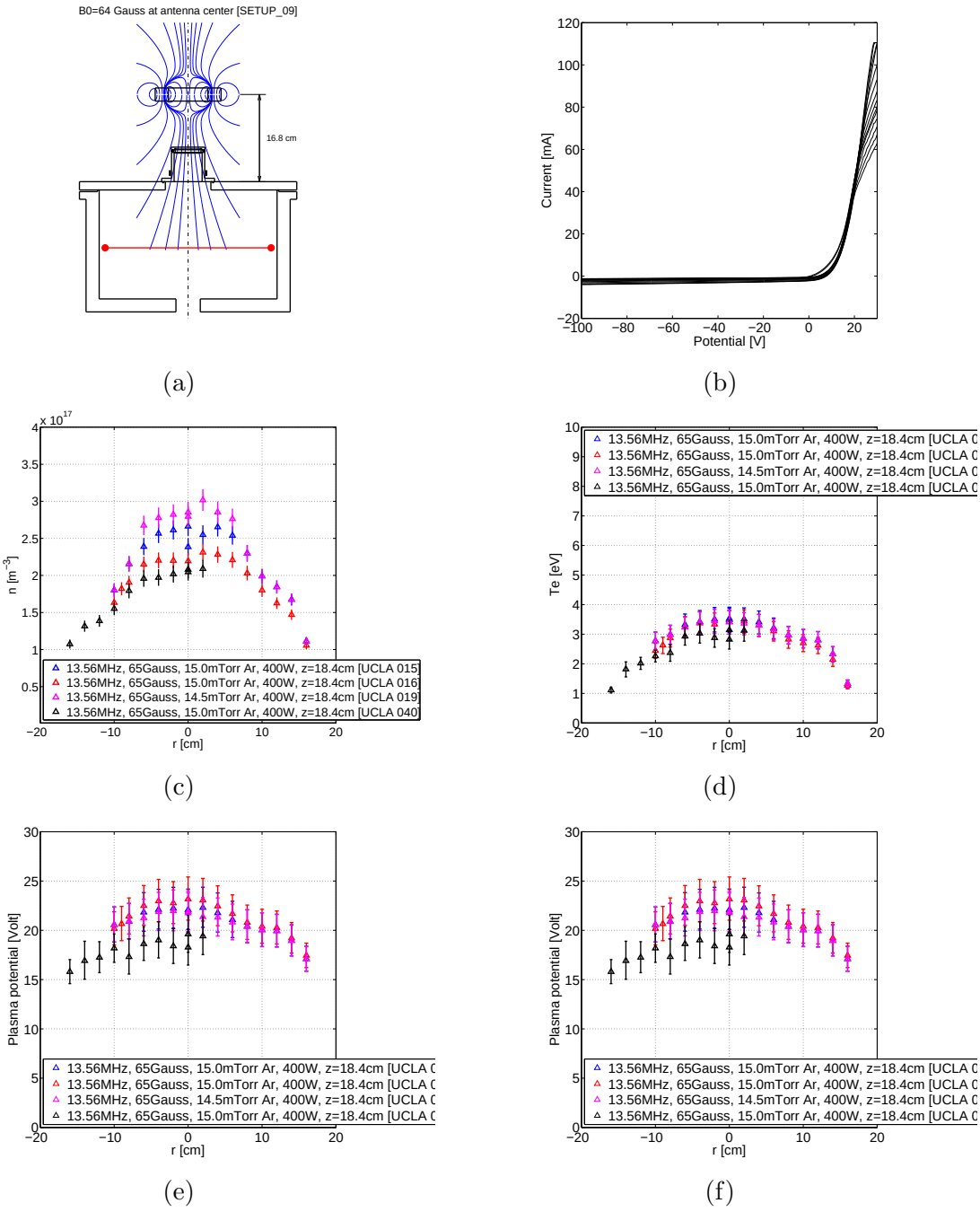

Figure 3.20: Radial scan at 13.56MHz and 400 Watt along the radius of the chamber. [2a]

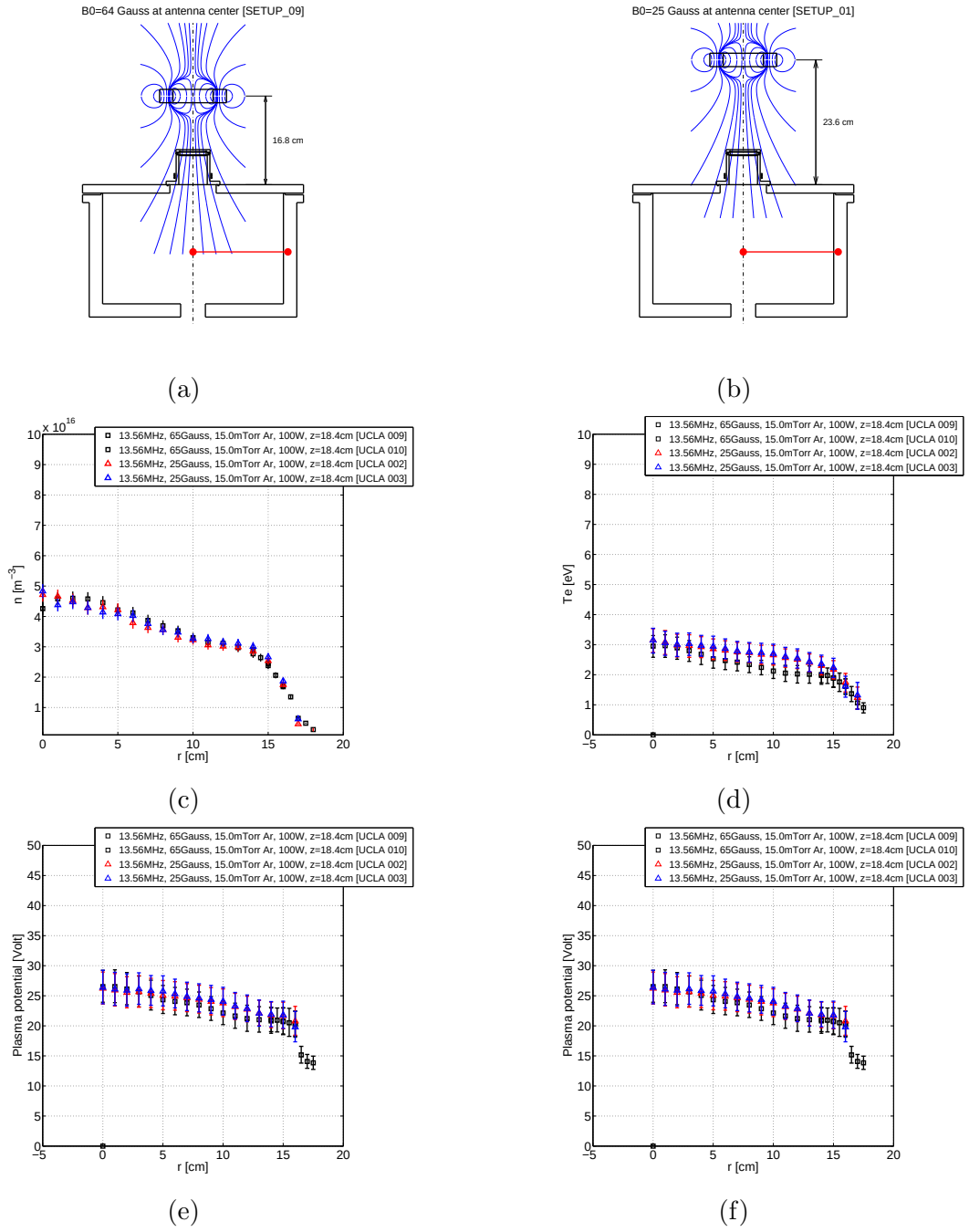

Figure 3.21: Radial scan at 13.56MHz and 400 Watt along the radius of the chamber. [2b]

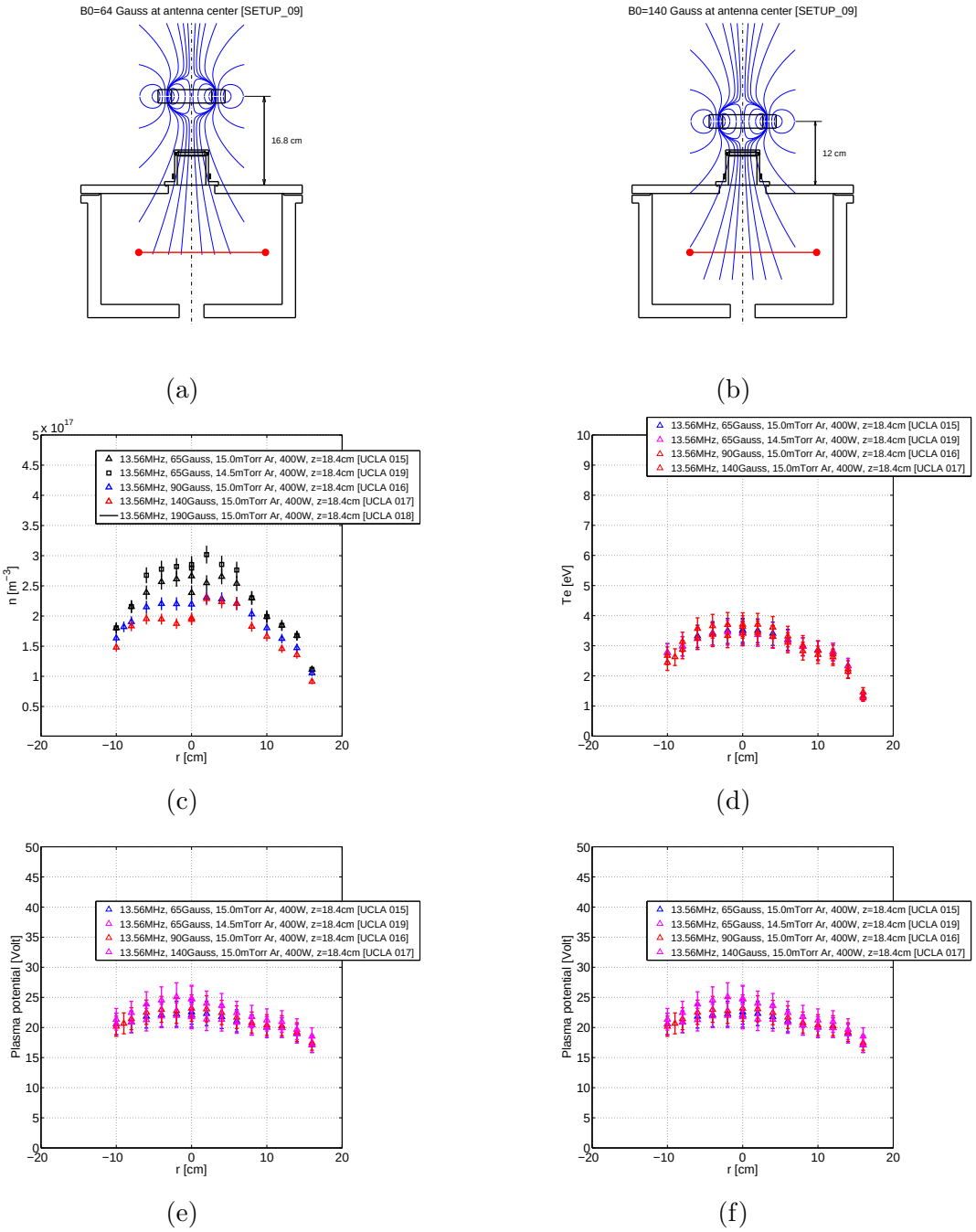

Figure 3.22: Radial scan at 13.56MHz and 400 Watt and several B fields, along the radius of the chamber. [res06]

Power scan at several pressures 13.56MHz, inside the helicon source, 3.23, 3.24, 3.25, 3.26 and 3.27.

Several power scans at different pressures 1.0-20 mTorr have been executed with the Langmuir probe placed at the center of the plasma source. The setup is shown in Fig. 3.23.a, with the probe tip marked with a red dot. Pressures have been chosen within an interesting range of expected performances of a thruster. During the experiments the Argon was flown inside the chamber, and taken to the constant desired pressure. Then the plasma was ignited at the desired power, the matching obtained (with zero-Watt of reflected power), and the acquisition done. The gas pressure wasn't changed until all the interested power range was probed. Figure 3.23 shows few selected cases that allow to understand the main trend of the plasma behavior.

Figure 3.23.a shows the plasma density, as obtained from the fitting of the experimental traces with the OML curve. The 15.0mTorr case (blue measures) is equivalent to the curves reported in Fig. 3.11. When the pressure is decreased to lower values, the absolute value of the plasma density decreases. The plasma density is proportional to the neutral gas pressure. As an example, at 300Watt, a density around 6×10^{17} m^{-3} with 15 mTorr of gas can be achieved, against a density of around 2.5×10^{17} m^{-3} with a density of the neutral gas 5 times less at 3.0mTorr of neutral gas. However, at lower pressures the source is actually working at higher ionization fractions, i.e. it is more efficient. This can be seen from Fig. 3.23.f, where the ionization fraction has been estimated as the ratio between the calculated plasma density and the number density of the neutral gas assuming a temperature of 400K. The ionization fraction at lower pressures (ex. 3.0 mTorr) is higher than at higher pressures. The mechanism of higher ionization efficiency can be explained considering the behavior of electrons at low pressures.

Figure 3.23.d show the calculated Maxwellian temperature of electrons, as estimated from the data of electronic currents. The collision-dominated behavior of the 15.0mTorr presented in Fig. 3.23.d gradually shifts towards a collisionless domain. At lower pressures electrons have more inter-collisional space to be heated by the RF electric field, and their temperature can increase. At higher T_e their ionization cross-section increases, and consequently the ionization fraction increases too, as obtained in Fig. 3.23.f.

The detailed analysis of electronic currents curves reveals even more interesting features at low pressures (Figs. 3.24, 3.25, 3.26 and 3.27). At 10.0 mTorr and with a low power of 50 Watt, Fig. 3.24.a-b, the ions behavior is well approximated by the OML theoretical prediction; electrons are Maxwellian and at temperatures around 4eVs. When the power is increased, ions are still OML-like, and electrons are still approximated by a Maxwellian at 4eVs. An exception has been observed in the low-medium 80-100 Watt range, where higher T_e and plasma potential have been encountered (Figs. 3.24.c-d). At 7.5 mTorr (1 Pascal) of Argon pressure, Fig. 3.25 the electron current is fitted by Maxwellians at higher temperatures (Fig. 3.25.b-d-f). When the pressure is further reduced, down to 5.0 mTorr (Fig. 3.26) and 3.0 mTorr (Fig. 3.27), the electron temperature is increased

up to the 10 eV range. At such low pressures, an influence of the intensity of the RF field on the ion currents was observed. See for example Fig. 3.27, where the 3.0 mTorr case is reported. At low powers of 50 Watt, the ion current can still be fitted by the ionic OML curve; when the power is increased the OML-like behavior is gradually lost, as reported for example in Fig. 3.27.e. In this regime of low pressure and high powers, despite electrons are still Maxwellian inside the uncertainty of the probe (Fig. 3.27.f), the plasma potential shifts upward to 70-80 Volts (4 times than usual), and kinetic effects on ions might become relevant. In this regime, the OML fit appears only as a theoretical limit. Ions might be influenced by the higher plasma potential, and plausible conditions for an efficient acceleration are encountered. This regime appears to be an interesting regime for an helicon thruster to operate.

Pressure scan at low-powers 13.56MHz, inside the helicon source, Figs.3.28, 3.29 and 3.30; wave-heating cut-off

In order to investigate the feasibility of an helicon ambipolar accelerator in the low-power range of 50-150 Watt, a pressure scan inside the helicon source was made, Fig. 3.28. This test differs from the previously described for the following reason. Here the power is maintained at a fixed level, and the chamber pressure is varied, instead of vice-versa. Three power levels have been chosen, equal to 50, 100 and 150 Watt. Figure 3.28.c shows the resulting plasma density, 3.28.d the electron temperature, 3.28.e the plasma potential, and the estimate of the ionization fraction 3.28.f. Tests were possible in the range 1.5-15.0 mTorr. At lower pressure the helicon discharge was at its cut-off, that is only a glow-discharge was possible. Electron temperatures of the order of 10eVs has been encountered in the 1.0 mTorr range. The plots of electron currents are reported in Fig. 3.29 and Fig. 3.30, showing the increase of electron temperature. Ions behave OML-like at the upper range of pressures, and then they gradually departs from the OML line, especially at the region of IV transition, when the pressure is decreased. At very low pressures and near the wave-heating cut-off, i.e. slightly above $\approx$ 1.5 mTorr, the electron behavior is strongly related to pressure (Fig. 3.30), insomuch as variations of $\pm$0.1 mTorrs in pressures (Fig. 3.30) involve variations of 1-2eVs in T_e. Despite this regime looks favorable for an appropriate acceleration of ions in an helicon thrusters, the sensitivity of T_e to the pressure is too high, and this might introduce problems in the thruster development, like strict requirements in the pressure/mass-flow control system.

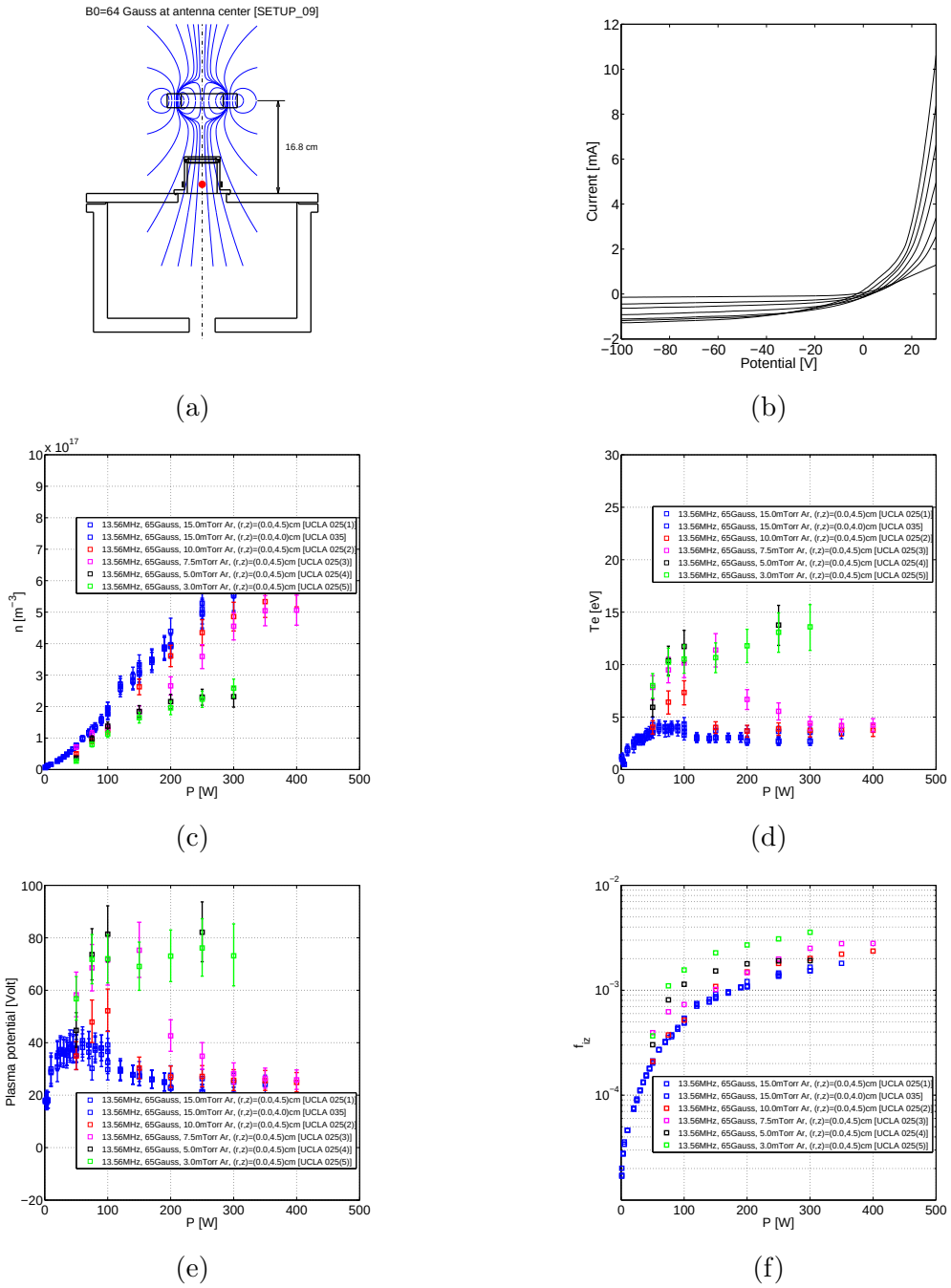

Figure 3.23: Power scan at several pressures (a) experimental setup, with the Langmuir probe position marked with a red dot; (b) experimental IV traces at 3.0mTorr; (c) plasma density vs. power; (d) electron temperature vs. power; (e) plasma potential vs. power; (f) estimate of the ioniation fraction. [4a]

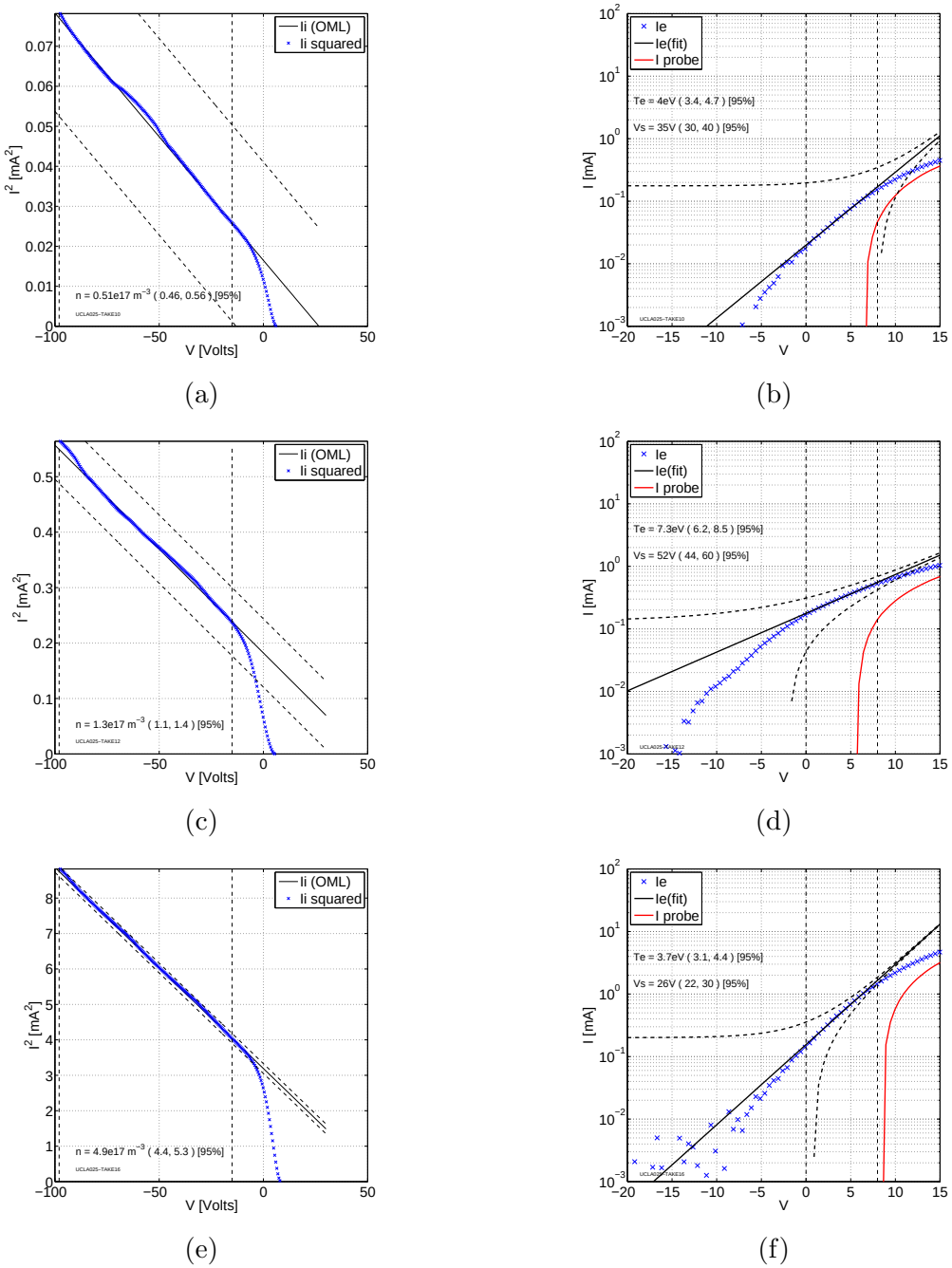

Figure 3.24: Ion and electron fit at 10.0 mTorr for powers of (a) (b) 50 Watt, (c) (d) 100 Watt, (e) (f) 300 Watt [res4a]

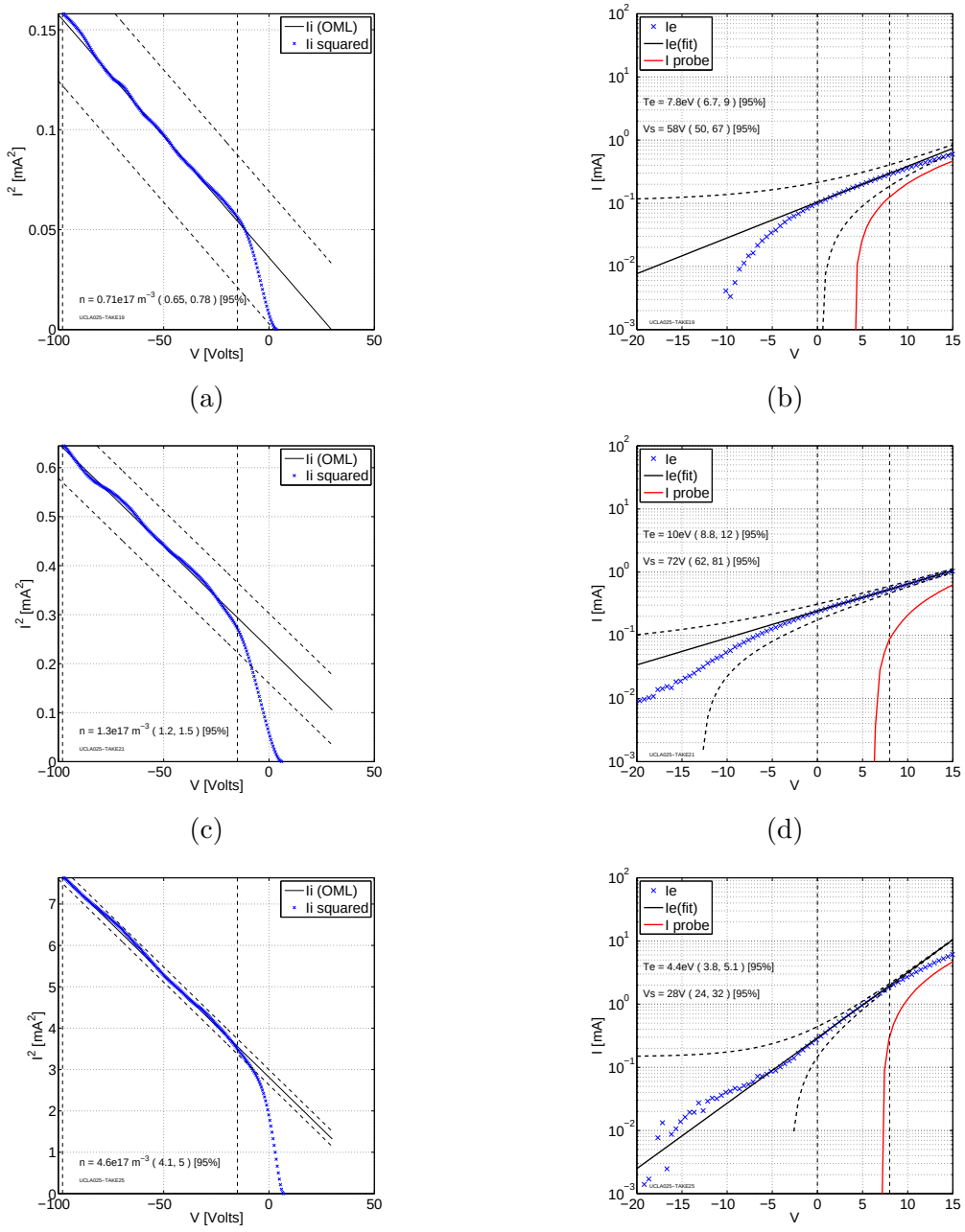

Figure 3.25: Ion and electron fit at 7.5 mTorr for powers of (a) (b) 50 Watt, (c) (d) 100 Watt, (e) (f) 300 Watt [res4a]

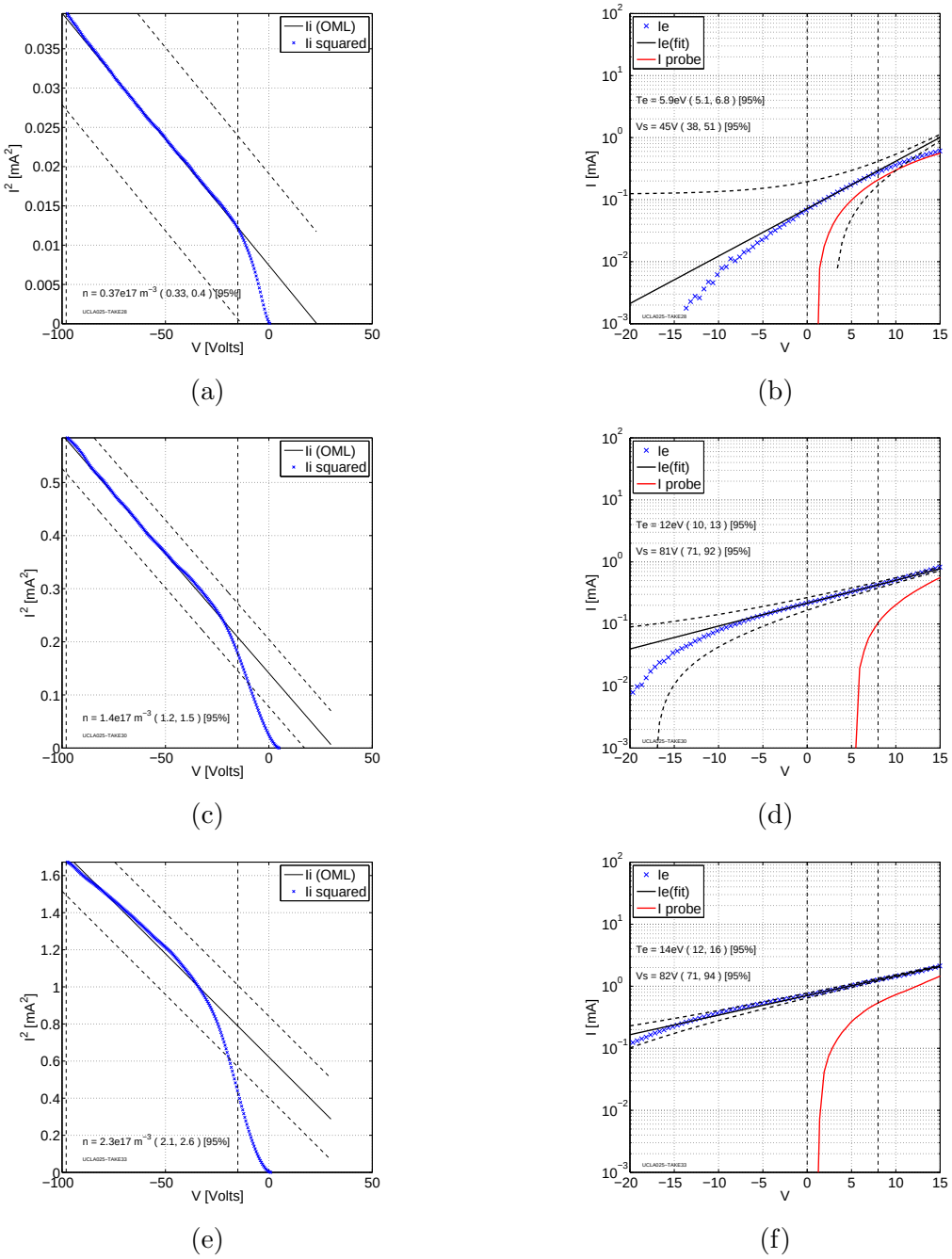

Figure 3.26: Ion and electron fit at 5.0 mTorr for powers of (a) (b) 50 Watt, (c) (d) 100 Watt, (e) (f) 250 Watt [res4a]

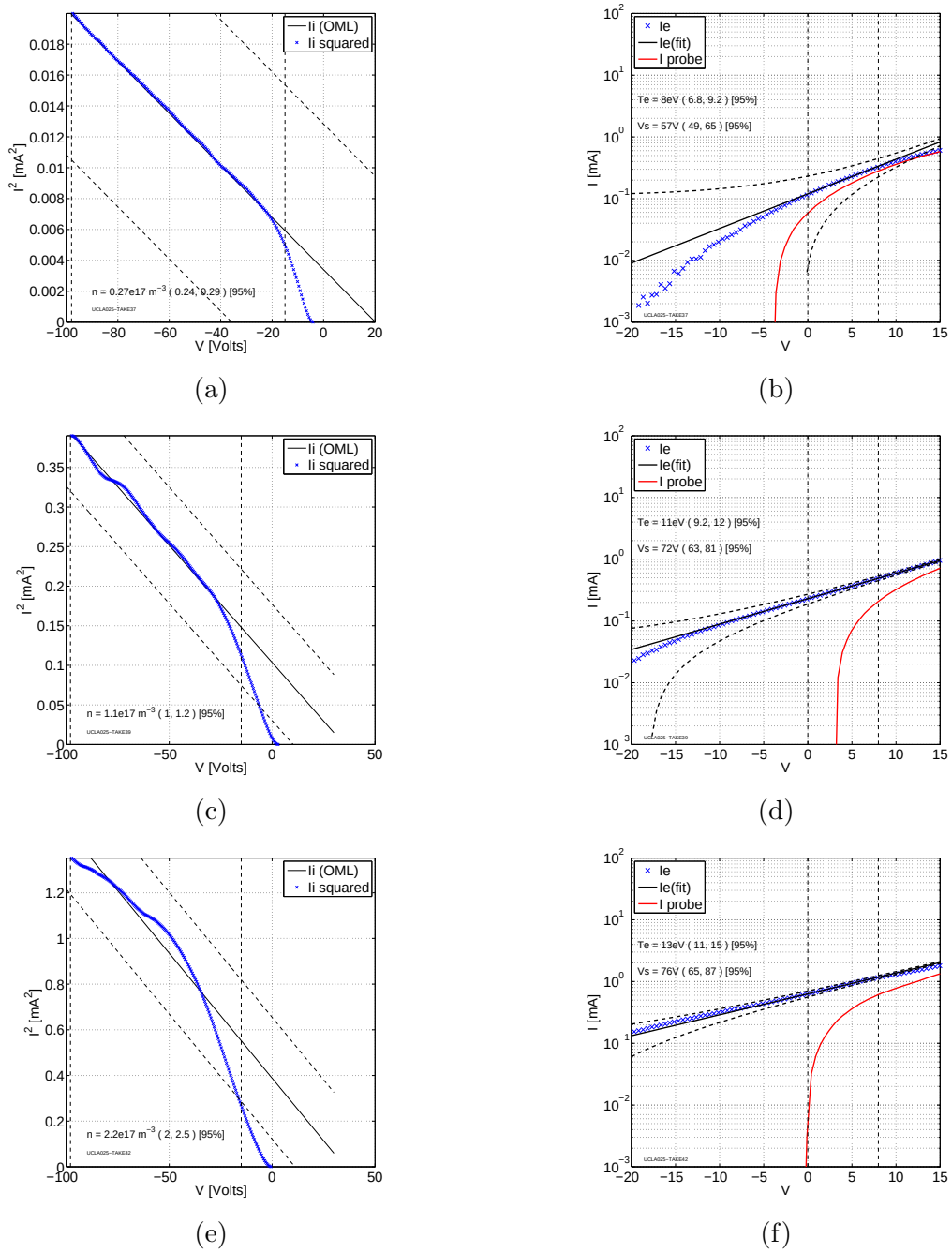

Figure 3.27: Ion and electron fit at 3.0 mTorr for powers of (a) (b) 50 Watt, (c) (d) 100 Watt, (e) (f) 250 Watt [res4a]

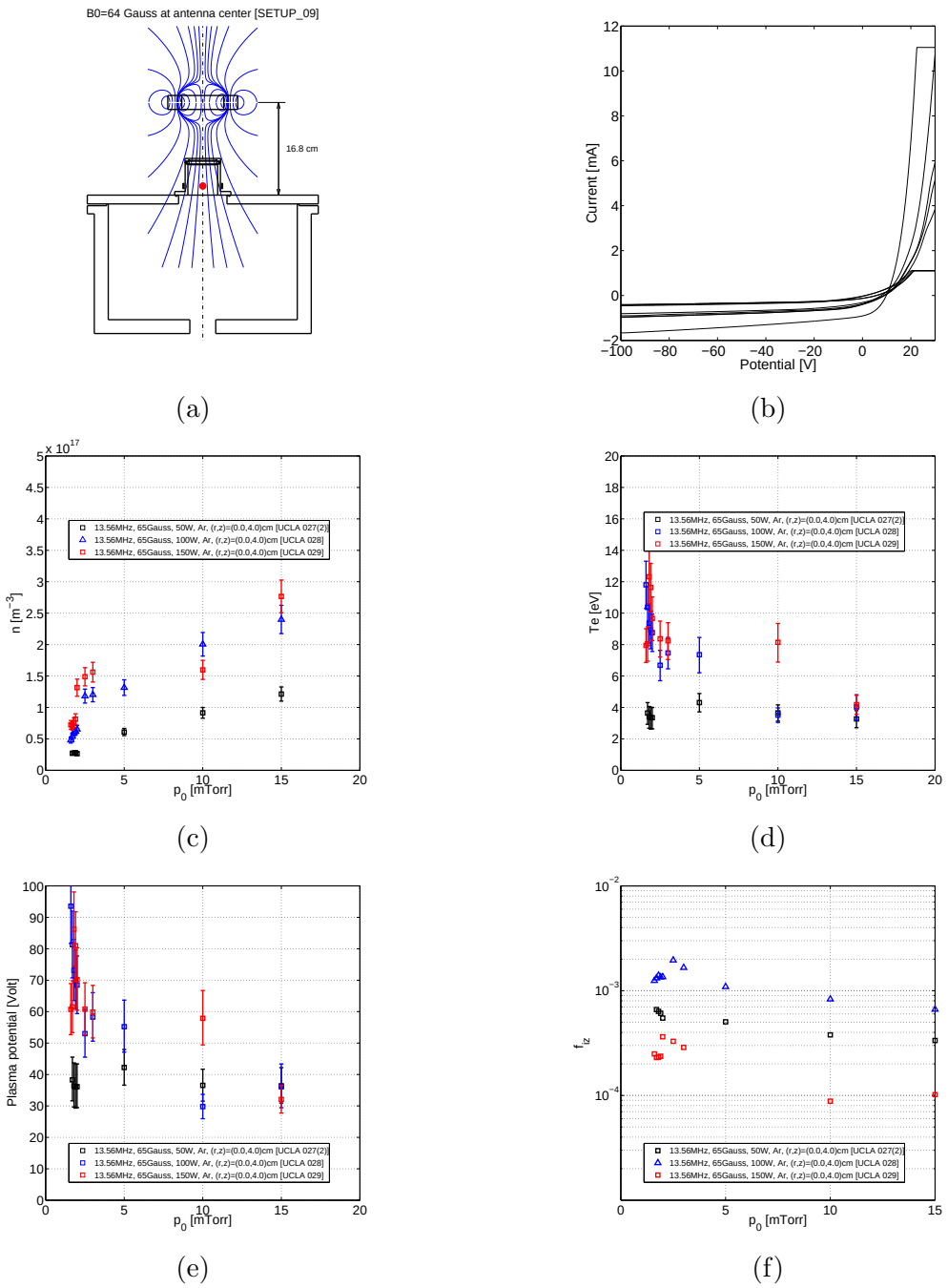

Figure 3.28: Pressure scan at low-power, inside the helicon source, (a) experimental setup, with the Langmuir probe position marked with a red dot; (b) experimental IV traces at 150 Watt; (c) plasma density vs. power; (d) electron temperature vs. power; (e) plasma potential vs. power; (f) estimate of the ioniation fraction. [4b]

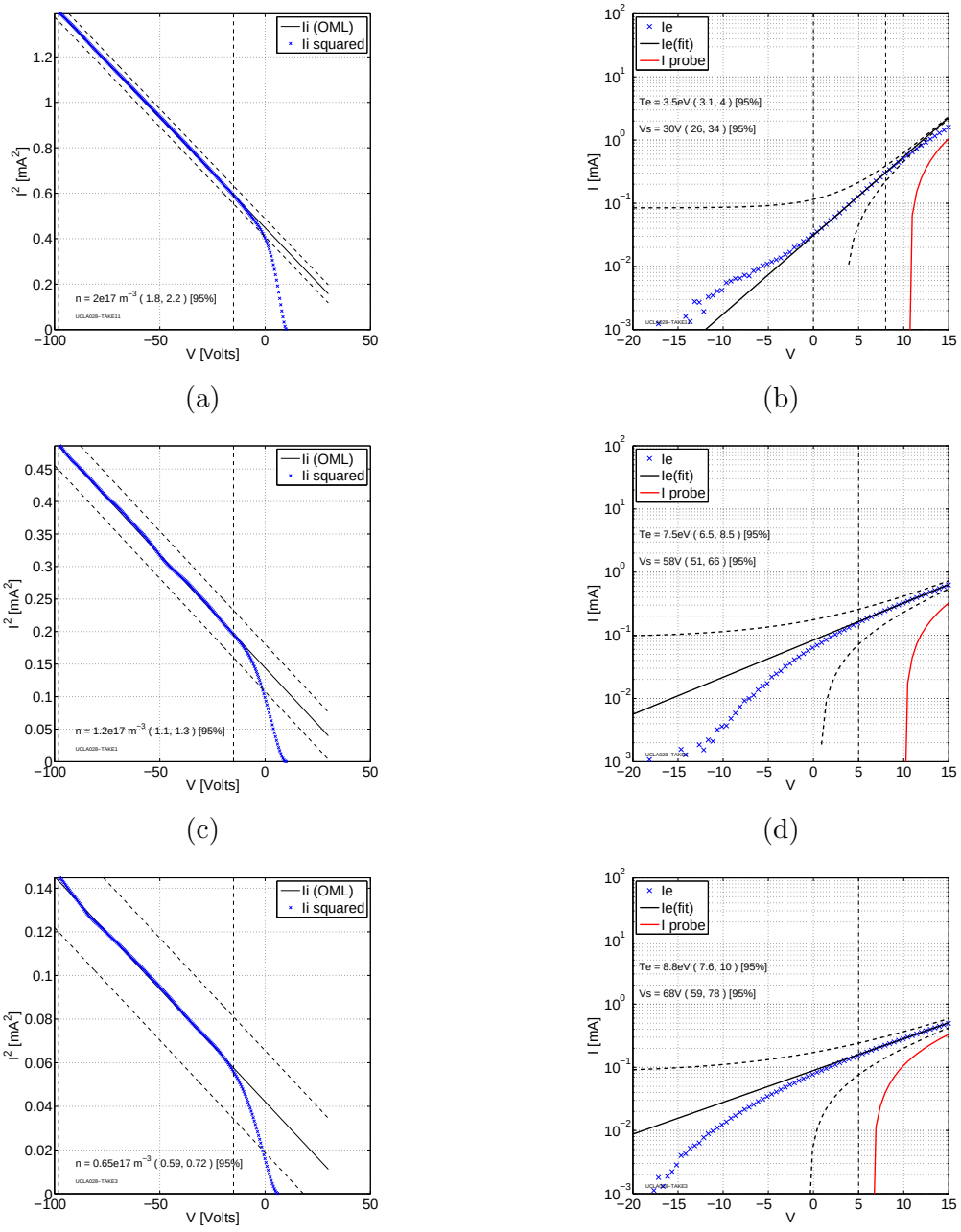

Figure 3.29: Ion and electron current fit (100 Watt RF power) of (a) 10 mTorr; (b) 3.0 mTorr; (c) 2.0 mTorr [res4b]

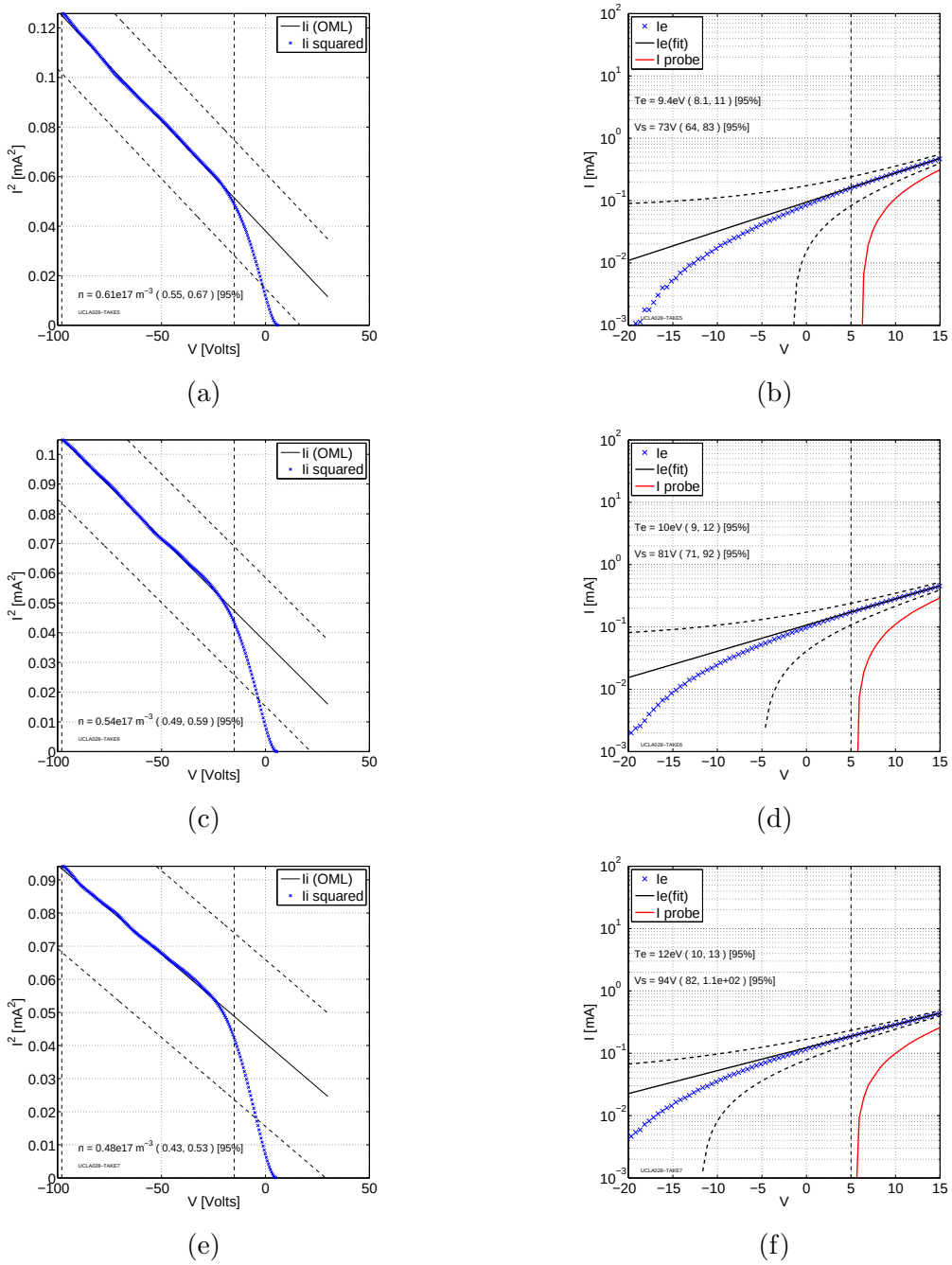

Figure 3.30: Ion and electron current fit (100 Watt RF power) of (a) 1.8 mTorr; (b) 1.7 mTorr; (c) 1.6 mTorr [res4b]

Tests at 27.12MHz, Figs.3.31, 3.32 and 3.32

The same tests done up to here were repeated in a second independent vacuum chamber, similar in size and geometry, but using a 27.12MHz RF generator instead of the 13.56MHz. For brevity, here we will show only few results of this second set of experiments.

Figure 3.31 shows the power scan for a fixed pressure of 15.0 mTorr. Langmuir probe takes were taken inside the helicon source, at a position marked with the red dot in Fig. 3.31.a. All the plasma parameters (ion density, electron temperature, plasma potential, ionization fraction) are in the same range and with a similar trend to the 13.56MHz. No noticeable variations was observed.

Figure 3.32 and Figure 3.33 show the spatial structure of the 27.12MHz plasma, being the axial and the radial scan respectively. Here some differences appear. No potential drop occurs at 27.12 MHz (Fig. 3.32.e), and as a consequence the topology of ion density and electron temperature along the axis results to be different. However, the absolute values occurs in the same range as the 13.56MHz case, with no other drastic change imputable to the doubled frequency than the absence of the potential drop at the exit of the Pyrex tube. The radial structure of the plasma along the radius of the 27.12MHz discharge is reported in Fig. 3.33, exhibiting a triangular profile. Electron temperatures are in the < 2eV range, and plasma potentials occur in the < 15Volt range.

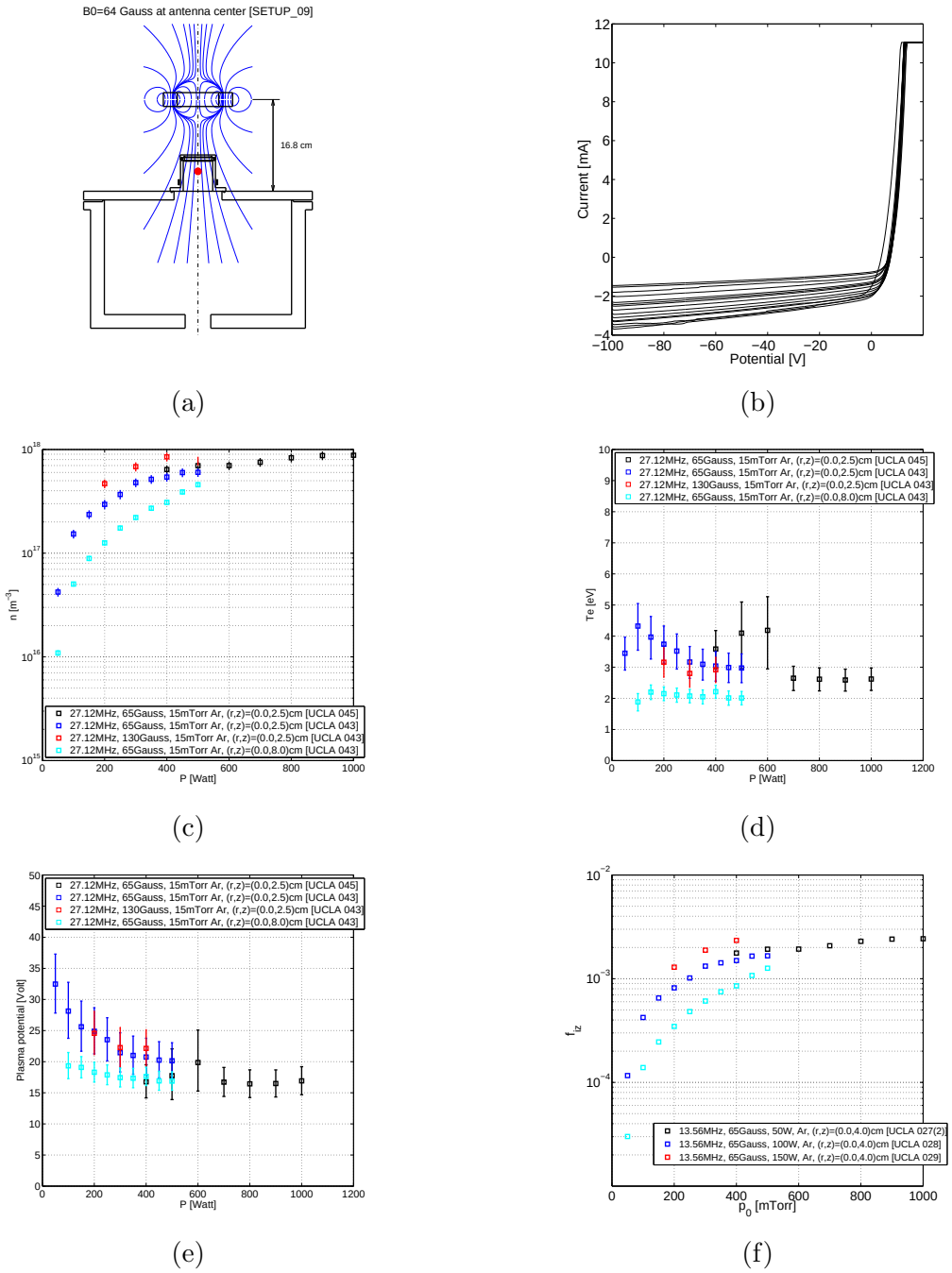

Figure 3.31: Power scan at 27.12MHz and for a fixed pressure of 15.0mTorr, inside the helicon source, (a) experimental setup, with the Langmuir probe position marked with a red dot; (b) experimental IV traces for increasing power levels; (c) plasma density vs. power; (d) electron temperature vs. power; (e) plasma potential vs. power; (f) estimate of the ioniation fraction. [res07]

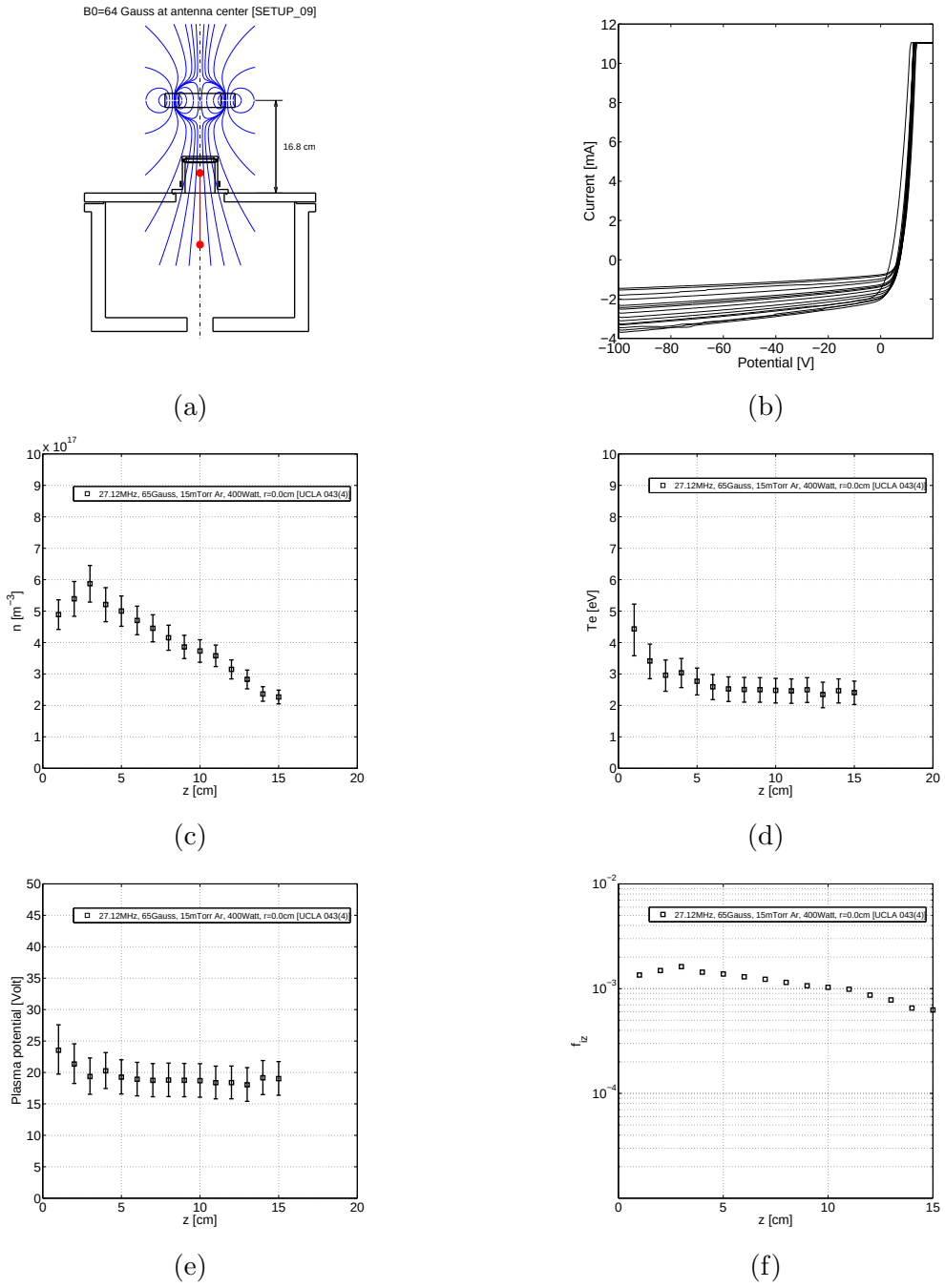

Figure 3.32: Axial scan at 27.12MHz and 400 Watt along the cylinder. [res09]

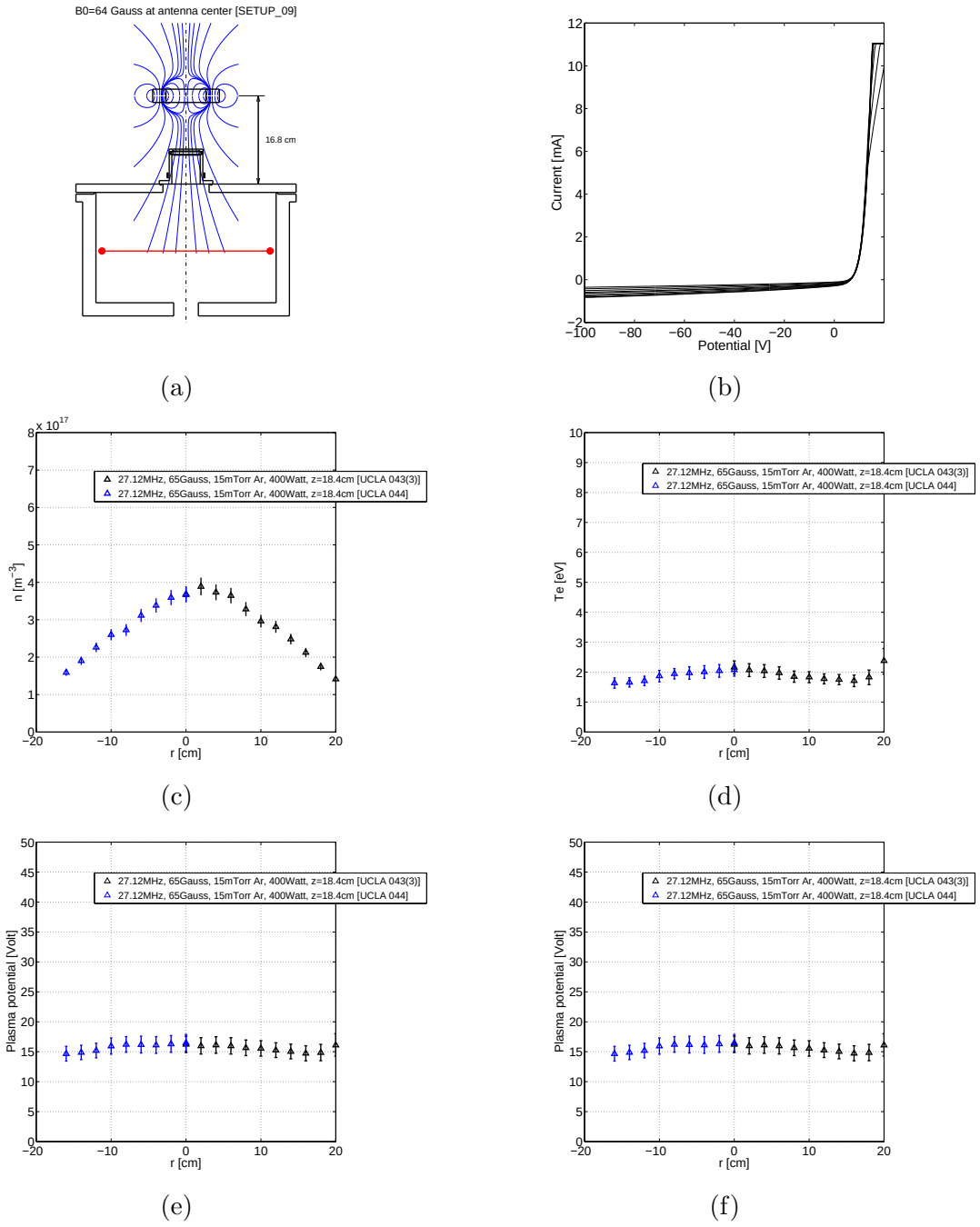

Figure 3.33: Radial scan at 27.12MHz and 400 Watt along the radius of the chamber. [res08]

Tests with the small diameter source, Figs. 3.34 and 3.35

As a conclusive appendix to the experimental tests, a smaller Pyrex source of 19mm of inner diameter and 180mm long was tested. The source is depicted in Fig. 3.34.a. The gas was fed from a 12mm-ID aperture (at the right in the Figure), flown inside the tube, and released outward after an expansion bell of 51mm ID (at the left on the Figure). The plasma reaction chamber, 180mm long, was wrapped with a Boswell-typ antenna and fed with RF power at 27.12MHz. The permanent magnet was placed around the plasma reaction chamber with its center at 120mm from the the gas inlet. In this configuration the maximum B-field of approximatively 1000 Gauss occurs at the beginning of the plasma reaction chamber, and the magnetostatic cusp of the permanent magnet occurs inside the reaction chamber. Despite a perfect matching was not expected due to plasma instabilities and turbulence, the matching was always possible with reflected power less than 1%. Thanks to the axial dynamics of this elongated source, the plasma density is expected to be maximum at the end of the reaction chamber. There a lateral aperture was made in order to host a Langmuir probe.

Figures 3.34.b shows the IV traces taken at powers of 100, 200 and 300 Watts. Unfortunately during this experiment the gas pressure was monitored only with the Convectron, and not as usual with the Baratron. As a consequence, the gas pressure is know with an uncertainty much higher than before, 15 ± 5mTorr, instead that ± 50.1mTorr. The resulting plasma density occurs in the range 1-4$\times 10^{17}$ m^{-3} (Fig. 3.34.c). Electron temperature are comprised 3.5-4.5eVs (Fig. 3.34.d), with plasma potentials unexpectedly high in the range 35-45Volts (Fig. 3.34.e). The test has given a first indication that sources of smaller diameter allows to deal with higher power densities, higher electron temperature and higher plasma potentials, all favorable features for low-power thrusters. Ion and electron fits are finally shown in Fig. 3.35.

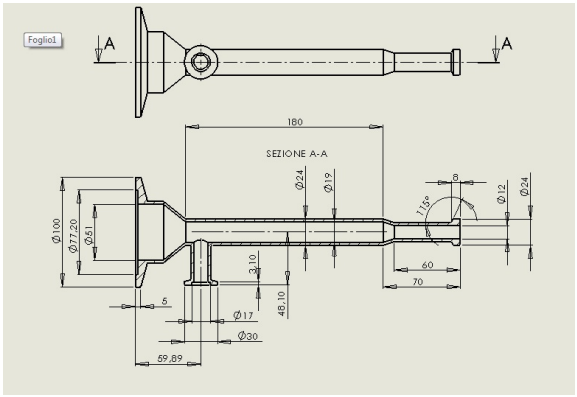

(a)

(b)

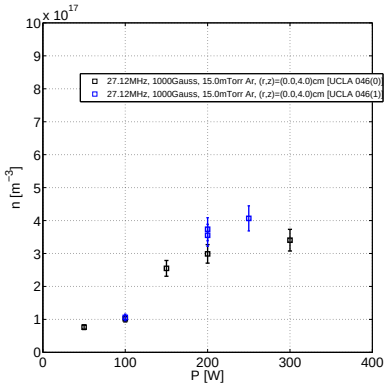

(c)

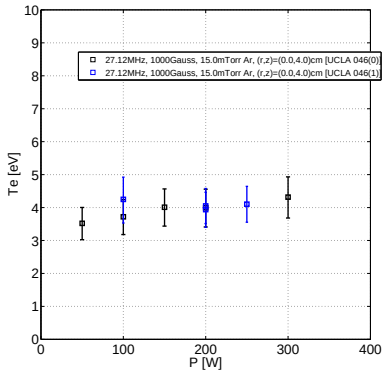

(d)

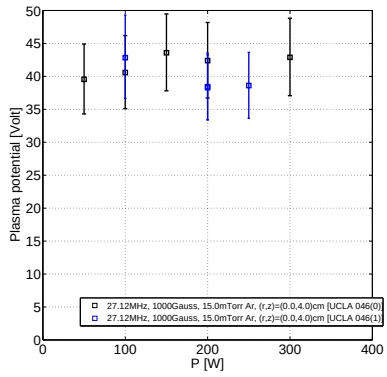

(e)

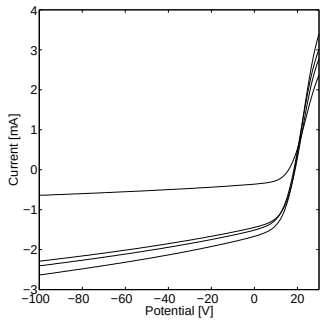

(f)

Figure 3.34: Tests on the 2-cm inner diameter source, 27.12MHz, $B = (1000 \pm 100)$ Gauss, $p_0 = (10 \pm 5)$ mTorr (a) design of the tube, with the Langmuir probe entrance on its side; (b) photo of the experimental apparatus; (c) plasma density vs. power; (d) electron temperature vs. power; (e) plasma potential vs. power; (f) experimental IV traces for increasing power levels. [res12]

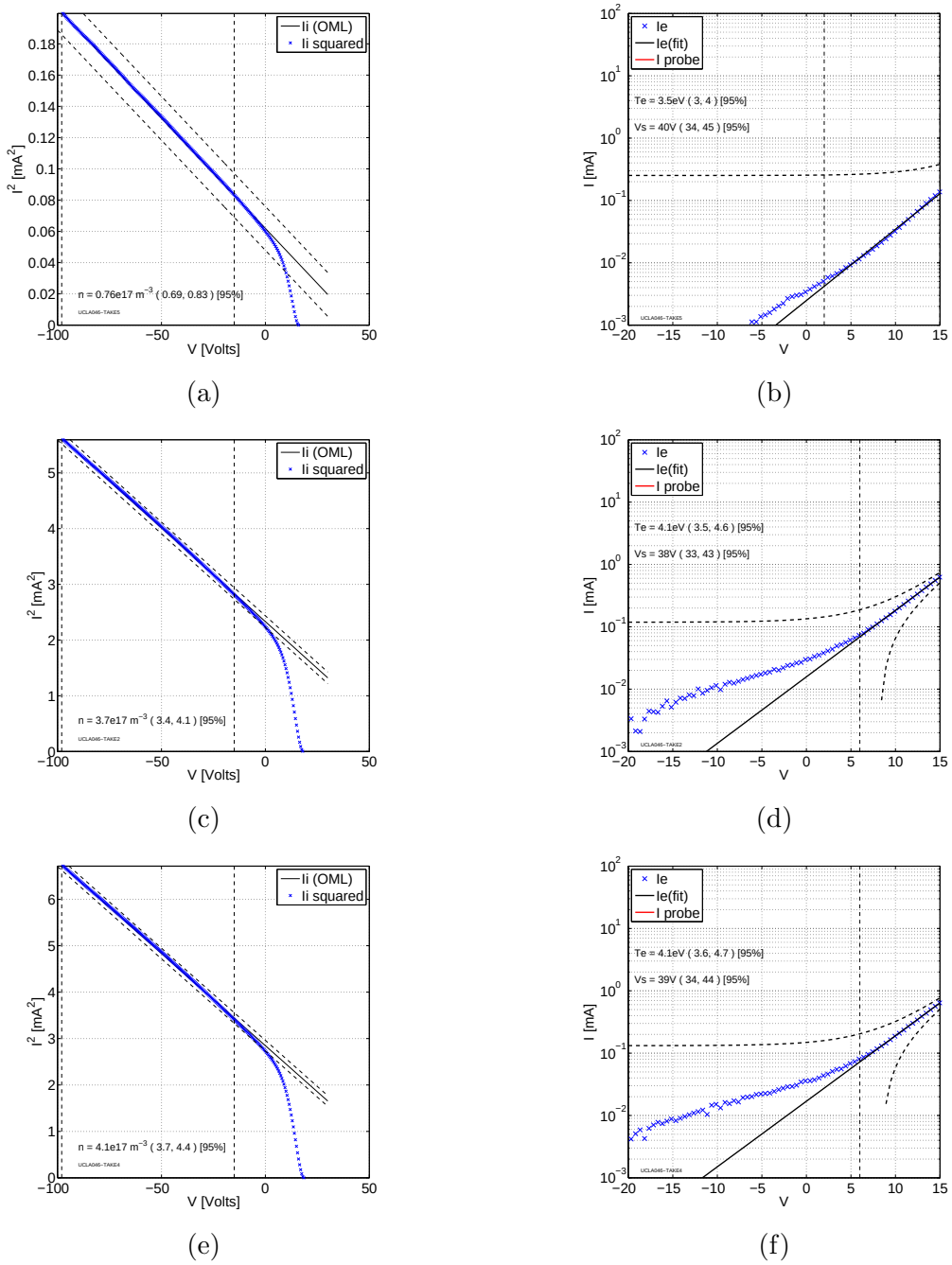

Figure 3.35: Ion and electron current fit (a) 100Watt; (b) 200Watt; (c) 250Watt [res12]

3.4 Comparison of experimental data with theory and discussion

The main features observed from the measurements can be predicted using the theory and the HELIC-EQM code. In this section a comparison of the code calculations with the experimental data is reported.

The power scan of Fig. 3.11 has been reproduced numerically with HELIC-EQM, in order to validate and calibrate the model. The reference conditions were the following. The discharge radius was set equal to the Pyrex tube inner diameter, $a = 2.5$ cm, and filled with 15.0 mTorr of Argon. A loop antenna ($m = 0$) at 13.56 MHz was placed at radius $b = 3.3$ cm, and 5 cm far from the metallic backplate closing the end-wall of the cylinder. The magnetostatic field was assumed constant and equal to the measured field at the antenna center, 65 Gauss. The input power was set to the desired value, for example 200 Watt, and then the two codes HELIC and EQM were iterated together. The initial guess was assumed equal to uniform profiles along the radius. The iterative process converges toward the equilibrium solution of the plasma column, as forced by the deposition of power from the RF wave.

Figures 3.36 shows the comparison between the measured and calculated plasma densities, in the range $100 < P_{RF} < 400$ Watt. The range of code uncertainties has been calibrated as a function of the axial extension of power deposition L_z. The values of L_z are found to be in agreement with the axial integral $P(z)$ of power deposition along the zeta-axis, within a range $L_z = 20 \pm 5$ cm; $P(z)$s are reported in Fig. 3.37.

The values of electron temperatures at the center of cylinder radius are shown in Fig. 3.38, where the experimental and calculated values are compared. Values are in agreement within the considered power range $100 < P_{RF} < 400$ Watt.

The profiles at convergence for one case with $P_{RF} = 200$ Watt are shown in Fig. 3.39. The profile of power deposition $P(r)$ shows that the RF power is deposited mostly on the external layer of the cylinder. This is due mostly thanks to the TG mode, which is rapidly absorbed near the boundary. Another fraction of the power is absorbed at the center of the discharge, thanks to the Helicon mode. The low magnetic field of 65 Gauss takes the two radial modes close together in the modal space. At the center of the discharge the plasma density is 4.2×10^{17} m^{-3}, and with a B = 65 Gauss the allowed radial modes have a wavelength of 5.2 cm at $k = k_{min} = 18.2$ rad/m, and 1.5cm$< \lambda <$18 cm at $k = k_{max} = 34.6$ rad/m. At the boundary of the discharge the allowed k modes are in the range of $12 < k < 23$ rad/m, with longer Helicons but shorter TG modes. The H mode at the center of the discharge is compatible with its radius, and in fact the helicon deposition is activated in this case. The $\vec{B}, \vec{E}, \vec{J}$ fields are shown in Fig.3.39, where the features of the H and TG modes can be recognized. The long-wavelength H mode, well visible on B_r, propagates until the center of the discharge; the short-wavelength TG mode is absorbed at the boundary instead. The TG mode can be appreciated almost on all the

fields components except on E_ϕ. The power is then deposited into the column as $\vec{E}^* \cdot \vec{J}$. The peculiar deposition affects macroscopically the equilibrium of the discharge. More plasma is created at the boundary, and the resulting profile of plasma density $n(r)$ is as reported in Fig. 3.39. The quasineutral region of the plasma exhibits a potential drop of -3 Volts; the plasma is electropositive, with $\phi = 0$ at the center of the cylinder. Summing the sheath potential of 14 Volt (calculated with the 1D radial pic, shown in Fig.2.18), the total expected plasma potential is of the order of ≈17 Volt. The measured potential at 200 Watt (Fig. 3.13.b) is equal to 20V (17.5, 23) [95%]. The pressure is only slightly depleted at the center of the cylinder, as shown by p [mTorr] in Fig. 3.39. The electron temperature occurs in a range between 2.7 and 3.8 eVs, with some heating near the boundary due to greater deposition at that location.

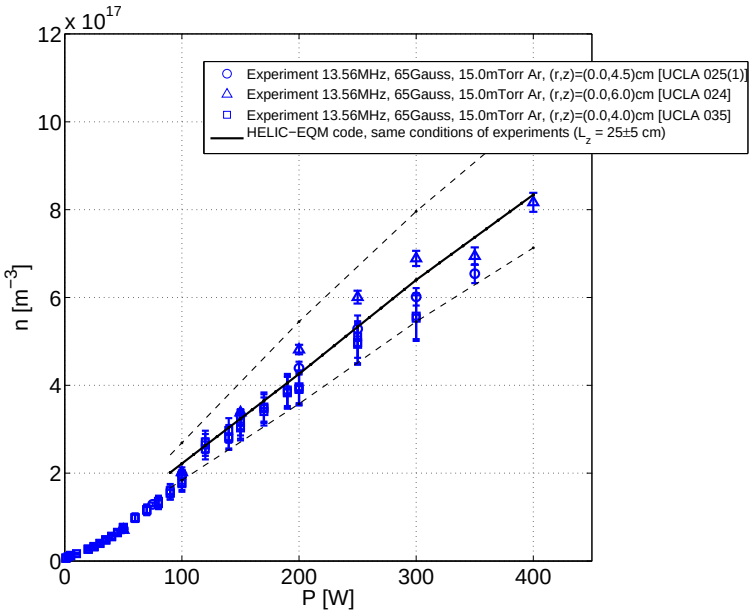

Figure 3.36: Comparison of measured plasma density with the values calculated by the HELIC-EQM code, as a function of RF input power.

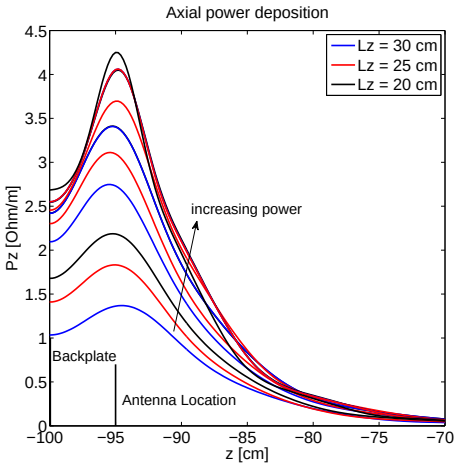

Figure 3.37: Axial power deposition along the axis of the cylinder, obtained from HELIC-EQM.

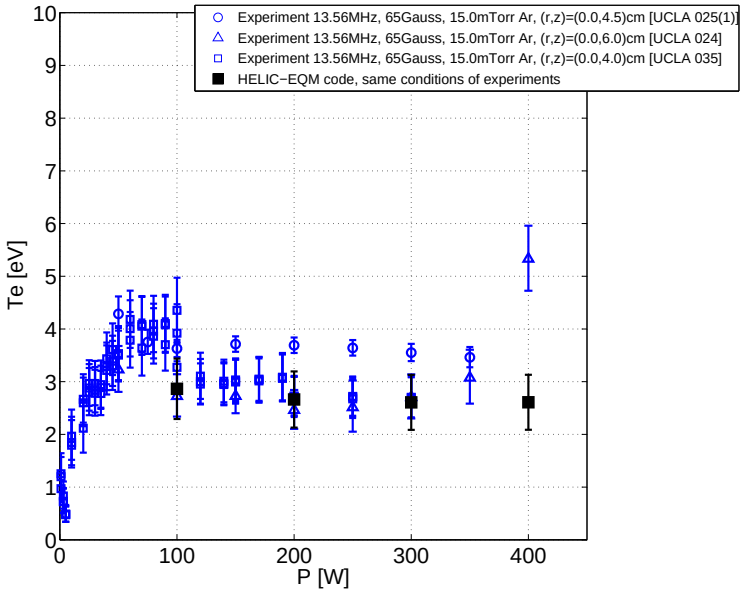

Figure 3.38: Comparison of measured electron temperature with the values calculated by the HELIC-EQM code, as a function of RF input power.

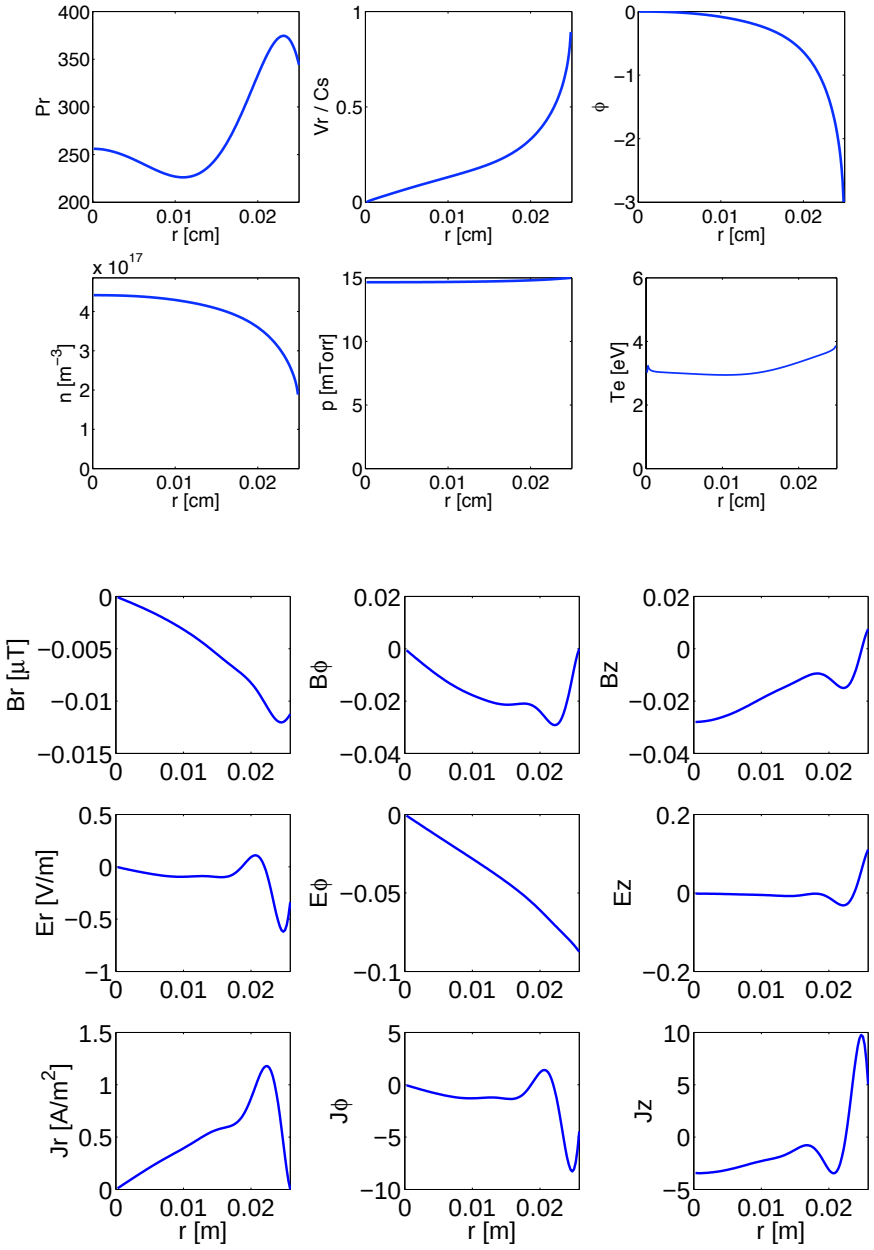

Figure 3.39: Example of radial profiles obtained at convergence after HELIC-EQM iterations, $P_{RF} = 200$ Watt. Starting from the left corner on top: $P(r)$ [Ohm/m] power deposition, v_r/C_s ratio between the radial drift velocity and the local Bohm acustic velocity, ϕ [Volt] plasma potential, n [m^{-3}] plasma density, p [mTorr] neutral pressure, T_e [eV] electron temperature; the three Real components of the RF magnetic field B_r, B_ϕ, B_z $[\mu T]$, of the RF electric field E_r, E_ϕ, E_z $[V/m]$, and of RF plasma currents J_r, J_ϕ, J_z $[A/m^2]$ (fields are normalized for an antenna current of $I_0 = 1.0A$).

3.5 An experimental note about the influence of stray elements on the impedance matching

Figure 3.40 shows the standard matching network used to couple the RF power generator to the antenna in an inductive plasma system. The power system is in most of the cases a 50Ω generator working at a fixed frequency. The industrial standards of frequencies are 13.56MHz and 27.12MHz.

The circuit load is an LR load, where L is the inductance of the antenna, and R is the plasma resistance as seen by the antenna. A matching box is interposed between the generator and the load, in order to match a 50Ω resistive impedance. The connections are done by means of coaxial cables.

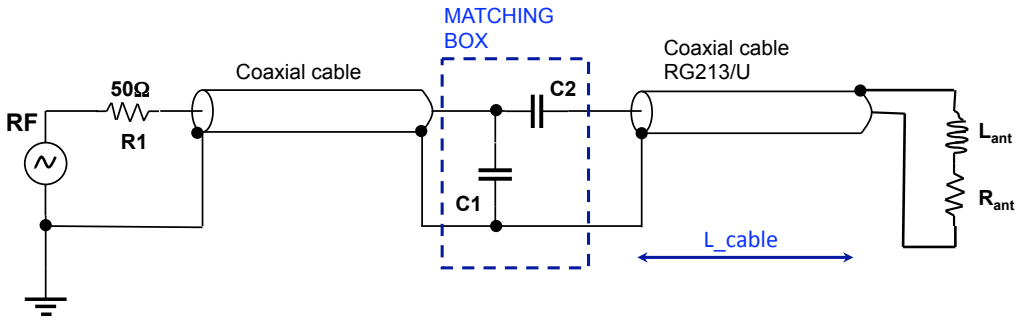

Figure 3.40: Standard matching network configuration

An electric equivalent of such a system has been made in order to characterize its impedance. Measurements of the impedance were done[6] using an HP 4195A network analyzer, showed in Fig. 3.41.a.

All the main electrical parameters involved were considered using lumped electronic components. The list of electronic components is reported in Tab. 3.2.

In order to understand the influence of stray elements of the circuit, an experimental test board with nodes equally spaced was constructed (Fig. 3.42.a). The mesh was composed by 4×8 nodes, numbered as in Fig. 3.42.a. Each node had a copper joint where the electronic components could be soldered. Thanks to this board, the number of possible connections was limited, and the geometry of each mesh was fixed. The stray inductance due to the areas of the circuit can be taken into account simply considering the area of the meshes of the network. Figure 3.42.b shows an example. The inductance of the area enclosed by the nodes 1-8-32-25 was of 530nH (±2%), as measured by means of the HP4195A. Measurements were done also with a resonance inductance meter (the R&S BN6100, showed

[6]Measurements showed in this paragraph were done in the laboratory of Ing. A. Selmo, in San Bonifacio (Verona).

(a) (b)

Figure 3.41: (a) HP (Hewlett Packard) 4195A network analyzer, (b) Rohde & Schwart LRT BN6100 inductance meter

Table 3.2: List of electronic components used during tests

Components	Value	Uncert.	Type
C1	1500 pF	±10%	Non-inductive polyester capacitor
C2	820 pF	±2%	Non-inductive polyester capacitor
C3	47 pF	±5%	Non-inductive polyester capacitor
L1	633 nH	±2%	Internal inductance of the resistive load
L2	37 μH	±2%	Inductance copper coil
R	5.4 Ω	±2%	Resistive load

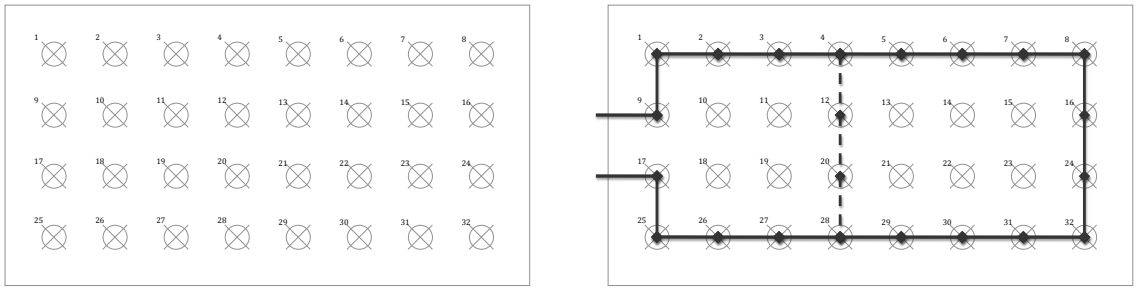

(a) (b)

Figure 3.42: (a) Experimental test board; nodes are equally spaced, for an easier evaluation of stray inductances (b) stray inductance of two portions of the test board

in Fig. 3.42.b), giving the same value of 530nH (±5%). The inductance of the area enclosed by the nodes 1-4-28-25 was 300nH, as measured with both the instruments. Each vertical ring of the board (ex. 1-2-26-25) gives a contribute of 75nH to the stray inductance.

3.5.1 High-L loads

At first, an highly-inductive load was considered. The high inductance of the load allows to overcome the stray inductances of the network. The electric circuit is reported in Fig.3.43.a. The LR load of the plasma source was simulated by making an electrical equivalent with two ceramic resistors (of measured internal parameters 633nH and 5.4Ω) connected in series with a copper coil (37μH and 1.5Ω). The load was connected between nodes 4 and 28. The matching box was simulated by the capacitors C1 and C2. The coaxial cable from the matching box to the LR load was simulated with C3, a lumped 47pF capacitor, connected between nodes 3 and 27. At this first step, no coaxial cable was used between the generator and the matching box.

The measured impedance is reported in Fig. 3.43.b (black squared dots), for a range of frequencies from 1.0kHz to 2.1MHz. The upper plot shows the module of impedance and the lower shows the phase in degrees. The theoretical profiles of the impedance are over-imposed on the same plot, as calculated by solving the electrical network of Fig.3.43.a. The first profile (blue) is evaluated without the stray elements of the circuit. The second profile (green) accounts also for stray elements. An optimum agreement is found in both the cases.

A physical coaxial cable 2-meters long has then been added at the entrance of the network, as showed in Fig.3.43.c. The cable gives an additional capacitance of 101 pF/m and an additional stray inductance of 270nH/m, as measured with the HP 4195A. The measured and calculated impedances are reported in Fig.3.43.d. The shift to lower frequencies

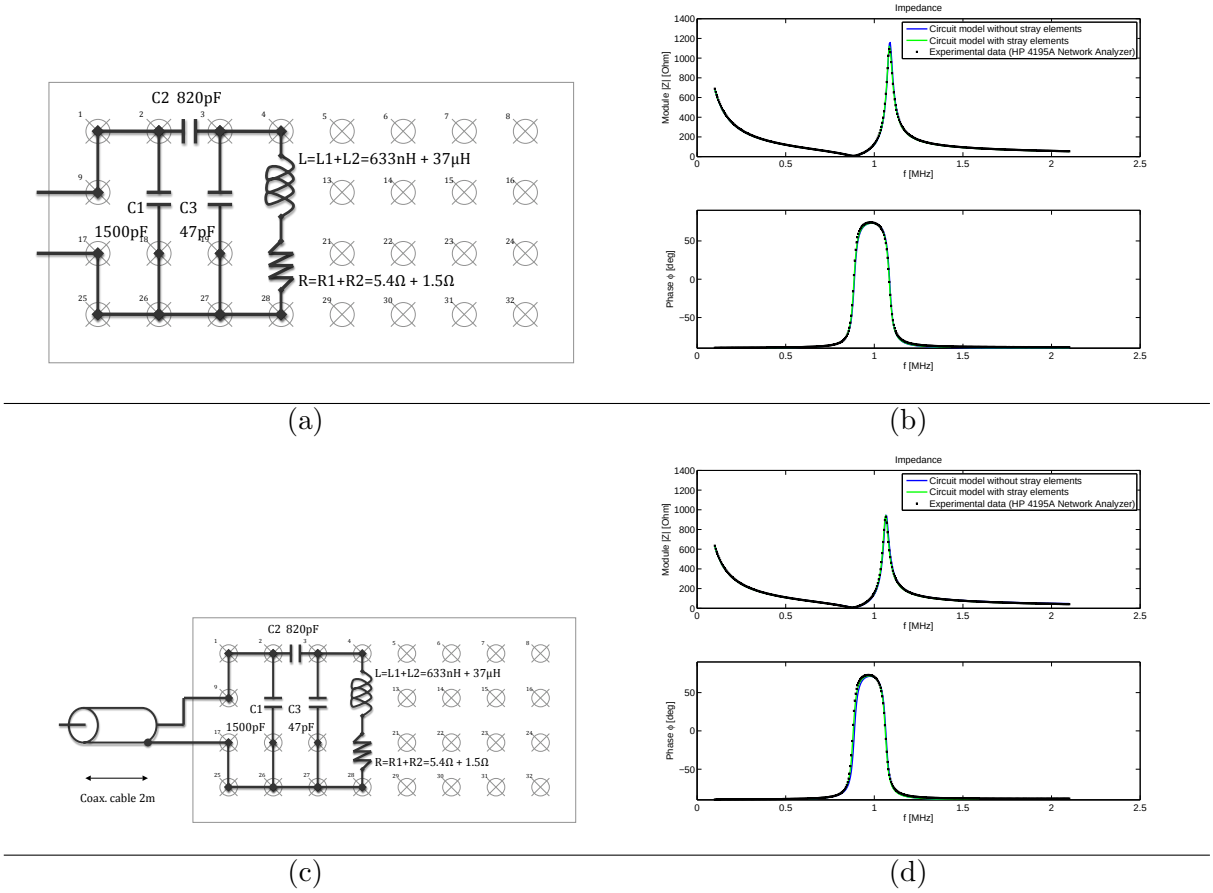

Figure 3.43: Experimental tests on high-inductance load: (a),(c) circuits, (b),(d) comparison of measured and calculated impedances

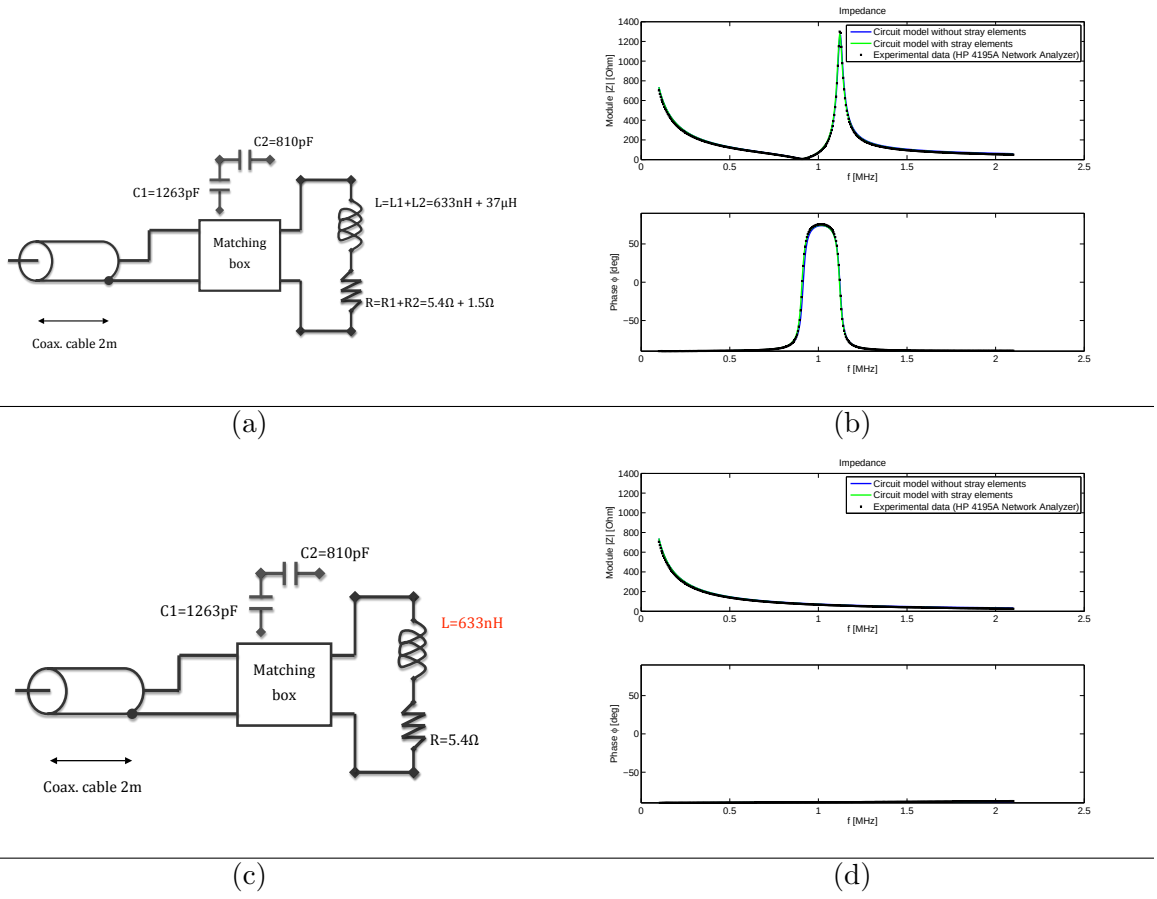

Figure 3.44: Experimental tests on high-inductance antenna and with the matching box: (a),(c) circuits, (b),(d) comparison of measured and calculated impedances

due to the addition of the coaxial cable is small. The main trend of the impedance remains the same as in the previous case.

A matching box with vacuum capacitances has then been substituted to its lumped counterparts C1 and C2, all the other elements remaining the same, as showed in Fig. 3.44.a. The matching box was set to have C1=1263pF and C2=810pF. The measured and calculated impedance is reported in Fig. 3.44.b. The main trend of the inductance is the same as before, with an almost perfect agreement between the theory and the measurements.

Finally, the high-inductance copper coil was removed from the circuit (Fig. 3.44.c), leaving only the small inductance L=633nH. The measured and calculated impedance is reported in Fig. 3.44.d. The lower inductance causes a shift of the resonances toward higher frequencies, above the 2.1 MHz upper limit. The network analyzer was thus re-set to work at higher frequencies, in order to fit with the behavior with low-inductive loads. The tests at higher frequencies have been reported in the next section.

3.5.2 Low-L loads

When the inductance L of the load is small, the resonance frequencies fall on an higher range, 1.0-50.0 MHz. In this range of frequencies the stray elements becomes much more important than before. They can't be neglected in the electrical description of the circuit.

This can be seen even from the simple case of an LRC-series resonator, as the one reported in Fig. 3.45.a. The measured and calculated impedance is showed in Fig. 3.45.b. The blue line is the impedance evaluated without considering the stray elements of the circuit. The minimum of the curve occurs at the theoretical resonance frequency of $1/(2\pi\sqrt{LC}) \approx 6.99$MHz, which is wrong with respect to the measured minimum. Also, the curve does not fit the experimental data for frequencies higher than 1.0MHz. However, when the stray inductance of the circuit is taken into account in the calculation (green line), the resonance frequency shifts at the lower value of 6.1MHz and the trend of the theoretical line agrees with the experimental data.

When the shunt capacitor C1=1500pF is added (Fig. 3.45.c), the inductance modifies as showed in Fig. 3.45.d. The circuit model without the stray elements (blue line) departs considerably from the measured data. Furthermore, an additional resonance frequency at 10.5MHz appears from the data. Considering in the circuit model also the stray elements of the circuit allows to describe correctly the experimental data (green line).

The addition of the capacitor C3=47pF, as showed in Fig. 3.46.a, does not considerably affect the trend of the impedance, Fig. 3.46.b, with respect to the previous case.

When the coaxial cable 2-meters long is connected at the entrance of the network (Fig. 3.46.c), the trend of the impedance is strongly modified by the stray inductances, as reported in Fig. 3.46.d. The high-frequency resonance is lowered by the higher capacitive and inductive components of the cable. The identification of stray inductances becomes critical and a good theoretical fit of experimental data is troublesome.

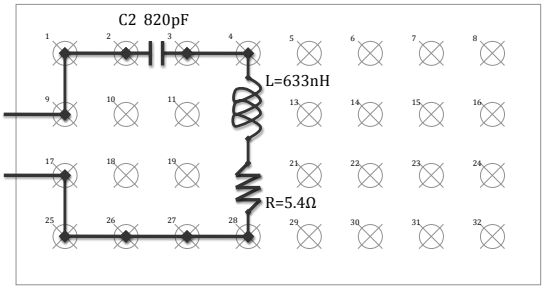

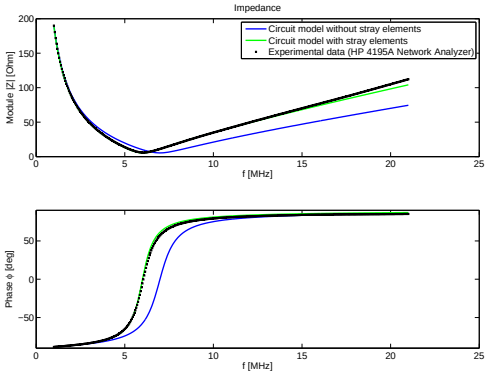

(a) (b)

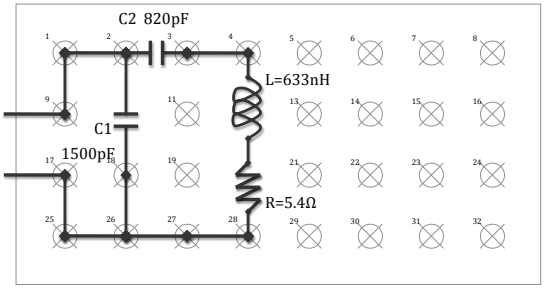

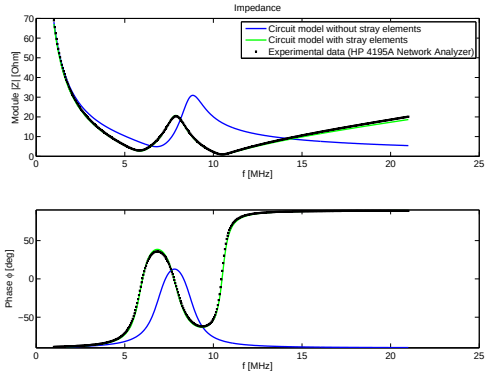

(c) (d)

Figure 3.45: Experimental tests on low-inductance antenna: (a),(c) circuits, (b),(d) comparison of measured and calculated impedances

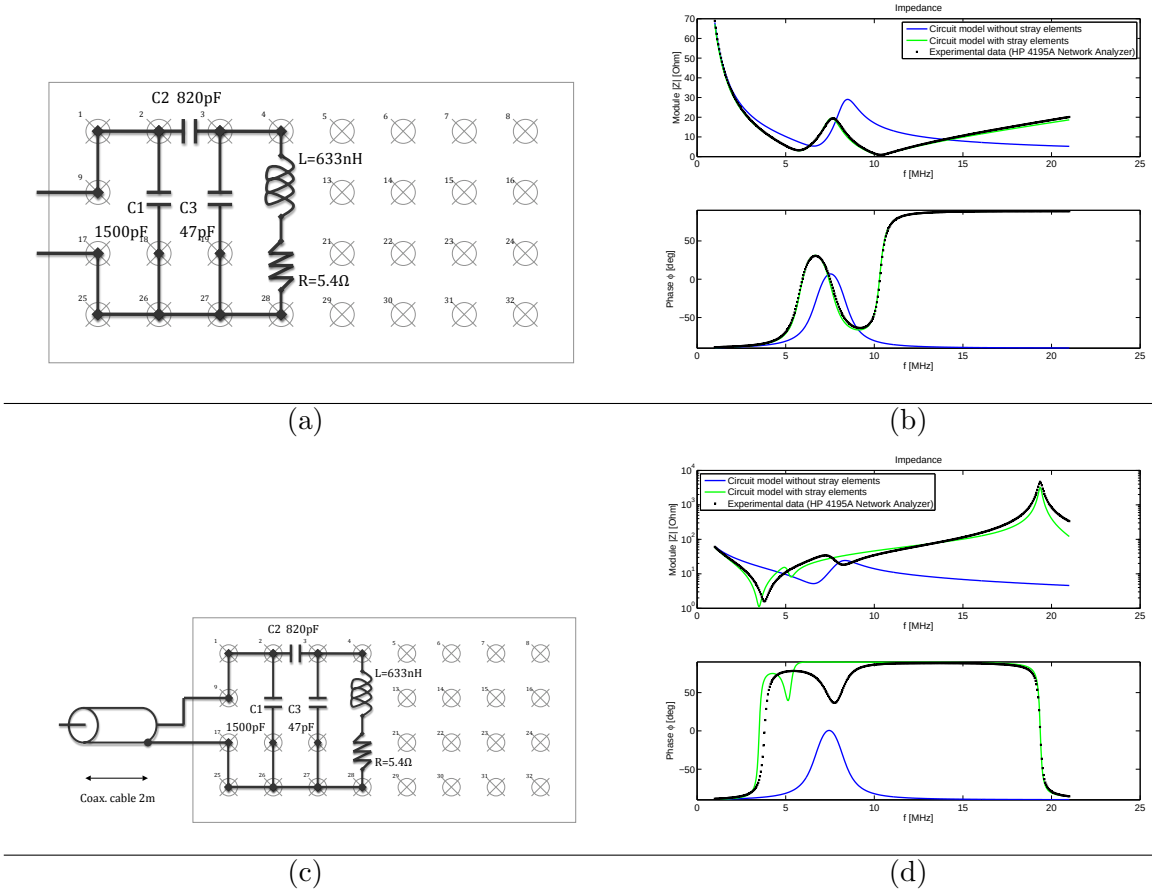

Figure 3.46: Experimental tests on low-inductance antenna: (a),(c) circuits, (b),(d) comparison of measured and calculated impedances

Chapter 4

Applications

4.1 Plasma propulsion using helicon sources

4.1.1 Propulsive parameters

The net thrust F exerted by this system is given by:

$$F = \dot{m}_i v_i + \dot{m}_n v_n \tag{4.1}$$

where $\dot{m}_i$ is the mass flow rate of exiting ions, v_i the velocity of the ions, $\dot{m}_n$ is the mass flow rate of exiting neutrals, v_n the velocity of neutrals. A more convenient form for Eq.4.1 is:

$$F = M_i \Gamma_i A_i v_i + M_n \Gamma_n A_n v_n \tag{4.2}$$

The specific impulse is given by:

$$I_{sp} = \frac{\dot{m}_i v_i + \dot{m}_n v_n}{(\dot{m}_i + \dot{m}_n) g_0} \tag{4.3}$$

The propulsive efficiency of the system is given by the ratio between the jet power and the power effectively deposited into the plasma:

$$\eta_{prop} = \frac{\frac{1}{2}\dot{m}_i v_i^2}{P_{pl}} \tag{4.4}$$

The efficiency of transfer between the RF generator and the plasma is given by:

$$\eta_{RF} = \frac{P_{pl}}{P_{RF}} = \frac{R_{pl}}{R_{pl} + R_{circ}} \tag{4.5}$$

and it depends on plasma load resistance R_{pl} and on the circuit resistance R_{circ}. The total efficiency of the thruster becomes:

$$\eta_{tot} = \eta_{RF} \eta_{prop} \tag{4.6}$$

Ideal conditions

In ideal conditions the source is supposed to ionize all neutrals, so that only plasma particles are expelled by the thruster. In this case the thrust is at its maximum, and it's given by:

$$F^{ideal} = M_i \Gamma_i A_i v_i \tag{4.7}$$

Also the specific impulse is at its maximum and it is only related to the ion exiting velocity:

$$I_{sp}^{ideal} = \frac{v_i}{g_0} = \frac{\Gamma_i / n}{g_0} = \frac{\alpha C_s}{g_0} \tag{4.8}$$

where the plasma flux Γ_i is given by:

$$\Gamma_i = n v_i = n \alpha C_s \tag{4.9}$$

where $v_i = \alpha C_s$ is the exhaust velocity of ions, $C_s = (kT_e/M_i)^{1/2}$ is the Bohm acoustic velocity of the ions, and the parameter α (Bohm parameter) takes into account for an accelerating mechanism,

$$\alpha = 1.0 \qquad \text{no accelerating mechanism} \tag{4.10}$$

$$\alpha > 1.0 \qquad \text{accelerating mechanism} \tag{4.11}$$

The acceleration can be a magnetic nozzle [65], a double layer [66], an hot population of electrons, or an additional selective heating system. Excluding additional heating systems, the parameter α can reasonably span in the range $1 < \alpha < 2$. Figure 4.1 shows the trend of the specific impulse as a function of the atomic mass number for three different values of T_e and assuming $\alpha = 2.0$ (as seen from double layer experiments). The figure shows that lighter nuclei allows higher specific impulses. Figures 4.2 and 4.3 shows the trend of F^{ideal} and I_{sp}^{ideal} for a thruster of radius of 1.0 cm (Figure 4.2) and of 2.5 cm (Figure 4.3) versus the Bohm parameter. Curves are evaluated for hydrogen, neon and argon. In a small thruster of 1 cm of radius, an ideal thrust of 1-2 mN can be obtained with an high-density (10^{18} m^{-3}), high-Te (¿4-5 eV) plasma accelerated in the supersonic regime over Mach 2. Figure 4.2 also shows that higher diameters are preferable when an higher thrust is desired.

Non ideal conditions

In non-ideal conditions the thruster the propellant is not completely ionized, and a fraction of the gas is lost at neutrals acoustic speed instead that at the ion acoustic speed. As a consequence, the maximum achievable specific impulse and thrust are reduced. We define the ionization fraction f_{iz} as the ratio between the ion density and the total number density of ions plus neutrals,

$$f_{iz} = \frac{n_i}{n_n} \tag{4.12}$$

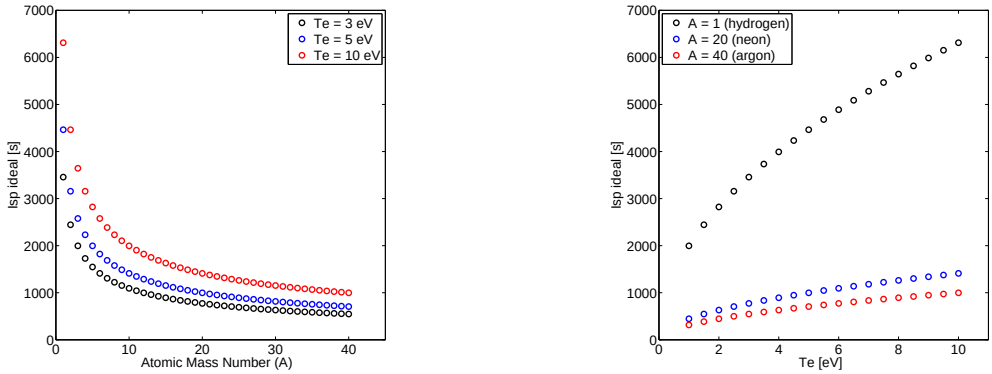

(a) (b)

Figure 4.1: (a) Ideal specific impulse vs. atomic mass number A (number of nucleons), for three values of the electron temperature; (b) ideal specific impulse vs. electron temperature, for three values of atomic mass number. A Bohm factor $\alpha = 2.0$ has been assumed, i.e. ions are supposed to be accelerated twice the Bohm velocity, as expected from double layers experiments.

We then define the mass-flow ionization fraction as the ratio between the ion and the total mass-flow,

$$f_{\dot{m}} = \frac{\dot{m}_i}{\dot{m}_i + \dot{m}_n} = \frac{n_i v_i}{n_i v_i + n_n v_n} \tag{4.13}$$

The relation between 4.12 and 4.13 is given by:

$$f_{iz} = \left[1 + \frac{v_i}{v_n}\left(\frac{1}{f_{\dot{m}}} - 1\right)\right]^{-1} \tag{4.14}$$

The specific impulse in non-ideal conditions results to be reduced by $f_{\dot{m}}$ to the values:

$$I_{sp} = f_{\dot{m}}\frac{v_i}{g_0} + (1 - f_{\dot{m}})\frac{v_n}{g_0} \tag{4.15}$$

The mass-flow ionization fraction weights the two contributes of ions and neutrals velocities to the total I_{sp}. Figure 4.4 shows an example of calculations of F and I_{sp} as a function of f_{iz}, for fixed parameters. The figure shows that when the ionization fraction f_{iz} increases, the specific impulse is enhanced from the cold-gas-thrusters range at very low (negligible) ionization fractions, to the plasma-enhanced range of hundreds-to-thousands seconds. In the cold-gas-thruster range, the expulsion of mass is governed by the ion acoustic sound speed; in the plasma-enhanced range the expulsion of mass is regulated by the ion acoustic Bohm velocity C_s, or an α-multiple of C_s.

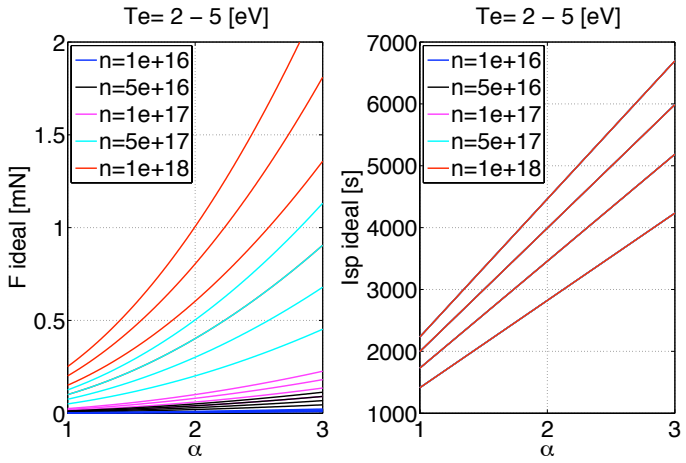

(a)

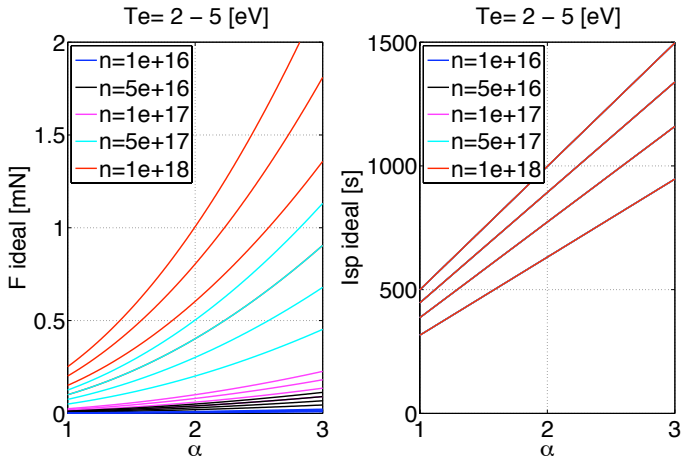

(b)

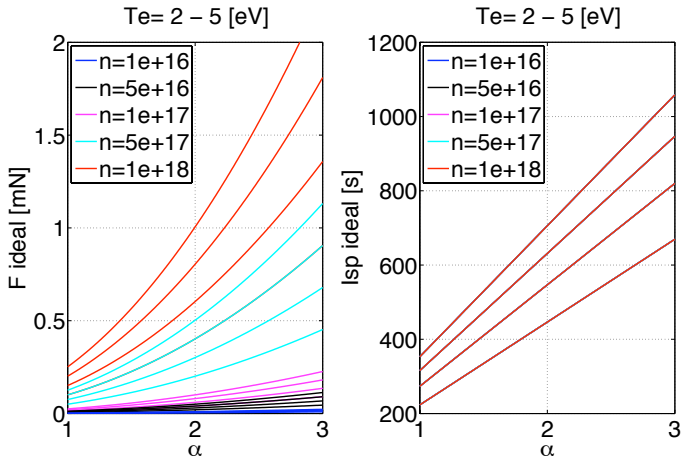

(c)

Figure 4.2: Ideal thrust and specific impulse vs. Bohm parameter ($\alpha = v_i/C_s$) for a helicon thruster of $r = 1.0$ cm-radius using (a) hydrogen, (b) neon, (c) argon.

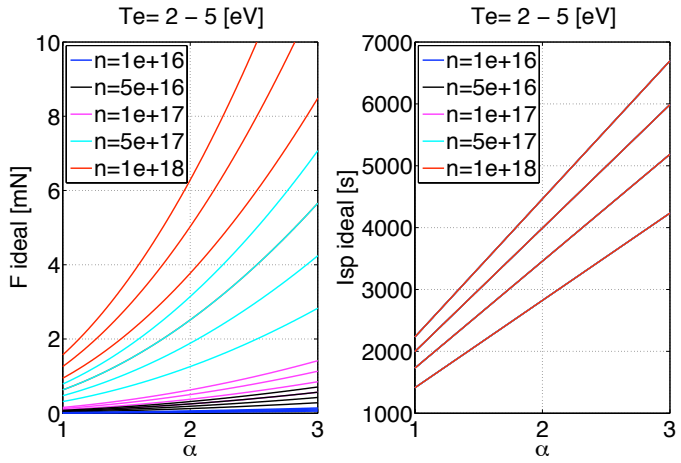

(a)

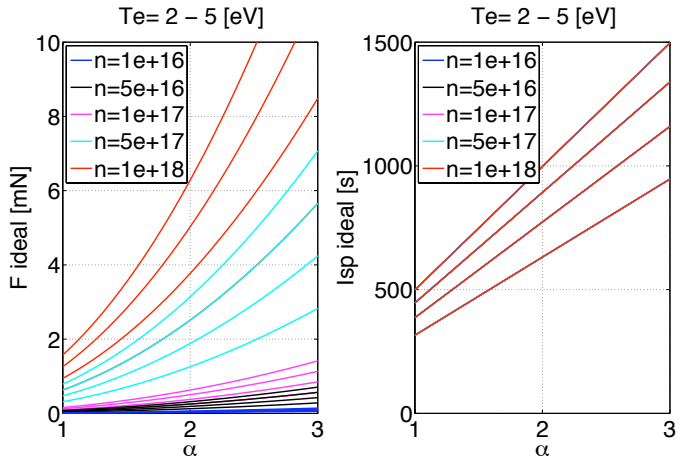

(b)

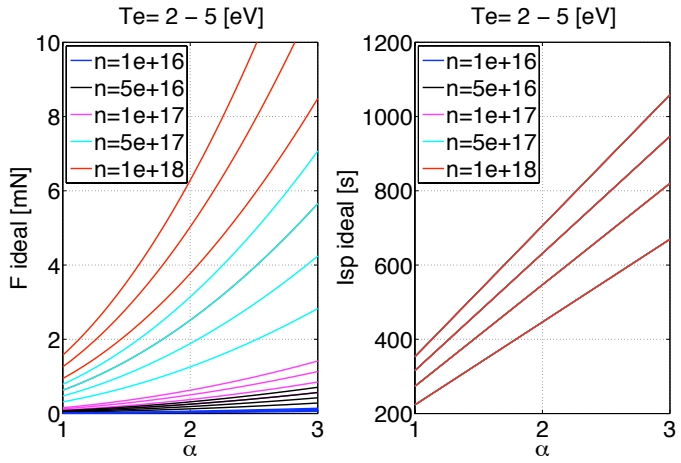

(c)

Figure 4.3: Ideal thrust and specific impulse vs. Bohm parameter ($\alpha = v_i/C_s$) for a helicon thruster of $r = 2.5$ cm-radius using (a) hydrogen, (b) neon, (c) argon.

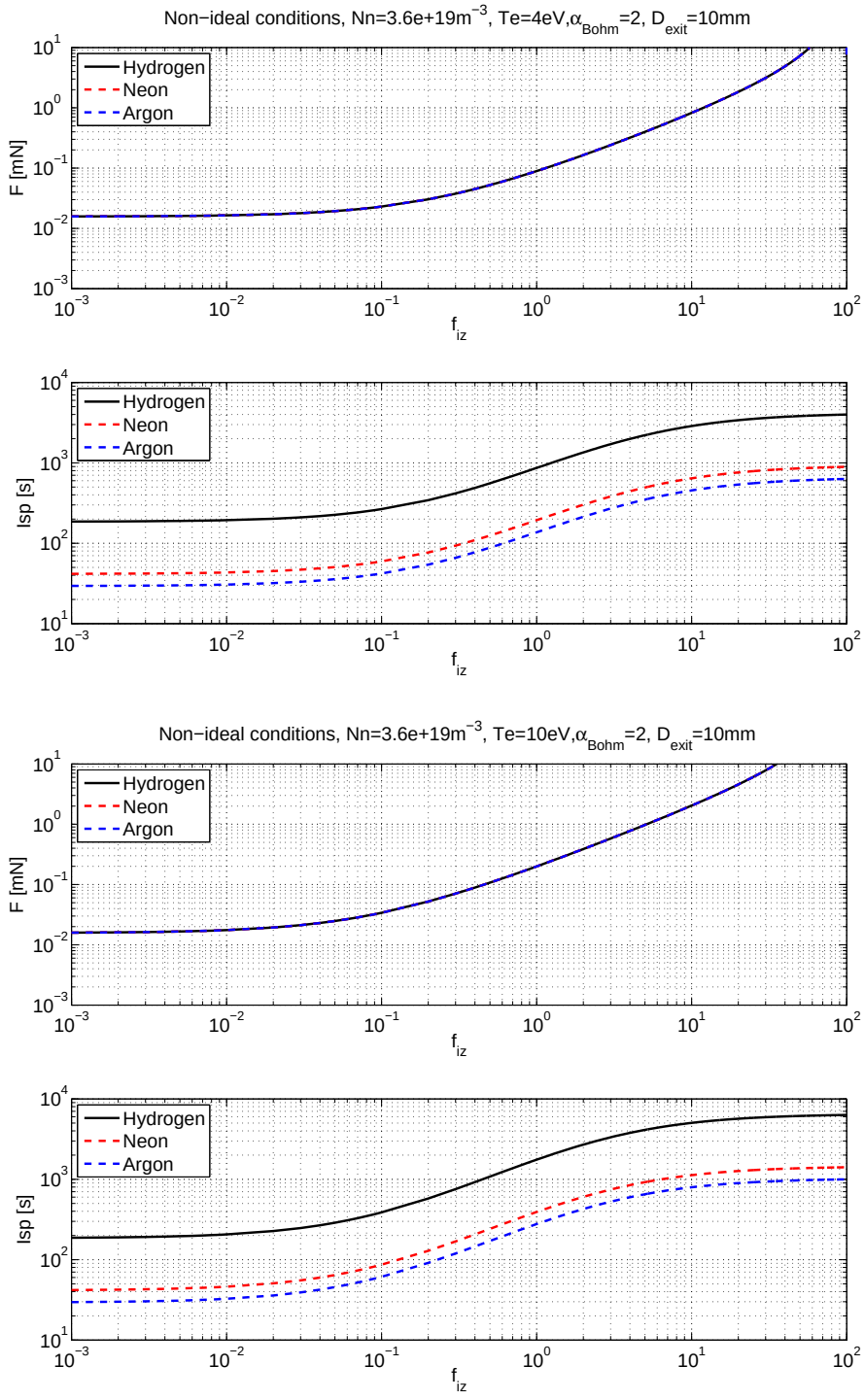

Figure 4.4: Non-ideal thrust [mN] and specific impulse [s] vs. ionization fraction [%]

4.1.2 Identification of thruster configurations

Combining informations from the theory developed (plasma-wave coupling plus the macroscopic transport), the numerical results from the codes, the expertise from the experimental campaign, a preliminary design of an helicon thruster has been performed. We will address the problem trying to achieve the following goal: specific impulse higher than 1000 s, thrust higher than 1mN. In order to better understand the complexity of the procedure and the strategy adopted it is worthwhile to briefly describe the main issues involved in design of such an apparatus. An helicon plasma thruster presents most of the problems invoved in the design of an helicon source for industrial applications, plus some further complication due to the fact that ionization must be high in order to allow high specific impulses. In fact, ionization efficiency must be in the range between 15-40%. To allow a better understanding of the process we will provide a brief indication of the effect of each parameter of the plasma source on the overall thruster performances.

Geometrical paramters

Diameter. The radial cross section of the thruster affect the surface losses and wave propagation into the plasma. Higher plasma source radius increases the wall losses at the injector and outlet (this is true if the outlet is not completely open because in this case it is not considered a plasma loss but it is the out coming flow providing thrust). Higher plasma radius allow better propagation of helicon waves into plasmas, as it is seen in Fig. 4.5, showing the plasma resistance versus the plasma density for sources of different radii.

It is worth it to mention that the diagram present just one case applying a fixed magnetic field shape but the behavior is very influenced by the value and profile of the static magnetic field. The diameter influence also the weight of the thruster because the magnetic coils need to be bigger and thus heavier.

Length: Source length influences modal wave reflection onto the end plates. Source length need to be optimized depending on the antenna type, frequency, and magnetic field value and shape to maximize the power deposited into plasmas (Fig. 4.6). The length of the plasma source also influences power losses at the wall thanks to the increased area exposed to plasmas. The length however increase the resident time of gas in the source thus increasing ionization probability . Finally the length influences the mass budget increasing the mass of the structure itself and of the magnetic system, since it requires to maintain the necessary magnetic field all over the source length.

Outlet diameter: The outlet diameter influence the mass flow rate of ions and neutrals ejected into vacuum. It plays a fundamental role in combination with the injected mass flow rate to determine the pressure regime inside the plasma source. Higher aperture for a specific mass flow rate causes lower neutral pressure regimes within the source, and thus lower collisionality, which reduces plasma coupling, as it is seen in the following diagram of the plasma resistance. The decrease is non-linear, density-dependent and hard-

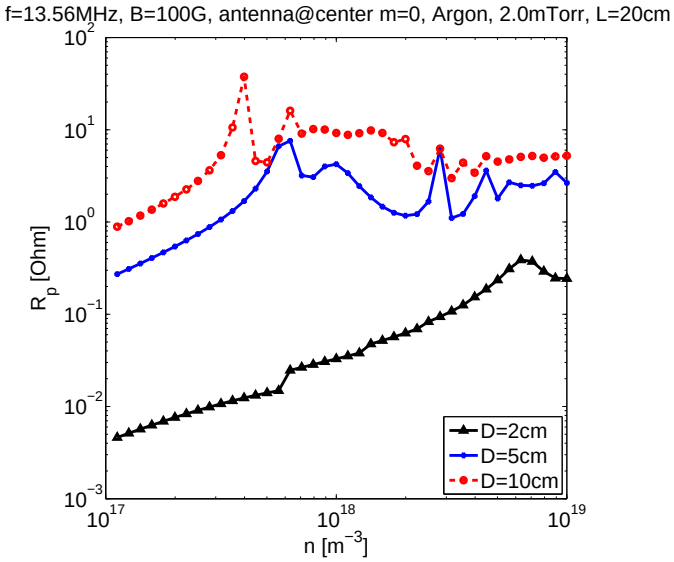

Figure 4.5: Different value of plasma resistance for different diameter of the plasma source versus plasma density at a fixed value of the magnetic field

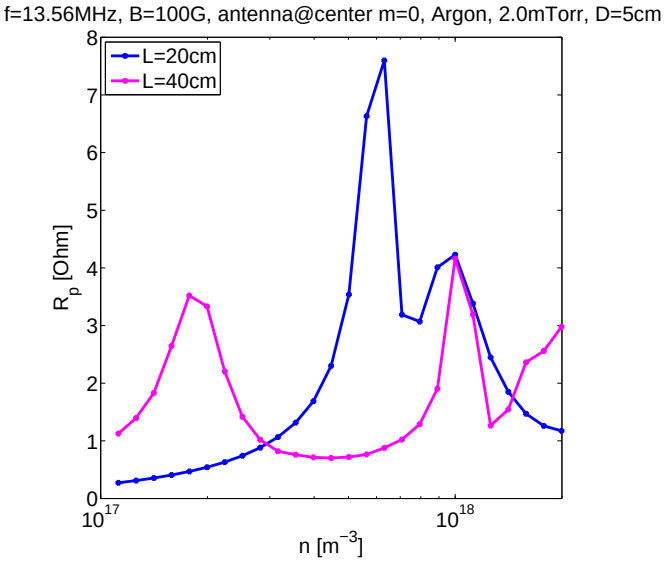

Figure 4.6: Different value of plasma resistance for different source length for a fixed antenna type feeding frequency magnetic field and plasma radius as function of plasma density

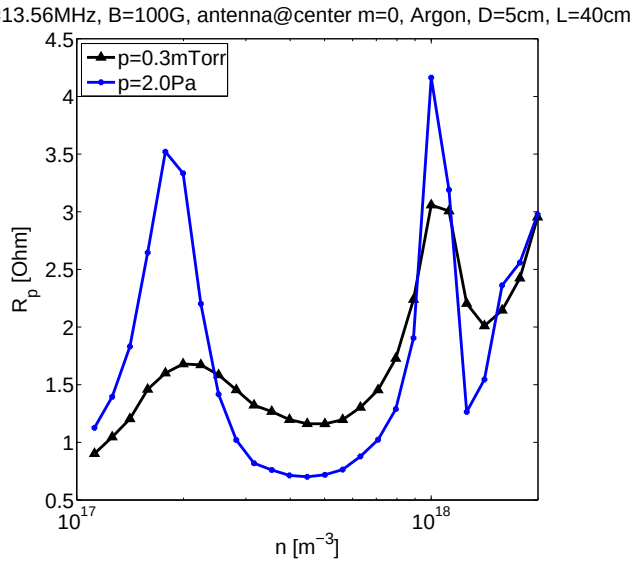

Figure 4.7: Different value of plasma resistance for different background pressure at fixed plasma density and otehr operative conditions

to-predict. However, a lower ionization collision reduces power losses of electrons thus increasing electron temperature and increasing the ionization fraction.

Mass flow rate: The mass flow rate together with the outlet diaphragm influence the pressure profile within the source. It is worth it to be remarked that the pressure profile within the source is strongly effect by a phenomena which can be improperly called "pumping" which take place at high ionization ratio (higher than 15%) due to removal of neutrals due to ionization and expulsion of high speed of ions (Fig.4.8).

It can be seen that neutrals from a initial density of 2×10^{19} m^{-3} falls down during the discharge to 2×10^{18} m^{-3} thanks to this "pumping" effect. This is not normally the case on a source used for industrial application since the initial density of neutrals is much higher than in case of a thruster and this reduction not so relevant. The pressure profile also change within the source due to the flow into the tube.

Functional parameters

Magnetic field Magnetic field plays a fundamental role on many different aspects: (i) confinement, higher magnetic field allows better confinement of particles; however, it should be remarked that till collisionality is high the effect on confinement becomes important at very high value of magnetic field (¿m1000 G) The magnetic field value and shape also affects wave propagation, both in radial and axial direction. Axial propagation and reflection onto

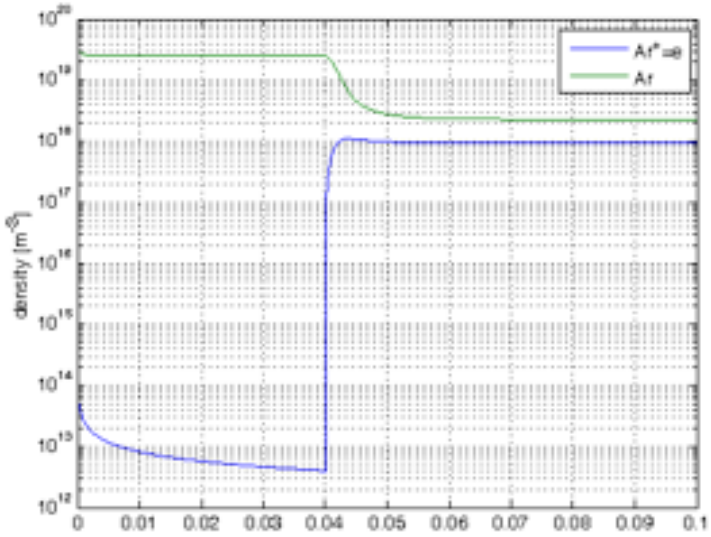

Figure 4.8: Plasma source evolution within an helicon thruster

the front and back plates allow to obtain a "resonant chamber", a cavity, that can maximize or destroy the deposition of power. In the following diagrams is seen the effect or magnetic field on plasma resistance for different ion densities.

Strongly coupled effects In very small cavities, the geometrical modes of wave propagations can constructively made to interfere in order to have a maximum of power coupling in regions where a good coupling is not expected. This can be seen in a small source of 2 cm diameter and 6 cm long, where a peak at very low magnetic fields is foreseen by the simulations: Fig. 4.10, obtained using a loop antenna $m = 0$. In these conditions the peak is foreseen to occur at 65 Gauss.

Antenna type and frequency Each antennas have its own spectrum and power deposition profile (both axially and radially) as it is seen in Fig. 4.11.a and 4.11.b.

Plasma resistance change also as function of antenna frequency as is seen in Fig. 4.9. Moreover, an higher frequency determines higher parasitic losses in the coupling circuit, thus reducing the overall electrical efficiency of the system.

The design procedure has to take into account all the parameters mentioned before to identify the best compromise among them. Moreover also the thermal control issue has to be considered. Power fluxes to the external surface has to be controlled in order to avoid overheating of the thruster, thus the thermal control of thruster need to be sized based on the expected power losses. As it has been seen the design of a plasma thruster require a very detailed control on several parameters. The strategy adopted is showed in Fig. 4.12

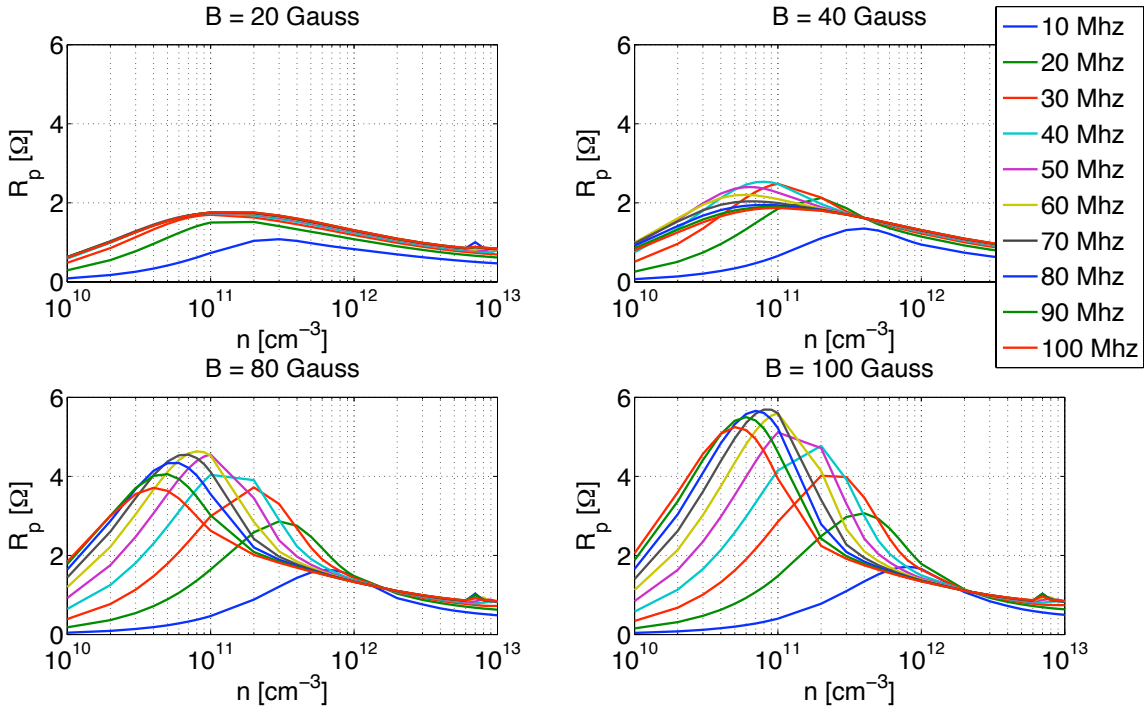

Figure 4.9: Different value of plasma resistance for different value of the magnetic field for different plasma densities (on a discharge of 10cm of diameter)

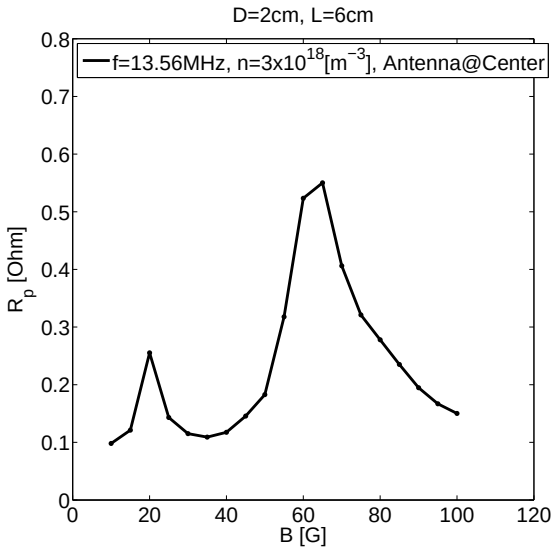

Figure 4.10: Low-B field peak in a small plasma cavity of 2 cm diameter and 6 cm long.

The input parameter are: (i) Available power, (ii) Magnetic field value, (iii) Antenna type and position in the source, (iv) source length and diameter, mass flow rate. As can be seen, the only fixed parameter is the power available, the other parameter are decided in a range defined during a preliminary design depending on the specific mission profile. The optimal value of them is the object of the optimization process. Input parameter are varied by an optimization algorithm till a "optimal" set of parameter is found.

The input parameter are put into the plasma simulation module which find the plasma expected plasma parameter as expected plasma density, plasma temperature, plasma distribution function, neutral density. The plasma tool is a combination of 1-D wave code (HELIC) and particle /fluid code (EQM or kinetic codes). The fluid code EQM is used to simulate plasmas as a first step assuming Maxwellian distribution. Than the results are put as starting condition for the kinetic code to identify the expected distribution function deviating from the Maxwellian. Structural simulation calculate the mass for the major structural components of the engine which are magnets and heat exchanger based on the magnetic field provided chosen as initial parameter and the power flux to be managed by heat exchanger.

The plasma parameter are put in the acceleration/detachment module. The acceleration detachment module implement a look-up table providing expected exhaust speed as function of electron temperature, magnetic field value, electron distribution function (fitted with a Bi-Maxwellian) distribution.

Thruster performances in term of specific impulse I_{sp} and thrust F and inert mass are

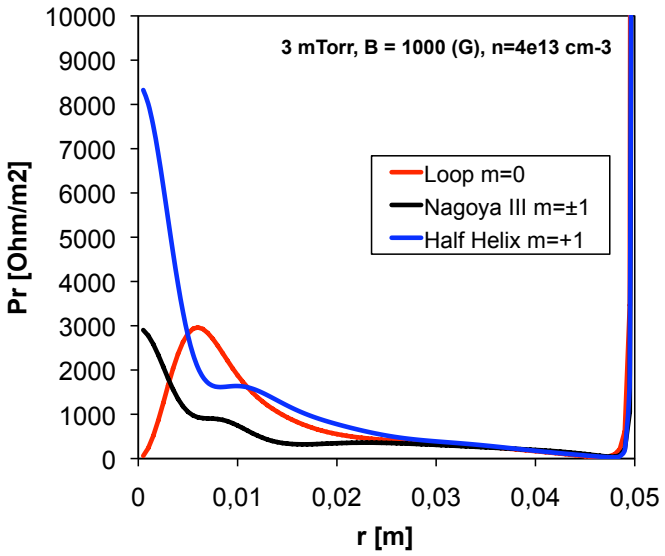

(a)

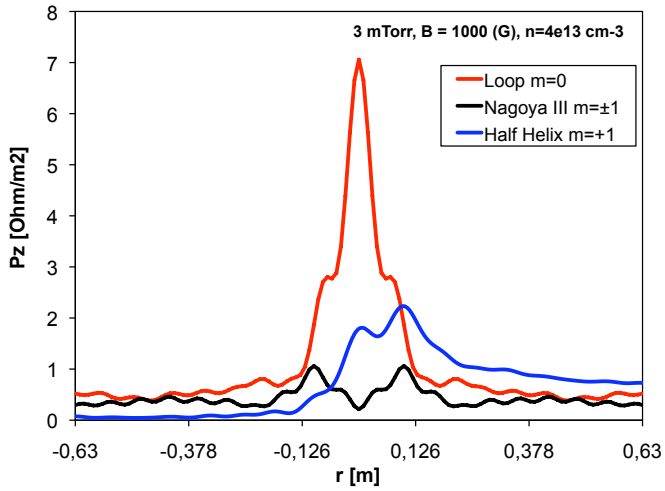

(b)

Figure 4.11: (a) radial power deposition profile for different antennas; (b) axial power deposition profile for different antennas

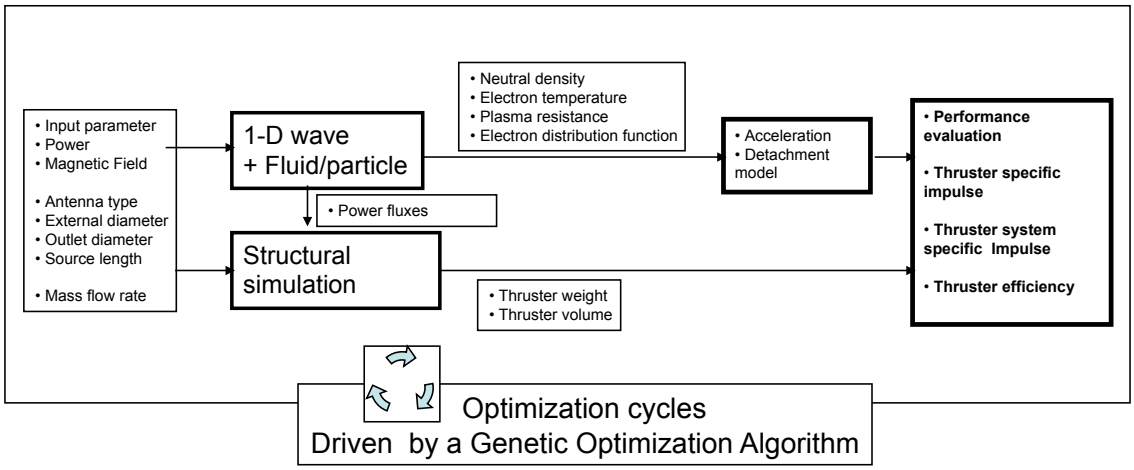

Figure 4.12: Design scheme adopted for the thruster design

finally calculated; a genetic algorithm runs till optimization is reached.

The following thruster configuration has been selected to perform with: I_{sp} higher than 1050 s, Thrust higher than 1.05 mN, Inert mass lower than 1.2 kg (Magnetic field and thermal control system). Exception are thruster 5 and 9 which have been selected because of the expected efficiency.

#	D_{source} [mm]	D_{exit} [mm]	L_{source} [mm]	B_0 [G]	$\dot{m}$ [10^{-7} kg/s]	Antenna type, freq.
1	20	7	50	65	1	m=0 L=30mm 13.56MHz
2	20	10	50	65	2.2	m=0 L=30 mm 13.56MHz
3	20	15	50	65	3	m=0 L=30mm 13.56MHz
4	20	10	100	250	2.2	m=0 L=100 mm 13.56MHz
5	20	10	100	500	2.2	m=0 L=100 mm 27.12MHz
6	50	50	60	65	3.5	m=0 L=25mm 13.56MHz
7	50	50	60	120	3.5	m=0 L=30mm 27.12MHz
8	20	10	80	65	2.2	m=+1 L=80 mm 13.56MHz
9	20	10	200	1000	2.2	m=+1 L=200 mm 13.56MHz
10	20	10	60	150	2.2	m=+1 L=70 mm 13.56MHz

Table 4.1: Helicon thruster, identified configurations

4.2 Propellantless propulsion using tethers

4.2.1 Exploitation of environmental plasma for propulsion

In this final section we consider a propellantless electrodynamic system, the electrodynamic tether (EDT), as a system that exploits environmental plasma instead that creating plasma on board. In factn electrodynamic tether uses the plasma already present in the space environment to operate, and thus it can be considered as one possible esoreactor case of the (endoreactor) plasma thruster. In fact, in the case of the tether, the plasma is not generated inside the system and then accelerated outside, but the plasma is kept from the external environment to obtain a thrust in a more direct fashion. The principle of operation of the tether is not based on the acceleration of a fluid and the reaction principle, but it relies on a direct electrodynamic interaction of the system with the external environment through the Lorentz force. A bare electrodynamic tether orbiting inside a planetary plasmasphere (intended as plasma plus magnetic field) can be considered as a conducting wire moving inside a magnetized plasma. The electric charges contained inside the conducting cable experience a motional electric field, caused by the relative motion with respect the external magnetic field. When electrons are repelled by means of an electron emitter (like an hollow cathode), an electric current flows along the wire. Replenishment of electrons occurs through the collection of environmental electrons from the ionospheric plasma. A Lorentz force arises from the interaction of the electric current with the local magnetic field of the planet. The Lorentz force coming from the interaction of the cable with the plasmasphere can conveniently be used for propellantless propulsion [26], for example in orbit raising and lowering maneuvers. Several applications of such a concept have been considered in the past (see [27], [28], [29], [30]). Significant flight and development activities have also been conducted on EDT systems (TSS-1, TSS-1R, PMG, and ProSEDS). Furthermore, EDTs have been demonstrated to be capable of extracting power from space plasmas, i.e. from the plasmasphere of a planet or the solar wind [31]. Relevant applications at Jupiter have been proposed, [32] [33] [34] [35]. For these reason EDTs have seriously been considered as a future efficient tool for power generation and maneuvering in all space applications where an appropriate plasmasphere is present [36]. In the following section we explicitly derive the expression of the electrodynamic force acting on a tether.

4.2.2 Electrodynamic force and power

We consider a bare EDT [46] of length L and rectangular section $w \times h$ (tape tether), mounted on a satellite with a load impedance Z_c. The motion of electric charges of the conductor with respect to the background magnetic field is responsible for a motional electric field (e.f.) $\vec{\boldsymbol{E}}$, given by:

$$\vec{\boldsymbol{E}} = (\vec{\boldsymbol{v}}_{sc} - \vec{\boldsymbol{v}}_{pl}) \times \vec{\boldsymbol{B}} \tag{4.16}$$

where the plasma is assumed to be frozen to the magnetic field. The motional e.f. projected along the tether line, $E_t = \vec{\boldsymbol{E}} \cdot \hat{\boldsymbol{u}}$, provides the potential that drives the electrical current flowing along the tether. Figure 4.13 shows a schematic model of the tether.

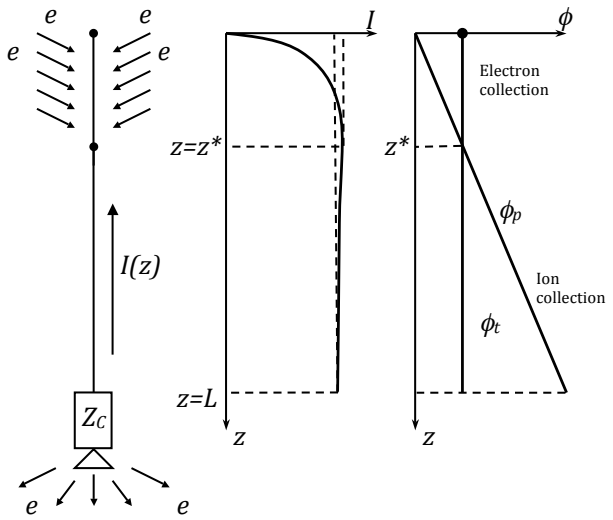

Figure 4.13: Bare tether schematic (generator mode). The two graphs shows the profiles of the current I, of the tether potential ϕ_t and of the plasma potential ϕ_p as a function of tether abscissa z.

When ohmic losses are neglected, the electric circuit equation is:

$$E_t L = E_t z^* + Z_c I \tag{4.17}$$

where it was assumed no impedance of the plasma contactor at the cathode, Z_c is the impedance of the load, and z^* is the zero-bias position along the tether, measured from the anodic tip. Ohmic losses cannot be neglected in presence of a dense plasmasphere, but they are negligible for the less dense plasma of Jupiter and a low-resistance wire. For the plasma density of Jupiter, the tether radius is much less than the Debye length and the electron Larmor radius and, consequently, electrons are collected according to the Langmuir's Orbital Motion Limited model [59], [48]. Under the OML assumptions, the collected current is a function of the tether-line abscissa z [46]:

$$\frac{dI}{dz} = \frac{2w}{\pi} q_e n_e \sqrt{2 \frac{q_e}{m_e} E_t (z^* - z)} \tag{4.18}$$

After analytic integration of Eq. 4.18 the current profile $I(z)$ can be obtained with the condition $I(z = 0) = 0$, and the length-averaged value $I_{avg} = (1/L) \int_0^L I(z) dz$ is given by (see [24] for the derivation):

$$I_{avg} = I_0 \left(1 - \frac{2}{5}\zeta\right) \zeta^{3/2} \tag{4.19}$$

where:

$$I_0 = \frac{4}{3}\frac{w}{\pi} q_e n_e L^{3/2} \sqrt{2\frac{q_e}{m_e} E_t} \tag{4.20}$$

and $\zeta = z^*/L$ is the non-dimensional zero-bias position.
The power that can be extracted at the load is a function of ζ:

$$P = Z_C I_C^2 \approx Z_C I_{avg}^2 = I_0 E_t L (1 - \zeta)\zeta^{3/2} \tag{4.21}$$

and it has a maximum at $\zeta_{opt} = 3/5$. The optimal power condition can be obtained with an appropriate control of the load-impedence. The optimal impedance Z_C^{opt} is proportional to the following set of parameters [24], which is variable along the trajectory as a function of $\sqrt{E_t}/N_e$,

$$Z_C^{opt} \propto \frac{1}{N_e w}\sqrt{\frac{E_t}{L}} \tag{4.22}$$

The Lorentz force due to the interaction of the current with the magnetic field is:

$$\vec{\boldsymbol{F}}_{el} = \int_0^L I(z) d\hat{\boldsymbol{u}} \times \vec{\boldsymbol{B}} = I_{avg} L B \hat{\boldsymbol{u}} \times \hat{\boldsymbol{b}} \tag{4.23}$$

where $\hat{\boldsymbol{b}}$ is the unit vector of the magnetic field vector $\vec{\boldsymbol{B}}$, and the current is parallel to the line element of the tether. The unit vector $\hat{\boldsymbol{u}}$ is assumed to have the same direction of the conventional electric current, pointing from the cathode to the anode. The tether current flow involves a particular caveat when dealing with rotating tethers, whereby cathode and anode reverse one another during each tether rotation. Substituting Eq. 4.19 in Eq. 4.23 yields:

$$\vec{\boldsymbol{F}}_{el} = I_0 \left(1 - \frac{2}{5}\zeta\right) \zeta^{3/2} L B \hat{\boldsymbol{u}} \times \hat{\boldsymbol{b}} \tag{4.24}$$

Eq. 4.24 shows that the Lorentz force is proportional to:

$$F_{el} \propto n_e B E^{1/2} w L^{5/2} \propto n_e v_{rel}^{1/2} B^{3/2} w L^{5/2} \tag{4.25}$$

The scaling of the Lorentz force as a 2.5 power of the length enables the extraction of significant power levels from the plasmasphere using tethers of moderate lengths. In fact, the electrical energy extracted by the EDT during an infinitesimal time step is:

$$\epsilon_{load} = \phi_{load} I_{avg} dt \tag{4.26}$$

and the associated electrical power is:

$$P_{el} = \vec{\boldsymbol{F}}_{el} \cdot \vec{\boldsymbol{v}}_{rel} = I_0 \left(1 - \frac{2}{5}\zeta\right) \zeta^{3/2} LB(\hat{\boldsymbol{u}} \times \hat{\boldsymbol{b}}) \cdot \vec{\boldsymbol{v}}_{rel} \tag{4.27}$$

The maximum power can be obtained when the tether line $\hat{\boldsymbol{u}}$ is both perpendicular to the magnetic field and to the relative velocity vector; in this situation we have $(\hat{\boldsymbol{u}} \times \hat{\boldsymbol{b}}) \cdot \hat{\boldsymbol{v}}_{rel} = 1$ and the power is :

$$P_{el} = \frac{4}{3}\frac{w}{\pi} q_e n_e v_{rel} B L^{5/2} \sqrt{2\frac{q_e}{m_e}} \sqrt{E_t} \left(1 - \frac{2}{5}\zeta\right) \zeta^{3/2} \tag{4.28}$$

Like the electrodynamic force, the electrical power P_{el} scales as $L^{5/2}$.

From a thermodynamic point of view, the EDT can be seen as a machine capable to convert directly the kinetic energy of its motion into electrical energy, by virtue of the induction law. The environmental plasma allows the closure of the electrical circuit and the possibility to have a current flowing through the tether and possibly a load. The kinetic energy associated with the relative motion is:

$$\varepsilon_{kin}^{rel} = \frac{1}{2} m_{sc} v_{rel}^2 = \frac{1}{2} m_{sc} \left(\frac{E}{B \ \sin\varphi}\right)^2 \tag{4.29}$$

where $E = v_{rel} B \sin\varphi$, and φ is the angle between $\vec{\boldsymbol{v}}_{rel}$ and $\vec{\boldsymbol{B}}$. The efficiency of power production of the EDT can be expressed as the ratio between the electrical power at the load and the total available power:

$$\eta = \frac{P_{el}}{\dot{\varepsilon}_{kin}^{rel}} \tag{4.30}$$

In the following discussion we will assume the load impedance being actively controlled (for example by using variable resistance), in order to track the condition for optimal matching.

4.2.3 New insights on the orbital dynamics of an EDT

The local nature of the electrodynamic force acting on a tether leads to a complex orbital dynamics of such a system. The orbital dynamics of EDTs has usually been investigated with a two-body description of the motion of the system's center of mass around the central body. In these models, the tether is modeled as a rigid dumbbell, with attitude uncorrelated to its orbital dynamics. Even with such simple models, complex dynamical features and non-trivial stability properties appear, as already outlined by many authors (see [24], [25]).

The dynamics of an EDT in a three-body gravitational environment has received a lesser attention than the two-body case. Pioneering studies of tethers in the three-body

environment were done by Colombo [37] and, later, by Farquhar [38]. These studies investigated a cable-connected satellite for station-keeping around a collinear libration point. Subsequent works were done by Misra [39] and Wong [40], [41], and recently by Peláez and Scheeres [42], [43], [44]. A recent study lead by the Advanced Concept Team of the European Space Agency investigated the dynamics of tethered satellites at Lagrangian points [45]. The lack of studies of EDTs in the three-body is justifiable when we consider that in the Earth-Moon system the presence of a third body, the Moon, can be treated just like a perturbation for LEO applications. This is not true when we deal with more general cases and with planetary systems like Jupiter. A whole family of new dynamical features appears when we study the tether dynamics by using the dynamical paradigm of the circular restricted three body problem. Relevant consequences on power production and spacecraft maneuvering can be inferred, like for example the possibility to extract power while maintaing a quasi-stable position with respect to the corotating frame.

The tethered satellite is assumed to have a rectilinear rigid shape of length L, with total mass m. The center of mass of the satellite is the point C and the unit vector defining its orientation is $\hat{\boldsymbol{u}}$ (Figure 4.14). The gravitational potential acting over an element mass dm of the tether placed at a distance R_{dm} from an attracting center is given by:

$$V_{gr} = -\int_m \frac{\mu}{R_{dm}} dm \tag{4.31}$$

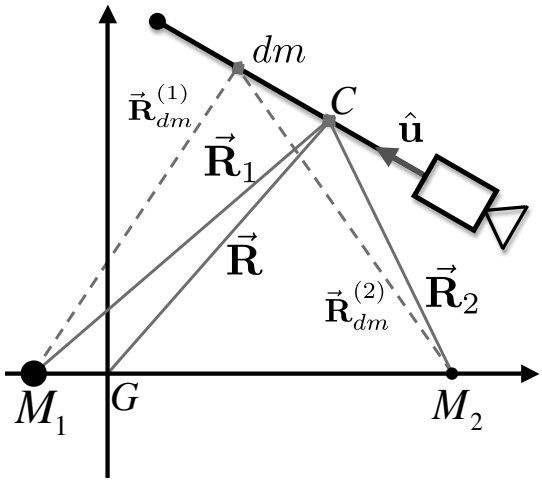

Figure 4.14: Gravitational actions on the tether.

The ratio $1/R_{dm}$ can conveniently be rewritten using Legendre polynomials:

$$\frac{1}{R_{dm}} = \frac{1}{R\sqrt{1+2\lambda cos\gamma+\lambda^2}} = \frac{1}{R}\sum_{n=0}^{\infty}(-1)^n\lambda^n P_n[cos\gamma] \tag{4.32}$$

Substituting Eq. 4.32 into Eq. 4.31 the gravitational potential becomes:

$$V_{gr} = -\frac{m\mu}{R}\left(1+\sum_{n=2}^{\infty}(-1)^n\left(\frac{L}{R}\right)^n a_n P_n[cos\gamma]\right) \tag{4.33}$$

Eq. 4.33 shows that the potential is given by the sum of a zeroth-order term $-m\mu/R$ corresponding to the potential of a point mass, and a power series of the ratio L/R, where L is the tether length and R the distance of center of mass C of the tether system from the attracting primary. The ratio L/R is usually small and the corresponding terms negligible, but this condition does not hold for an extremely long tether or for a tether orbiting very close to one of the primaries.

The resultant of gravitational forces can similarly be derived:

$$\vec{\boldsymbol{F}}_{gr} = -\frac{m\mu}{R^3}\vec{\boldsymbol{R}}\left(1+\sum_{n=2}^{\infty}(-1)^n\left(\frac{L}{R}\right)^n a_n\left(S_n[cos\gamma]\hat{\boldsymbol{R}} - S_{n-1}[cos\gamma]\hat{\boldsymbol{u}}\right)\right) \tag{4.34}$$

where the $S_n[\cos\gamma]$ are the polynomials of the series:

$$S_1[x] = 3x \tag{4.35}$$

$$S_2[x] = \frac{3}{2}(5x^2-1) \tag{4.36}$$

$$S_3[x] = \frac{5}{2}(7x^3-3x) \tag{4.37}$$

$$S_4[x] = \frac{15}{8}(21x^4-14x^2+1) \tag{4.38}$$

In the limiting case when the ratio between tether length L and distance R from the gravitational attractor is small, the gravitational force coincides with the point-mass Newton law:

$$L/R \to 0 \quad : \quad \vec{\boldsymbol{F}}_{gr} = -\frac{m\mu}{R^3}\vec{\boldsymbol{R}} \tag{4.39}$$

When placed in a three-body environment the gravitational attractions of the two primaries M_1 and M_2 must be summed together. Here we will assume $M_1 > M_2$, and we will indicate with the subscripts 1 and 2 the relative distances between the tether center of mass from M_1 and M_2 respectively. The motion of the center of mass, expressed in the synodic frame (the frame corotating with the primaries), is expressed by the classical CRTBP equations plus the perturbation due to the EDT electrodynamic force:

$$\ddot{\vec{\boldsymbol{R}}} + 2\vec{\boldsymbol{\Omega}} \times \dot{\vec{\boldsymbol{R}}} + \vec{\boldsymbol{\Omega}} \times \left(\vec{\boldsymbol{\Omega}} \times \vec{\boldsymbol{R}}\right) = -\frac{\mu_1}{R_1^3}\vec{\boldsymbol{R}}_1 - \frac{\mu_2}{R_2^3}\vec{\boldsymbol{R}}_2 + \vec{\boldsymbol{f}}_{el} \tag{4.40}$$

with the assumption of a vanishing L/R ratio. When the tether length is not neglegible, the full gravitational force of Eq. 4.34 must be considered. The non-dimensional form of Eq. 4.40 is:

$$\ddot{\xi} - 2\dot{\eta} = \xi - \frac{\nu_1}{\rho_1^3}(\xi + \nu_2) - \frac{\nu_2}{\rho_2^3}(\xi - \nu_1) + \frac{F_{el,x}}{md\Omega^2} \tag{4.41}$$

$$\ddot{\eta} + 2\dot{\xi} = \eta - \frac{\nu_1}{\rho_1^3}\eta - \frac{\nu_2}{\rho_2^3}\eta + \frac{F_{el,y}}{md\Omega^2} \tag{4.42}$$

$$\ddot{\zeta} = -\frac{\nu_1}{\rho_1^3}\zeta - \frac{\nu_2}{\rho_2^3}\zeta + \frac{F_{el,z}}{md\Omega^2} \tag{4.43}$$

where (ξ, η, ζ) are the non-dimensional coordinates of the orbital position. Length, mass and time have been respectively non-dimensionalized with the distance between primaries d, the total mass of the planetary system $M_1 + M_2$, and the inverse of the mean angular velocity of the primaries $1/\Omega$. Figure 4.15 shows the geometry of the synodic frame with the non-dimensional coordinates (ξ, η) centered in the center of mass of the planetary system (with $M_1 > M_2$).

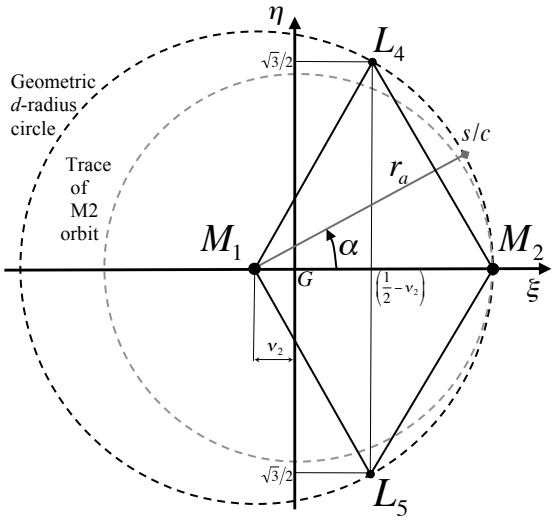

Figure 4.15: Geometry of synodic plane with non-dimensional quantities.

The non-dimensional mass parameters of the two primaries are:

$$\nu_1 = 1 - \nu_2 = \frac{M_1}{M_1 + M_2} \tag{4.44}$$

$$\nu_2 = \frac{M_2}{M_1 + M_2} \tag{4.45}$$

and the non-dimensional distances of the center of mass of the spacecraft from the two primaries are:

$$\rho_1 = \sqrt{(\xi + \nu_2)^2 + \eta^2 + \zeta^2} \tag{4.46}$$

$$\rho_2 = \sqrt{(\xi - \nu_1)^2 + \eta^2 + \zeta^2} \tag{4.47}$$

From Eq. 4.46 and 4.47 together with Eqs. 4.41–4.43, it can be shown that in the unperturbed case the equilibrium points must lie in the intersections of two circumferences with their centers in $(-\nu_2, 0)$ and $(\nu_1, 0)$ and radii equal to ρ_1 and ρ_2 respectively.

The system of Eqs. 4.41–4.43 describes the dynamics of an active electrodynamic tether in a three–body case, which corresponds to a perturbation of the classical three body problem, with a perturbing force due to the specific Lorentz force $\vec{\boldsymbol{f}}_{el}$.

When $\vec{\boldsymbol{f}}_{el} = 0$, the system falls back to the case of the classical circular restricted three body problem, with equilibrium positions consisting of the well-known five Lagrangian points. Small oscillations around Lagrangian points are expressed by the usual linear-variational solution of Szebehely [49]:

$$\begin{bmatrix}\xi \\ \eta\end{bmatrix} = \begin{bmatrix}C_1 \\ \bar{C}_1\end{bmatrix} cos(s_1 t) + \begin{bmatrix}S_1 \\ \bar{S}_1\end{bmatrix} sin(s_1 t) + \begin{bmatrix}C_2 \\ \bar{C}_2\end{bmatrix} cos(s_2 t) + \begin{bmatrix}S_2 \\ \bar{S}_2\end{bmatrix} sin(s_2 t) \tag{4.48}$$

Eigenfrequencies at triangular points have the closed form:

$$s_{1,2} = Im\left[\sqrt{(1/2)(-1 \pm \sqrt{1 - 27\nu_2(1-\nu_2)})}\right] \cdot \Omega \qquad [rad/s] \tag{4.49}$$

expressing a motion that is a combination of short-period terms, associated with the eigenfrequency s_1 and long-period terms, associated with s_2. The two characteristic eigenfrequencies are a function of the planetary system parameter ν_2.

The system of Eqs. 4.41–4.43 has no closed analytical solution, and a numerical analysis is required to solve for the trajectories. However, key features of this dynamical system can be derived with a qualitative dynamics analysis. In the following section equilibrium positions of the perturbed CRTBP are obtained, and the EDT equilibrium is analyzed.

4.2.4 Equilibrium positions

When the EDT orbits in a three-body environment with a plasmasphere, the Lorentz force (Eq. 4.24) perturbs the natural three-body motion and equilibrium positions different than Lagrangian points appear. When placed in these positions, the satellite can stay in equilibrium with respect to the synodic frame, because of the non-zero electrodynamic force acting on the tether.

The equilibrium positions in the perturbed case are the singular points (null acceleration and velocity) of the dynamical system described by Eqs. 4.41–4.43. The singular points are the solutions of the following equations:

$$\frac{\nu_1}{\rho_1^3}(\xi+\nu_2)+\frac{\nu_2}{\rho_2^3}(\xi-\nu_1)=\xi+f_\xi \tag{4.50}$$

$$\frac{\nu_1}{\rho_1^3}\eta+\frac{\nu_2}{\rho_2^3}\eta=\eta+f_\eta \tag{4.51}$$

$$\frac{\nu_1}{\rho_1^3}\zeta+\frac{\nu_2}{\rho_2^3}\zeta=f_\zeta \tag{4.52}$$

where f_ξ, f_η and f_ζ are the three non-dimensional components of the perturbing force,

$$(f_\xi, f_\eta, f_\zeta)=\left(F_{el,x}/md\Omega^2, F_{el,y}/md\Omega^2, F_{el,z}/md\Omega^2\right) \tag{4.53}$$

with components expressed in the synodic frame. From the system of Eq. 4.50–Eq. 4.52 the locations of the equilibrium positions (ξ_0, η_0, ζ_0) can be readily found, as a function of the perturbing electrodynamic force. Eq. 4.52 shows that the equilibrium positions outside the orbital plane of the two primaries are theoretically possible:

$$\zeta_0=\frac{f_\zeta}{\nu_1/\rho_1^3+\nu_1/\rho_1^3} \tag{4.54}$$

When the out-of-plane force vanishes $f_\zeta=0$, the equilibrium positions lie on the orbital plane $\zeta_0=0$. In our simplified model of the electrodynamic force for the EDT we have assumed $f_\zeta\approx 0$, thus no equilibrium positions exists in the out-of-plane region.

Making the substitution $\tau=1/\rho_1^3$ and $\chi=1/\rho_2^3$ the two-dimensional system of Eqs. 4.50–4.51 yields:

$$\begin{bmatrix}\nu_1(\xi+\nu_2) & \nu_2(\xi-\nu_1)\\ \nu_1\eta & \nu_2\eta\end{bmatrix}\begin{bmatrix}\tau\\ \chi\end{bmatrix}=\begin{bmatrix}\xi+f_\xi\\ \eta+f_\eta\end{bmatrix} \tag{4.55}$$

The determinant of the matrix on the left-hand side of Eq. 4.55 is $\nu_1\nu_2\eta$, and for $\eta\neq 0$ the matrix can be inverted to obtain (τ,χ). This corresponds to searching equilibrium positions outside the axis $\eta=0$ that joins the two primaries. Solving Eq. 4.55, the two distances ρ_1, ρ_2 of the equilibrium point from the two primaries are found as:

$$\rho_1 = \sqrt[3]{\frac{\nu_1\eta}{\nu_1\eta + f_\xi\eta + f_\eta(\nu_1 - \xi)}} \tag{4.56}$$

$$\rho_2 = \sqrt[3]{\frac{\nu_2\eta}{\nu_2\eta - f_\xi\eta + f_\eta(\nu_2 + \xi)}} \tag{4.57}$$

For $(f_\xi, f_\eta) = (0, 0)$ the external force vanishes, the distances from the primaries become unitary $\rho_1 = \rho_2 = 1$, and the equilibrium positions are the classical triangular Lagrangian points: $(\xi_0, \eta_0) = (1/2 - \nu_2, \pm\sqrt{3}/2)$.

For $(f_\xi, f_\eta) = (f_\xi, 0)$ the force acts purely in a direction parallel to the synodic ξ–axis. In this case Eqs. 4.56–4.57 show that the dependence of ρ_1, ρ_2 on the ξ coordinate disappears and an analytical solution of the equilibrium points (ξ_0, η_0) can be readily obtained:

$$\xi_0 = \frac{1}{2} - \nu_2 + \frac{1}{2}\left(\frac{1-\nu_2}{1-\nu_2+f_\xi}\right)^{2/3} - \frac{1}{2}\left(\frac{\nu_2}{\nu_2 - f_\xi}\right)^{2/3} \tag{4.58}$$

$$\eta_0 = \pm\sqrt{\left(\frac{1-\nu_2}{1-\nu_2+f_\xi}\right)^{2/3} - \left[\frac{1}{2} + \frac{1}{2}\left(\frac{1-\nu_2}{1-\nu_2+f_\xi}\right)^{2/3} - \frac{1}{2}\left(\frac{\nu_2}{\nu_2 - f_\xi}\right)^{2/3}\right]^2} \tag{4.59}$$

For $(f_\xi, f_\eta) \neq (0, 0)$ the perturbing components are both different from zero; no closed form exist, and the equilibrium position must be derived by means of a numerical method.

Interesting properties of the equilibrium locations can be inferred when we shift to a polar coordinate system (r_a, α), by making the substitutions: $\xi = r_a cos\alpha - \nu_2$ and $\eta = r_a \sin\alpha$, with r_a the non-dimensional radial distance from the first primary M_1 (see Fig. 4.15). In this new set of coordinates the distances from the primaries take the form:

$$\rho_1 = r_a \tag{4.60}$$

$$\rho_2 = \sqrt{r_a^2 + 1 - 2r_a\cos\alpha} \tag{4.61}$$

On the circle centered in M_1 and joining the triangular points with the second primary the radius r_a is unitary, $r_a = 1$, and the components of the force necessary for maintaining the equilibrium positions takes the simple expression:

$$\begin{bmatrix} f_\xi \\ f_\eta \end{bmatrix} = \nu_2\left(\frac{1}{\rho_2^3} - 1\right)\begin{bmatrix} \cos\alpha - 1 \\ \sin\alpha \end{bmatrix} \tag{4.62}$$

where $\rho_1 = 1$ and $\rho_2 = \sqrt{2 - 2\cos\alpha}$. Eq. 4.62 is the non-dimensional force that the tether (or any other thrust-device) must supply to remain stationary with respect to the synodic reference frame at a given angular position α in the circle joining the triangular points with the second primary. In dimensional units the magnitude of the force is:

$$F = md\Omega^2\sqrt{f_\xi^2 + f_\eta^2} = md\Omega^2\nu_2\rho_2\left|\frac{1}{\rho_2^3} - 1\right| \tag{4.63}$$

Eq. 4.63 shows that no external force is required to maintain an object at $|\alpha| = 60$ deg, that is at a triangular Lagrangian point, as expected. Figure 4.16 shows the two components f_ξ, f_η of the electrodynamic force from Eq. 4.62 of the non-dimensional force vs. the angle α, for all admissible values of the mass parameter $0 < \nu_2 < 1/2$. Note that a null external force is required at the Lagrangian triangular points ($\alpha = 60°$, $\alpha = 300°$). Singular conditions occur at $\alpha = 0° = 360°$, where the angular position of the second primary is reached by the spacecraft.

Figure 4.17 shows the non-dimensional force as a vector field superimposed to the synodic plane of the Jupiter-Io system ($\nu_2 = 4.7 \times 10^{-5}$). In the figure Jupiter is placed at $(-\nu_2, 0)$, Io at $(\nu_1, 0)$, and the five Lagrangian points are marked with a cross. The circle centered in Jupiter and joining Io with the triangular points is marked with a dotted circle. Each arrow in the figure shows the direction and the magnitude (with different scales as explained later) of electrodynamic force required to keep the spacecraft in equilibrium with respect to the synodic frame at locations different from Lagrangian points. Two main zones can be identified. The first one is a narrow zone encircling the circle centered in Jupiter and joining Io with the triangular points. In this region the force has its smaller magnitude (a scale $\times 2500$ has been used for visualization) and has a non-null tangential component. The second region is the remaining part of the synodic plane, which is cut into an inner and an outer zone by the orbit of Io. In this region the force is predominantly directed in the radial direction, pointing outward in the inner region ($0 < r < 1$) and pointing inward in the outer region ($r > 1$).

4.2.5 Self-powering at equilibrium positions

When the EDT is placed at an equilibrium position away from a Lagrangian point, a non-zero electrodynamic force acts upon it, and the EDT can supply electrical power to the spacecraft itself. The region of allowed equilibria for technologically feasible tethers lies inside the narrow region encircling the circle centered in M_1 and joining the triangular points with the second primary. When $M_2 << M_1$, as in all practical cases of the Solar System, the equilibrium points are all placed very close to the orbital path of the second primary, and their effective location is a function of environmental parameters (i.e., plasmasphere and planetary system), tether size, and plasma collection device.

In a general case, the attitude of the tether affects the magnitude and orientation of the electrodynamic force, and consequently the location of the equilibrium points. Assuming the EDT is self-balanced [50], the force vector acts on the center of mass of the system, and no net electrodynamic torques affect the orientation of the system. Under this hypothesis the equilibrium locations of the EDT can be obtained by considering only the effect of electrodynamic force, substituting the electrodynamic force (Eq. 4.23) in the equilibrium

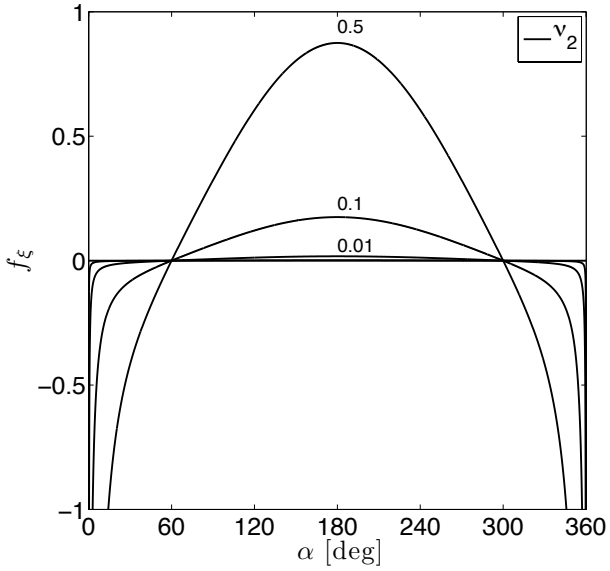

(a) f_ξ

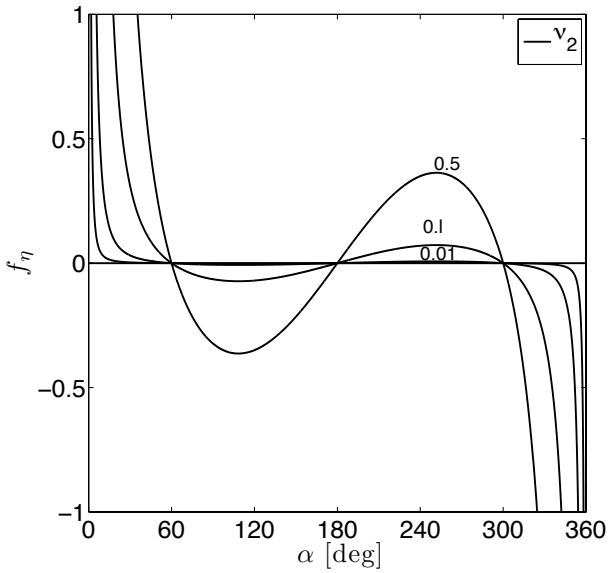

(b) f_η

Figure 4.16: (a) Non-dimensional force component f_ξ and (b) f_η required to maintain an equilibrium position with respect to the synodic frame as a funciton of the angle α.

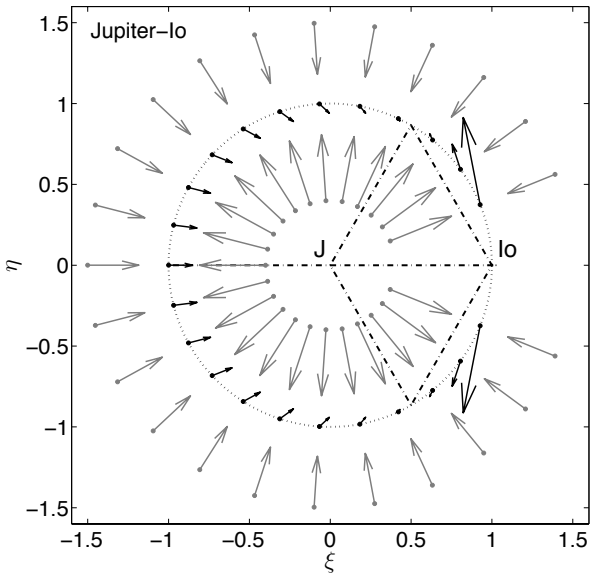

Figure 4.17: Non-dimensional force components (f_ξ, f_η) required to stay in equilibrium in the synodic frame at locations (marked by dots) different than classical Lagrangian points.

equations of the three-body (Eq. 4.50–4.52). A nonlinear least-squares algorithm has been used to find the roots of the system formed by Eq. 4.23 and Eqs. 4.50–4.52. A family of equilibrium locations has been obtained, stemming from the unperturbed triangular points L_4 and L_5. Numerical examples are shown in the following paragraph.

A useful simplified model has been derived to describe the powering conditions, under the following hypotheses: 1) the tether system is contained in the synodic plane (ξ, η) and points toward M_1; 2) the tether system is above the stationary orbit of M_1; 3) aligned and centered magnetic field generated by the first primary and rotating with the angular velocity of the primary Ω_1; 4) orientation of $\vec{\boldsymbol{B}}$ is from north to south (as in Jupiter and Saturn), thus in the synodic plane the unit vector of $\vec{\boldsymbol{B}}$ is $\hat{\boldsymbol{b}} = (0, 0, -1)$.

Under these simplifications, when the tether is at equilibrium (meaning that it has a zero velocity with respect the synodic frame), the projection of the motional electric field on the tether is simply given by:

$$E_t = B \cdot d \cdot (\Omega_1 - \Omega + \Omega\nu_2 \cos\alpha) \tag{4.64}$$

The Lorentz force vector, with its components expressed in the synodic frame, has the following simple expression which represents a counterclockwise force, tangential to the orbit of the second primary mass:

$${}^{syn}\vec{\boldsymbol{F}}_{el} = F_{el}\hat{\boldsymbol{u}} \times \hat{\boldsymbol{b}} = F_{el}(-\sin\alpha; \cos\alpha; 0) \tag{4.65}$$

where the force magnitude is given by:

$$F_{el} = \left(\frac{4}{3}\frac{q_e}{\pi}\sqrt{2\frac{q_e}{m_e}}\right)\left(1-\frac{2}{5}\zeta\right)\zeta^{3/2}\left(wL^{5/2}\right)\left(n_e B\sqrt{E_t}\right) \tag{4.66}$$

In these expressions the tether line $\hat{\boldsymbol{u}} = (\cos\alpha; \sin\alpha; 0)$ takes into account the direction of the current, which is imposed by the motional electric field pointing outward.

As shown previously a non-zero ED force is required to keep the EDT system in an off-Lagrangian equilibrium position. The scalar product of this force with the velocity relative to the plasma gives the ideal electrical power generated.

Under the hypotheses of the simplified model the ideal power for a tether placed at an angle α_0 along the orbit of the second primary is:

$$P_{id} = I_{avg} LBd\left(\Omega - \Omega_1 - \Omega\cos\alpha_0\nu_2\right) \tag{4.67}$$

In the two–body case, the mass parameter ν_2 vanishes and Eq. 4.67 simplifies to:

$$P_{id} = I_{avg} LBd\left(\Omega - \Omega_1\right) \tag{4.68}$$

From the comparison of simplified expressions Eq. 4.67 and Eq. 4.68 some important differences between the classical 2-Body case and the 3-Body case can be inferred. In the two-body the ideal power is simply driven by the difference $(\Omega - \Omega_1)$ between the orbital and plasma angular velocities. In the three body case the ideal power is reduced by the small term $\cos\alpha_0\nu_2$. The reduction term is of geometrical nature, and is due to the displacement between the centers of rotations of the plasmasphere and the corotating frame. The reduction term reaches the maximum value of 0.5 only in the limiting case when the planetary system has $M_1 = M_2$ and the equilibrium point reaches $\alpha_0 \approx 0$ at the location of the second primary. In all cases of practical relevance within the Solar System, the mass parameter is always small, $\nu_2 < 10^{-3}$ (except for system of asteroids), and the reduction of power due to the three-body effect is negligible. As a result, the power obtained in the three-body case is of the same order of magnitude of the two-body case, but has the additional feature of keeping the spacecraft at an equilibrium point without deorbiting.

4.2.6 Applications in the Jupiter Plasma Torus

As an example, the case of Jupiter-Io-EDT system is here discussed. Jupiter offers a unique environment for an EDT, due to the outstanding morphology of its magnetosphere and the fast rotation of the planet. All around the orbit of the Galilean moon Io, a region of increased plasma density called the Plasma Torus modifies and affects the Jupiter magnetosphere. The presence of the Plasma Torus is a consequence of the volcanic activity of the moon Io and its strong tidal heating. The motion of a spacecraft within the Torus is influenced by two main gravitational attractors, Jupiter and Io. Furthermore, all the

Lagrangian points of the Jupiter-Io-spacecraft system are contained inside the Torus. At first approximation, the motion of an EDT-spacecraft inside the Torus can be described by the equations of the circular restricted three body problem, with the addition of the electrodynamic force produced by the interaction of the EDT with the plasmasphere.

By using the model described in the previous sections, the dynamics of an EDT satellite inside the Jupiter Plasma Torus has been studied as a special case. High power levels (kilo-Watts and more) can be obtained by means of an EDT in the Io Torus. These power levels could be of great interest for Jovian missions, which are always handcuffed by the scarcity of power.

The Jupiter magnetic field rotates at the same angular velocity of the planet, with velocity $v_B = \Omega_1 r$, where $\Omega_1 \approx 1.76 \times 10^{-4}$ rad/s is the Jupiter angular rotation rate and r is the distance in the equatorial plane. Due to the high rotation rate of the planet, the stationary quote is relatively low at 2.238 R_j, and the velocity of the mangetic field at Io's orbit (5.9 R_j) is about 74 km/s. As a consequence, a spacecraft co-orbiting on the same orbital path of Io ($v_{sc} \approx 17.3$ km/s) has a velocity relative to the Jupiter's magnetic field $v_{rel} \approx 57$ km/s, that results in a motional electric field $E \approx 0.1$ V/m for a local magnetic field $B \approx 2 \times 10^{-6}$ T. The resulting electrodynamic force for a spacecraft placed in that location is a thrust force directed along the orbital velocity of the spacecraft.

An aligned dipolar model has been used for the Jupiter magnetic field:

$$\vec{\boldsymbol{B}}(\vec{\boldsymbol{r}}) = \frac{m}{r^3}\left[3\left(\hat{\boldsymbol{m}} \cdot \hat{\boldsymbol{r}}\right)\hat{\boldsymbol{r}} - \hat{\boldsymbol{m}}\right] \tag{4.69}$$

where $\vec{\boldsymbol{m}} = \mu_m R_j^3 \hat{\boldsymbol{m}}$ is the magnetic dipole moment vector of the planet, $\hat{\boldsymbol{m}}$ is its unit vector, μ_m is the intensity of the dipole [Tesla], R_j is the planet equatorial radius, $\vec{\boldsymbol{r}}$ is the position vector of the spacecraft.

The electron density N_e in the Torus is derived from the Divine and Garrett model [51], shown in Fig. 4.18 as a function of the radial distance from Jupiter. The locations of Io and of the four inner moonlets are marked by vertical lines in the figure. The presence of the plasma torus can be inferred from the electron density increase around the Io orbit at 5.9 R_j.

The expressions of equilibrium locations given by the system of Eqs. 4.50–4.52 plus Eq. 4.65–4.66 have been used to size tethers capable of maintaining the spacecraft in equilibrium in the corotating frame of the Jupiter-Io system. The angle α_0 identifys the equilibrium position of the tether on the circle centered in Jupiter and joining Io with the triangular points. It has been numerically determined for a set of cases as a function of the parameters L, w, m, that are the tether length, tether width and spacecraft mass, respectively. As expected, we found that the EDT parameters influence the magnitude of the force and, consequently, the location of the equilibrium point. Figure 4.19 shows for a 5 cm width tape tether the equilibrium angle α_0 vs. the spacecraft mass ranging from 200 to 1200 kg, for five tether lengths L=8,10,20,30,40 km. As can be seen from Figure 4.19, a "short" tether is sufficient to stay in equilibrium near a triangular point. The more the

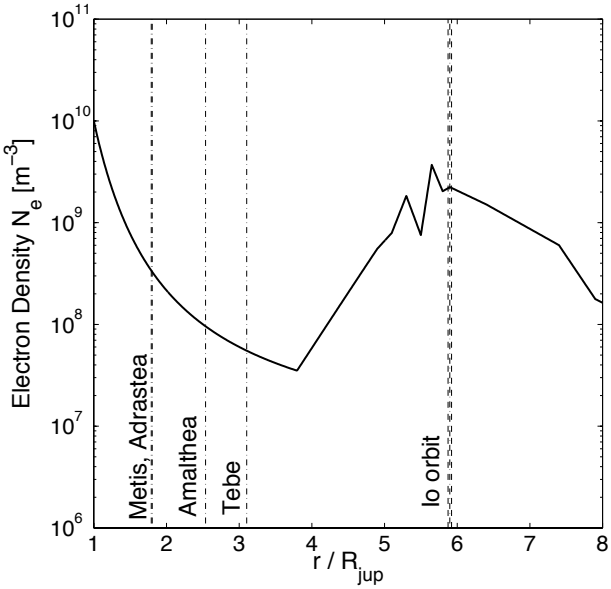

Figure 4.18: Electron density at Jupiter according to Divine and Garrett model (adapted from [51]).

position moves away from a triangular point toward the second primary (Io), the longer is the tether required or the smaller the satellite mass. This in turn implies that a greater electrodynamic force must be exerted to stay near the second primary body. For example, a tether with a constant length of 10 km, and a suitable spacecraft mass can have equilibrium positions within the range $\alpha = 34$ to 52 deg. Using a controlled variable-length tether and a constant-mass spacecraft, the equilibrium positions can be moved in region very close to the Io's orbital path and inside the Plasma Torus. The equilibrium positions coincide with the classical triangular points at $\alpha = \pm 60$ deg only when the electrodynamic force is equal to zero.

The useful power extracted by the EDT at equilibrium is shown in Figure 4.20, for the librating tether case. The ideal power given by Eq. 4.27 can be converted into about 30% for a librating tether, and 20% for a rotating tether (see [24] for details). The power is proportional to the tether length, with a law $P \propto L^{5/2}$, as mentioned earlier and also shown in this figure. Kilowatt-level of useful power can be delivered by the EDT to the spacecraft, by extracting the energy from the Jupiter plasmasphere.

A set of numerical simulations with an upgraded 3D model was carried out. This model integrates the 3D orbital dynamics of a rigid dumbbell satellite in the 3-body system (as described by Eq.4.40), plus the two angular degrees of freedom of its attitude dynamics. The two attitude angles evolve under the effect of the external gravitational torques of the two primaries. The numerical integration of the governing equations is carried out with a

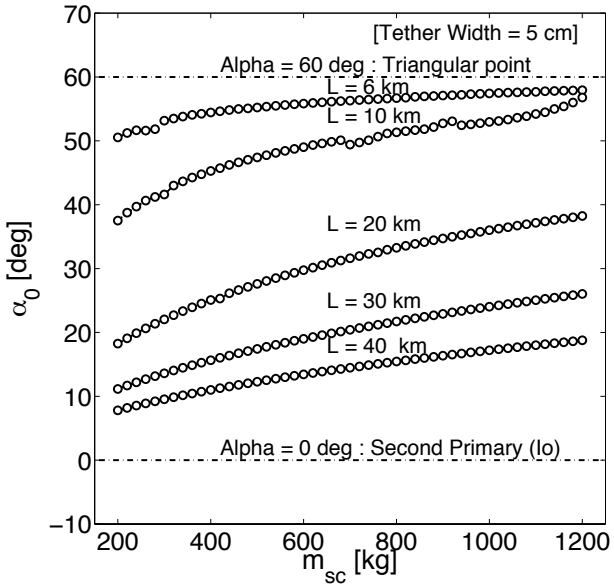

Figure 4.19: Equilibrium locations of an EDT as a function of the angle α in the Jupiter-Io system, on the orbital path of the second primary (Io).

standard Adam-Bashforth-Moulton 11th-order PECE routine [52]. A detailed description of the code implementing this model, together to its validation for a set of relevant cases of both orbital and attitude motion, can be found in [45]. A tilted dipolar magnetic field of Jupiter is considered to model the perturbing effects due to the oscillating field. The Divine and Garrett model [51] is adopted for the plasma electron density. The higher fidelity model confirmed the results obtained with the simplified model, finding that the EDT can remain in equilibrium at off-Lagrangian locations. Several values of mass, length and width were considered, in order to identify the equilibrium position for each configuration.

Figure 4.21 (a) shows a 20 km tether of 5 cm tape width and a 600 kg mass spacecraft in equilibrium in the corotating frame of Jupiter and Io, for a simulation time $t = 40T_{rev} \approx 70.76$ days (Io's $T_{rev} = 1.77$ days). The position of the spacecraft is at $\alpha_0 = 29.63°$, marked with the arrow-tail sign in the figure. The simplified model predicts an equilibrium position at $\alpha_0 = 29.75°$, in accordance with the higher fidelity model. Jupiter and Io are to scale, and their triangular points are also marked in the figure. Figure 4.21 (b) depicts small oscillations around the equilibrium point that exhibits a motion characterized by two eigenfrequencies, analogous to the unperturbed motion around the natural Lagrangian points. The two eigenfrequencies of the classical circular restricted three body problem [49] are expressed by Eq. 4.49.

A Lorentz force of about 0.06 N is exerted on the system, producing a useful power of about 1130 Watts for on-board use (see Fig. 4.22). The perturbation due to the other

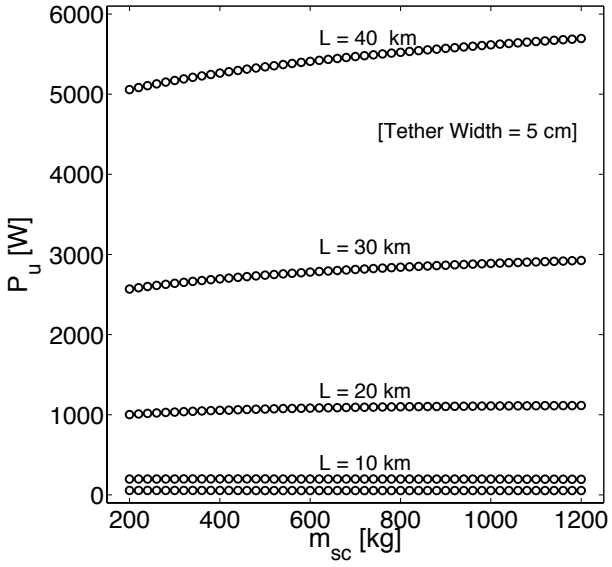

Figure 4.20: Useful power at equilibrium for a librating tether vs. spacecraft mass.

Galilean satellites is always smaller than this electrodynamic force. The main perturbation is given by the attraction of Europa and Ganymede, being in the worst case one order of magnitude less than the electrodynamic force. However, the effect of the other moons could not be completely neglected because of the Laplace resonance 1:2:4 between the orbital periods of Io, Europa and Ganymede, that can lead to a pumping effect to a satellite placed on the Io orbit. These kind of effects are not addressed in the present study. Numerical simulations with a 4-body simulator have revealed that equilibrium can be reached also in the perturbed case and the equilibrium is disrupted after a long period of time.

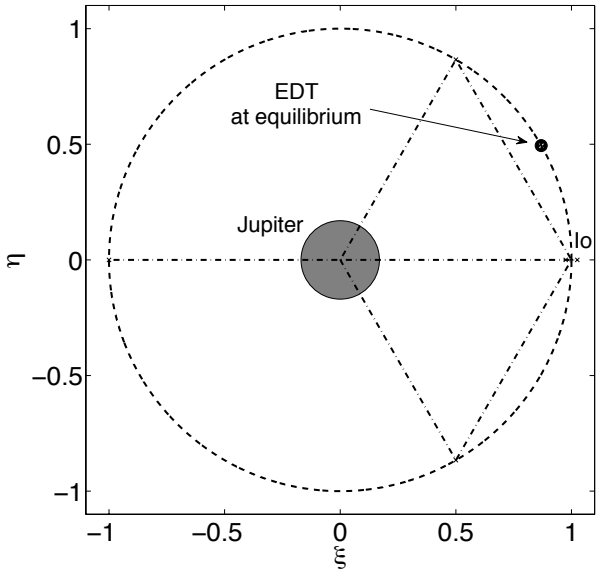

(a)

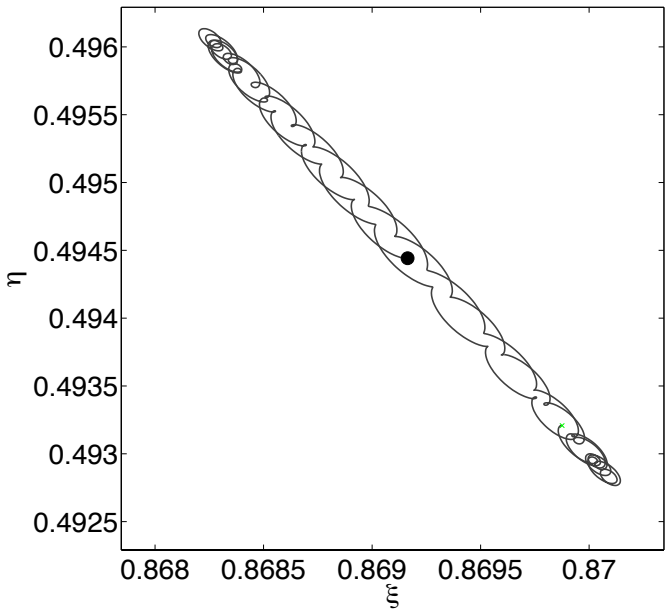

(b)

Figure 4.21: (a) EDT at equilibrium in the Jupiter-Io system, and (b) small oscillations around the equilibrium position.

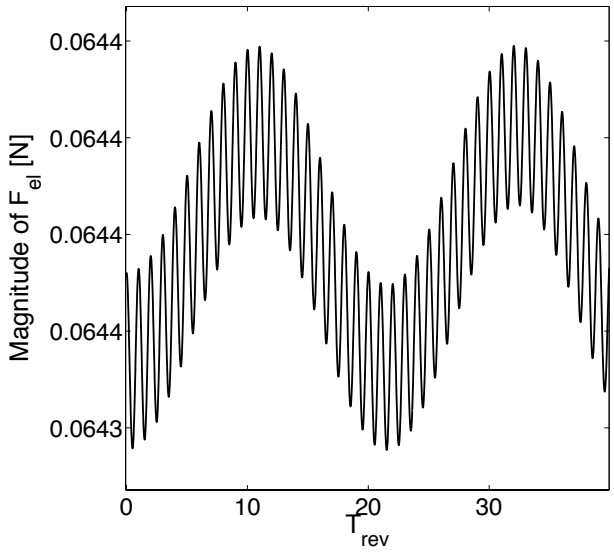

(a)

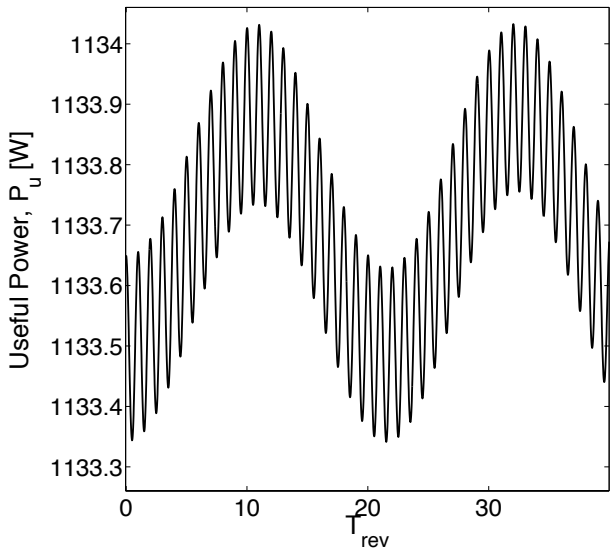

(b)

Figure 4.22: (a) Electrodynamic force and (b) generated power vs orbital revolutions (Io's $T_{rev} = 1.77$ days) by a 20-km EDT at equilibrium at Jupiter obtained with the higher fidelity model EDT3BODY. These results are in accordance with the simplified model, which gives $F_{el} = 0.064\ N$ and $P_u = 1082\ W$.

Conclusion

In the present work, helicon plasma sources have been analyzed in detail, in order to identify strategies for high-density and high-electron-temperature plasmas, necessary for system design of an advanced and innovative kind of thruster.

At first, a theory describing the equilibrium of a cylindrical helicon discharge has been derived. This involved an in-depth analysis of the phenomena occurring inside an helicon discharge and the development of a quantitative model of the interested plasma parameters. This problem was solved only partially in literature. Two theoretical sub-problems have been resolved, the first regarding the plasma-wave coupling, the second regarding the macroscopic transport of ions electrons and neutrals inside the plasma discharge. It has been found that the two sub-problems are strictly related one to the other, and that only when considered together they concur to the determination of the global equilibrium of the plasma. The plasma-wave coupling problem has been solved using a classical treatment, the theory of Chen-Arnush [2],[3],[4]. This theory describes the coupling of electrons to the radio-frequency field by means of two families of plasma waves, Trivelpiece-Gould and Helicon; this model allows the evaluation of the electromagnetic fields occurring inside the plasma column for assumed profiles of charged and neutral species. These profiles comes from the solution of the second problem, the macroscopic transport. The transport theory has been developed within the contest of this thesis. It solves for a quasi-neutral plasma along the radius of the cylinder, considering local collisional process, local ionization balance and local power deposition. The system is closed by taking into account the short circuit effect of electrons at the axial end walls of the plasma cylinder. The local input power comes from the solution of the plasma-wave coupling. The theory allows the evaluation of profiles at equilibrium of drift velocity, plasma potential, plasma density, neutral density and electron temperature. A numerical code implementing the theory has been developed and used for the calculations of equilibrium conditions. The HELIC code developed at UCLA [4] was used for the solutions of the plasma-wave coupling. A second code, called EQM, was developed for the solution of the macroscopic transport problem. From the iteration of the two codes together the equilibrium of an helicon plasma column has been calculated. One of the results from the theory development allowed a direct evaluation of the discharge profiles for a given amount of power. Examples under several conditions are reported. The code allowed study of helicon discharges. All the involved parameters

are strongly coupled together; electrons are heated locally by the electromagnetic fields, and their temperature modifies the local acoustic velocity of ions. This in turns affects the drift velocity and the resulting profile of plasma. Neutral depletion is also taken into account. Neutrals are depleted by the plasma, mostly at the center of the cylinder.

An extensive experimental campaign at UCLA Laboratory[1] has been done, to validate the theory. Helicon sources were tested under several operative conditions, with measurements done using RF-compensated Langmuir probes. The I-V characteristics of the probes have been analyzed using the standard OML theory, to obtain plasma densities, electron temperature and plasma potential. Power scans, radial scans, axial scans at several pressures and for two RF frequencies (13.56 and 27.12 MHz) have been done. From the comparison of experimental measures with the calculated data, an agreement has found within their uncertainties. The numerical model developed is not only a very useful tool for preliminary design a plasma thruster, but it's also a powerfull tool to perfom indirect measurements on its physical parameters.

The theory has thus been applied for the preliminary design of a thruster using an helicon source. The helicon-source-only propulsive system was thought, composed by a cylindrical plasma chamber with the propellant excited by an helicon antenna. The presence of an additional acceleration mechanisms (magnetic nozzle, double layers, etc.) is desirable but not necessary. As expected, it has been found that this system receives an enhancement in performances as a function of the ionization fraction, shifting gradually from the cold-gas-thruster regime at low f_{iz} to the helicon-thruster regime at high f_{iz}. A target system with thrust 1mN and Isp 1000 seconds working at very low power has been addressed. The strong intercorrelations between the design parameters in described. A list of possible thruster configurations satisfying the target requisites has been obtained.

Finally, a propellantless plasma system has been considered, an electrodynamic tether, and innovative applications of such a systems have been proposed. The Lorentz force produced by an electrodynamic tether placed inside the plasmasphere of a three-body planetary system has been modeled, with a focus on system dynamics and power generation at equilibrium points of the gravitational system. It was found the Lorentz force produced by the tether through the interaction with the super-rotating plasma sphere perturbs the natural Lagrangian equilibrium points, and new equilibrium positions appears with respect to the synodic frame corotating with the primary bodies. The equilibrium is among the two gravitational forces of the two primaries, the inertial forces and the local Lorentz force. The results of simplified model developed to derive the equilibria locations in the synodic plane shows that for technologically feasible tethers those points are located along the circle centered in the first primary and joining the triangular points with the second primary. Differently from the two body case, in the three-body scenario an EDT can be placed at equilibrium position and at the same time generate electrical power, without de-orbiting. The electrical power is generated at the expense of the corotating plasma energy. A higher

[1] Low Temperature Plasma Technology Laboratory, University of California Los Angeles

fidelity numerical model confirmed the presence of equilibrium positions and the possibility to place an electrodynamic tether in their neighborhood while extracting power from the environmental plasma. The analysis has been applied to the Jupiter-Io system, where the presence of the Plasma Torus make this region an attractive place for an EDT to operate. An EDT in the Plasma Torus can generate in a continuous way kilo-Watts of useful power (with a tether length of order 20 km and more), that can be used on board the spacecraft.

Bibliography

[1] Klozenberg J. P., McNamara B., Thonemann P. C., *The dispersion and attenuation of helicon waves in a uniform cylindrical plasma*, J. Fluid Mech. 21, 545 (1965).

[2] F. F. Chen and D. Arnush, *Generlized theory of helicon waves. Part I Normal modes*, Phys. Plasmas 4, 3411 (1997).

[3] F. F. Chen and D. Arnush, *Generlized theory of helicon waves. Part II Excitations*, Phys. Plasmas 5, 1239 (1998).

[4] D. Arnush, *The role of Trivielpiece-Gould waves in antenna coupling to helicon waves*, Phys. Plasmas 7, 3042 (2000).

[5] W. P. Allis, S. J. Buchsbaum, and A. Bers, *Waves in Anisotropic Plasmas*, MIT Press, Cambridge, MA, 1963.

[6] Tonks and Langmuir, *A General Theory of the Plasma of an Arc*, Phys. Rev. 34, 876-922, (1929), doi: 10.1103/PhysRev.34.876

[7] K. B. Person, Physics of Fluids, 5, 1625 (1962).

[8] G. S. Kino and E. K. Shaw, Phys. Fluids 9, 587 (1966).

[9] S. A. Self and H. N. Ewald, Physics of Fluids, 9, 2486 2986 (1966).

[10] V. Godyak, *Soviet Radio Frequency Discharge Research*, Delphic Associates (1986).

[11] L. Cervenan and V. Martisovitz, Czech Journal of Physics, B26, 507 (1976).

[12] E. Clementi, D. L. Raimondi, and W. P. Reinhardt (1967), Journal of Chemical Physics, volume 47, page 1300.

[13] A. V. Phelps, Chris H. Greene and J. P. Burke Jr., *Collision cross sections for argon atoms with argon atoms for energies from 0.01 eV to 10 keV*, J. Phys. B, 33 (2000) 2965–2981.

[14] D. Rapp and W. E. Francis, *Charge Exchange between gaseous ions and atoms*, J. of Chemical Physics, Vol.37, pp.2631-2645 (1962)

[15] B M Smirnov *The Sena effect*, Phys.-Usp. 51 291-293 (2008). doi: 10.1070/PU2008v051n03ABEH006542

[16] Vladimir Aleksandrovich Rozhanski?, Lev D. Tsendin, *Transport phenomena in partially ionized plasma*, Taylor & Francis, 2001, ISBN 0415271878, 9780415271875

[17] F.F. Chen, *Introduction to Plasma Physics and Controlled Fusion*, Vol. 1, 2 ed. (Plenum, New York, 1984), p. 173.

[18] A. Simon, Phys. Rev. 98, 317 (1955).

[19] F. F. Chen and J.P. Chang, Principles of Plasma Processing (Kluwer/Plenum, New York, 2002), p. 70ff.

[20] F.F. Chen and H. Torreblanca, Plasma Sources Sci. Technol. 16, 593 (2007).

[21] V. Vahedi, *Modeling and simulation of rf discharges used for plasma processing*, Thesis, University of California, Berkeley (1993). Recent data are from P. Vitello, LLNL.

[22] D. Curreli and F. F. Chen, *A Novel Equilibrium Theory of Helicon Discharges*, 63rd Gaseous Electronics Conference and 7th International Conference on Reactive Plasmas, 4-8 October 2010, Maison de la Chimie, Paris.

[23] F. F. Chen, *The low-field density peak in helicon discharges*, Physics of Plasmas, Vol. 10, N. 6, June 2003

[24] Bombardelli, C., Lorenzini, E. C., and Sanmartìn, J. R., "Jupiter Power Generation with Electrodynamic Tethers at Constant Orbital Energy," *Journal of Propulsion and Power*, Vol. 25, March-April 2009, pp. 415–423.
doi: 10.2514/1.38764

[25] Peláez, J., Lorenzini, E. C., Lopez-Rebollal, O., and Ruiz, M., "A New Kind of Dynamic Instability in Electrodynamic Tethers," *Advances in Astronautical Sciences*, Vol. 105, 2000, pp. 1367–1368.

[26] Dobrowolny, M., Arnold, D., Colombo, G., and Grossi, M., "Mechanisms of electrodynamic interactions with a tethered satellite system and the ionosphere," *Reports in Radio and Geoastronomy*, Vol. 6, August 1979.

[27] Estes, R. D., Lorenzini, E. C., Sanmartín, J. R., Peláez, J., Martínez-Sanchez, M., Johnson, C. L., and Vas, I. E., "Bare Tethers for Electrodynamic Spacecraft Propulsion," *Journal of Spacecraft and Rockets*, Vol. 37, March-April 2000, pp. 205–211.
doi: 10.2514/2.3567

[28] Takeichi, N., "Practical Operation Strategy for Deorbit of an Electrodynamic Tethered System," *Journal of Spacecraft and Rockets*, Vol. 43, November-December 2006, pp. 1283–1288.
doi: 10.2514/1.19635

[29] Johnson, L., Estes, R. D., Lorenzini, E. C., Martínez-Sanchez, M., and Sanmartín, J. R., "Propulsive Small Expendable Deployer System Experiment," *Journal of Spacecraft and Rockets*, Vol. 37, no. 2, 2000, pp. 173– 176.
doi: 10.2514/2.3563

[30] Gilchrist, B. E., Bilen, E., Sven, G., and Johnson, L., "Space Electrodynamic Tether Propulsion Technology - System Considerations and Future Plans," *AIAA/ASME/SAE/ASEE Joint Propulsion Conference and Exhibit, 35th*, Los Angeles, CA, United States, 1999.

[31] Alfven, H., "Spacecraft Propulsion: New Methods," *Science*, Vol. 176, 14 April 1972, pp. 167–168.
doi: 10.1126/science.176.4031.167

[32] Gabriel, S. B., Jones, R. M., and Garrett, H. B., "Alfven Propulsion at Jupiter," *International Conference on Space Tethers for Science in the Space Station Era*, L. Guerriero and I. Bekey, eds., Vol. 14, 4-8 October 1987.

[33] Sanmartín, J. R., and Lorenzini, E. C., "Exploration of Outer Planets Using Tethers for Power and Propulsion," *Journal of Propulsion and Power*, Vol. 21, May–June 2005, pp. 573–576.
doi: 10.2514/1.10772

[34] Sanmartín, J. R., Charro, M., Bramanti, C., Bombardelli, C., Lorenzini, E. C., and Garrett, H. B., "Electrodynamic Tether Microsats at the Giant Planets," Tech. Rep. Final Report Ariadna Study 05/3203, Advanced Concept Team ESA, September 2006.

[35] Bombardelli, C., Lorenzini, E. C., Curreli, D., Sanjurjo-Rivo, M., Lucas, F., and Lara, M., "Io Exploration with Electrodynamic Tethers," *AIAA/AAS Astrodynamic Specialist Conference*, AIAA-2008-7384, AIAA/AAS Astrodynamics Specialist Conference and Exhibit, Honolulu, Hawaii, Aug. 18-21, 2008.

[36] Penzo, P., "A Survey of Tether Applications to Planetary Exploration," *Tethers in Space, Proceedings of First International Conference on Tethers in Space*, Advances in the Astronautical Sciences, Sept. 17-19, 1986, Arlington, VA, 1987, Eds. Peter M. Bainum, Ivan Bekey, Luciano Guerriero and Paul A. Penzo.

[37] Colombo, G., "The Stabilization of an Artificial Satellite at the Inferior Conjunction Point of the Earth-Moon system," Special Report 80, Smithsonian Astrophysical Observatory, September 1961.

[38] Farquhar, R. W., "The Control and Use of Libration-Point Satellites," NASA TR R-346, September 1970.

[39] Misra, A. K., "Dynamics of a Tethered System Near the Earth-Moon Lagrangian Points," *Advances in Astronautical Sciences*, Vol. 109, Quebec City, Canada, 2001, pp. 415–435.

[40] Wong, B. and Misra, A. K., "Dynamics of a Multi-Tethered System Near the Sun-Earth Lagrangian Point," Vol. 13th AAS/AIAA Space Flight Mechanics Meeting, Ponce, Puerto Rico, February 2003.

[41] Wong, B. and Misra, A. K., "Dynamics of a Libration Point Multi-Tethered System," *Proceedings of 2004 International Astronautical Congress*, IAC-04-A.5.09, 2004.

[42] Peláez, J., and Sheeres, D. J., "A Permanent Tethered Observatory at Jupiter. Dynamical Analysis," *AAS/AIAA Space Flight Mechanics Meeting*, Sedona, Arizona, January 28 - February 1 2007.

[43] Peláez, J., and Sheeres, D. J., "On the Control of a Permanent Tethered Observatory at Jupiter," *AAS/AIAA Astrodynamics Specilist Conference*, Mackinac Island, Michigan, August 19-23 2007.

[44] Sanjurjo-Rivo, M., Lucas, F., Peláez, J., Bombardelli, C., Lorenzini, E. C., Curreli, D., Sheeres, D. J., and Lara, M., "On the Dynamics of a Tethered System Near the Collinear Libration Point," *AIAA/AAS Astrodynamic Specialist Conference*, AIAA 2008-7380, 2008.

[45] Peláez, J., Sanjurjo-Rivo, M., Lara, M., Lorenzini, E. C., Curreli, D., Sheeres, D. J., Bombardelli, C., and Izzo, D., "Dynamics and Stability of Tethered Satellites at Lagrangian Points," Tech. Rep. Final Report Ariadna Study 07-4201, Advanced Concept Team ESA, November 2008, available online http://www.esa.int/gsp/ACT/ariadna/studies.htm.

[46] Sanmartín, J. R., Martínez-Sanchez, M., and Ahedo, E., "Bare Wire Anodes for Electrodynamic Tether," *Journal of Propulsion and Power*, Vol. 9, 1993, pp. 352–320.
doi: 10.2514/3.23629

[47] Mott-Smith, H. M. and Langmuir, I., "The Theory of Collectors in Gaseous Discharges," *Physical Review*, Vol. 28, No. 4, 1926, pp. 727–763.
doi: 10.1103/PhysRev.28.727

[48] Chen, F. F., "Langmuir probe analysis for high density plasmas ," *Physics of Plasmas*, Vol. 8, No. 6, June 2001, p. 3029-3041.
doi: 10.1063/1.1368874

[49] Szebehely, V., "Motion near the Equilibrium Points," *Theory of Orbits - The Restricted Problem of Three Bodies*, , Academic Press, New York and London, 1967, pp. 231-308.

[50] Peláez, J., "Self Balanced Electrodynamic Tethers," *AIAA/AAS Astrodynamics Specialist Conference and Exhibit*, 16-19 August 2004.

[51] Divine, N., and Garrett, H. B., "Charged Particle Distributions in Jupiter's Magnetosphere," *Journal of Geophysical Research*, Vol. 88, September 1983, pp. 6889–6903. doi: 10.1029/JA088iA09p06889

[52] Shampine, L. F., "Numerical Solution of Ordinary Differential Equations". New York: Chapman & Hall, 1994.

[53] Trivelpiece A. W. and Gould R. W., J. Appl. Phys. 30, 1784 (1959).

[54] D. D. Blackwell, T. G. Madziwa, D. Arnush, and F. F. Chen, *Evidence for Trivelpiece-Gould Modes in a Helicon Discharge*, Phys. Rev. Letters, 88, 14 (2002); doi:10.1103/PhysRevLett.88.145002

[55] D. D. Blackwell and F. F. Chen, *Two dimensional imagin of a helicon discharge*, Plasma Sources Sci. Technol. 6 (1997) 569-576.

[56] I. D. Sudit and F. F. Chen, Plasma Sources Sci. Technol., 3, 162, 1994.

[57] F. F. Chen, *Physical mechanism of current-free double layers* , Phys. Plasmas 13, 034502 (2006); doi:10.1063/1.2179393

[58] M. Brambilla, *Kinetic theory of Plasma Waves*, International series of monographs on Physics, Oxford Science Publications, 1998.

[59] H. M. Mott-Smith and Irving Langmuir, *The Theory of Collectors in Gaseous Discharges*, Phys. Rev. 28, 727–763 (1926).

[60] F. F. Chen, *Electric Probes*, in "Plasma Disgnostic Techniques", ed. by R. H. Huddlestone and S. L. Leonard (Academic Press, New York), Chap. 4, pp. 113-200 (1965).

[61] Lagarias, J.C., J. A. Reeds, M. H. Wright, and P. E. Wright, "Convergence Properties of the Nelder-Mead Simplex Method in Low Dimensions," SIAM Journal of Optimization, Vol. 9 Number 1, pp. 112-147, 1998.

[62] M. J. Druyvesteyn, Z. Phys. 64, 781 (1930)

[63] F. F. Chen, *Time-varying impedance of the sheath on a probe in an RF plasma*, Plasma Sources Sci. Technol. 15 (2006) 773-782, doi:10.1088/0963-0252/15/4/022

[64] F. F. Chen, *Langmuir probes in RF plasma: surprising validity of OML theory*, Plasma Sources Sci. Technol. 18, (2009) 035012 (13pp).

[65] S. A. Andersen, V. O. Jensen, P. Nielsen, and N. D'Angelo, Phys. Fluids 12, 557 (1969).

[66] M. A. Lieberman, C. Charles, *Theory of formation of a Low-Pressure, current-free Double Layer*, Physical Review Letters, PRL 97, 045003 (2006).

Appendix A

Plasma waves

A.1 Dielectric tensor of a cold plasma ($T = 0$)

The dielectric tensor of an infinite homogeneous cold ($T = 0$) plasma can be treated using the motion of a single particle in an electromagnetic field:

$$m\frac{d}{dt}\vec{v}_j = q_j(\vec{E} + \vec{v} \times \vec{B}) \tag{A.1}$$

where j is the species index, and the fields are the solution of Maxwell equations:

$$\nabla \times \vec{E} = -\frac{\partial \vec{B}}{\partial t} \tag{A.2}$$

$$\nabla \times \vec{B} = \mu_0 \left(\vec{J} + \epsilon_0 \frac{\partial \vec{E}}{\partial t} \right) \tag{A.3}$$

Assuming small perturbations

$$\vec{E} = \vec{E}_1 e^{i(\vec{k}\cdot\vec{r} - \omega t)} \tag{A.4}$$

$$\vec{B} = \vec{B}_0 + \vec{B}_1 e^{i(\vec{k}\cdot\vec{r} - \omega t)} \tag{A.5}$$

$$\vec{v} = \vec{v}_1 e^{i(\vec{k}\cdot\vec{r} - \omega t)} \tag{A.6}$$

and

$$|\vec{B}_1| << |\vec{B}_0| \tag{A.7}$$

$$\vec{B}_0 = (0, 0, B_z) \tag{A.8}$$

the motion of particles becomes linear:

$$-i\omega m_j \vec{v}_{1j} = q_j(\vec{E}_1 + \vec{v}_{1j} \times \vec{B}_0) \tag{A.9}$$

The solution (analytical) is:

$$v_{xj} = \frac{iq_j}{m_j(\omega^2 - \omega_{cj}^2)}(\omega E_x + \text{sign}(j) i\omega_{cj} E_y) \tag{A.10}$$

$$v_{yj} = \frac{iq_j}{m_j(\omega^2 - \omega_{cj}^2)}(-i\text{sign}(j)\omega_{cj} E_x + \omega E_y) \tag{A.11}$$

$$v_{zj} = \frac{iq_j}{m_j\omega} E_z \tag{A.12}$$

where sign(j) is the sign of charges belonging to the species j, and $\omega_{cj} = |q_j|B_0/m_j$ is the cyclotron frequency of the species j. In the rotating frame the velocity becomes $v_\pm = v_x \pm iv_y$ and the (circularly polarized) electric field $E_\pm = (E_x \pm iE_y)/\sqrt{2}$, so that

$$v_\pm = \frac{iq_j}{m_j(\omega \mp \text{sign}(j)\omega_{cj})} E_\pm \tag{A.13}$$

The plasma current density is thus given by:

$$J_\pm = i\epsilon_0 \sum_j \frac{\omega_{pj}^2}{\omega \mp \text{sign}(j)\omega_{cj}} E_\pm \tag{A.14}$$

$$J_z = i\epsilon_0 \sum_j \frac{\omega_{pj}^2}{\omega} E_z \tag{A.15}$$

where ω_{pj} is the plasma frequency of the species j,

$$\omega_{pj}^2 = \frac{n_j q_j^2}{m_j \epsilon_0}. \tag{A.16}$$

The total current (plasma plus displacement), leads to the following constitutive (Ohm) relation for the cold plasma:

$$\vec{J}_{tot} = \vec{J} - i\omega\epsilon_0 \vec{E} = -i\omega\epsilon_0 \left[K\right] \vec{E} \tag{A.17}$$

where the dielectric tensor is given by (using classical notation by Stix, 1962):

$$[K] = \begin{bmatrix} S & -iD & 0 \\ iD & S & 0 \\ 0 & 0 & P \end{bmatrix} = \begin{bmatrix} K_1 & K_2 & 0 \\ -K_2 & K_1 & 0 \\ 0 & 0 & K_3 \end{bmatrix} \tag{A.18}$$

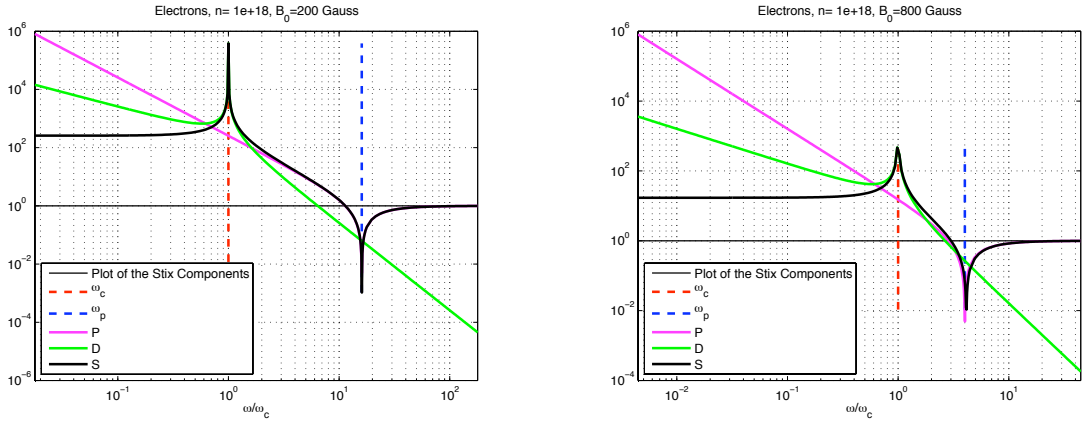

Figure A.1: Values of the Stix components S, D, P for a single-species electrons plasma

with

$$K_1 = S = \frac{1}{2}(R+L) = 1 - \sum_j \frac{\omega_{pj}^2}{\omega^2 - \omega_{cj}^2} \tag{A.19}$$

$$iK_2 = D = \frac{1}{2}(R-L) = \sum_j \frac{\text{sign}(j)\omega_{cj}}{\omega} \frac{\omega_{pj}^2}{\omega^2 - \omega_{cj}^2} \tag{A.20}$$

$$K_3 = P = 1 - \sum_j \frac{\omega_{pj}^2}{\omega^2} \tag{A.21}$$

$$R = S + D = K_1 + iK_2 = 1 - \sum_j \frac{\omega_{pj}^2}{\omega^2} \frac{\omega}{\omega + \text{sign}(j)\omega_{cj}} \tag{A.22}$$

$$L = S - D = K_1 - iK_2 = 1 - \sum_j \frac{\omega_{pj}^2}{\omega^2} \frac{\omega}{\omega - \text{sign}(j)\omega_{cj}} \tag{A.23}$$

Figure A.1 shows the three Stix components for a single species plasma of electrons. The two quantities L and R are the diagonal components of the dielectric tensor in the rotating frame (circularly polarized),

$$[K] = \begin{bmatrix} L & 0 & 0 \\ 0 & R & 0 \\ 0 & 0 & P \end{bmatrix} \tag{A.24}$$

The transformation matrix between the two systems (cartesian x, y, z and rotating polar-

ized $+, -, z$) is given by:

$$\begin{bmatrix} E_+ \\ E_- \\ E_z \end{bmatrix} = \begin{bmatrix} 1/\sqrt{2} & i/\sqrt{2} & 0 \\ 1/\sqrt{2} & -i/\sqrt{2} & 0 \\ 0 & 0 & 1 \end{bmatrix} \begin{bmatrix} E_x \\ E_y \\ E_z \end{bmatrix} \tag{A.25}$$

Now substituting $\vec{J}_{tot}$ in the Fourier transform of the two Maxwell wave equations

$$i\vec{k} \times \vec{E} = i\omega\vec{B} \tag{A.26}$$

$$i\vec{k} \times \vec{B} = -i\omega\epsilon_0\mu_0 \, [K] \, \vec{E} \tag{A.27}$$

the following wave equation of the index refraction vector is finally found:

$$\vec{n} \times (\vec{n} \times \vec{E}) + [K] \, \vec{E} = 0 \tag{A.28}$$

where

$$\vec{n} = \frac{\vec{k}c}{\omega} \tag{A.29}$$

is the index refraction vector, pointing in the same direction of the wave vector and with magnitude equal to the local refraction index. Usually the equation of the refraction index vector is expressed in a convenient reference frame. Deciding that $\vec{n}$ lies in the x, z plane ($\vec{B}_0$ is already aligned to the z axis), and calling θ the angle between $\vec{n}$ and z, the index refraction vector equation becomes:

$$\begin{bmatrix} S - n^2\cos\theta & -iD & n^2\cos\theta\sin\theta \\ iD & S - n^2 & 0 \\ n^2\cos\theta\sin\theta & 0 & P - n^2\sin\theta \end{bmatrix} \begin{bmatrix} E_x \\ E_y \\ E_z \end{bmatrix} = 0 \tag{A.30}$$

Non-trivial solutions (the determinant of the matrix) constitutes the dispersion relation, which is:

$$An^4 + Bn^2 + C = 0 \tag{A.31}$$

where

$$A = S\sin^2\theta + P\cos^2\theta \tag{A.32}$$

$$B = RL\sin^2\theta + PS(1 + \cos^2\theta) \tag{A.33}$$

$$C = PRL \tag{A.34}$$

The solution is usually given in term of the angle, to better express cutoffs and resonances:

$$\tan^2\theta = -\frac{P(n^2 - R)(n^2 - L)}{(Sn^2 - RL)(n^2 - P)} \tag{A.35}$$

The plasma wave propagates parallel to $\vec{B}_0$ when the numerator vanishes (plasma oscillations, right-handed and left-handed polarized waves), and perpendicular to $\vec{B}_0$ when the denominator vanishes (ordinary and extraordinary waves). Propagation at arbitrary θ includes torsional and compressional Alfvén waves, and whistler waves. The CMA diagram is the usual way to resume the behavior of a cold uniform plasma in a single graph, for fast recognition of resonances and cutoffs.

A.2 Dielectric tensor with fluid collisions

In presence of electron-neutral collisions, the Krook model can be used (neutrals are much slower than electrons), and the equation of motion becomes:

$$m_e n_e \left[\frac{\partial \vec{v}_e}{\partial t} + \vec{v}_e \cdot \nabla \vec{v}_e\right] = -enn_e(\vec{E} + \vec{v}_e \times \vec{B}) - \nabla p_e - m_e n_e \vec{v}_e \nu \tag{A.36}$$

where ν_{en} is the electron neutral collision frequency. In frequency domain,

$$(\nu - i\omega) m_e n_e \vec{v}_e = -en_e(\vec{E} + \vec{v}_e \times \vec{B}) - \nabla p_e \tag{A.37}$$

and thus the modification in the dielectric tensor is done with the formal substitution of the electron mass $m_e \to m_e/(1 + i\nu\omega)$. It results:

$$K_1 = S = \frac{1}{2}(R + L) = 1 - \sum_j \frac{\omega_{pj}^2(\omega + i\nu_j)}{\omega[(\omega + i\nu)^2 - \omega_{cj}^2]} \tag{A.38}$$

$$iK_2 = D = \frac{1}{2}(R - L) = \sum_j \frac{\text{sign}(j)\omega_{cj}}{\omega} \frac{\omega_{pj}^2}{(\omega + i\nu)^2 - \omega_{cj}^2} \tag{A.39}$$

$$K_3 = P = 1 - \sum_j \frac{\omega_{pj}^2}{\omega(\omega + i\nu)} \tag{A.40}$$

$$R = S + D = K_1 + iK_2 = 1 - \sum_j \frac{\omega_{pj}^2}{\omega^2} \frac{\omega}{\omega + i\nu_j + \text{sign}(j)\omega_{cj}} \tag{A.41}$$

$$L = S - D = K_1 - iK_2 = 1 - \sum_j \frac{\omega_{pj}^2}{\omega^2} \frac{\omega}{\omega + i\nu_j - \text{sign}(j)\omega_{cj}} \tag{A.42}$$

A.3 Generalization to non-Maxwellian plasmas

Here we will show how the dielectric tensor of the plasma is modified by a generic non-Maxwellian distribution. For the treatment we will follow an approach proposed by [cite

M. Brambilla]. We split the distribution function of each plasma species α into a stationary and oscillating part,

$$f_\alpha(\vec{r},\vec{v},t) = F_\alpha(\vec{r},\vec{v}) + \tilde{f}_\alpha(\vec{r},\vec{v},t) \tag{A.43}$$

where the two terms satisfy the steady-state Vlasov equation and the linearized Vlasov equation respectively (the Fokker-Planck integral can be neglected if $\omega >> \nu_{coll}$):

$$\vec{v}\cdot\nabla F_\alpha + \frac{eZ_\alpha}{m_\alpha}\left(\frac{\vec{v}}{c}\times\vec{B}_0\right)\frac{\partial F_\alpha}{\partial\vec{v}} = 0 \tag{A.44}$$

$$\frac{d\tilde{f}_\alpha}{dt} = \frac{\partial\tilde{f}_\alpha}{\partial t} + \vec{v}\cdot\vec{\nabla}f_\alpha + \frac{eZ_\alpha}{m_\alpha}\left(\frac{\vec{v}}{c}\times\vec{B}_0\right)\frac{\partial\tilde{f}_\alpha}{\partial\vec{v}} = -\frac{eZ_\alpha}{m_\alpha}\left(\vec{E}+\frac{\vec{v}}{c}\times\vec{B}\right)\frac{\partial F_\alpha}{\partial\vec{v}} \tag{A.45}$$

The perturbing fields $\vec{E},\vec{B}$ are assumed of small amplitude, in order to linearize the kinetic equation and get a dielectric tensor. The solution, obtained with the method of characteristics, is:

$$\tilde{f}_\alpha(\vec{r},\vec{v},t) = -\frac{eZ_\alpha}{m_\alpha}\int_{-\infty}^{t}\left[\vec{E}(\vec{r}',t') + \frac{\vec{v}'}{c}\times\vec{B}(\vec{r}',t')\right]\frac{\partial F_\alpha}{\partial\vec{v}'} \tag{A.46}$$

where $\vec{r}' = \vec{r}'(\vec{r},\vec{v},t-t')$ and $\vec{v}' = \vec{v}'(\vec{r},\vec{v},t-t')$ are the solutions of the unperturbed equations of motion:

$$\frac{d\vec{r}'}{dt'} = \vec{v}' \tag{A.47}$$

$$\frac{d\vec{v}'}{dt'} = \frac{eZ_\alpha}{m_\alpha}\left(\frac{\vec{v}'}{c}\times\vec{B}_0\right) \tag{A.48}$$

Substituting the solution in the definition of current density:

$$\vec{j}(\vec{r},t) = \sum_\alpha eZ_\alpha\int\vec{v}f_\alpha(\vec{r},\vec{v},t)d\vec{v} \tag{A.49}$$

we obtain

$$\vec{j}(\vec{r},t) = -\sum_\alpha\frac{n_\alpha e^2Z_\alpha^2}{m_\alpha}\int\vec{v}d\vec{v}\int_{-\infty}^{t}dt'\left\{\left[\vec{E}(\vec{r}',t')+\frac{\vec{v}'}{c}\times\vec{B}(\vec{r}',t')\right]\frac{\partial F_\alpha}{\partial\vec{v}'}\right\} \tag{A.50}$$

The integral is non-local, since $\vec{j}$ depends on motion of particles at previous times. We thus consider quantities (plane waves) in the Fourier space,

$$\vec{E}(\vec{r},t) = \vec{E}_{\vec{k},\omega}e^{i(\vec{k}\cdot\vec{r}-\omega t)} \tag{A.51}$$

$$\tilde{f}_\alpha(\vec{r},\vec{v},t) = \vec{f}^{\alpha}_{\vec{k},\omega}e^{i(\vec{k}\cdot\vec{r}-\omega t)} \tag{A.52}$$

where locality is re-obtained[1]. The distribution function becomes

$$f^{\alpha}_{\vec{k},\omega}(\vec{v}) = -\frac{eZ_\alpha}{m_\alpha}\int_{-\infty}^{t} dt' e^{-i[\vec{k}(\vec{r}-\vec{r}')-\omega(t-t')]}\left\{\left[\vec{E}_{\vec{k},\omega}+\frac{\vec{v}'}{\omega}\times(\vec{k}\times\vec{E}_{\vec{k},\omega})\right]\frac{\partial F_\alpha}{\partial \vec{v}'}\right\} \tag{A.53}$$

and substituting in the current density and comparing the result with the definitions of conductivity tensor and dielectric tensor,

$$\vec{j}_{\vec{k},\omega} = [\sigma]_{\vec{k},\omega}\vec{E}_{\vec{k},\omega} \tag{A.54}$$

$$\epsilon_{ij}(\vec{k},\omega) = \delta_{ij} + \frac{4\pi i}{\omega}\sigma_{ij}(\vec{k},\omega) \tag{A.55}$$

the dielectric tensor is finally obtained:

$$\epsilon_{ij}(\vec{k},\omega) = \delta_{ij} + \sum_\alpha \frac{\omega^2_{p\alpha}}{\omega^2}\int d\vec{v}\left\{-i\omega\int_{-\infty}^{t} dt' e^{-i[\vec{k}\cdot(\vec{r}-\vec{r}')-\omega(t-t')]}\left[\left(1-\frac{\vec{k}\cdot\vec{v}'}{\omega}\right)\frac{\partial F_\alpha}{\partial v'_j}+\left(\frac{\vec{k}}{\omega}\frac{\partial F_\alpha}{\partial \vec{v}'}\right)v'_j\right]\right\} \tag{A.56}$$

where $\omega_{p\alpha} = 4\pi e^2 Z_\alpha n_\alpha/m_\alpha$ is the plasma frequency of the species α.

The general expression of the dielectric tensor has to be written in a reference frame to be explicitly calculable. In order to make results comparable with the Stix cold tensor, we use the same reference frame (x, y, z) with z-axis along the magnetostatic field $\vec{B}_0$ and the x-axis oriented so that the wavevector $\vec{k}$ lies in the (x, z) plane. In the velocity space a convenient reference frame is the cylindrical system with symmetry axis in the direction of $\vec{B}_0$ ($v_\perp$ and $v_{//}$ are constants of motion). In this reference frame the dielectric tensor results:

$$\epsilon_{ij}(\vec{k},\omega) = \delta_{ij} + \sum_\alpha \frac{\omega^2_{p\alpha}}{\omega^2}\int_{-\infty}^{\infty} dv_{||}\int_{-\infty}^{\infty} v_\perp dv_\perp \int_0^{2\pi} d\phi\left\{-i\omega\int_{-\infty}^{t} dt' G^{\alpha}_{\vec{k},\omega}T^{\alpha}_{ij}\right\} \tag{A.57}$$

where

$$G^{\alpha}_{\vec{k},\omega} = G^{\alpha}_{\vec{k},\omega}(v_\perp, v_{||}, \phi, t-t') = e^{-i[\vec{k}\cdot(\vec{r}-\vec{r}')-\omega(t-t')]} \tag{A.58}$$

is the propagator (i.e., the phase of the wave seen by the particle along the unperturbed

[1]Thanks to properties of Helmholtz decomposition

orbit), and the tensor $T_{ij}^{\alpha} = T_{ij}^{\alpha}(\vec{k}, \omega; \vec{v}; t - t')$ is:

$$T_{xx}^{\alpha} = v_{\perp} \cos\phi \left(\frac{\partial F_{\alpha}}{\partial v_{\perp}} + \frac{k_{||}}{\omega} \Theta_v F_{\alpha} \right) \cos\beta \tag{A.59}$$

$$T_{xy}^{\alpha} = v_{\perp} \cos\phi \left(\frac{\partial F_{\alpha}}{\partial v_{\perp}} + \frac{k_{||}}{\omega} \Theta_v F_{\alpha} \right) \sin\beta \tag{A.60}$$

$$T_{xz}^{\alpha} = v_{\perp} \cos\phi \left(\frac{\partial F_{\alpha}}{\partial v_{||}} - \frac{k_{\perp}}{\omega} \Theta_v F_{\alpha} \cos\beta \right) \tag{A.61}$$

$$T_{yx}^{\alpha} = v_{\perp} \sin\phi \left(\frac{\partial F_{\alpha}}{\partial v_{\perp}} + \frac{k_{||}}{\omega} \Theta_v F_{\alpha} \right) \cos\beta \tag{A.62}$$

$$T_{yy}^{\alpha} = v_{\perp} \sin\phi \left(\frac{\partial F_{\alpha}}{\partial v_{\perp}} + \frac{k_{||}}{\omega} \Theta_v F_{\alpha} \right) \sin\beta \tag{A.63}$$

$$T_{yz}^{\alpha} = v_{\perp} \sin\phi \left(\frac{\partial F_{\alpha}}{\partial v_{||}} - \frac{k_{\perp}}{\omega} \Theta_v F_{\alpha} \cos\beta \right) \tag{A.64}$$

$$T_{zx}^{\alpha} = v_{||} \left(\frac{\partial F_{\alpha}}{\partial v_{\perp}} + \frac{k_{||}}{\omega} \Theta_v F_{\alpha} \right) \cos\beta \tag{A.65}$$

$$T_{zy}^{\alpha} = v_{||} \left(\frac{\partial F_{\alpha}}{\partial v_{\perp}} + \frac{k_{||}}{\omega} \Theta_v F_{\alpha} \right) \sin\beta \tag{A.66}$$

$$T_{zz}^{\alpha} = v_{||} \left(\frac{\partial F_{\alpha}}{\partial v_{||}} - \frac{k_{\perp}}{\omega} \Theta_v F_{\alpha} \cos\beta \right) \tag{A.67}$$

where

$$\beta = \phi + \Omega_{c\alpha}(t - t') \tag{A.68}$$

and the differential operator

$$\Theta_v F_{\alpha} = v_{\perp} \frac{\partial F_{\alpha}}{\partial v_{||}} - v_{||} \frac{\partial F_{\alpha}}{\partial v_{\perp}} \tag{A.69}$$

represents the derivative of F_{α} with respect to the pitch angle of the velocity, equal to zero for isotropic velocity distributions.

Two integrations (in time and in ϕ) of Eq.A.57 can be resolved in analytic form using Bessel function expansion, and obtain

$$\epsilon_{ij}(\vec{k}, \omega) = \delta_{ij} - \sum_{\alpha} \frac{\omega_{p\alpha}^2}{\omega^2} \int_0^{\infty} v_{\perp} dv_{\perp} \int_{-\infty}^{\infty} dv_{||} \left[2\pi \sum_{n=-\infty}^{\infty} \frac{\omega}{\omega - n\Omega_c - k_{||} v_{||}} Q_{ij}^{\alpha,n} \right] \tag{A.70}$$

where

$$Q_{xx}^{\alpha,n} = -\frac{n^2}{\xi_\perp^2} J_n^2(\xi\perp) \left(v_\perp \frac{\partial F_\alpha}{\partial v_\perp} + \frac{k_{||} v_\perp}{\omega} \Theta_v F_\alpha \right) \tag{A.71}$$

$$Q_{xy}^{\alpha,n} = -i \frac{n}{\xi_\perp} J_n(\xi_\perp) J_n'(\xi_\perp) \left(v_\perp \frac{\partial F_\alpha}{\partial v_\perp} + \frac{k_{||} v_\perp}{\omega} \Theta_v F_\alpha \right) \tag{A.72}$$

$$Q_{xz}^{\alpha,n} = -\frac{n}{\xi_\perp} J_n^2(\xi\perp) \left(v_\perp \frac{\partial F_\alpha}{\partial v_{||}} - \frac{n\Omega_{c\alpha}}{\omega} \Theta_v F_\alpha \right) \tag{A.73}$$

$$Q_{yx}^{\alpha,n} = -Q_{xy}^{\alpha,n} \tag{A.74}$$

$$Q_{yy}^{\alpha,n} = -J_n^2(\xi\perp) \left(v_\perp \frac{\partial F_\alpha}{\partial v_\perp} + \frac{k_{||} v_\perp}{\omega} \Theta_v F_\alpha \right) \tag{A.75}$$

$$Q_{yz}^{\alpha,n} = i J_n(\xi_\perp) J_n'(\xi_\perp) \left(v_\perp \frac{\partial F_\alpha}{\partial v_{||}} - \frac{n\Omega_{c\alpha}}{\omega} \Theta_v F_\alpha \right) \tag{A.76}$$

$$Q_{zx}^{\alpha,n} = -\frac{n}{\xi_\perp} J_n^2(\xi_\perp) \left(v_{||} \frac{\partial F_\alpha}{\partial v_\perp} + \frac{k_{||} v_{||}}{\omega} \Theta_v F_\alpha \right) \tag{A.77}$$

$$Q_{zy}^{\alpha,n} = -i J_n(\xi_\perp) J_n'(\xi_\perp) \left(v_{||} \frac{\partial F_\alpha}{\partial v_\perp} + \frac{k_{||} v_{||}}{\omega} \Theta_v F_\alpha \right) \tag{A.78}$$

$$Q_{zz}^{\alpha,n} = -J_n^2(\xi_\perp) \left(v_{||} \frac{\partial F_\alpha}{\partial v_{||}} - \frac{n\Omega_{c\alpha}}{\omega} \frac{v_{||}}{v_\perp} \Theta_v F_\alpha \right) \tag{A.79}$$

where the argument of the Bessel function is $\xi\perp = k_\perp v_\perp / \Omega_{c\alpha}$. The Onsager symmetry relations assure some symmetries in the dielectric tensor, $\epsilon_{xy} = -\epsilon_{yx}$, $\epsilon_{xz} = -\epsilon_{zx}$ and $\epsilon_{yz} = -\epsilon_{zy}$, independently on the particular equilibrium distribution function.

A.4 Finite temperature ($T \neq 0$) Maxwellian plasma

When the equilibrium distribution function of each species in the plasma is Maxwellian,

$$F_\alpha(\vec{v}) = \frac{e^{-v^2/v_{th\alpha}^2}}{\pi^3 v_{th\alpha}^3} = F_\alpha^M(v) \tag{A.80}$$

with $v_{th\alpha} = \sqrt{(}2T_\alpha/m_\alpha)$ the most probable (thermal) velocity, then the dielectric tensor results:

$$\epsilon_{xx} = 1 - \sum_\alpha \frac{\omega_{p\alpha}^2}{\omega^2} \sum_{n=-\infty}^{n=+\infty} \frac{n^2}{\lambda_\alpha} I_n(\lambda_\alpha) e^{-\lambda_\alpha} (-x_{0\alpha} Z(x_{n\alpha})) \tag{A.81}$$

$$\epsilon_{xy} = -i \sum_\alpha \frac{\omega_{p\alpha}^2}{\omega^2} \sum_{n=-\infty}^{n=+\infty} n \left[I_n'(\lambda_\alpha) - I_n(\lambda_\alpha) \right] e^{-\lambda_\alpha} (-x_{0\alpha} Z(x_{n\alpha})) \tag{A.82}$$

$$\epsilon_{xz} = -\frac{1}{2} n_\perp n_{||} \sum_\alpha \frac{\omega_{p\alpha}^2}{\omega \Omega_{c\alpha}} \frac{v_{th\alpha}^2}{c^2} \sum_{n=-\infty}^{n=+\infty} \frac{n}{\lambda_\alpha} I_n(\lambda_\alpha) e^{-\lambda_\alpha} (x_{0\alpha}^2 Z'(x_{n\alpha})) \tag{A.83}$$

$$\epsilon_{yx} = -\epsilon_{xy} \tag{A.84}$$

$$\epsilon_{yy} = 1 - \sum_\alpha \frac{\omega_{p\alpha}^2}{\omega} \sum_{n=-\infty}^{n=+\infty} \left\{ \frac{n^2}{\lambda_\alpha} I_n(\lambda_\alpha) - 2\lambda_\alpha [I_n'(\lambda_\alpha) - I_n(\lambda_\alpha] \right\} e^{-\lambda_\alpha} (-x_{0\alpha} Z(x_{n\alpha})) \tag{A.85}$$

$$\epsilon_{yz} = \frac{i}{2} n_\perp n_{||} \sum_\alpha \frac{\omega_{p\alpha}^2}{\omega \Omega_{c\alpha}} \frac{v_{th\alpha}^2}{c^2} \sum_{n=-\infty}^{n=+\infty} [I_n'(\lambda_\alpha) - I_n(\lambda_\alpha)] e^{-\lambda_\alpha} (x_{0\alpha}^2 Z'(x_{n\alpha})) \tag{A.86}$$

$$\epsilon_{zx} = \epsilon_{xz} \tag{A.87}$$

$$\epsilon_{zy} = -\epsilon_{yz} \tag{A.88}$$

$$\epsilon_{zz} = 1 - \sum_\alpha \frac{\omega_{p\alpha}^2}{\omega^2} \sum_{n=-\infty}^{n=+\infty} I_n(\lambda_\alpha) e^{-\lambda_\alpha} (x_{0\alpha} x_{n\alpha} Z'(x_{n\alpha})) \tag{A.89}$$

where the dimensionless quantities are :

$$\lambda_\alpha = \mu_\alpha^2/2 = k_\perp^2 v_{th\alpha}^2 / 2\Omega_{c\alpha}^2 \tag{A.90}$$

$$x_{n\alpha} = \frac{\omega - n\Omega_{c\alpha}}{k_{||} v_{th\alpha}} \tag{A.91}$$

$$\mu_\alpha = r_{L\alpha} k_\perp \qquad \text{ratio of Larmor radius over the wavelength} \tag{A.92}$$

$$r_{L\alpha} = v_{th\alpha}/\Omega_{c\alpha} \qquad \text{thermal Larmor radius} \tag{A.93}$$

and the plasma dispersion function is

$$Z(\zeta) = \frac{1}{\sqrt{\pi}} \int_{-\infty}^{\infty} \frac{e^{-u^2}}{u - \zeta} du + i\sigma\sqrt{\pi} e^{-\zeta^2} \tag{A.94}$$

with

$$\sigma = 0 \quad \text{for } Im(\zeta) > 0 \tag{A.95}$$

$$\sigma = 1 \quad \text{for } Im(\zeta) = 0 \tag{A.96}$$

$$\sigma = 2 \quad \text{for } Im(\zeta) < 0 \tag{A.97}$$

The dispersion function can be calculated using one of the following formulae (only one can be chosen depending on the computational needs):

$$Z(\zeta) = i\sqrt{\pi}\mathrm{Erfc}(i\zeta) \tag{A.98}$$

$$Z(\zeta) = i\sqrt{\pi}e^{-\xi^2} - 2\zeta\sum_{n=0}^{\infty} c_n\zeta^{2n} \quad c_0 = 1 \quad c_{n+1} = -2c_n/(2n+1) \tag{A.99}$$

$$Z(\zeta) \approx i\sigma\sqrt{\pi}e^{-\zeta^2} - \frac{1}{\zeta}\sum_{n=0}^{\infty}\frac{d_n}{\zeta^{2n}} \quad d_0 = 1 \quad d_{n+1} = \frac{2n+1}{2}d_n \quad \text{(for large } \zeta) \tag{A.100}$$

$$Z(\zeta) = e^{-\zeta^2}\left[i\sqrt{\pi} - \zeta\sum_{n=0}^{\infty}\frac{\zeta^{2n}}{n!(2n+1)}\right] \quad (\text{for } |\zeta| = O(1)) \tag{A.101}$$

and its derivative is:

$$Z'(\zeta) = -2[1 + \zeta Z(\zeta)] \tag{A.102}$$

The series comparing in the dielectric tensor is rapidly convergent for small λ_α. When $\lambda_\alpha \to 0$ only the $n = 0$ term does not vanishes (cold plasma). In the regime of small $\lambda_\alpha << 1$ the terms $\epsilon_{xz} = \epsilon_{zx}$ and $\epsilon_{yz} = \epsilon_{zy}$ are one power of λ_α smaller than the others, i.e. they tend to the cold plasma limit. The anti-Hermitian part of the dielectric tensor (related to the irreversible exchange of energy between the wave and the plasma) is different than zero when $|x_{n\alpha}| = O(1)$, occurring at Cerenkov resonance ($n = 0$), cyclotron resonances ($n = 1$) and cyclotron harmonics ($n > 1$).

A.5 Plasma with two Maxwellian populations

When the plasma is composed by two Maxwellian populations at a different temperatures (B: Bulk and T: Tail),

$$F(v_B, v_T) = \nu_B\frac{e^{-v^2/v_{thB}^2}}{\pi^{3/2}v_{thB}^3} + \nu_T\frac{e^{-v^2/v_{thT}^2}}{\pi^{3/2}v_{thT}^3} \tag{A.103}$$

with $\nu_{B,T}$ their concentrations, it is sufficient to treat each population as a separate species in the treatment described in the previous paragraph.

A.6 Finite Larmor radius effects

When the wavelengths are larger than the ion thermal Larmor radius, or of the same order of magnitude, a Larmor radius expansion of the dielectric tensor is convenient. The original distribution function is rewritten as a sum of anisotropic Maxwellian distributions,

$$F_\alpha(v_\perp, v_{||}) = \sum_\nu F_{\alpha\nu}(v_\perp, v_{||}) = \sum_\nu \frac{e^{-v_\perp^2/\alpha_{\perp\nu}^2}}{\pi\alpha_{\perp\nu}^2}\frac{e^{-v_{||}^2/\alpha_{||\nu}^2}}{\sqrt{\pi}\alpha_{\perp\nu}^2}\Psi_\nu(v_\perp^2, v_\perp) \tag{A.104}$$

with $\alpha_{||\nu}$ and $\alpha_{\perp\nu}$ now the thermal speeds. The dielectric tensor results:

$$\epsilon_{xx} = 1 - \sum_\alpha \frac{\omega_{p\alpha}^2}{\omega^2} \sum_{n=-\infty}^{+\infty} \frac{n^2}{\lambda} \sum_{k=0}^{\infty} \frac{C_{n,k}}{n!k!} \left(\frac{\lambda}{2}\right)^{|n|+k} \left[-x_0 \tilde{Z}^{(|n|+k-1)}(x_n) - \frac{1}{2} n_{||}^2 \frac{\alpha_{||}^2}{c^2} Y^{(|n|+k)}(x_n) \right] \tag{A.105}$$

$$\epsilon_{xy} = -i \sum_\alpha \frac{\omega_{p\alpha}^2}{\omega^2} \sum_{n=-\infty}^{+\infty} \frac{n|n|}{\lambda} \sum_{k=0}^{\infty} \frac{D_{n,k}}{n!k!} \left(\frac{\lambda}{2}\right)^{|n|+k} \left[-x_0 \tilde{Z}^{(|n|+k-1)}(x_n) - \frac{1}{2} n_{||}^2 \frac{\alpha_{||}^2}{c^2} Y^{(|n|+k)}(x_n) \right] \tag{A.106}$$

$$\epsilon_{xz} = -\frac{1}{2} n_{||} n_\perp \sum_\alpha \frac{\omega_{p\alpha}^2}{\Omega_{c\alpha}\omega} \frac{\alpha_\perp^2}{c^2} \sum_{n=-\infty}^{+\infty} \frac{n}{\lambda} \sum_{k=0}^{\infty} \frac{C_{n,k}}{n!k!} \left(\frac{\lambda}{2}\right)^{|n|+k} \left[x_0^2 \tilde{Z}'^{(|n|+k)}(x_n) + \frac{n\Omega_\alpha}{\omega} \frac{\alpha_{||}^2}{\alpha_\perp^2} Y^{(|n|+k)}(x_n) \right] \tag{A.107}$$

$$\epsilon_{yx} = -\epsilon xy \tag{A.108}$$

$$\epsilon_{yy} = 1 - \sum_\alpha \frac{\omega_{p\alpha}^2}{\omega^2} \sum_{n=-\infty}^{+\infty} \frac{n^2}{\lambda} \sum_{k=0}^{\infty} \frac{T_{n,k}}{n!k!} \left(\frac{\lambda}{2}\right)^{|n|+k} \left[-x_0 \tilde{Z}^{(|n|+k-1)}(x_n) - \frac{1}{2} n_{||}^2 \frac{\alpha_{||}^2}{c^2} Y^{(|n|+k)}(x_n) \right] \tag{A.109}$$

$$\epsilon_{yz} = \frac{i}{2} n_{||} n_\perp \sum_\alpha \frac{\omega_{p\alpha}^2}{\Omega_{c\alpha}\omega} \frac{\alpha_\perp^2}{c^2} \sum_{n=-\infty}^{+\infty} \frac{|n|}{\lambda} \sum_{k=0}^{\infty} \frac{D_{n,k}}{n!k!} \left(\frac{\lambda}{2}\right)^{|n|+k} \left[x_0^2 \tilde{Z}'^{(|n|+k)}(x_n) + \frac{n\Omega_\alpha}{\omega} \frac{\alpha_{||}^2}{\alpha_\perp^2} Y^{(|n|+k)}(x_n) \right] \tag{A.110}$$

$$\epsilon_{zx} = \epsilon xz \tag{A.111}$$

$$\epsilon_{zy} = \epsilon yz \tag{A.112}$$

$$\epsilon_{zz} = 1 - \sum_\alpha \frac{\omega_{p\alpha}^2}{\omega^2} \sum_{n=-\infty}^{+\infty} \sum_{k=0}^{\infty} \frac{C_{n,k}}{n!k!} \left(\frac{\lambda}{2}\right)^{|n|+k} \left(\frac{\omega - n\Omega_\alpha}{\omega}\right) \left[x_0^2 \tilde{Z}'^{(|n|+k)}(x_n) + \frac{n\Omega_\alpha}{\omega} \frac{\alpha_{||}^2}{\alpha_\perp^2} Y^{(|n|+k)}(x_n) \right] \tag{A.113}$$

where the non-dimensional parameters are:

$$\lambda = \mu^2/2 = k_\perp^2 \alpha_\perp^2 / 2\Omega_c^2 \tag{A.114}$$

$$x_n = \frac{\omega - n\Omega_c}{k_{||}\alpha_{||}} \tag{A.115}$$

$$w = v_\perp/\alpha_\perp \tag{A.116}$$

$$u = v_{||}/\alpha_{||} \tag{A.117}$$

the plasma dispersion functions are

$$\tilde{Z}^p(\zeta) = \frac{1}{\sqrt{\pi}} \int_{-\infty}^{+\infty} \frac{e^{-u^2}}{u-\zeta} g^{(p)}(u) du \tag{A.118}$$

$$\tilde{W}^p(\zeta) = \frac{1}{\sqrt{\pi}} \int_{-\infty}^{+\infty} \frac{e^{-u^2}}{u-\zeta} \frac{dg^{(p)}(u)}{du} du \tag{A.119}$$

$$Y^{(|n|+k)}(x_n) = x_0^2 \left[\tilde{Z}'^{(|n|+k-1)}(x_n) - \tilde{W}^{(|n|+k-1)}(x_n) - \frac{\alpha_\perp^2}{\alpha_{||}^2} \tilde{Z}'^{(|n|+k)}(x_n) \right] \tag{A.120}$$

the reduced distribution is:

$$g^{(p)}(u) = \frac{2}{p!} \int_0^\infty w^{2p+1} e^{-w^2} \Psi(w,u) \tag{A.121}$$

and the other factors are

$$D_{n,k} = \left(1 + \frac{k}{|n|}\right) C_{n,k} \tag{A.122}$$

$$T_{n,k} = \left[1 + \frac{2k(2|n|+k)(|n|+k-1)}{n^2(2|n|+2k-1)}\right] C_{n,k} \tag{A.123}$$

$$C_{n,k} = \frac{(-1)^k |n|! [2(|n|+k)]!}{(2|n|+k)!(|n|+k)!} \tag{A.124}$$